Design of Radical Materials and Systems Towards Opto-spintronics

Swansea University
Prifysgol Abertawe

John Hudson

Department of Chemistry
Swansea University

supervised by
Dr Emrys Evans

Submitted to Swansea University in fulfilment of
the requirements for the degree of

Doctor of Philosophy

June 2024

Declarations

This work has not previously been accepted in substance for any degree and is not being concurrently submitted in candidature for any degree.

Signed: John Hudson Date: 16/02/2025

This thesis is the result of my own investigations, except where otherwise stated. Other sources are acknowledged giving explicit references, with a bibliography appended.

Signed: John Hudson Date: 16/02/2025

I hereby give consent for my thesis, if accepted, to be available for electronic sharing.

Signed: John Hudson Date: 16/02/2025

The University's ethical procedures have been followed and, where appropriate, that ethical approval has been granted.

Signed: John Hudson Date: 16/02/2025

Abstract

Luminescent organic radicals can exploit optical transitions between doublet-spin ground and excited states for which potential applications are being explored in more efficient organic light-emitting diodes (OLEDs). In this thesis we investigate how the unpaired electron in radicals enable fundamental mechanisms for energy and spin control that could be used in future optoelectronic and opto-spintronic technologies. The design of photon-spin mechanisms towards target functions requires understanding of how the 'extra spin' of radicals affects their optical, spin and magnetic properties. Here we study the emergent photo- and spin physics from pairing known closed-shell organic molecules with luminescent open-shell radicals. Following a description of the photophysical mechanisms and magnetic interactions of closed-shell and open-shell molecular species, we set out a review on the use of radicals as emissive components in optoelectronics. We then explore the potential of exploiting reversible energy transfer between triplet and doublet states to establish magnetosensitive luminescence and spin polarisation. This is followed by experimental work combining the organometallic deep-blue phosphor FIr6 with the 'fruit-fly' TTM-1Cz radical. Förster-mediated triplet-doublet energy transfer with nanosecond lifetime ($k = 3.1 \times 10^7$ s^{-1}), high efficiency ($85 \pm 25\%$), and without the need for triplet diffusion in film blends is demonstrated. Finally, we explore the magnetosensitivity of systems involving energy transfer between radical doublet and acene triplet species. From photophysical and spin-resonance analysis, we focus on the interaction of doublet states with paramagnetic triplet species towards establishing design rules for applications that span from OLEDs to 'spin sensitisers' and magnetic-field inclination sensors.

Acknowledgements

I would like to give thanks to those who over the past four years have provided both the professional and personal support to make this thesis possible, as well as the Engineering and Physical Sciences Research Council and the SCI for their support of this research.

In particular, I would like to thank Dr Emrys Evans for exceeding every expectation of what it means to be a great supervisor. The support and passion that you bring to research is inspiring, and I am grateful for how you have always prioritised my professional and scientific development. I feel privileged to have been your student. Diolch yn fawr iawn.

Thank you to the many researchers at Swansea University in the Department for Chemistry, as well as in the SPECIFIC and SerSAM research groups. Through offering lab space, equipment and training you allowed me to carry out my research and showed the collaborative spirit that makes Swansea a very special place to work. In particular, I would like to thank Dr Drew Riley for his mentorship on ultrafast spectroscopy as well as Dr Rodrigo Garcia-Rodriguez. To Kieran, Michael and Jacob: it is a pleasure to work alongside you. To the technical and support staff at Swansea University, thank you for your invaluable work that allowed me to focus on the science.

Outside of Swansea, I would like to thank collaborators in the group of Prof. Feng Li and Prof. Tetsuro Kusamoto for the synthesis of the luminescent radicals that are studied within this thesis. Many thanks are also given to Dr Emma Richards at Cardiff University for help with electron spin resonance measurements of radical systems.

On a personal note, I am grateful to my friends and family for providing an escape from research and sharing the beauty of South Wales with me over the past 4 years. To my Dad, thank you for your encouragement to push myself and for many enjoyable hours on our bikes. To my Mum, thank you for being my first inspiration and for your love and guidance. To my partner Julia, I feel very lucky for your love, friendship and support. The last six years of my life have been bright for having you in them.

Contents

Chapter 1

Introduction

The field of opto-spintronics looks to create devices that interface the interactions of light, charge and spin. Together with molecular quantum information science, opto-spintronics motivate the development of π-conjugated organic semiconductors that have potential for excellent optical and spin properties. This thesis focusses on new mechanisms for control and read-out of spin by light in molecular materials based on organic radicals.

Organic radicals possess unpaired electrons that result in paramagnetic doublet-spin ($S = 1/2$) ground and excited-state manifolds, enabling optical transitions beyond the singlet-triplet photophysics of closed-shell systems with diamagnetic singlet ($S = 0$) ground states. However, organic radicals have typically been considered as dark and reactive species, with mechanisms for radical interaction often inferred by their effects on the photophysical or magnetic response of closed-shell species. Many radicals undergo fast non-radiative relaxation that prevents photophysical characterisation of the processes or states formed when radicals interact with other species.

The emergence of luminescent triphenylmethyl-based radicals with nanosecond lifetimes of emission enables optical characterisation of doublet excited states, opening understanding for how radical spin character influences the dynamics of charge and energy in molecular systems. In this thesis we explore the interplay of optical, spin and magnetic properties of luminescent radicals towards understanding and exploiting photon-spin mechanisms. Taking advantage of the paramagnetic nature of radical ground and excited states, we look to combine radicals with closed-shell chromophore systems to study new photon-spin physics resulting from energy and charge transfer. Through studying the photophysical properties of luminescent radicals systems, we establish system design rules towards applications including efficient energy harvesters, triplet sensitisers, and magnetic field inclination sensors.

In Chapter 2, we set out a theoretical framework for understanding emission from luminescent radicals and their integration into optoelectronic technologies such as organic light-emitting diodes (OLEDs). This is followed in Chapter 3 by an outline of the photophysical and spin-resonance techniques used to characterise the optical, spin and magnetic properties of radical systems.

In Chapter 4, we explore the potential for exploiting reversible energy transfer between triplet and doublet species towards generating magnetosensitive photoluminescence and spin-polarisation in systems. The dependence of the proposed photon-spin mechanism on the sign and size of the exchange interaction between species is investigated, such that we set out design rules for maximising the magnetic response of triplet-doublet systems.

In Chapter 5, we look at the interaction of luminescent radicals with triplets in organometallic complexes possessing high levels of spin-orbit coupling. We demonstrate efficient dipole-mediated triplet-doublet energy transfer to radical species, without the need for triplet diffusion. We then set out how long-range FRET transfer to radicals could be maximised towards energy harvesting, as well as discussing the role of spin-orbit coupling in systems towards the generation of spin polarisation.

The magnetosensitivity of photoluminescence from radical-acene systems is then set out with a particular focus on intermolecular radical-acene processes. In Chapter 6, the use of radicals as energy harvesters in solid-state acene films is investigated with a particular focus on quenching of the intensity and magnetosensitivity of rubrene emission. In Chapter 7, sensitisation of acene triplet states by radical doublets is investigated by photophysical and spin resonance techniques. Magnetosensitivity of systems showing reversible doublet-triplet energy transfer is explored in the context of the findings of Chapter 4.

Finally, in Chapter 8 we outline how our investigations inform the design of radical systems towards opto-spintronic systems, including how future avenues for research could exploit the unique combination of optical, spin and magnetic properties of luminescent radicals.

Chapter 2

Background and Theory

Sections 2.4-2.8 detailing the principles of emission from luminescent radicals and their applications in emissive optoelectronics have been adapted from a perspective article published in collaboration with Dr Tim Hele and Dr Emrys Evans.[1]

2.1 Photophysics of Molecular Organic Semiconductors

2.1.1 Electronic Structure

Organic molecules primarily consist of covalently bonded carbon and hydrogen atoms, with further molecular versatility and functionality provided by heteroatoms including nitrogen, oxygen and sulphur.[2] Molecular backbones are constructed from σ-orbitals with electron density between atomic centres. In organic molecular semiconductors, delocalisation over the p-orbitals of neighbouring atoms results in the formation of molecular π-orbitals with electron density above and below the plane of the molecular backbone.[3] Functional spin-optical properties in molecular materials as explored in this thesis are derived from electrons associated with these molecular π-orbitals.

For even-electron molecular systems, constructive and destructive interference of p-orbitals results in the formation of bonding and anti-bonding π-molecular orbitals respectively.[2] Greater levels of π-delocalisation in molecules are seen to result in smaller energetic splitting of bonding and anti-bonding orbitals. Typical molecules show splitting of π bonding and anti-bonding orbitals in the range of light in the visible spectrum (1.0-3.0 eV), such that visible photons can mediate π-orbital molecular transitions.[2] We note that whilst transitions of electrons in σ-orbitals are additionally possible, they have substantially higher energy (on order of 10 eV)[3] than that of visible light, and so are ignored for this thesis.

2.1.2 Excitons as Molecular Excitations

The lowest energy electronic excitation of a molecule typically results from the promotion of an electron from the highest occupied molecular orbital (HOMO) to the lowest unoccupied molecular orbital (LUMO). Coulombic attraction between the positively charged hole within the HOMO and the negatively charged electron within the LUMO results in the formation of bound electron-hole pairs known as excitons. In molecular systems, strong coulombic attraction results in excitonic binding energies on the order of 0.5-1.0 eV, where electron and hole are either on the same molecule or neighbouring molecules.[4] This is energetically large compared to the available thermal energy at room temperature ($k_B T \approx 25$ meV) such that excitons cannot easily dissociate to form free charges.

Strong coulomb interactions generally result in high degrees of overlap between electron and hole wavefunctions, leading to strong exchange interactions (see Section 2.3.2) on the order of 0.1-1.0 eV.[4] Excitons in molecular semiconductors as a result have distinct overall spin character, with different exciton spin configurations being physically distinct, having different energy and undergoing different photophysical processes as discussed below. In closed-shell molecules, the ground state of a molecule has singlet (S=0) character, whilst excited states can have both singlet or triplet (S=1) character.

2.1.3 Transitions Between Intramolecular Excitonic States

This thesis is primarily concerned with the role and control of spin in molecular photophysical processes. Transitions between excitonic states can occur due to coupling of states by molecular interactions, with the rate of transition being described using Fermi's Golden Rule:[5,6]

$$k_{\mathrm{if}} = \frac{2\pi}{\hbar} \left| \langle \psi_f \left| \hat{H}' \right| \psi_i \rangle \right|^2 \rho_E \tag{2.1}$$

where k_{if} is the rate of transition between initial and final molecular states i and f, respectively, ψ_i and ψ_f are the electronic wavefunctions of initial and final states, $\hat{H}'$ is the Hamiltonian for an electronic coupling interaction, and ρ_E is the energetic density of states for the final state.

In describing the overall wavefunctions of molecular excited states, we can use the Born-Oppenheimer approximation to separate the wavefunction for a molecule into separate electronic, vibration and spin components:

$$|\psi\rangle = |\psi_{\mathrm{el}}\rangle \, |\psi_{\mathrm{vib}}\rangle \, |\psi_{\mathrm{spin}}\rangle \tag{2.2}$$

where $|\psi_{\text{el}}\rangle$, $|\psi_{\text{vib}}\rangle$ and $|\psi_{\text{spin}}\rangle$ are the electronic, vibrational and spin components for a wavefunction $|\psi\rangle$ respectively.

Light-Mediated Intramolecular Transitions

The distribution of π-orbital electrons can differ between initial and final states of an intramolecular transition, such that the transition has an associated electric dipole. The oscillating electric field of a photon can interact with this dipole via the transition dipole operator, $\hat{\mu}$. Using equation 2.1, the rate of a light-mediated transition can be described as:

$$k_{\text{if}} = \frac{2\pi}{\hbar} \left| \langle \psi_f \, | \hat{\mu} | \, \psi_i \rangle \right|^2 \rho_E \tag{2.3}$$

$\langle \psi_f \, | \hat{\mu} | \, \psi_i \rangle$ is referred to as the transition dipole moment between initial and final states, and can be used to define the strength of transitions involving either absorption or emission of a photon by a molecule.[5,6] $\hat{\mu}$ can be considered to only interact with the electronic distribution of a molecule, such that the transition dipole moment can be rewritten as:

$$\langle \psi_f \, | \hat{\mu} | \, \psi_i \rangle = \langle \psi_{\text{el},f} \, | \hat{\mu} | \, \psi_{\text{el},i} \rangle \, \langle \psi_{\text{vib},f} | \psi_{\text{vib},i} \rangle \, \langle \psi_{\text{spin},f} | \psi_{\text{spin},i} \rangle \tag{2.4}$$

In this form, we observe that the rate of transition between states with different spin character is expected to be zero. Whilst these 'spin-forbidden' transitions can still occur, they are typically orders of magnitude weaker than other 'spin-allowed' processes. Emission due to a transition between states of similar spin-character is called 'fluorescence' and typically occurs with radiative rates on the order of 10^7-10^{10} s^{-1}.[4] Meanwhile, emission resulting from a transition between states of different spin character is called 'phosphorescence' and typically occurs much slower with rates of 10^4-10^6 s^{-1}. Absorption for fully spin-allowed transitions can be up to 7 orders of magnitude stronger than spin-forbidden transitions.[4]

Considering the electronic component of the transition dipole moment, we see that orbital overlap of initial and final states must be non-zero to enable a transition. Strong transition dipole moments typical of molecular semiconductors can be understood through the polarisability of π-orbitals enabling both a high orbital overlap and strong electric dipole between initial and final states. Excited states with minimal electronic overlap with the molecular ground state are classified as having substantial charge-transfer character, with greater charge-transfer character typically associated with weaker transition dipole moments.[6]

Finally, the need for overlap of the vibrational component of initial and final states

can result in additional structure in the absorption and emission spectra of molecules. Vibrational energy levels are typically separated by 100-300 meV, such that typically only the lowest vibrational mode of a molecule is populated following relaxation.[4] The lowest energy absorption for an electronic transition occurs between the zeroth order vibrational mode of initial and final states, with further vibronic features seen at higher energy for transition to higher final state vibrational modes. The highest energy emission for an electronic transition occurs similarly between the zeroth order vibrational mode of initial and final states, with transitions to higher vibrational modes of the final state resulting in lower energy vibronic features. For a molecule without molecular re-organisation in the excited state, it would be expected for the lowest energy absorption and highest energy emission of the excited state to occur at the same energy. In practice, the lowest energy absorption and highest energy emission do not overlap, with this difference in energy referred to as the 'Stokes shift' giving a sense of the degree of molecular reorganisation in the excited state.[4]

Non-Radiative Intramolecular Transitions

Transitions between molecular excited states can additionally occur non-radiatively, with states coupled by interactions other than the electric dipole operator. Nuclear motion can couple excited molecular states, resulting in fast relaxation from higher vibrational modes to the zeroth order vibrational mode of an electronic state on femtosecond-to-picosecond timescales. Nuclear motion can additionally couple an electronic state to higher vibrational modes of lower energy electronic states. Where transition is between states with the same spin manifold, this process is called internal conversion. The 'energy-gap law' states that the rate of internal conversion is expected to increase exponentially as the energy gap between electronic states is reduced. In practice, this results in Kasha's rule where internal conversion between closer spaced higher-order electronic levels of a given spin multiplicity (S_n to S_1, T_n to T_1) is expected to be much faster than emission, whereby we can expect emission to come solely from the lowest energy electronic state of a given spin manifold (S_1,T_1).[6]

Non-radiative transitions are additionally possible between states with different spin character, being classified as intersystem crossing. The rates of intersystem crossing can be enhanced for systems which possess high levels of spin-orbit coupling. Higher levels of spin-orbit coupling are typically seen for molecular systems containing heavier atomic elements, with both radiative and non-radiative transitions enhanced due to greater mixing of spin character between excited states.

2.2 Energy Transfer for Opto-Spintronics

Excitations in amorphous systems can perform incoherent energy transfer to other molecular species. In addition to 'trivial' energy transfer where a molecule emits a photon that is subsequently reabsorbed by another molecule,[4] energy can transfer through non-radiative coupling of molecules. Using Fermi's Golden Rule as outlined in equation 2.1, the rate of a transition between intermolecular states can be related to their non-radiative electronic coupling. For molecular systems, we assume that non-radiative coupling can occur through the coulomb interaction to result in Förster Resonance Energy Transfer (FRET), or through the exchange interaction to result in Dexter Energy Transfer.

2.2.1 Förster Resonance Energy Transfer (FRET)

Electric dipoles between molecular ground and excited states are typically strong in molecular organic semiconductors. In FRET, the coulomb interaction couples the electric-dipole of an excited state molecule to those of neighbouring molecules that are in the ground state.

The rate of FRET shows an R^{-6} dependence, where R is the distance between donor and acceptor species. This dependence results from both the probability that the pair of electric dipoles are in resonance and the R^{-3} dependence expected for transfer between resonant dipoles.[7–9]

Towards experimental prediction of FRET rates, we are able to measure the spectral overlap integral, J, between donor and emitter species:

$$J = \int I_D(\lambda)\, \epsilon_A(\lambda)\, \lambda^4 d\lambda \tag{2.5}$$

where $I_D(\lambda)$ is the photoluminescence spectra for the donor normalised to an area of 1, $\epsilon_A(\lambda)$ is the extinction coefficient in $\mathrm{M^{-1}cm^{-1}}$ of the acceptor, and λ is the wavelength of radiation.[4] The spectral overlap provides an experimentally measureable quantity that can be related to the likelihood of resonance between donor and acceptor electric dipoles.

FRET is expected to quench donor emission. Using J, a FRET radius, R_0, is estimated at which the FRET rate is equal to the instrinsic rate of decay for an isolated photoexcited species:

$$R_0^6 = \frac{9 \ln 10}{N_A} \frac{1}{2^7 \pi^5 n^4} \Phi \kappa^2 J \tag{2.6}$$

where N_A is Avogadro's constant, n is the refractive index of the medium surrounding

the donor and acceptor molecules, Φ is the photoluminescence quantum yield of the isolated donor, and κ^2 is the orientation factor that accounts for the alignment of donor and acceptor dipoles ($\kappa^2 = 2/3$ for randomly orientated dipoles).

Using R_0, the FRET rate between donor and acceptor k_{FRET} can be found for a given distance R:

$$k_{\text{FRET}} = \frac{1}{\tau_D^0}\left(\frac{R_0}{R}\right)^6 \tag{2.7}$$

where τ_D^0 is the lifetime of the donor in the absence of FRET.[10] Typical values for R_0 range from 2-5 nm depending on the level of spectral overlap. This results in FRET typically occuring for distances up to 10 nm, such that it is considered a 'through space' interaction. FRET is typically maximised for molecular systems with bright emission as a result of strong electric dipoles for emission.

2.2.2 Dexter Energy Transfer

Dexter energy transfer is mediated by the electron-exchange interaction, involving the correlated transfer of two electrons between donor and acceptor species.[11] As it is mediated by the exchange interaction, Dexter energy transfer requires overlap between electron density on both the excited state donor molecule and a ground state acceptor molecule. The Dexter energy transfer rate decreases exponentially with increasing distance between donor and acceptor, R:

$$k_{\text{DET}} \propto \exp\left(-\frac{2R}{L}\right) \tag{2.8}$$

where L is a constant related to van de Waals' radius of donor and acceptor, which is assumed to decrease exponentially with distance. The exponential dependence of Dexter energy transfer on donor-acceptor distance results in energy typically transferring to nearest neighbours, with typical distances for transfer ranging from 0.1-1 nm.[12] Unlike FRET, Dexter energy transfer can occur for states that have weak or no emission.

2.2.3 Spin Considerations in Energy Transfer

Whilst covered more fully in other reference texts,[4] the interaction energy $\beta = \langle \psi_f \left| \hat{H}' \right| \psi_i \rangle$ between donor and acceptor can be separated for a two-electron system into coulombic β^C and exchange-related β^E terms if interactions are assumed to not couple electronic and spin degrees of freedom. It can be shown that $\beta = \beta^C - \beta^E$ with:

$$\beta^C = \left\langle \psi_{\mathrm{el,D}}(1)\,\psi^*_{\mathrm{el,A}}(2) \left| \hat{H}' \right| \psi^*_{\mathrm{el,D}}(1)\,\psi_{\mathrm{el,A}}(2) \right\rangle \left\langle \psi_{\mathrm{spin,D}}(1) \left| \psi^*_{\mathrm{spin,D}}(1) \right\rangle \left\langle \psi^*_{\mathrm{spin,A}}(2) \left| \psi_{\mathrm{spin,A}}(2) \right\rangle \right.\right. \tag{2.9}$$

$$\beta^E = \left\langle \psi_{\mathrm{el,D}}(1)\,\psi^*_{\mathrm{el,A}}(2) \left| \hat{H}' \right| \psi^*_{\mathrm{el,D}}(2)\,\psi_{\mathrm{el,A}}(1) \right\rangle \left\langle \psi_{\mathrm{spin,D}}(1) \left| \psi_{\mathrm{spin,A}}(1) \right\rangle \left\langle \psi^*_{\mathrm{spin,A}}(2) \left| \psi^*_{\mathrm{spin,D}}(2) \right\rangle \right.\right. \tag{2.10}$$

where $\psi_{\mathrm{el,A}}(1)$ represents the electronic wavefunction for electron 1 in the ground state of the acceptor, and $\psi^*_{\mathrm{spin,D}}(2)$ represents the spin wavefunction for electron 2 on the excited state of the donor.

From this we can see that the coulombic term requires spin-overlap for both the ground and excited state of the donor, as well as the ground and excited state of the acceptor. However, there is absolutely no requirement placed on the relative spins of the donor and acceptor species - with the interaction being ‘through-space’, meaning no spin-information can be passed to an acceptor during FRET.

Meanwhile, the exchange term requires overlap of spin for the ground state of both the acceptor and donor, as well as the excited state of both the acceptor and donor. In Dexter energy transfer the spin-character of the donor is therefore passed to the acceptor molecule via the ‘through bond’ interaction allowing for spin-information to be maintained in the system.

2.3 Magnetic Interactions of Organic Molecular Systems

In this thesis we are concerned with understanding the magnetic response of radical-triplet systems, which are primarily governed by the Zeeman, exchange and triplet zero-field splitting (ZFS) interactions.

2.3.1 Zeeman

The Zeeman interaction $\hat{\mathrm{H}}_{\mathrm{Z}}$ describes the energy of a spin within an externally applied magnetic field **B**. Considering electronic spins:

$$\hat{\mathrm{H}}_{\mathrm{Z}} = g_e \mu_B \mathbf{B} \cdot \hat{\mathbf{S}} \tag{2.11}$$

where g_e is the electronic g-factor(~ 2.0023), μ_B is the Bohr magneton and $\hat{S}$ is the spin operator for a spin experiencing magnetic field **B**.[13] In systems dominated by the Zeeman interactions, states have energy $\mathrm{E} = -m_z g_e \mu_B B$ where B is the magnitude of the applied magnetic field, and m_z is the spin projection quantum number for the spin in the applied magnetic field.

In the case of molecular spins, spin-orbit coupling interactions from electrons within the molecule can both shield or amplify the magnetic field applied to the system such that a spin experiences a different magnetic field strength locally. Differences in the energetic splitting of different spin states are accounted for by the use of an 'effective' g-value that accounts for the local electronic spin environment.[14] In systems combining molecular states with different effective g-values, we can see mixing between spin states via a Δg-mechanism.

2.3.2 Exchange

The exchange interaction $\hat{\mathrm{H}}_{\mathrm{ex}}$ is a quantum mechanical modulation of the coulomb interaction in systems comprising two or more spins:

$$\hat{\mathrm{H}}_{\mathrm{ex}} = -J\hat{\mathbf{S}}_1 \cdot \hat{\mathbf{S}}_2 \tag{2.12}$$

where J is the exchange coupling paramater for two spins $\hat{\mathbf{S}}_1$ and $\hat{\mathbf{S}}_2$.[13] The exchange interaction arises from the need for electronic wavefunctions to have overall antisymmetric symmetry, and that this can result in the spatial wavefunctions differing for states with different spin character.

The classic example of this occurs in closed-shell systems, where the intramolecular exchange interaction causes a splitting between singlet and triplet states. Singlet and

triplet states have antisymmetric and symmetric spin wavefunctions respectively. To preserve overall antisymmetric symmetry, this results in the spatial wavefunctions for singlet and triplet states being symmetric and antisymmetric respectively. The antisymetric spatial wavefunction of the triplet therefore has a greater coulombic stability, resulting in a lower energy.

However, the exchange interaction is not limited to two electron systems and can additionally occur intermolecularly. Systems where $J > 0$ are ferromagnetic, driving spins towards alignment, whilst systems with $J < 0$ are antiferromagnetic and drive spins to anti-align with each other. The magnitude of the exchange interaction $|J|$ is generally increased with greater overlap of the electronic wavefunctions of the two spins. Intramolecular systems can show exchange interactions between spins as large as 1.0 eV, whereas intermolecular systems could have $|J| < \mu$eV.

2.3.3 Zero-Field Splitting (ZFS)

The ZFS interaction $\hat{H}_{\text{ZFS}}$ occurs in systems with $S > 1/2$ as the result of magnetic dipole-dipole interaction between different electronic spins. It acts to lift the degeneracy of the spin sublevels of the excited triplet state at zero field. For a system with spin operator $\hat{\mathbf{S}}$:

$$\hat{H}_{\text{ZFS}} = \hat{\mathbf{S}} \cdot \mathbf{D} \cdot \hat{\mathbf{S}} \tag{2.13}$$

where $\mathbf{D}$ is the ZFS tensor for a system.[15] Molecules are not typically spherical, such that magnetic dipole-dipole interactions can be anisotropic and do not cancel to zero. The anisotropy of $\mathbf{D}$ can be written in terms of principle axes $D_{x,y,z}$ which result from finding the eigenvalues of $\mathbf{D}$ and reflect the underlying symmetry of the molecule:

$$\hat{H}_{\text{ZFS}} = D_x \hat{S}_x^2 + D_y \hat{S}_y^2 + D_z \hat{S}_z^2 \tag{2.14}$$

with $D_x + D_y + D_z = 1$. This can be re-written as:

$$\hat{H}_{\text{ZFS}} = D\left[\hat{S}_z^2 - \frac{1}{3}S(S+1)\right] + E(\hat{S}_x^2 - \hat{S}_y^2) \tag{2.15}$$

where $D = \frac{3}{2}D_z$, and $E = \frac{1}{2}\left(D_x - D_y\right)$. D is defined to lie along the axis of maximum symmetry for a molecule. Typically, $D < 0$ for triplet systems with prolate electronic distributions and $D > 0$ for systems with oblate molecular distributions.[16] D is expected to be largest for systems where spins have the highest degree of overlap, allowing for $|D|$ to be used towards describing the level of delocalisation of the triplet states for molecular systems. E gives an indication of the degree of ellipticity of the electronic wavefunction perpendicular to the axis of greatest symmetry.

2.4 Doublet Emission for OLED Devices

Electron and hole recombination from conduction and valence bands can result in light emission for semiconductor systems, with formed electron-hole excited states known as excitons. Organic semiconductors intrinsically screen the coulombic interaction of electric charges less than their inorganic counterparts, a result of the lower dielectric constant in organic molecular solids.[4] The stronger interaction of charges within organic semiconductors can give rise to Frenkel excitons, where electron-hole pairs are more tightly bound than those in the Wannier-Mott excitons found in more classical inorganic semiconductors. Frenkel excitons generally have stronger transition dipole moments for more efficient light emission in optoelectronic devices. The 'organic' approach allows more flexible manufacture of light-emitting layers than devices based on III-nitride semiconductors,[17,18] as well as easily tuneable properties from chemical synthesis.[2]

However, strong coulomb interactions in organic semiconductors also impose efficiency limits for light emission from charge recombination - a consequence of the quantum-mechanical spin properties of singlet (S_1) and triplet (T_1) excitons. Singlet and triplet electronic states have total spin quantum numbers, $S = 0$ and $S = 1$, respectively. Due to a singlet ground state in typical organic semiconductors, triplet excitons should be dark and non-emissive due to the rule of spin conservation in transitions for light emission. As triplet excitons are formed in 75% of charge recombination events for such organic semiconductors,[4] spin statistics would limit the electroluminescence efficiency of OLEDs to 25%. The generally larger coulomb interaction in organic semiconductors compared to inorganic systems results in a larger exchange interaction and singlet-triplet exciton energy gap; triplets act as excitonic, non-luminescent traps if their emissive properties are not enhanced.

Substantial progress has been made towards real-life applications in display and lighting technologies by brightening triplet excitons directly with the inclusion of iridium complexes to promote phosphorescence,[19,20] and indirectly by converting dark triplet to bright singlet excitons in delayed emission, e.g. thermally activated delayed fluorescence (TADF)[21–23] - see Figure 2.1b. We note that triplet emission occurs on much slower timescales than spin-allowed singlet emission in these systems. Spin-forbidden phosphorescence results in emission timescales on the order of microseconds to hundreds of nanoseconds.[19,20] Similar emission times are observed in TADF systems, where the rate-limiting steps for emission are singlet-triplet spin-flip processes.[24–27] These timescales are 2-3 orders of magnitude slower than seen for spin-allowed, direct transitions between singlet exciton and ground states in standard organic semiconductor systems.

Generally, we consider that faster light emission will reduce the chance of exciton quenching processes which can limit the OLED device lifetime[28] and operational efficiency.[29] There is therefore a commercial appetite for alternative solutions to circumvent the OLED spin statistics efficiency limit using emitters which do not contain low-abundance metals such as iridium and have shorter light emission timescales, enabling more sustainable manufacture and improved device performance.

Radical-based organic semiconductors have unpaired electrons in non-bonding singly occupied molecular orbitals (SOMOs) which are intermediate to the highest occupied and lowest unoccupied molecular orbitals (i.e. HOMO and LUMO; valence and conduction bands). As discussed in the next section, the SOMO results in doublet-spin physics which can allow radical emitters to undergo charge recombination with unity light emission efficiency (Figure 2.1a). In a sense, organic radical doublet emitters in LEDs are similar to their inorganic counterparts in not being limited by spin considerations, whilst also having the efficient emission characteristic of organic semiconductor systems.

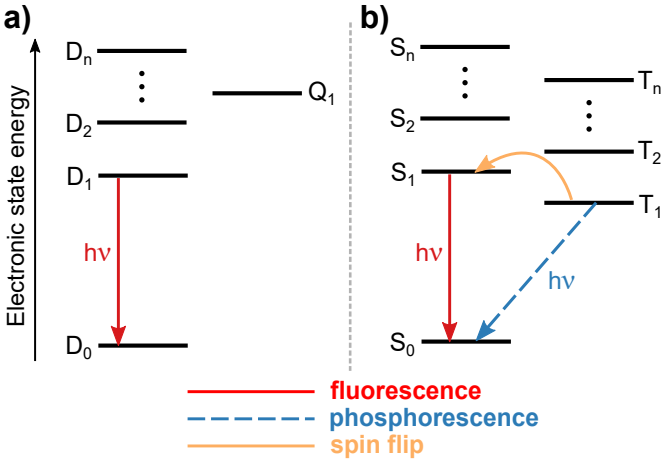

Figure 2.1: Emission mechanisms for doublet- and singlet/triplet-based organic emitters. Jablonski energy diagrams of the a) doublet-quartet manifold, indicating doublet-doublet fluorescence and b) singlet-triplet manifold indicating singlet-singlet fluorescence, triplet-singlet phosphorescence and spin flip processes e.g. intersystem crossing (ISC, $T_1 \rightarrow S_1$) in TADF; triplet-triplet annihilation (TTA, $2\ T_1 \rightarrow S_1 + S_0$).

These factors have allowed the development of radical based semiconductors with nanosecond emission timescales and high photoluminescence quantum efficiency (PLQE).[30–35] Some of the most efficient π-radical emitters have been based on derivatives of tris(2,4,6-trichlorophenyl)methyl (TTM),[36,37] perchlorotriphenylmethyl (PTM)[38,39] and (3,5-dichloro-4-pyridyl)-bis(2,4,6-trichlorophenyl)methyl (PyBTM)[32] radicals - see Figure 2.2. Using these materials, highly efficient light-emitting devices have been shown to surpass the singlet-triplet efficiency limit that is otherwise imposed on non-radical organic

semiconductors.[31,37,40]

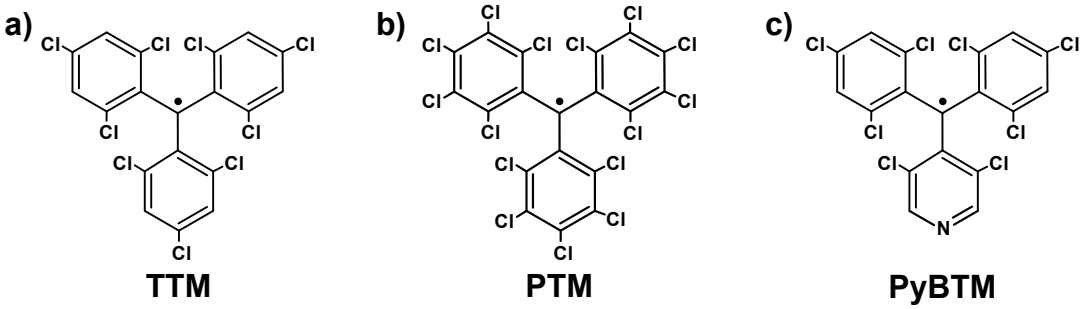

Figure 2.2: Stable π-radical chemical structures. Chemical structures of a) tris(2,4,6-trichlorophenyl)methyl (TTM),[41] b) perchlorotriphenylmethyl (PTM),[42] and c) (3,5-dichloro-4-pyridyl)-bis(2,4,6-trichlorophenyl)methyl (PyBTM)[32] radicals.

The opportunities to use radical emitters in optoelectronics were not widely appreciated until the last decade. Organic radicals were generally thought to be dark and strong luminescence quenchers as mediators of electron exchange-induced intersystem crossing and charge transfer processes.[43–47] The seminal work of Julia et al. in brightening the dark TTM moiety by functionalisation with carbazole to form a TTM-carbazole derivative,[48] and subsequent advancements to produce the first generation of radical light-emitting devices[30,31] by Li and co-workers have already been set out in a review,[49] and is not detailed in this chapter.

2.5 Doublet Manifold and Emission Mechanisms

In organic radicals, an odd number of valence electrons leads to the presence of an unpaired electron which does not participate in the valence and conduction bands. Consequently, a radical species has a doublet ground state which is classified as D_0, with total spin quantum number, $S = 1/2$, and total spin projection, $M_S = +1/2, -1/2$. In Figure 2.3, the D_0 state is depicted where electrons doubly-occupy levels from lower-energy orbitals up to the HOMO, with single-electron occupancy of the SOMO, and no electrons in the LUMO and higher-energy orbitals. The unpaired electron prohibits the formation of singlet and triplet excitons without the addition or removal of electrons to form even-electron systems.

By considering the requirement for spin conservation in optical excitation, transitions can occur from D_0 to higher energy $D_{x>0}$ states within the doublet-spin manifold in radicals.

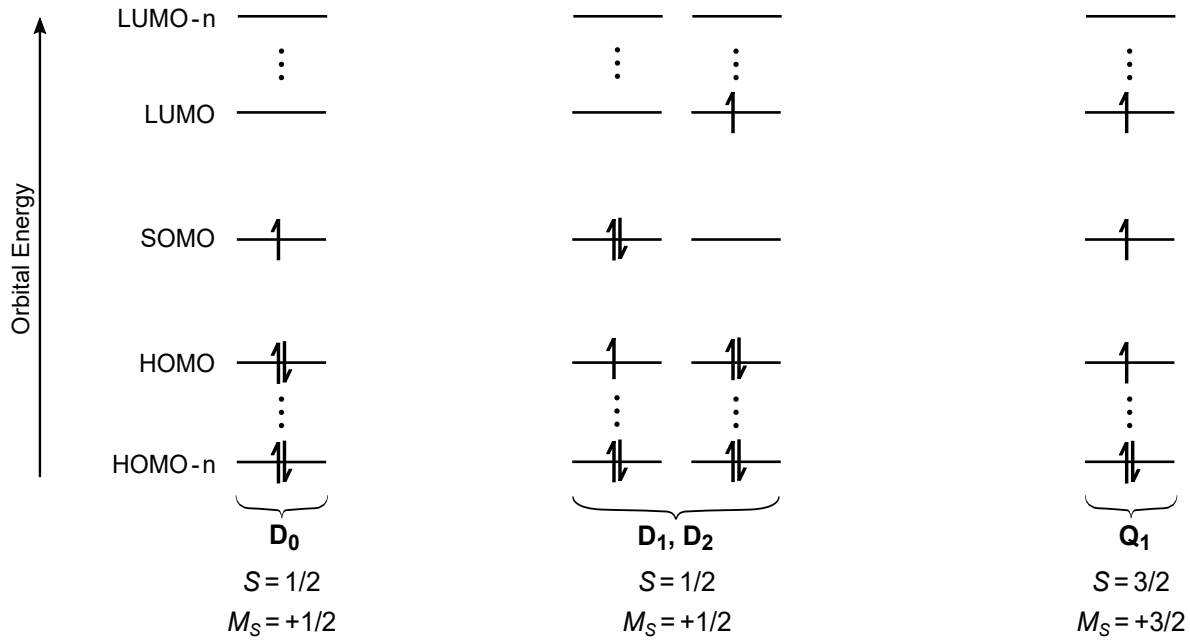

Figure 2.3: Orbital occupancy of radical emitter electronic states. Molecular orbital diagrams for a doublet emitter showing electron occupancy in ground state (D_0) and excited states (D_1, D_2, Q_1). The D_1 state will be the lower in energy of the two possible configurations indicated for D_1, D_2. Similarly, the D_2 state will be the higher in energy of the two possible configurations indicated for D_1, D_2. Whilst not shown, an understanding of higher energy electronic states and differing spin projections will require excitations to be formed of a superposition of orbital configurations.

The D_1 lowest energy excitation can be described by HOMO to SOMO and SOMO to LUMO transitions, depending on the relative energies of these orbitals (Figure 2.3). Where the HOMO-SOMO and SOMO-LUMO energy differences are non-degenerate, the D_1 and D_2 states will be the lower and higher energy transitions, respectively. Critically, the D_1 state is bright because like the ground state (D_0), it has $S = 1/2$, and can therefore radiatively decay by fluorescence to the ground state. In Figure 2.3, the D_0 and D_1 states are depicted with $M_S = +1/2$ ($M_S = -1/2$ analogues of these states also exist but are not shown). Whilst odd-electron systems prohibit the formation of singlet or triplet states in any electron configuration, it is feasible that quartet states ($S = 3/2$) could be formed. In Figure 2.3 the Q_1 state with $M_S = +3/2$ is shown. The quartet state is considered dark due to the spin flip required for transitions to the doublet ground state. They are the dark triplet analogues on going from non-radical 'closed-shell' to radical 'open-shell' species.

Generally, the lowest energy excited states in non-radical ($S = 0$ ground state) and radical ($S = 1/2$ ground state) systems are dark and bright, respectively. In the singlet-triplet manifold for non-radical organic semiconductors, the dark triplet T_1 is generally lower energy than singlet S_1. For organic radicals, the Q_1 quartet state is

described by a HOMO to LUMO excitation (Figure 2.3) which will be higher energy than D_1 (in the absence of substantial exchange interaction).[50] The quartet state derived from a HOMO-LUMO transition is not expected to play a significant role in the emission mechanism for radical-based OLEDs as electron charge trapping will have a thermodynamic tendency to the lower-energy SOMO rather than higher-energy LUMO (Figure 2.4).

With the understanding that dark states can be eliminated from the functional photophysics of radical emitters as indicated in Figure 2.3 and 2.4, we consider why π-radical systems such as TTM and PTM are not strongly emissive.

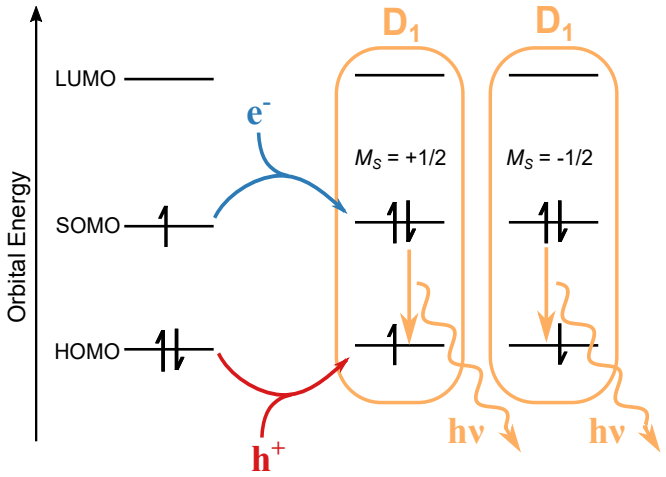

Figure 2.4: Electroluminescence scheme for radical OLEDs by charge trapping. Radical-based electroluminescence scheme for charge trapping of electrons (e^-) and holes (h^+) on doublet ground state to form emissive doublet excitons, D_1. Doublet emission-type is highlighted by emission channels for $+1/2$ and $-1/2$ total projection spin quantum numbers.

2.6 Radiative and Non-Radiative Behaviour of Organic Radical Emitters

2.6.1 Excitation Mixing of Alternant Symmetry Systems

Alternant π-hydrocarbon systems are conjugated molecules whose π-system atoms can be divided into two sets [commonly denoted starred (*) or unstarred, Figure 2.5a] such that no two atoms of the same set are adjacent. We illustrate this with an example of a three-ring alternant π-system (anthracene) in Figure 2.5a. Alternant systems contain even-membered rings only (Figure 2.5a), whereas non-alternant hydrocarbons have odd-membered rings as shown in Figure 2.5b and/or contain heteroatoms.

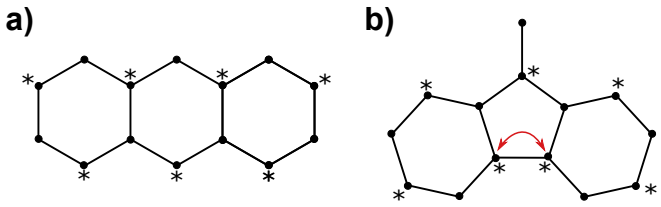

Figure 2.5: Alternant and non-alternant three membered rings. Example structures of a) alternant and b) non-alternant three membered rings (π-system not shown for clarity). Alternancy symmetry allows for the atoms forming a delocalised system to be separated into two separate sets (starred and non-starred), for which no atom is adjacent to another atom of the same set. It is impossible for b) to have starred and non-starred atom assignment such that no two atoms of the same set are adjacent (see red double-headed arrow).

The Coulson-Rushbrooke theorem states that for closed shell, alternant hydrocarbons the bonding and antibonding orbitals are distributed symmetrically in energy, and that energy-adjacent orbitals (such as HOMO and LUMO, or HOMO-n and LUMO-n, where n is an integer) differ only by sign on every other carbon atom.[51,52] Further, in alternant π-radicals such as TTM and PTM (Figure 2.2) extensions to the Coulson-Rushbrooke Theorem by Longuet-Higgins lead to the splitting of anti-bonding and bonding π-orbitals with equal energy spacing about the non-bonding SOMO level,[53–55] such that E(SOMO)-E(HOMO) = E(LUMO) - E(SOMO), where E(x) is the energy of molecular orbital, x. They also state that the SOMO only has orbital amplitude on atoms which can bear a radical dot in its principle resonance structures. For the monoradicals considered in this chapter, this usually means that the SOMO will have orbital amplitude (and therefore electron density) on (N+1)/2 carbon atoms and none on the remaining (N-1)/2, where N is the number of conjugated carbon atoms in the molecule. This theoretical prediction is confirmed in DFT calculations of the SOMO of alternant π-radical systems.[31,56]

Considering the orbital structure of these systems, the HOMO-SOMO and SOMO-LUMO transitions are understood to be degenerate with identical magnitude of their transition dipole moments (Figure 2.6a,b)[53,54]. One can further show[54] that these two transitions are mixed by the electronic Hamiltonian to form out-of-phase, $|D_{1(TTM)}\rangle$ and in-phase, $|D_{2(TTM)}\rangle$ combinations (Figure 2.6b). Crucially in what follows, the out-of-phase dark transition will always be at lower energy and the in-phase, bright transition at higher energy (Figure 2.6c).

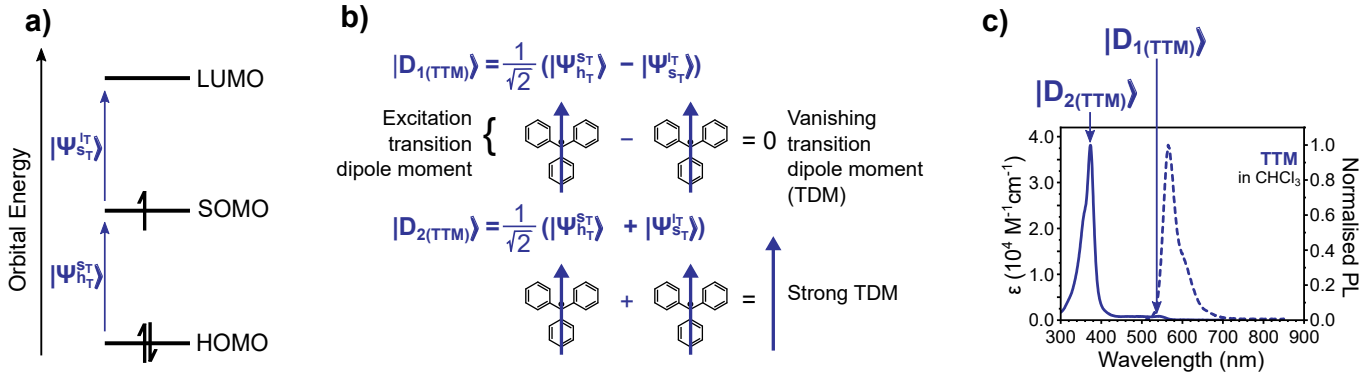

Figure 2.6: Excitation mixing in alternant radical systems. a) Schematic diagram of the frontier molecular orbitals of TTM, with the HOMO-SOMO, $|\psi_{h_T}^{s_T}\rangle$, and SOMO-LUMO, $|\psi_{s_T}^{L_T}\rangle$, labelled. b) The mixing of the $|\psi_{h_T}^{s_T}\rangle$ and $|\psi_{s_T}^{L_T}\rangle$ transitions to form the dark $|\mathrm{D}_{1(\mathrm{TTM})}\rangle$ and bright $|\mathrm{D}_{2(\mathrm{TTM})}\rangle$ excitations. c) Absorption (solid) and emission (dashed) spectra of TTM in $CHCl_3$ with the D_1 and D_2 transitions labelled for absorption. b) and c) have been adapted with permission from Nat. Mater. 19, 1224-1229 (2020). Copyright 2020 Springer Nature.[40]

This means that the lowest energy excited state (D_1) of an alternant organic radical will have a vanishingly small transition dipole moment; this can be seen in < 1000 M^{-1} cm^{-1} extinction coefficients for the lowest energy absorption bands in alternant hydrocarbon radicals.[40] As the rate of spontaneous emission is proportional to the square magnitude of the dipole moment,[5] light emission from such organic radicals ($k_r \sim 10^6$ s^{-1}) is generally outpaced by non-radiative internal conversion processes to the ground state. In theory the D_2 state should be highly emissive, but by Kasha's rule, in the event a molecule were to form this state it would rapidly undergo internal conversion to the dark D_1 state. The key result is that alternant radical hydrocarbons are likely to have very poor emission from D_1, which is outpaced by non-radiative losses, and are therefore likely to be unsuitable for radical OLEDs.[40]

In Figure 2.7 we show a selection of bright and dark radical systems. Careful inspection shows that all dark systems are alternant radicals, and all bright systems are non-alternant, confirming the theoretical predictions. We stress that not being alternant substantially increases the likelihood of a radical being emissive, but is not in itself a sufficient criterion for a radical to be emissive; in addition to breaking the alternacy symmetry a molecule's radiative rate will also need to outcompete non-emissive processes such as internal conversion. Conversely, there may also be cases (such as tris(2,3,5,6-tetrachloro-4-iodophenyl)methyl radical (3I-PTM)[57] discussed later) where an alternant radical has a very weak D_1 absorption (and no emission when in pure solid), but by immobilising it in a host matrix, and therefore restricting conformational changes that facilitate nonradiative decay, emission is observed.

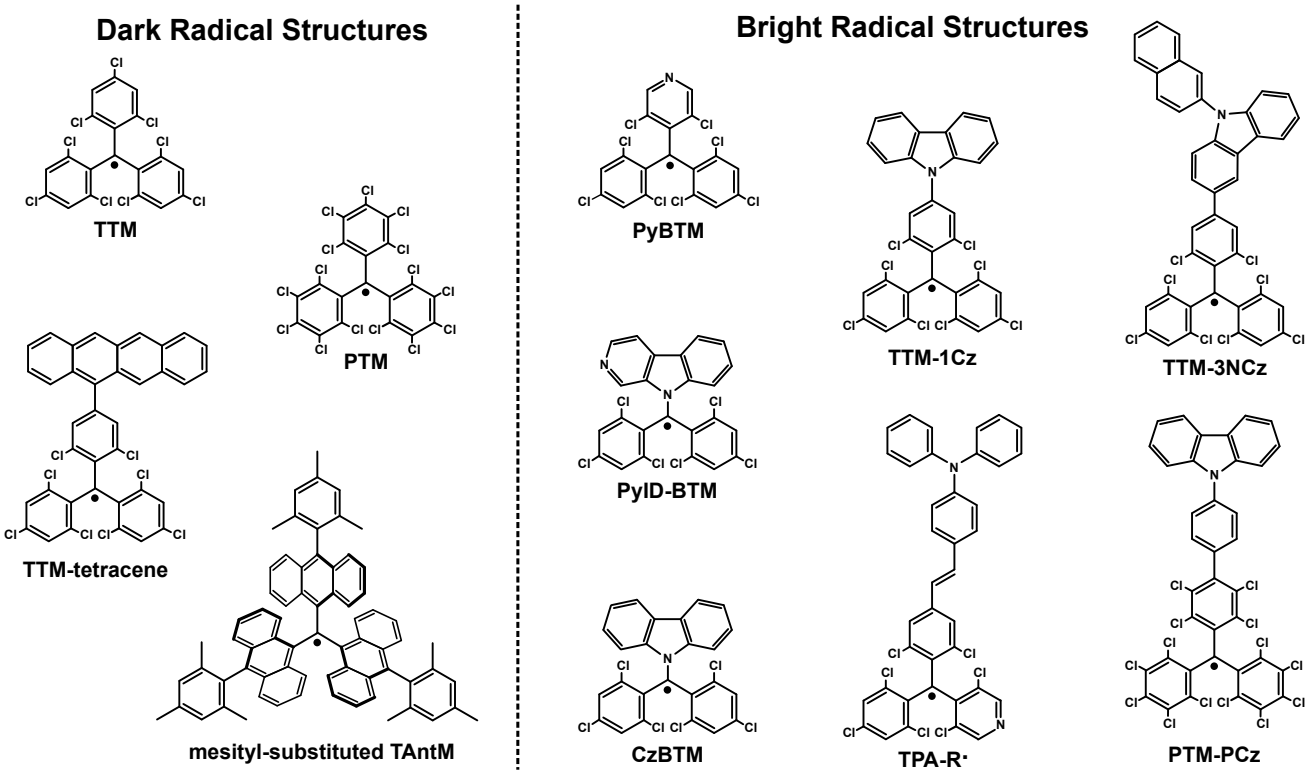

Figure 2.7: Dark and bright radical structures. Chemical structures of the dark TTM,[41] PTM,[58] and TTM-tetracene[40] radicals as well as the bright PyBTM,[32] PyID-BTM,[33] CzBTM,[59] TTM-1Cz,[48] TTM-3NCz,[31] TPA-R,[60] and PTM-PCz[38] radicals. Alternant radicals (left) are generally non-emissive, while non-alternant radicals (right) can have efficient light emission. We also give the structure of the unusual alternant radical mesityl-substituted tri(9-anthryl)methyl (TAntM),[61] which is similarly found to have a very weak D_1 absorption.

2.6.2 Breaking the Alternancy Symmetry

Non-Alternant Radical Structures

If the alternancy symmetry in π-radicals can be broken, either by having conjugated rings with an odd number of atoms, or heteroatoms, or both, then the HOMO-SOMO and SOMO-LUMO transitions cease to be degenerate. This can then allow the D_1 state to achieve a higher transition dipole moment and radiative rate. Radical structures without alternant symmetry have been found in the PyBTM[32] and (N-pyrido[3,4-b]indolyl)bis(2,4,6-trichlorophenyl)methyl (PyID-BTM)[33] radicals (Figure 2.7), as well as the (N-carbazolyl) bis(2,4,6-trichlorophenyl)-methyl radical (CzBTM)[59] radical. In PyBTM the higher electronegativity of the nitrogen atom perturbs the alternancy symmetry of the triaryl system, whereas in PyID-BTM the five-membered central ring of the carbazole (and the nitrogen atom) breaks this symmetry in the molecule.

Some indications of higher PLQE in these materials compared to TTM (2.0% in cyclohexane[40]) and PTM (1% in cyclohexane[38]) were reported, namely 26% for PyBTM dispersed in a PMMA matrix[32] and 19.5% for PyID-BTM dissolved in cyclohexane.[33] Radiative rates for PyID-BTM being measured at 1.39×10^7 s^{-1} place them an order of magnitude faster than those for TTM at 1.22×10^6 s^{-1} (both in cyclohexane).[33]

More substantial improvement in radiative rates ($k_r > 10^6$ s^{-1}) and PLQE is conceivable from discovery of new chemistry strategies for using non-alternant radical motifs in doublet emitters.

Non-Alternant Donor-Acceptor Radical Systems

Organic radicals with overall non-alternant hydrocarbon properties can be designed from alternant radical moieties if functionalised with non-alternant chemical groups. This has proven to be the most successful strategy to date, where non-alternant electron donor groups attached to TTM and PTM have led to an order of magnitude increase in the radiative rates of their derivatives.[37,38,62,63]

The rationale for this is shown by comparing Figures 2.6 and 2.8. In Figure 2.6, the HOMO-SOMO and SOMO-LUMO excitations are degenerate, leading to a D_1 state that is a dark, out-of-phase combination of these excitations as discussed earlier. If, however, the radical is bonded to an electron-rich, non-alternant molecule with a high HOMO (such as carbazole), as shown in Figure 2.8a, then the lowest-energy excited state becomes the charge-transfer excitation from the electron donor-HOMO to radical-SOMO, and there is no corresponding SOMO-LUMO excitation of the same energy for this to destructively interfere with. Alternatively, the radical can be bonded to an electron-acceptor molecule as shown in Figure 2.8b, where D_1 is now the charge-transfer excitation from the radical-SOMO to acceptor-LUMO, and there is no degenerate HOMO-SOMO excitation for this to interfere with.

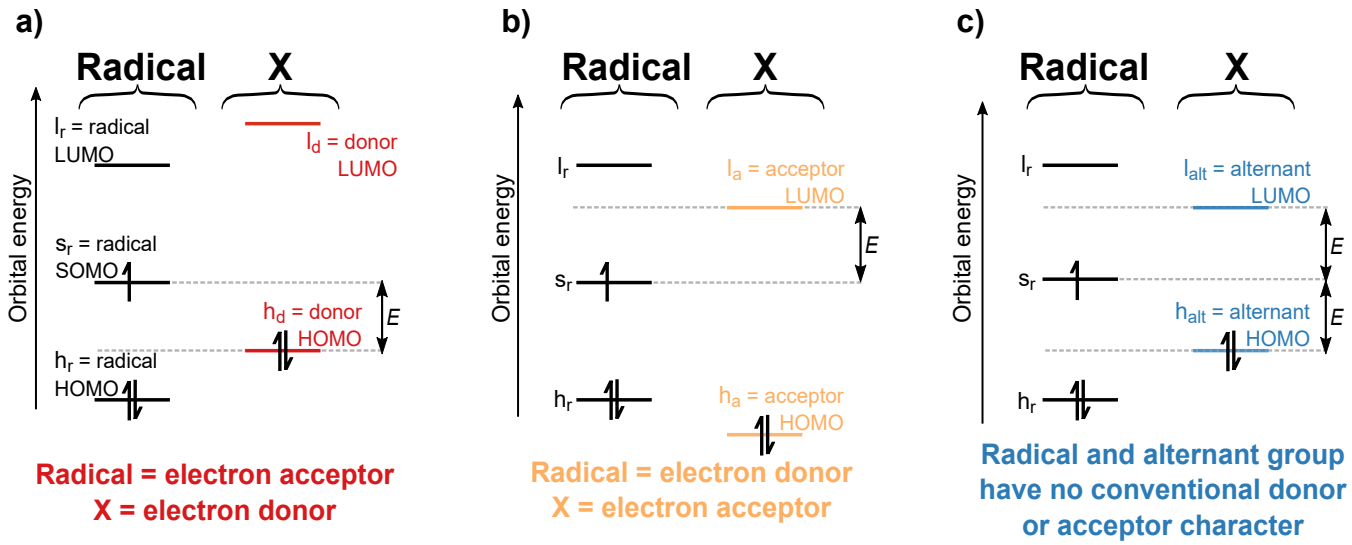

Figure 2.8: Charge-transfer radical excitations. Schematic molecular orbital diagrams for a radical moiety and functional group for a) a radical acceptor-electron donor configuration, b) a radical donor-electron-acceptor configuration, and c) a radical functionalised to an alternant group. E indicates the lowest energy excitation ignoring two electron (Coulomb and exchange) effects. This figure has been adapted with permission from Abdurahman et al., Nat. Mater. 19, 1224-1229 (2020). Copyright 2020 Springer Nature.[40]

This has been demonstrated in practice by functionalisation of the dark TTM radical moiety with a carbazole group to produce the bright TTM-1Cz doublet emitter. The radiative rate increases roughly tenfold from 10^6 to 10^7 s^{-1} and the PLQE increases from 3% to 53% in cyclohexane.[48] For TTM-1Cz, an emission band is observed at 603 nm in cyclohexane, which is lower energy than both TTM (537 nm) and carbazole (331 nm) only photoluminescence.[48] Furthermore, the protonated (non-radical) precursor, αH-TTM-1Cz, displays distinctly higher energy emission (335 nm) than TTM-1Cz in cyclohexane.[48] The lower energy emission feature in TTM-1Cz is derived from a carbazole-HOMO to TTM-SOMO charge transfer-type (CT) transition (Figure 2.8a); such lower energy features emerge in all electron donor-acceptor hydrocarbon radicals. Using non-alternant groups functionalised to TTM moieties, PLQE values in excess of 80% have been observed and can be translated to devices with external quantum efficiencies as high as 27%.[31]

We also expect good emission properties in systems where the radical is paired with a non-alternant electron acceptor, but such systems have not been demonstrated to date, likely due to the difficulty in finding acceptor groups with sufficiently low LUMO levels to have energetic matching with the radicals' low-energy orbitals.

Conversely, in the case that a donor-acceptor radical is obtained from an alternant hy-

drocarbon functional group [Figure 2.8c], the overall radical will still have alternancy symmetry. Alternant donor-acceptor radical systems also follow the Coulson-Rushbrooke theorem and have degenerate transitions derived from the functional group-HOMO to radical-SOMO and radical-SOMO to functional group-LUMO. Slow radiative rates from weak D_1 transition dipole moments hinder the emission properties of these CT systems, even where orbital transitions occur between distinct parts of the molecule.[40] The dipole-cancelling effect from the out-of-phase combination of HOMO-SOMO and SOMO-LUMO excitations is still seen. This effect is observed in TTM-Tetracene where the lowest energy D_1 absorption band at 630 nm has an extinction coefficient value of 1174 M^{-1} cm^{-1}, and no light emission was reported.[40] This is also observed for the alternant mesityl-substituted tri(9-anthryl)methyl (TAntM) radical,[61] where the lowest energy D_1 absorption band at 1020 nm has an extinction coefficient value of ∼250 M^{-1} cm^{-1}.

2.6.3 Brightening of Dark Charge Transfer States

The D_1 excitation being primarily of intramolecular charge-transfer character is a common feature in the leading, highly emissive radical systems reported to date.[31,48,64] We note that charge transfer states are usually dark because, by construction, the orbital from which the electron is excited, and the orbital to which it is excited, are spatially separated and non-overlapping, leading to a vanishing transition dipole moment.[65] Radical systems whose lowest energy excited state (D_1) is mainly charge-transfer (CT) in character will therefore need to acquire locally excited (LE) state character in order to be emissive, such as by mixing with bright electronic transitions centered on the radical moiety.

Several groups have provided theoretical examinations for the brightening of the D_1 state in radical doublet emitters[40,66] using frameworks of intensity borrowing or hybridisation between states. We emphasise that the following discussions for brightening CT states are similar to discussions for TADF materials. However, while luminescent donor-acceptor radicals generally require non-alternant hydrocarbon electronic symmetry[40] as outlined in Sections 2.4-2.6.2 (whereas TADF emitters in general do not), radical emitters do not have to navigate the trade-off in low and high excited-state CT character for good oscillator strength and efficient reverse intersystem crossing that is seen in TADF.[67–69]

In previous work, it was suggested that the D_1 state in TTM-1Cz can be described as dark CT excitation from the donor (carbazole) HOMO to acceptor (TTM) SOMO mixing with, and therefore borrowing intensity[65,70] from the D_2 transition of TTM.[40] This is evidenced by the intense near-UV absorption peak of TTM (∼375 nm) decreasing in intensity on going from TTM to TTM-1Cz, accompanied by a bright D_1 absorption for TTM-1Cz. In this analysis of TTM-1Cz radicals, the TTM and carbazole groups are

first treated as separate moieties. LE states are defined to be those involving orbitals localised solely on the TTM moiety (or solely on carbazole) and CT states to involve electronic transitions from an orbital entirely on the donor (carbazole) to entirely the acceptor (radical). While CT states could also form by electron transfer from the TTM SOMO to Cz LUMO, this excitation was not considered as it is too high in energy to participate in the functional photophysics involving the lowest energy excited states. The true D_1 electronic state was suggested to be composed of CT excitation from the carbazole HOMO to TTM SOMO with a contribution from the bright TTM LE state seen experimentally around 370 nm. The mixing of LE character arises from the consideration of the TTM and carbazole moieties and the resulting electronic interactions of bringing these groups together from separation.[70] Mixing of CT-LE states can then be explained by intensity borrowing perturbation theory,[65,70] having a cosine dependence on the dihedral angle linking the TTM and carbazole moieties,[40] and leads to a non-zero transition dipole moment between the ground state $|D^{(0)}_{0(\text{TTM-1Cz})}\rangle$ and (perturbed) first excited state $|D^{(1)}_{1(\text{TTM-1Cz})}\rangle$, i.e., $\langle D^{(0)}_{0(\text{TTM-1Cz})}|\hat{\mu}|D^{(1)}_{1(\text{TTM-1Cz})}\rangle \neq 0$, where $\hat{\mu}$ is the transition dipole moment operator.

On the other hand, Cho et al. in their analysis of PTM-TPA systems take the alternative approach of calculating the electronic structure for the entire radical molecule rather than starting their consideration with separate moieties.[66] They find that the lowest energy D_1 state is principally composed of charge-transfer excitation and is emissive. However, they denote this adiabatic D_1 state CT, such that this state has oscillator strength with the ground state. They then consider the hybridisation of their CT state with the ground state and LE states, and compute and explain the radiative and nonradiative decay rates.[66]

These studies[40,66] echo the result that lowest energy excitations in bright donor-acceptor radical systems contain predominantly charge-transfer character but are brightened by mixing of LE character and can be considered as a part of general design rules for obtaining luminescent emitters.

2.6.4 Energy Ordering of HOMO, LUMO, SOMO Toward Alternative Doublet Emission

Cornil, Robvira, and Veciana et al. have described the emission properties of PTM derivatives using hybridisation of the ground state orbitals.[56] In these studies, the extent of thiophene substitution onto PTM cores was investigated, showing the importance of energy-level alignment between thiophene and PTM moieties in HOMO delocalization for good oscillator strength properties.

The hybridization of the ground state orbitals was also used to rationalise organic radicals with non-Aufbau inversion of their electron orbital occupancy.[71] In molecules following the Aufbau electron distribution principle, molecular orbitals are filled progressively from low to high energy. In non-Aufbau radicals, the highest energy occupied orbital is not the SOMO,[39,60] but rather the double-electron occupied HOMO of the donor group attached to the radical moiety. On going from TTM-3NCz to PTM-3NCz, the electronic structures of these systems were observed to switch from Aufbau to non-Aufbau configurations.[39] The difference occurs because of the extra Cl bulk in PTM-3NCz, leading to PTM and 3NCz moieties being almost orthogonal and resulting in less hybridisation than in equivalent groups in TTM-3NCz. Photostability improvements of up to 2-3 orders of magnitude were observed in donor-acceptor non-Aufbau materials compared to parent radicals and were partly attributed to the energetically higher lying HOMO preventing chemical reactions with the SOMO.

It is noteworthy that doublet emitters have also been designed in materials where radicals are appended to chromophores and do not participate in electronic transitions for the lowest energy exciton states. Beldjoudi et al. have demonstrated that pairing of pyrene (Py) with the dithiadiazolyl (DTDA) radical moiety does not produce luminescence at a new wavelength, with respect to emission from its constituent radical and non-radical components.[72] The radical center imparts its doublet-spin property on the singlet and triplet-spin excited states of pyrene to yield overall doublet states for efficient light emission (PLQE = 50%, Py-DTDA in MeCN). The presence of radical leads to moderate reduction in efficiency compared to Py only which has PLQE = 98% (Py is pyrene without radical present). This is attributed to energy mismatch between the Py HOMO, LUMO, and DTDA SOMO orbitals, which minimises electron-exchange-mediated exciton quenching. Using this material, radical-based OLEDs with up to 1.4% EQE were reported with sky-blue emission (EL maximum at 492 nm). The design of new emitters of this type will require careful tuning of the energetic order of frontier orbitals: HOMO, LUMO, and SOMO from radical and non-radical constituents, as well as intramolecular spin interactions. Substantial gains in efficiency for spectator-type OLEDs with non-radical-centered excited states are expected in the future. For the remainder of this thesis, we will keep a focus on doublet emitters with radical-centered excitons.

2.6.5 Non-Radiative Relaxation of the Doublet Manifold

The doublet manifold intrinsically contains fewer non-radiative pathways, a result of intersystem crossing being unable to populate 'dark' states below emissive D_1 excitation. The main emission quenching mechanism of D_1 is internal conversion to the D_0 ground state.

Internal conversion results from the non-adiabatic coupling of the lowest vibrational mode of the D_1 state to the excited D_0 vibrational modes. Analogous to closed shell systems, an 'energy gap law' dependence is seen for emission as a result of Franck-Condon factors for transition, with decreased non-radiative rates for systems with increased HOMO-SOMO splitting. Variation of the ortho-halogens of the pyridyl group in PyBTM from Br to Cl to F successively increased the HOMO-SOMO splitting from 2.51 to 2.55 to 2.61 eV, respectively. The increased energy gap was accompanied by decreased non-radiative rates of 1.68×10^8, 1.28×10^8, and 5.2×10^7 s^{-1} (in chloroform) for the Br-, Cl-, and F-substituted PyBTM molecules, respectively.[73]

The order of magnitude reductions in non-radiative rates is seen from charge-transfer systems, with the spatial separation of the electron density of the ground and excited states leading to reduced vibronic coupling and internal conversion. The functionalisation of PTM with differently substituted phenyl-carbazolyl groups (-Pz and -3Pz) as well as triphenylamine (TPA) reducing the non-radiative rate by up to an order of magnitude from 1.62×10^8 s^{-1} for PTM to 4.85×10^7, 2.11×10^7, and 1.65×10^7 s^{-1} for PTM-TPA, PTM-PCz, and PTM-3PCz, respectively (all in cyclohexane). Similarly, TTM functionalisation with carbazolyl (Cz), bi-carbazolyl (BiCz), and tri-carbazolyl (TCz) groups reduces the non-radiative rate from 1.56×10^8 to 1.13×10^7 s^{-1} for TTM and TTM-1Cz in dichloromethane[40] and from 1.52×10^8 to 8.42×10^7 and 4.3×10^7 s^{-1} for TTM, TTM-1BiCz, and TTM-TCz in cyclohexane, respectively.[62]

Furthermore, reductions in internal conversion are seen for rigid and immobilised molecular systems, due to the intrinsic dependence of non-adiabatic coupling on the thermally induced fluctuations of vibrational modes. The immobilisation of radical emitters in a rigid matrix restricts vibrational and rotational modes seen in solution, with PLQE efficiencies for PyBTM being boosted from 3% when in chloroform solution to 26% for when PyBTM was immobilised in a rigid polymethyl methacrylate (PMMA) matrix.[32] Similarly, the lower population of thermally induced modes leads to enhanced radical emission at lower temperatures, with PyBTM showing PLQE values of 81% when embedded in an EPA matrix (diethylether:isopropanol:ethanol) at 77 K.[32]

Theoretically calculated values for radical non-radiative rates, calculated from the sum of non-adiabatic vibrational coupling constants, have given insights into the intrinsic non-radiative mechanisms for organic radical excited states.[74,75] As well as consideration of excited state-ground state hybridisation in non-radiative decay,[66] Bredas and co-workers have taken steps to better understand the in-device behavior for radical emitters in a combined molecular dynamics and DFT approach, advancing the theoretical modelling of

these systems to include host-emitter interactions.[50] Furthermore, vibrational couplings for TTM-3NCz were found to be reduced by up to 30% when embedded in a CBP host (1% dilution of the radical emitter in host). This reduction comes with a modest penalty of static disorder; minimising static disorder reduces its detrimental effect on charge mobility, leading to increased OLED efficiency and reduced turn-on voltages.[50]

Approaching the design of radical emitters with the aim to reduce internal conversion and increasing transition dipole moments will enable systems with more efficient light emission.

We note that the non-luminescent nature of the majority of stable radical systems is generally attributed to the rapid internal conversion resulting from small D_1-D_0 splittings; however, radical systems with energy gaps comparable to that of singlet emitters remain dark. In some circumstances, this can be alternatively explained by the radical emitter being an alternant hydrocarbon, or very nearly alternant, such that the D_1 state has a low transition-dipole moment, leading to a low radiative rate that is outcompeted by decay processes.[40] Nevertheless, greater research is required to elucidate which properties of bright radicals allow them to avoid ultrafast non-radiative relaxation.

2.7 Challenges for Radical-Based Emitters

2.7.1 Device Efficiency Roll-Off and the Underlying Mechanisms

Despite radical semiconductors having nanosecond emission timescales and high PLQE, the exploitation of these properties to improve on the state of the art in organic optoelectronics has not been fully realised. Given that radical emission is orders of magnitude faster than microsecond phosphorescent,[19,20] TTA[76] and TADF[21–23] emitters, radical OLEDs should be able to improve on the device characteristics and performance of these more established OLED technologies. As we have already mentioned, faster light emission should reduce the probability of exciton quenching processes that can lead to device and efficiency breakdown.

OLEDs based on radical semiconductors have been shown with high peak external quantum efficiency, but generally all devices suffer substantial reductions in efficiency above current densities of 1 mA/cm^2. This reduction of OLED efficiency at increased current density is commonly referred to as ‘roll-off’, and acts as a critical limitation for the commercialisation of light-emitting devices based on organic radicals (see Figure 2.9a).[31]

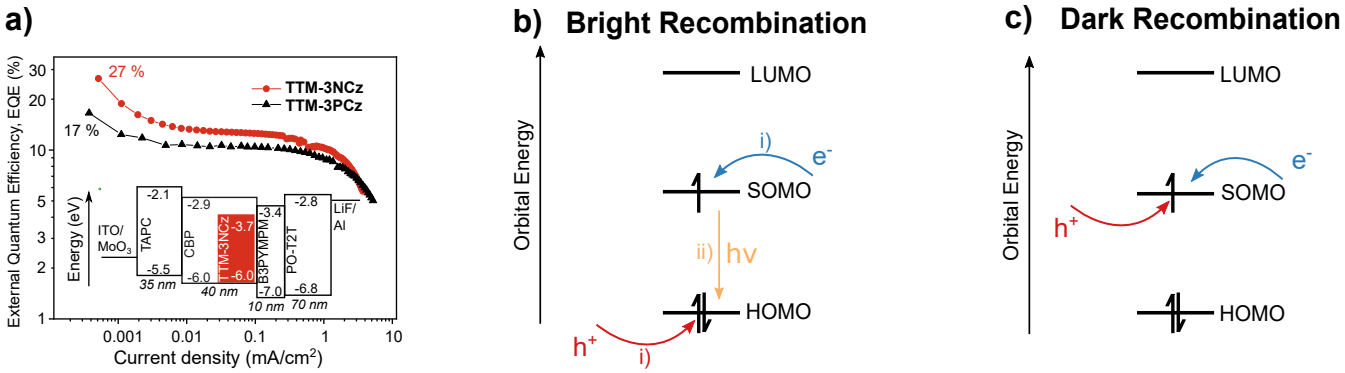

Figure 2.9: Efficiency roll-off and charge balance in radical devices. a) EQE-current density curves for TTM-3NCz (red) and TTM-3PCz (black) LEDs. The inset shows the TTM-3NCz device layout; the labels give the energy levels in electron volts and the thickness of layers in nanometers. a) has been reproduced with permission from Ai et al., Nature 563, 536-540 (2018). Copyright 2018 Springer Nature.[31] b) Schematic molecular orbital diagram indicating i) the stepwise process of separate electron transfer into the radical SOMO and hole transfer to the radical HOMO before ii) light emission following recombination. c) shows dark recombination that results in no light emission following electron and hole transfer to the SOMO.

Optical spectroscopy on working radical OLEDs has been used to study efficiency roll-off mechanisms.[77] In such experiments for radical OLEDs, devices were electrically biased from 0 to 12 V in the pulsed mode, and a secondary laser pulse was used to achieve a small population perturbation for which the decay lifetime was recorded.[40] The transient decay lifetime was unchanged for different voltages (and consequently exciton density, charge density, and electric field conditions), suggesting that excited state quenching of doublet excitons by self-annihilation, charges, and electric fields could be ruled out from the cause of the efficiency roll-off. This is in agreement with roll-off mechanisms studied in non-radical organic emitters with nanosecond lifetimes. In such systems, excited state quenching of nanosecond emitters is not generally expected until 100 mA/cm^2 and higher current densities.[29] When these results are considered together with the high redox- and photo-stability of organic radical emitters such as TTM-xPyID, TTM-3NCz, and others,[31,40,78] it is likely that current roll-off effects and device limitations originate from the device physics rather than photophysics of radical OLEDs.

2.7.2 Charge Balance Effects

The mechanism of electrical excitation in radical OLEDs is not fully understood. One of the suggested origins for EL efficiency roll-off beyond 1 mA/cm^2 in radical OLEDs is charge balance in electrical excitation.[40] A sequential charge trapping mechanism was previously considered, in which electrons and holes undergo charge transfer from host to radical in TTM-3NCz OLEDs (Figure 2.9b).[31] It should be emphasised that electroluminescence from radical OLEDs is surprising given the trap-like properties of

the SOMO as the thermodynamically preferred site for both electron and hole occupancy. By this pathway (electron and hole insertion into the SOMO), it was not expected for charge recombination on radical dopant centers to result in electroluminescence (Figure 2.9c). The highest efficiency radical-based OLEDs to date use host materials (CBP) with good HOMO energy alignment to the radical (TTM-3NCz) HOMO.[31]

Work by Suo et al. investigated the rate of electron and hole transfer from host to radical dopants using the charge hopping model in Marcus theory.[74] The electron and hole transfer rates from CBP to TTM-1Cz radical dopants were calculated to be 5.4×10^{11} and 4.0×10^{9} s^{-1} respectively, indicating the strong electron-trap properties of the radical in this device. A sequential electron-to-SOMO then hole-to-HOMO transfer has been put forward for a charge trapping-based electroluminescence mechanism in radical OLEDs. We speculate that charge imbalance results in light-emitting devices where the recombination zone is pinned to the emissive and electron transport layer.

Further research is needed to explore the variation of electron and hole transport properties for improved charge balance while sustaining low turn-on voltages. Due to the presence of the SOMO and its ambipolar charge trapping properties, established device considerations and architectures for phosphorescent and TADF OLEDs may not directly translate to success in radical-based OLEDs.

2.7.3 Blue-Shifted Emission

Donor-acceptor radical systems have been demonstrated with efficient emission in the red and deep-red optical range, 600-700 nm.[30,31,37,39,40,63,79] Lowering the emission wavelength to green and blue colors for radical OLEDs has proven challenging. The difficulty in obtaining higher energy emitters is the limited radical chemistry available, with most reports involving halogenated triaryl radical moieties.

Halogen substitutions have been extensively studied in triaryl systems, with a modest blueshift in emission on replacing Br with more electronegative Cl atoms: from 593 nm for tris(2,4,6-tribromophenyl)methyl (TTBrM)[80] to 569 nm for TTM in CCl_4.[81]

On the most electronegative halogen variant, the synthesis of a fully fluorinated version of TTM in TTFM has not been reported. Theoretical studies have suggested that the replacement of chlorines in TTM-3NCz with fluorine could cause emission wavelength to drop from 700 to 610 nm;[82] however, this is still far from 400-500 nm required for emitting in the blue.

For doublet emitters in the blue range, new radical moieties with intrinsically larger HOMO-LUMO gaps must be designed to enable larger HOMO-SOMO or SOMO-LUMO splitting. We note that as the D_1 energy is related to the minimum of the HOMO-SOMO excitation energy, the SOMO-LUMO excitation energy, and any linear combination of these transitions (see Figure 2.6). Consequently, the maximum D_1 emission energy of a radical emitter will be limited to approximately half the energy difference between the HOMO and the LUMO.

For higher energy doublet emitters, materials with less delocalised π-systems should be considered; i.e., less than the three phenyl groups in triphenylmethyl radical derivatives. Frontier HOMO and LUMO π-orbitals become higher and lower in energy, respectively, as a result of delocalisation.[83] The larger the extent of π-delocalisation, the closer the frontier π-molecular orbitals are in energy to the non-bonding SOMO level. As a result, higher energy doublet emission will be seen in systems with lower π-delocalisation, such as by incorporation of a sp^3 alkyl group adjacent to the trivalent radical carbon. To this end, there is a chemical synthesis challenge to reduce π-delocalisation in a non-alternant hydrocarbon radical for efficient and higher energy emission.

We note that delocalisation and steric hinderance of the radical moiety are important factors in stabilising radical emitters,[84] and newly designed materials must also possess sufficient stability to be OLED dopants. The currently limited chemical space for radical π-system emitters is one of the biggest issues which must be developed by innovation in organic chemistry. This is key to having radical emitters across the full visible range that could compete with current display and lighting technologies.

2.7.4 Stability of Radical Devices

While significant progress has been achieved recently to improve the intrinsic photostability of radical emitters, the operational lifetime of radical-based OLEDs must be improved beyond the minutes timescales that have been reported in order to push toward commercial viability.[40]

The PyBTM radical and the radical-acceptor electron-donor systems show substantially longer lifetimes for maintaining intensity of PL under UV radiation than the isolated TTM and PTM moieties.[32] When illuminated with radiation of 370 nm within cyclohexane, the intensity of PL from PyBTM decreases with a half-life of 2.58×10^4 s, which is 115 times longer than that of TTM (224 s).[32] Similarly the half-life of PTM under 355 nm radiation pulses (46.6 s) is significantly less than that of the PTM derivatives PTM-PCz (2.42×10^3 s), PTM-3PCz (8.73×10^3 s), and PTM-TPA (3.17

$\times 10^5$ s) when measured in deoxygenated cyclohexane.[38] By perturbing the alternant hydrocarbon nature of TTM and PTM radicals by aza-substitution (PyBTM) or forming donor-acceptor derivatives, the radicals appear to be less prone to cyclisation reactions that have been highlighted as one of the major degradation mechanisms.[39,85] We note that some bonds may be weakened on going from D_0 to D_1, leading to alternative degradation of organic radicals upon excitation. Better understanding of photostability should be supported by more detailed studies in future with quantum-chemical calculations and experiment, which could lead to the development of more stable radical emitters.

For redox stability, donor-acceptor triphenylmethyl radical derivatives have been shown to undergo reversible oxidation and reduction on the timescale of the electrochemistry experiments such as cyclic voltammetry. More long-term and solid-state redox stability has been demonstrated in molecular electronics demonstrations.[86–89] We consider that the stability may be attributed to the non-bonding nature of the SOMO, meaning that the overall bond order of a radical material does not decrease when it is oxidised by removing an electron from the SOMO or reduced upon addition of an electron to the SOMO. In non-radicals, electron oxidation occurs to bonding-type HOMO and reduction to anti-bonding-type LUMO, leading to a reduction in bond order for the molecule in both scenarios.

If we consider high photo-, redox-, and thermal stability for radical emitters such as TTM-xPyID, the short device lifetime stability cannot be explained from this.[40] It is not understood whether this device degradation is due to intrinsic instability of the radical molecule under electrical excitation or is related to the degradation of the device structure. Future efforts should focus on elucidating the degradation mechanisms to improve device lifetimes towards commercial expectations (running time of >5000 hours for blue OLEDs[90] and >10000 hours for red/green OLEDs[91] before a 5% drop in luminance from an initial value of 1000 cd/m^2).

2.8 Research Beyond Doublet Emission

2.8.1 New Functionality from Established Radical Motifs

In addition to ongoing research efforts for new radical moieties in doublet emitters, there has been important progress in the discovery of new functionalisation routes for existing π-radicals. As discussed in Sections 2.4-2.7, the functionalisation of TTM, PTM, and PyBTM by electron donor and acceptor groups has been explored in tuning the emissive properties of their radical derivatives, while also leading to improvements in thermal and photo-stability. In a sense, new radicals can be designed from old radical motifs.

Other chemical functionalisation efforts have led to well-known radical emitters such as TTM-1Cz being developed into polymers with non-conjugated backbones.[34] This has resulted in OLEDs with modest efficiencies of 3.0% for PS-CzTTM.[79] The other related report is by An et al. who have developed a super acid-catalysed route to radical polymers with carbazole-conjugated backbones, avoiding the use of heavy metal catalysts in polymerisation and producing 1.8% efficiency in electroluminescent devices.[92] We expect further progress in the area of radical polymer devices in future. Generally, we consider that the prospect of commercially relevant radical-based optoelectronics may be accelerated by established protocols of organic semiconductors in solution-processing of polymers, as well as vacuum-deposited devices from molecular radical emitters.

In other studies, functional groups have been used to attach organic radicals between metal electrodes for studying their charge transport properties.[86] On going from PTM to donor-acceptor-PTM derivatives, systems change from having free electrical current in both directions to acting as molecular rectifiers.[87] Alkyne-functionalised PTM radicals have also been shown to form self-assembled monolayers on gold and hydrogenated silicon surfaces, enabling use as photoswitchable capacitors and multistate electronic switches.[88,89] To this end, organic radicals could lead further advancements as useful components in molecular-scale electronics. Moving forward, optical and current readout from electrode-radical-electrode systems could be enabled by light-emitting radicals.

2.8.2 Electronic Tuning Without the Usual Heavy Atom Effect

As discussed, the quartet states in radicals are higher than the first excited doublet state, D_1, meaning that quartets will not form by intersystem crossing on thermodynamic grounds, and do not pose the same problems as triplet states in non-radical emitters.

Consequently, heavy atoms can be incorporated in radical systems to tune emission properties without increasing non-radiative losses by intersystem crossing pathways. The result is the ability to alter the electronic structure of triaryl radical moieties through inclusion of Br and I while maintaining non-radiative rates to within the same order of magnitude.[57,73] We note that the weakening of the carbon-halogen bond from the inclusion of heavier halogen atoms will also affect possible methods for device fabrication. The bond dissociation energy of C-halogen will decrease with increasing atomic number of the halogen: C-F > C-Cl > C-Br > C-I.[2] Therefore, molecules containing heavier halogens are likely to only be processable by solution-based methods such as spin-coating and are not stable enough to withstand thermal evaporation. We consider that the design of new materials will be led by processing requirements and consideration of the physical

properties of organic radicals (e.g., temperature stability) as well as electronic and optical properties.

The tri-iodinated radical compound, tris(2,3,5,6-tetrachloro-4-iodophenyl)methyl radical (3I-PTM)[57] mentioned earlier, is of particular interest as good emission properties are observed in a system we would otherwise understand to have alternancy symmetry and expect to be non-emissive. This motivates further research on fundamental design rules for radical emitters beyond our current understanding of the electronic structure in these systems.

The absence of the usual heavy atom effect in triplet formation also enables fluorescent metal complexes with doublet metal-ligand emission to be designed. The nitrogen lone pair in PyBTM derivatives has been employed in ligand-complexation to Zn(II), La(III),[93] and Au(I)[94,95] centers. Here, the emission energy can be altered by the substitution of the ion center, allowing a route to tunable doublet emission from a radical center proven to be stable and therefore without having to develop new radical motifs.[93] Furthermore, complexation of tripyrrindione to Zn(II) has shown radical emission at room-temperature (PLQE = 23% in THF) from a system not based upon the triaryl moiety.[96]

The coordination of radical moieties with Cu(II), Ni(II), Co(II), Fe(II), and Mn(II)[93] was observed to quench emission and has been attributed to electron-exchange-mediated mechanisms with partially filled d-orbitals.

2.8.3 Circularly Polarised Doublet Emission

Molecular chirality can lead to chiral, circularly polarised light emission.[97,98] One of the technology drivers for this research is to improve the light output efficiency of OLED displays.[99] 'Anti-glare' circularly polarising filters are commonly used in displays to trap the reflected ambient light in order to enhance display contrast. For standard OLEDs, as light is randomly polarised, this suggests that only half of the EL will leave the display. OLEDs with circularly polarised EL could double the efficiency of display technologies.

Intrinsic chirality has been recognised in the helical twist of the triaryl moiety in triphenylmethyl radicals. Bulky side-groups can lock these radicals into a particular handedness, preventing racemisation by the inversion of the twist and leading to reports of circularly polarised luminescence in TTM, PTM, and related radicals.[80,81,100] Circularly polarised PL in these demonstrations can be considered as 'local' type from the molecular site of emission.[101]

Intuitively, the racemisation energy barrier was observed to increase with increasing steric bulk of the halogen groups on going from chlorine in TTM to bromine in TTBrM; see chemical structures in Figure 2.10a. Circular polarised luminescence could be observed in TTBrM at room temperature with recorded polarisation values of $|g_{lum}| = 0.7 \times 10^{-3}$ [see Figure 2.10b],[80] whereas TTM samples exhibited racemisation and showed polarised emission at -20°C and lower temperatures.[81]

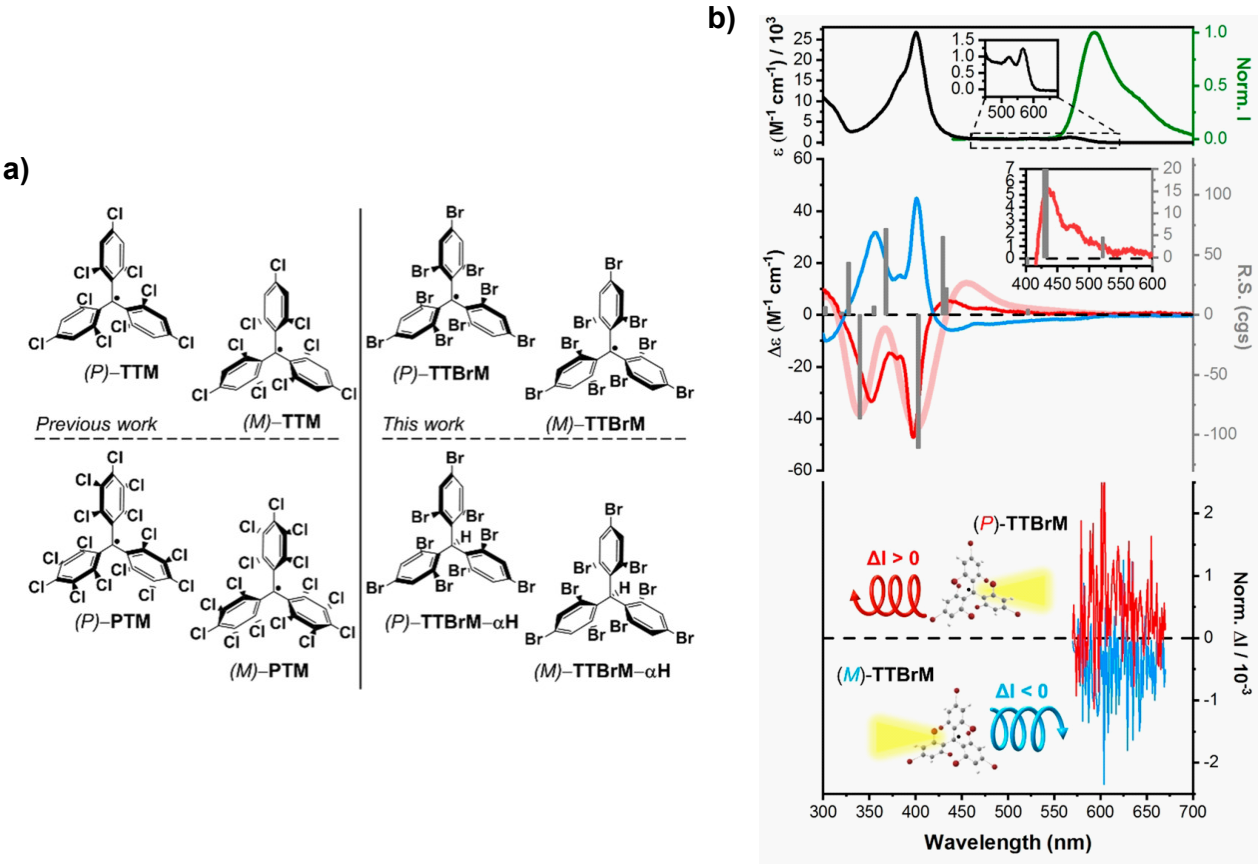

Figure 2.10: Circularly polarised light emission. a) Chemical structures for TTM, PTM, TTBrM, and TTBrM-αH indicating right-handed, (P)-, and left-handed, (M)-, helical symmetries. b) Top: Experimental UV/Vis absorption spectra (black) of TTBrM, together with total fluorescence spectra (green). Inset: Experimental UV/Vis absorption of lowest energy band. Central: Experimental circular dichroism spectra of (P)-TTBrM (thick light red line). The sticks (dark gray) indicate the positions and rotatory strengths of TD-DFT calculated transitions. Inset: Experimental and theoretical circular dichroism profiles for the lowest energy band. Bottom: Circularly polarised luminescence spectra of two enantiomeric fractions of TTBrM. Additionally, a schematic representation of the CPL response (ΔI) of the two enantiomers has been included, with $\Delta I > 0$ and $\Delta I < 0$ for (P)- and (M)-enantiomers, respectively. Figure and caption have been adapted with permission from Mayorga-Burrezo et al., Chem. A Eur. J. 26, 3776-3781 (2020). Copyright 2020 Wiley-VCH.[80]

From a different physical origin, circularly polarised doublet emission has also been shown in TTM-3PCz-PMMA films as induced by a magnetic field and Zeeman splitting

of the doublet-spin states.[100] This report also included the demonstration of circular polarised emission in TTM-1Cz and PTM-PCz from 'non-local' chirality origin. Light emission can be polarised by transmission through a chiral medium with dielectric anisotropy, here being chiral supramolecular and liquid crystal structures.[100]

It is expected that chiral radical emitters will be translated to circularly polarised OLEDs with doublet emission, where the benefits of higher internal quantum efficiency of radical-based electroluminescence can be combined with increased light-outcoupling properties.

2.8.4 Radical-Radical Interactions

Our discussion has concentrated on mono-radicals with doublet-spin-1/2 properties. However, two interacting radical groups can also form total spin-singlet-0 and spin-triplet-1 ground and excited state manifolds[75,102] and can occur within (intra) and between (inter) molecules.

Blasi et al. demonstrated that TTM radicals form stable and luminescent dimeric excimers with deep red excimer emission of 645-685 nm when doped in αH-TTM organic nanoparticles and ~734 nm when doped in a PMMA matrix.[102] Given the chlorine's steric bulk in protecting the radical center, it was surprising that substantial intermolecular π-interactions can be achieved in radical excimer formation. As well as red-shifted luminescence, radical excimer emission is substantially slower than radical monomeric emission. For excimer emission in 10.1% PyBTM/αH-PyBTM, up to 30% contribution of emission decay was found with exponential time constant higher than 500 ns; for 0.05% PyBTM/αH-PyBTM, the monomer emission decay was fitted to 115 ns time constant.[103]

Toward better understanding these systems, the spin properties of analogous PyBTM radical excimers have been probed by Kimura et al.[75,104] PyBTM was doped (0.05%-23%) in αH-PyBTM and displayed decreasing monomeric emission at 563 nm and increasing excimeric emission at 680 nm with increased doping (Figure 2.11a).[75] The monomer and excimer emission profiles in intermediate % doped samples (e.g., 10%) were found to be correlated, showing increasing monomer:excimer ratio with increasing field strength: for 4.2 K, ~0.45 at 0 T to ~1.3 at 18 T.[75] Follow-up studies have been conducted to probe the magnetic field dependence (up to 14.5 T) on the emission decay profiles in PyBTM/αH-PyBTM systems.[103,105] From the field dependence on monomer/excimer emission intensity and decay lifetime, the authors showed that these effects originated from magnetically sensitive singlet-triplet interconversion of the ground state, where the field dependence was translated to the higher-energy emission states upon photoexcitation. This is unusual be-

cause magnetic-field-dependent singlet-triplet photophysics usually originates in excited state levels (e.g., radical pairs) following charge transfer.[106] Here, radical-radical interactions between spin-1/2 species leads to new manifolds of singlet and triplet levels. This could be used as platforms for opto-spintronics where the relative singlet/triplet spin ratio is controlled by photoexcitation and magnetic fields.

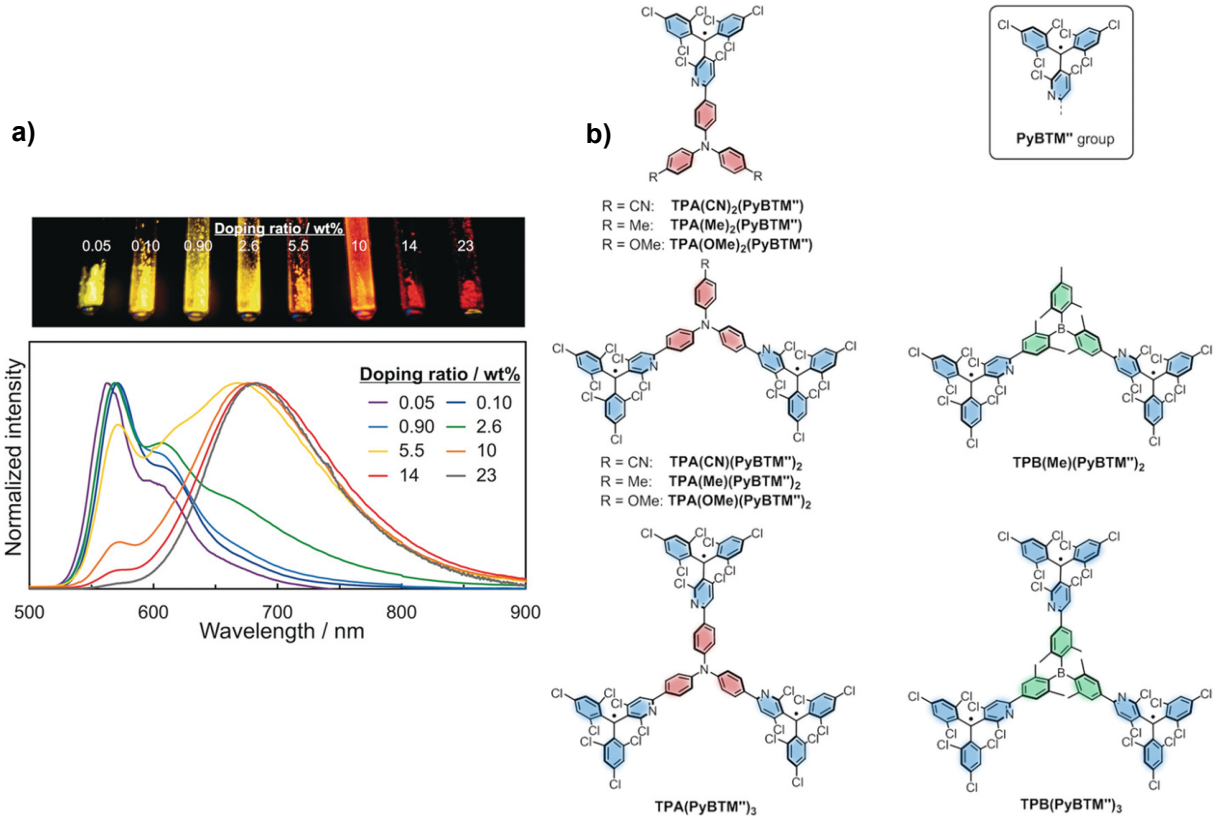

Figure 2.11: Radical-radical interactions and emission properties. a) Excimer emission in PyBTM systems. Monomeric (563 nm) and excimeric (680 nm) emission can be tuned by the doping ratio of the PyBTM radical within an αH-PyBTM matrix. a) has been reproduced with permission from Kimura et al., Angew. Chem. 130, 12893-12897 (2018). Copyright 2018 Wiley-VCH.[75] b) Chemical structures of bi- and tri-radicals as reported by Hattori et al.[64] b) has been reproduced from Hattori et al., Chem. A Eur. J. 25, 15463-15471 (2019). Copyright 2019 Wiley-VCH.[64]

We note that triplet excitons can be emissive in inter- and intra-molecular biradical systems due to the presence of ground states in the triplet manifold. The synthesis of intramolecular biradicals with singlet and triplet levels, and triradicals with doublet and quartet levels, has also been shown to yield luminescent systems that can be employed in light-emitting devices[64] (Figure 2.11b). Ballesteros et al. have also led work on cations of PTM-carbazole derivatives where conjugation can be broken due to steric bulk between electron acceptor and donor moieties, resulting in a biradical triplet ground state.[107] Research in this area has highlighted the potential of polyradicals, in addition to monoradicals, as dopants that eliminate dark excitons for more efficient OLEDs.

Chapter 3

Experimental Methods

3.1 Sample Preparation

Materials were stored under nitrogen atmosphere (<1 ppm O_2, < 0.5 ppm H_2O) to minimise any degradation of samples.

Solutions were prepared using anhydrous solvents under nitrogen atmosphere, with photophysical measurements carried out through transferring of samples into 1 mm path-length UV-grade quartz cuvettes (Hellma 110-1-40) that were sealed with a PTFE stopper and parafilm. In this thesis, photophysical characterisation of solutions were carried out in dilute solution (100-200 μM) such that optical densities were maintained below 0.3.

Thin films (nm-μm) of samples were generated through spin coating, in which sample solutions were deposited onto a rotating substrate. Samples were spun coat onto quartz-coated glass substrates that were cleaned through sequential sonication (10 minutes) in deionised water, acetone and isopropanol unless otherwise specified. Dynamic spincoating with high spin speeds (>3000 rpm) and high volatility solvents (e.g. chloroform) was used to minimise molecular aggregation and maximise uniformity of doped films. Meanwhile, static spincoating with lower volatility solvents (e.g. toluene) was used where a higher degree of molecular packing was desired. Specific details of spin coating methodologies are outlined within sample preparation sections for each of the experimental chapters. A comprehensive review of spin-coating theory and procedures has been outlined by Ossila.[108]

Sample solutions for trESR measurements were loaded into 3.8 mm UV-grade fused quartz EPR tubes under nitrogen atmosphere, before being sealed either using a flame or with vacuum grease and parafilm.

3.2 Determination of Excitonic and Orbital Energy

The energy of excitonic states was estimated from the wavelength of the peak intensity of emission unless stated otherwise. In closed-shell and open-shell materials, the fluorescence profile gives the singlet S_1 and doublet D_1 energy, respectively. The phosphorescence profile from gated photoluminescence experiments was used to determine triplet T_1 energy.

HOMO and LUMO energies for closed-shell systems were taken from literature unless stated otherwise. Orbital energies of luminescent radical species were estimated from cyclic voltammetry measurements performed by the group of Prof. Feng Li. In closed-shell systems, cyclic voltammetry can typically measure oxidation and reduction potentials for the molecule, allowing HOMO and LUMO levels to be estimated. However, cyclic voltammetry of radical systems instead measures the oxidation and reduction potential of the radical SOMO. The reduction potential for the SOMO is higher than that of the oxidation potential due to the extra coulombic repulsion resulting from addition of an electron into the singly-occupied molecular orbital.[39] For the luminescent radicals described in this thesis, oxidation potentials for the HOMO can not be directly measured within cyclic voltammetry, such that the HOMO was estimated through subtraction of the D_1 excitonic energy from the reduction potential of the SOMO.

CT state energies were estimated using the smallest possible energy difference between an electron excited to the SOMO/LUMO of one molecule, and a hole in the HOMO of the other molecule.

3.3 Steady State Photophysical Characterisation

3.3.1 Steady State Absorption

Steady-state absorption of solutions were measured on a Perkin-Elmer Lambda 365+ Double Beam UV-Visible Spectrophotometer. In the spectrophotometer, light was generated by either a deuterium (UV) or tungsten-halogen (visible) lamp before being passed through a monochromator. The monochromated light was collimated and passed through the sample, with transmission measured using a silicon photodiode. The absorbance, A, defined using the Beer-Lambert Law gives:

$$A = -\log_{10}\left(\frac{I}{I_0}\right) \tag{3.1}$$

where I and I_0 are the measured intensity for the sample and a blank reference sample respectively. The absorbance can be related to extinction coefficient for a sample through:

$$A = \epsilon c l \tag{3.2}$$

where ϵ is the extinction coefficient, c is the solution concentration and l is the measurement pathlength.

3.3.2 Steady State Photoluminescence

Samples were photoexcited at 405 nm, 520 nm or 658 nm using laser photodiodes (ThorLabs L405P20, L520P50 or L658P040) in combination with a laser diode mount (ThorLabs LDM56). The laser photodiodes were controlled using independent current and temperature controllers (ThorLabs LDC205C and TED200C). Temperature stability of the laser diode was achieved through optimisation of a proportional-integrative-derivative (PID) controller for the thermal load of each laser diode.

Photoluminescence was collected using a lens, spectrally filtered to remove any laser excitation and passed via a fibre-optic cable to an Oxford Instruments Kymera 328i Spectrograph. In the spectrograph, light incident on a grating was split in the horizontal direction into different wavelengths of light. These different wavelengths of light were then fed into an Andor Newton 920 CCD camera, whereby different columns of pixels on the CCD array were read out to allow for collection of spectrally resolved data.

Laser power was measured using a silicon photodiode and power meter (Thorlabs PM100D and S120C), whilst beam size was measured using a 2-dimensional silicon CCD camera as a beam profiler.

3.3.3 Photoluminescence Quantum Yield (PLQY)

The PLQY of a sample quantifies the probability of a photoexcited state in a sample emitting a photon. The PLQY of both solutions and films were measured with a Hamamatsu Quantaurus-QY Plus UV-NIR absolute PL quantum yield spectrometer (C13534-11). Broadband light from an 150 W xenon lamp was passed through a monochromator to provide variable excitation between 250-800 nm, with photoluminescence from samples collected using an integrating sphere and measured using a spectrally calibrated silicon photodetector. The photodetector port inside the integrating sphere was covered using a baffle, minimising the effect of variations in the path of the excitation beam or photoluminescence on the intensity read by the photodetector. The inside of the integrating sphere was coated with a material whose reflection was spectrally flat such that the collection efficiency for different wavelengths of light was the same.

The PLQY of samples was calculated using a two-step methodology, however, we note that PLQY can additionally be measured using the three-step de Mello methodology in which indirect excitation of the sample is also considered.[109] The PLQY, Φ, was calculated through dividing the area of spectrally resolved photoluminescence by the loss in area of the excitation peak due to sample absorption:

$$\Phi = \frac{P_s}{L_0 - L_s} \tag{3.3}$$

where P_s is the spectrally resolved area of sample photoluminescence, and L_0 and L_s are the areas of the spectrally resolved excitation peak for both a blank control and the sample. Using the PLQY, the ratio of radiative and non-radiative rates for an excited state can be calculated:

$$\Phi = \frac{k_r}{k_r + k_{nr}} \tag{3.4}$$

where k_r and k_{nr} are the rates of radiative and non-radiative decay of the excited state, respectively.

3.4 Transient Photophysical Characterisation

3.4.1 Time-Correlated Single Photon Counting (TCSPC)

TCSPC was measured using an Edinburgh Instruments FLS1000 Photoluminescence Spectrometer and controlled using the Edinburgh Instruments Fluoracle software. Photoexcitation was provided at 635 nm from a pulsed laser diode (Edinburgh Instruments EPL-635, 65 ps pulse width). Photoluminescence was collected perpendicular to the direction of excitation, spectrally filtered with a long-pass filter and passed through a series of monochromators (enabling variable measurement wavelength and bandwidth) to a photomultiplier tube (PMT). The maximum temporal window for measurement could be varied between 50 ns to 40 µs through control of the repetition rate of the laser (2.5 kHz - 20 MHz). An electronic triggering signal was sent from the pulsed laser to the TCSPC electronics, synchronised to each laser pulse released from the pulsed diode. Measurements were taken in 'reverse' mode, such that detection of a photon by the PMT initialised the TCSPC electronics to measure the time until the next electronic reference signal from the pulsed laser. Through successive measurements of the time between photon detection and the reference pulse, a histogram of the change in statistical intensity of photoluminescence following excitation could be built up.

The minimum lifetime that could be measured using TCSPC was defined by the width and shape of the Instrument Response Function (IRF) for the entire TCSPC system. For

the shortest measurement window of 50 ns, scatter from a blank control sample gave an asymmettrical IRF signal that limited lifetime characterisation to values above 200 ps. The temporal response for the IRF resulted from a combination of the finite laser pulse width, the temporal response of the photodetector and the measurement electronics, and light dispersion through the measurement system. Fitting of sample decays with lifetime on the order of the IRF was performed through convolution of an exponential fitting algorithm with an experimentally determined IRF:

$$\text{fit} = \left[A \exp\left(-t/\tau_1\right) + C\right] * \text{IRF} \tag{3.5}$$

where A and C are constant, t is the measurement time, τ_1 is the emissive lifetime, and IRF is the experimentally determined IRF. For transient spectra with more than a single lifetime, the IRF was convolved to a biexponential fitting function.

3.4.2 Femtosecond Pulsed Laser Generation

Photoexcitation for both spectrally-resolved transient photoluminescence and femtosecond transient absorption measurements were generated using a 1030 nm Yb:KGW femtosecond pulsed laser setup (Pharos, Light Conversion) operating at 25 kHz. In brief, a fibre-optic array is used to pump a ytterbium-doped monoclinic double tungstate gain medium (Yb:KGW, potassium gadolinium tungstate) within the laser's optical cavity. Pulsed laser excitation at 1030 nm is generated through Kerr-Lens mode-locking at a repetition rate of 76 MHz. These pulses are fed into a regenerative amplifier which combines multiple pulses to form a higher intensity pulse at a lower repetition rate (25 kHz). A pulse-picker enables for the repetition rate of the laser to be changed without altering the peak intensity of laser pulses, allowing a chosen fraction of generated laser pulses to leave the laser system.

Visible wavelengths for excitation were either provided from the 2nd (515 nm) and 3rd (343 nm) harmonic of the 1030 nm laser generated in a non-linear barium borate (BBO) crystal (PHM02-2H-3H, Light Conversion), or from a non-linear optical parametric amplifier (OPA) capable of generating femtosecond laser pulses between 300-2700 nm (Orpheus + Lyra, Light Conversion).

Beam sizes were estimated using the 'knife-edge' technique,[110] with laser power measured using a silicon photodiode and power meter (Thorlabs PM100D and S120C).

3.4.3 Spectrally-Resolved Transient Photoluminescence: Streak Camera

Spectrally-resolved transient photoluminescence spectra were measured using a HAMAMATSU Universal Streak Camera (Model C10910) capable of measuring photoluminescence with temporal resolution from picosecond to microsecond timescales. Measurement control was performed using the HAMAMATSU High-Performance Digital Temporal Analyser Software.

Photoluminescence was collimated and spectrally filtered to remove any scattered laser pump excitation. Photoluminescence was passed through a spectrometer such that different wavelengths of light were spatially separated in the horizontal plane. The spectrally resolved photons were passed into the streak tube onto a photocathode where they were converted into photoelectrons. These photoelectrons were accelerated by a high electric field through the streak tube, where they were passed through a pair of plates capable of generating strong electric fields in the vertical and horizontal directions. Measurements were taken using the 'single-sweep' module of the streak camera, in which the vertical electric field strength was linearly swept from high to low voltage during measurement. This resulted in photoelectrons being deflected vertically to different extents depending on the time they passed through the streak tube. Application of a horizontal electric field was used to deflect the photoelectron beam out of the measurement area whenever incoming photons were out of the desired measurement window. Resolved spectrally and temporally in the horizontal and the vertical plane respectively, photoelectrons were passed through a multi-channel gain medium which produced a cascade of electrons that passed onto a phosphorescent plate. Emission from the phosphor plate was collected, with an image of the phosphor plate focussed onto a CMOS chip where the signal was read out. Electronic triggerring for timing of the streak camera was taken from the oscillator of the Yb:KGW laser.

Measurement over different temporal ranges was enabled in the streak camera through varying the rate at which the vertical voltage was linearly swept, with shorter measurement windows and higher temporal resolution resulting from faster rates of electric field sweep. Streak camera measurements show broadening of temporal signals on the order of the measurement window as a result of divergence of the photoelectron beam through the streak camera and jitter in the triggering of the vertical sweep in comparison to the excitation of the sample.

Streak camera images were summed within desired wavelength ranges to form a collection of transient decays. Temporal broadening was approximated using a gaussian curve,

such that these transient decays were fit to an exponentially modified gaussian, which is the analytical expression for a gaussian convolved with an exponential decay:

$$\text{fit} = \frac{A}{2\tau_1} \exp\left(\frac{\sigma^2}{2\tau_1^2}\right) \exp\left(-\frac{t-t_0}{\tau_1}\right) \left(1 + \text{erf}\left(\frac{-(t-t_0)+\sigma^2/\tau_1)}{\sqrt{2}\sigma}\right)\right) + C \qquad (3.6)$$

where A and C are fitting constants, σ and t_0 are the width and center for the gaussian respectively, τ_1 is the decay lifetime, and erf is the error function. For transient decays with more than a single lifetime, fitting was performed using the analytical expression for a gaussian convolved with a biexponential decay.

3.4.4 Femtosecond Transient Absorption (fsTA)

Though transient photoluminescence can probe the excited-state dynamics for emissive species, we are often also interested in the dynamics of photoexcited species that do not emit light such as charge transfer and triplet excited states. We can measure the dynamics of such dark species through transient absorption, in which a 'pump' pulse of light is used to generate a population of excited states within a material that are then probed by a broadband 'probe' pulse of light. The differential absorption of this probe pulse gives a snapshot of the populations in the photoexcited sample. Through varying the time between pump and probe pulses using a delay stage, the kinetics of excited state species could be monitored.

In this thesis we use a commercial fsTA setup (HARPIA-TA, Light Conversion), in which both pump and probe pulses originate from the Pharos femtosecond-pulsed laser detailed in Section 3.4.2. A single 1030 nm pulse from the Pharos setup is split with 80% of power used to generate the pump pulse via the OPA detailed in Section 3.4.2, with the remaining 20% used to create the broadband probe pulse through white-light generation in a sapphire crystal. The path of pump and probe beams as shown on Figure 3.1 are detailed below:

Pump Beam Path

The pump beam pulse generated in the OPA was fed into the transient absorption spectrometer via a shutter (X1) through an optical chopper (C), which modulates whether light was blocked or passed on to the sample at a frequency of 75 Hz. The pump beam then passed through a Berek Compensator (BC) allowing for control of the linear and circular polarisation of the pump beam. A beamsplitter (BS1) was used to pass 5% of the pump excitation to a photodiode (PD1), with the remaining 95% passing through a manual ND wheel (ND1) allowing for control of pump fluence. The pump beam was finally focussed

by a parabolic mirror (PM1) to a point just before sample. The remaining pump was blocked by an iris following the sample stage.

Probe Beam Path

1030 nm radiation was fed into the transient absorption spectrometer through a shutter (X2), before having its polarisation rotated 45° by a linear polariser and quarter wave plate (PQW). It was then passed towards a delay stage (DS) comprising two gold retroreflectors (RR1 and RR2) and a mirror (M1). Through translation of the first retroreflector (RR1) along the delay stage rail, the probe path length was varied by a distance equivalent to 8 ns. Following its return from the delay stage, the 1030 nm polarisation was rotated a further 45 degrees such that it reflected off the linear polariser. The beam size was reduced using a telescope (T) to have a higher fluence for driving non-linear processes such as second-harmonic generation or white-light generation. 1030 nm radiation was then passed to a white light control (WLC) consisting of an iris and variable ND wheel that controlled the beam size and power used to seed white light. For transient absorption measurements in the UV range (360-520 nm), 515 nm radiation was required to seed the non-linear crystal. 1030 nm radiation was converted to 515 nm prior to the white light control using a second harmonic generation unit (SHG) comprising of a non-linear crystal and a polarisation filter. The white light seed beam was focussed by a lens (L1) onto a sapphire non-linear crystal (NLC) where broadband white light pulses were generated. The broadband pulses were collimated by a parabolic mirror (PB2), passed through a spectral filter (F) to remove any of the remaining white light seed pulse, and focussed onto the sample held on a sample stage (SS) by another parabolic mirror (PB3). Following transmittance through the sample, the broadband white light pulses were recollimated using another lens (L2) and passed through another ND wheel (ND2) to a spectrometer (S) consisting of a grating and a photodetector.

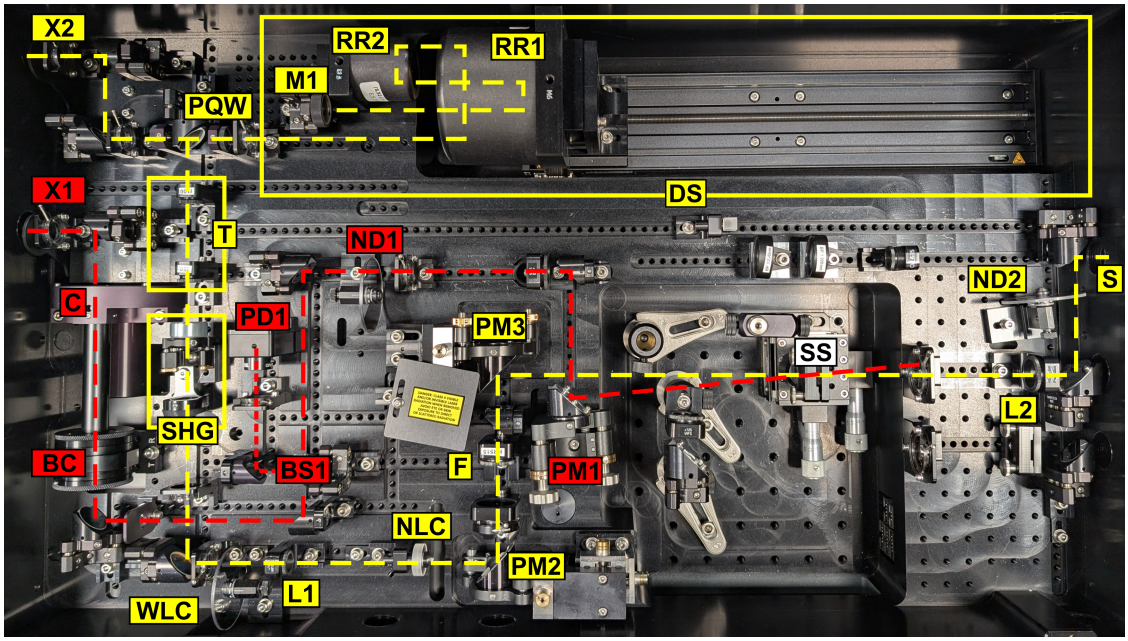

Figure 3.1: Optical layout of the pump (dashed red) and probe (dashed yellow) beams used for measurement of femtosecond transient absorption. Associated optical components are labelled for the pump (red box) and probe (yellow box) beams). Modules for the probe beam comprising several optical components are marked using a solid yellow line.

Differential absorption calculation

Measurement of the voltage on the pump photodiode (PD1) allowed for determination of when the optical chopper was open and closed such that the sample was excited and unexcited respectively. Measurements of the broadband probe pulse taken from the photodetector were binned into scans for the photoexcited sample (chopper open) or the unexcited sample (chopper closed). Scans obtained at the transition of the optical chopper between open and closed states were discarded, typically constituting 5-10% of the total acquired scans. 2000 averages were taken for both the excited and unexcited sample for each probe delay t across the wavelength range λ, with the spectrally resolved change in optical density of the sample over time, $\Delta\mathrm{OD}(\lambda, t)$, calculated as:

$$\Delta\mathrm{OD}(\lambda, t) = \log_{10}\left(\frac{I_{\text{not pumped}}(\lambda, t) - I^{\text{back}}_{\text{not pumped}}(\lambda)}{I_{\text{pumped}}(\lambda, t) - I^{\text{back}}_{\text{pumped}}(\lambda)}\right) \tag{3.7}$$

where $I_{\text{not pumped}}(\lambda, t)$ and $I_{\text{pumped}}(\lambda, t)$ were the averaged spectrally-resolved intensities of the broadband probe pulse on the photodetector for the not pumped and pumped samples respectively. $I^{\text{back}}_{\text{not pumped}}(\lambda, t)$ and $I^{\text{back}}_{\text{pumped}}(\lambda, t)$ were the background intensities measured by the detector with the probe pulse turned off.

Observed fsTA features

fsTA features examined in this thesis include the ground state bleach (GSB), excited state absorption (ESA) and stimulated emission (SE) of photoexcited samples. GSB results from photoexcitation depopulating the ground state of a sample, resulting in a negative absorption with spectral profile similar to that of the steady-state absorption of the ground state. ESA results from the absorption of light by photoexcited species, whilst SE results from photons in the probe beam having energy equal to that of the radiative transition of a photoexcited species, such that emission is stimualted from the excited state.

3.5 Magnetically-Sensitive Photoluminescence

Magnetically-sensitive photoluminescence was measured using the steady-state photoluminescence setup detailed in Section 3.3.2, with samples placed within an electromagnet (GMW 3480 dipole 45 mm) that was controlled by a Kepco BOP MG/ME 1 kW power supply. For initial measurements, photoluminescence was measured every second whilst a 0.05 Hz (20 s period) sinusoidal magnetic field was applied to the sample. The photoluminescence intensity for each scan was integrated, before measurements separated by 20 s were collected together to give the average PL intensity for the same point throughout the magnetic field cycle.

For later measurements, simultaneous control of both the Andor Newton 920 CCD camera and Kepco BOP MG/ME 1 kW power supply was achieved using custom software developed in LabView. A list of measurement voltages were supplied to the software, with each voltage in turn applied by the power supply to the electromagnet before a photoluminescence measurement was taken. With each new applied voltage, the system was given 10 s to reach steady state before a measurement was taken, and in between measurements the photoluminescence at zero magnetic field was measured as a reference for the sample. The reference at zero field allowed for degradation of the sample to be taken into account, with each pair of measurements being used to calculate the change in magnetic field effect (MFE) for photoluminescence:

$$\mathrm{MFE}\,(\%) = 100 \times \left(\frac{\mathrm{PL_V} - \mathrm{PL_0}}{\mathrm{PL_0}} \right) \tag{3.8}$$

where MFE(%) is the percentage change in photoluminescence as a result of applying voltage V, and $\mathrm{PL_V}$ and $\mathrm{PL_0}$ are the integrated photoluminescence intensities from the sample at the applied voltage and 0 voltage respectively. Several repeats of each set of voltages were measured, with the average MFE calculated. The error in the mean was taken from the standard deviation of the experimentally measured MFE values for a single voltage, divided by the square root of the number of averages.

The applied voltages were calibrated to the magnetic field between the electromagnet poles using a gaussmeter with tranvserse probe (GM08 Gaussmeter, HIRST Magnetic Instruments Ltd.), such that final results show the observed MFE versus the applied field.

3.6 Transient Electron Spin Resonance (trESR)

Electron spin resonance allows us to probe the magnetic interactions of paramagnetic species, observing differences in the population of paramagnetic spin sub-levels. In trESR, samples are photoexcited using pulsed laser excitation such that we can observe the temporal evolution of the spin-populations generated from excited-state processes.

Briefly, samples are placed within a microwave resonator cavity whereby a CW microwave source is used to generate a standing wave. A variable magnetic field is applied to the sample, causing energetic splitting between the spin sub-levels due to the Zeeman interaction as described in Section 2.3.1. When the energetic splitting of paramagnetic states due to applied magnetic field matches that of the applied microwave source, unequal population of spin sub-levels results in resonant transitions between sub-levels that cause absorption or emission of microwave radiation. As the magnetic field is sweeped, different spin sub-level transitions can come into resonance allowing us to probe the magnetic interactions of paramagnetic systems through their absorptive or emissive signals. From measuring the impedance of the cavity we are able to detect these absorptive or emissive signals, returning a 2-dimensional array showing the change in trESR signal with time and magnetic field. Spin sub-level populations and magnetic interactions can be fit to obtained trESR signal through software such as EasySPIN.

In this thesis, trESR spectra were collected both at the Centre for Advanced ESR (CAESR) in the Department of Chemistry of the University of Oxford and at the Department of Chemistry in Cardiff University. At CAESR, trESR spectra were collected from a Bruker BioSpin EleXSys I E680a at X-band (9.7 GHz, 0.2 mW) with an ER 4118X-MD5W resonator with the sample temperature controlled by an Oxford Instruments CF935O cryostat under liquid helium flow and an ITC-503S controller. Variable photoexcitation was provided by an optical parametric oscillator (Opotek Opolete HE355) which was synchronised to the spectrometer using a delay generator (Stanford Research DG645). At Cardiff University, trESR spectra were instead collected using a Bruker E580 at X-band (9.7 GHz, 2 mW).

For measurements taken on both setups, 2-dimensional trESR datasets were baseline corrected in both time and magnetic field.

Chapter 4

Radical Spin Polarisation and Magnetosensitivity from Reversible Energy Transfer

Molecular spins provide potential building units for future quantum information science and spintronic technologies. In particular, doublet ($S = 1/2$) and triplet ($S = 1$) molecular spin states have the potential for excellent optical and spin properties for these applications if useful photon-spin mechanisms at room temperature can be devised. In this chapter, we explore the potential of exploiting reversible energy transfer between triplet and doublet states to establish magnetosensitive luminescence and spin polarisation. The dependence of the photon-spin mechanism on the magnitude and sign of the exchange interaction between the doublet and triplet spin components in amorphous and crystalline model systems is investigated. Design of a magnetic field-inclination sensor is proposed from understanding the required 'structure' (spin interactions) to 'function' (magnetosensitivity).

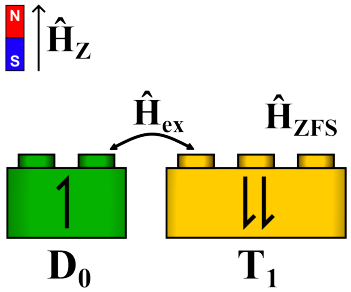

The findings presented in this chapter are published as paper [2] in the List of Publications.

4.1 Photon-Spin Mechanisms in Radical-Triplet Systems

Doublet ($S = 1/2$) and triplet ($S = 1$) spin states from molecules provide potential building units for creating designer materials platforms in quantum information science (QIS) and spintronic applications.[111,112] The challenge is to combine the potential for excellent optical and spin properties in π-conjugated organic materials and achieve useful photon-spin mechanisms at room temperature. In these systems, triplet states are derived from organic chromophore groups following photoexcitation and intersystem crossing.[46,47,113–115] Doublet states are obtained from the unpaired electron spin in stable radicals.[45,116–119] The emergence of luminescent radicals is expanding the range of spin and magnetic phenomena in doublet-triplet systems from the ground electronic state of radicals to excited states.[120]

In chromophore-radical systems, the 'extra spin' of the radical can accelerate conversion between singlet ($S = 0$) and triplet chromophore states in enhanced intersystem crossing (EISC).[45,121–124] Here it is necessary to consider the total spin of the chromophore-radical system rather than the individual moieties. A singlet chromophore (S_1) combined with a ground state radical doublet (D_0) forms an overall doublet state known as the sing-doublet. Triplet chromophore (T_1) and radical doublet pairs form overall doublet or quartet ($S = 3/2$) states that may be denoted trip-doublet and trip-quartet. A spin-conserving pathway for singlet-to-triplet conversion of the chromophore moiety in EISC can proceed via sing-doublet and trip-doublet states. Efficient doublet quenching of chromophore triplet states can also become spin-allowed via trip-doublet encounter pairs resulting in deexcitation to the sing-doublet ground state, as probed by its magnetic field dependence.[125]

Recent work showed that the interplay of trip-doublet and trip-quartet states with excited D_1 states of radicals can be exploited in demonstrations of spin initialisation, manipulation and read-out by light at room temperature.[126] The emergence of stable and luminescent radicals[30,31,48] with integration into radical-triplet intermolecular[127,128] and intramolecular systems[126] unlocks the possibility of optical read-out for studying the magnetosensitivity of radical-triplet pairs.

From previous work with non-luminescent radicals, it is established that ground state radical spin polarisation may be driven by interactions with unpolarised triplet states via the Radical-Triplet(/Quartet) Pair Mechanism (RTPM/RQPM) where radical and triplet components undergo diffusive translational motion,[129,130] and in terms of the Reversed Quartet Mechanism (RQM)[131,132] in systems where the components are fixed in space. In general, these mechanisms are initiated for strongly cou-

pled radical-triplet pairs that form trip-doublet $\left(M_S = \pm 1/2, |\mathrm{D}_{\pm 1/2}\rangle\right)$ and trip-quartet $\left(M_S = \pm 3/2 \text{ or } \pm 1/2, |\mathrm{Q}_{\pm 3/2}\rangle \text{ or } |\mathrm{Q}_{\pm 1/2}\rangle \text{ respectively}\right)$ states. A rapid, irreversible, and spin-selective process takes place such that the trip-doublet eigenstates of the radical-triplet pair are selectively populated or depopulated. Spin polarisation of the $|\mathrm{D}_{+1/2}\rangle$ and $|\mathrm{D}_{-1/2}\rangle$ states is generated by asymmetrical re-distribution of populations to and from the trip-quartet manifold.

4.2 Magnetosensitivity from Reversible Doublet-Triplet Energy Transfer

Here we consider radical-triplet pairs involving reversible energy transfer with excited states of luminescent radicals $\left(\mathrm{D}_1 + \mathrm{S}_0 \rightleftharpoons \mathrm{D}_0 + \mathrm{T}_1\right)$. New potential mechanisms for generating spin polarisation and magnetic field inclination sensing are explored. We investigate how magnetic interactions of the radical-triplet pair can lead to magnetic field effects with optical read-out through modulating the 'spin-allowed' character of energy transfer.

4.2.1 Spin-Dependent Energy Transfer Rates

Starting from the framework of the Merrifield model for radical-triplet pairs,[133] we apply a kinetic scheme where energy transfer takes place from an excited radical doublet, D_1, to the triplet, T_1, via the eigenstates of the radical-triplet pair, P_j:

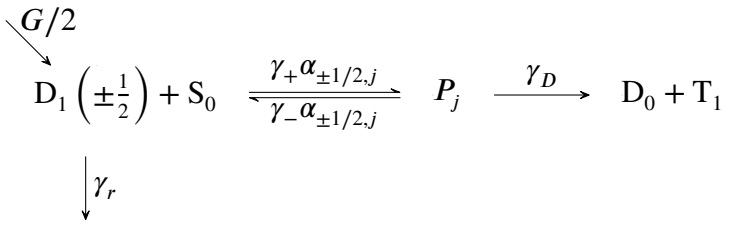

Scheme 4.1: Kinetic mechanism for magnetosensitivity in luminescent radical-triplet systems

In Scheme 4.1, D_1 is generated with unpolarised light at a rate G (such that both doublet states are generated equally at rate G/2) and can subsequently decay with radiative rate γ_r. Both radical doublet excited states $\mathrm{D}_1\left(\pm\frac{1}{2}\right)$ can undergo energy transfer to form one of the radical-triplet pair eigenstates P_j with rate constant $\gamma_+\alpha_{\pm 1/2,j}$, where $\alpha_{\pm 1/2,j}$ represents the overlap between the $|\mathrm{D}_{\pm 1/2}\rangle$ sing-doublet initial states and the radical-triplet pair eigenstate P_j: $\alpha_{\pm 1/2,j} = |\langle D_{\pm 1/2}|P_j\rangle|^2$. The radical-triplet pair eigenstates P_j can undergo reverse transfer with rate constant $\gamma_-\alpha_{\pm 1/2,j}$ to reform $\mathrm{D}_1\left(\pm\frac{1}{2}\right) + \mathrm{S}_0$, or dissociate into separate

$D_0 + T_1$ states with rate constant γ_D. Energy transfer rates for γ_+, γ_- and γ_D are assumed from previous studies into EISC[47,134] and triplet-triplet[135] systems to range from 100 ps-10 ns scale (Appendix A.2). To focus evaluation of the spin effects from doublet-triplet energy transfer, spin relaxation is ignored, reversibility of energy transfer is set between $D_1 + S_0$ and the pair states, and coherence effects between P_j states are ignored.

4.2.2 Spin-Interactions for a Radical-Triplet Pair

The radical-triplet pair eigenstates P_j are determined by the spin Hamiltonian $\hat{H}_{\mathrm{DT}}$:

$$\hat{H}_{\mathrm{DT}} = \underbrace{g\mu_{\mathrm{B}}\boldsymbol{B}\cdot\left(\hat{\boldsymbol{S}}_D + \hat{\boldsymbol{S}}_T\right)}_{\hat{H}_{\mathrm{Z}}} + \underbrace{J\left(\hat{\boldsymbol{S}}_D\cdot\hat{\boldsymbol{S}}_T\right)}_{\hat{H}_{\mathrm{ex}}} + \underbrace{D\left(\hat{S}^2_{T,z} - \frac{\hat{\boldsymbol{S}}^2_T}{3}\right)}_{\hat{H}_{\mathrm{ZFS}}} \tag{4.1}$$

where $\hat{H}_z$ is the Zeeman interaction for both the triplet and the radical doublet from an external magnetic field vector $\boldsymbol{B}$ with magnitude B; $\hat{\boldsymbol{S}}_D$ and $\hat{\boldsymbol{S}}_T$ are the spin operators for the doublet and triplet respectively; μ_{B} is the Bohr magneton, and g the Landé g-factor. $\hat{H}_{\mathrm{ex}}$ is the radical-triplet exchange interaction with coupling parameter $\boldsymbol{J}$, and H_{ZFS} represents the intramolecular zero-field splitting (ZFS) interaction of the triplet component with zero-field splitting parameter $\boldsymbol{D}$.

The P_j eigenstate energies are expected to vary for typical experimental fields (<2 T) from the μeV up to the meV scale due to $\hat{H}_{\mathrm{DT}}$. As energetic separation of D_1 and P_j states is typically on the order of 10 meV ($< k_B T$ for reversible energy transfer), modulation of energy transfer rates due to energetics is assumed to be small, with spin-interactions instead modulating energy transfer rates through controlling their 'spin-allowed' character.

This kinetic scheme is inspired by those employed by Merrifield and others to investigate magnetic field effects on triplet-triplet annihilation and singlet fission in chromophore systems.[125,133,135–140] The difference between triplet-triplet and radical-triplet systems is that the 'spin-allowed' pathway is governed by singlet and doublet character, respectively.[125,141]

Analogous to triplet-triplet systems, the use of a kinetic model between incoherent radical-triplet states in predicting radical-triplet MFEs is expected to be most accurate where fast reversible energy transfer (< ns) causes the lifetime of P_j to be short compared to spin-coherence lifetimes (∼ns timescale between states with μeV separation). In cases where spin-coherence between P_j states is significant, full evaluation of MFEs should be performed using density matrices for the radical-triplet pair.

4.2.3 Analytical Solutions for Excited State Doublet Photoluminescence and Spin Polarisation

Solutions for the excited radical doublet populations $\left[\mathrm{D}_{\pm 1/2}\right]$ in the radical-triplet pair system were derived (Appendix A.1) to write the total doublet photoluminescence, $\mathrm{PL} = \gamma_r \left(\left[\mathrm{D}_{+\frac{1}{2}}\right] + \left[\mathrm{D}_{-\frac{1}{2}}\right] \right)$ where $\epsilon = \gamma_-/\gamma_D$, $\kappa_j = \left(1 + \epsilon \left(\alpha_{+\frac{1}{2},j} + \alpha_{-\frac{1}{2},j} \right)\right)^{-1}$ and $\sum_j$ represents the summation over the radical-triplet eigenstates $\boldsymbol{P}_j$:

$$\mathrm{PL} = \frac{G\gamma_r}{\gamma_+} \left\{ \frac{\frac{\gamma_r}{\gamma_+} + 1 - \frac{\epsilon}{2} \sum_j \kappa_j \left(\alpha_{+\frac{1}{2},j} - \alpha_{-\frac{1}{2},j} \right)^2}{\prod_{i=\pm\frac{1}{2}} \left\{ \frac{\gamma_r}{\gamma_+} + 1 - \epsilon \sum_j \kappa_j \alpha_{i,j}^2 \right\} - \epsilon^2 \left(\sum_j \kappa_j \alpha_{+\frac{1}{2},j} \alpha_{-\frac{1}{2},j} \right)^2} \right\} \tag{4.2}$$

From this we derived the doublet spin polarisation in the excited state as:

$$\frac{\left[\mathrm{D}_{+\frac{1}{2}}\right] - \left[\mathrm{D}_{-\frac{1}{2}}\right]}{\left[\mathrm{D}_{+\frac{1}{2}}\right] + \left[\mathrm{D}_{-\frac{1}{2}}\right]} = \frac{\epsilon}{2} \frac{\sum_j \kappa_j \left(\left(\alpha_{+\frac{1}{2},j} \right)^2 - \left(\alpha_{-\frac{1}{2},j} \right)^2 \right)}{\frac{\gamma_r}{\gamma_+} + 1 - \frac{\epsilon}{2} \sum_j \kappa_j \left(\alpha_{+\frac{1}{2},j} - \alpha_{-\frac{1}{2},j} \right)^2} \tag{4.3}$$

Spin polarisation of the doublet excited state can be passed to the doublet ground state through emission. In this chapter we focus on the functional spin mechanisms in the excited state.

It is apparent from the dependence of Equations 4.2 and 4.3 on $\alpha_{\pm\frac{1}{2},j}$ and κ_j that magnetic fields can change the doublet photoluminescence yield and excited-state doublet spin polarisation of D_1. This occurs through magnetic fields altering the spin character of the radical-triplet eigenstates through the Zeeman interaction.

4.3 Strongly-Coupled ($|J| \gg |D|$) Radical-Triplet

4.3.1 Disordered Systems

Firstly, we consider spin simulations of the radical-triplet system in the strongly coupled regime ($|J| = 20|D|$, i.e. $|J| \gg |D|$).Amorphous samples were modelled by setting the triplet ZFS tensor at random orientations to an applied magnetic field, where $D = 5$ μeV (typical for triplets in molecular π-conjugated systems) with zero transverse component ($E = 0$). Figure 4.1 shows that for both radical-triplet systems in antiferromagnetic ($J < 0$) and ferromagnetic ($J > 0$) regimes of electron exchange, changes in doublet PL from the magnetic field effect, MFE $= 100\% \times (\mathrm{PL}(B)/\mathrm{PL}(0) - 1)$, and spin polarisation are observed at magnetic fields corresponding to doublet-quartet anticrossings.

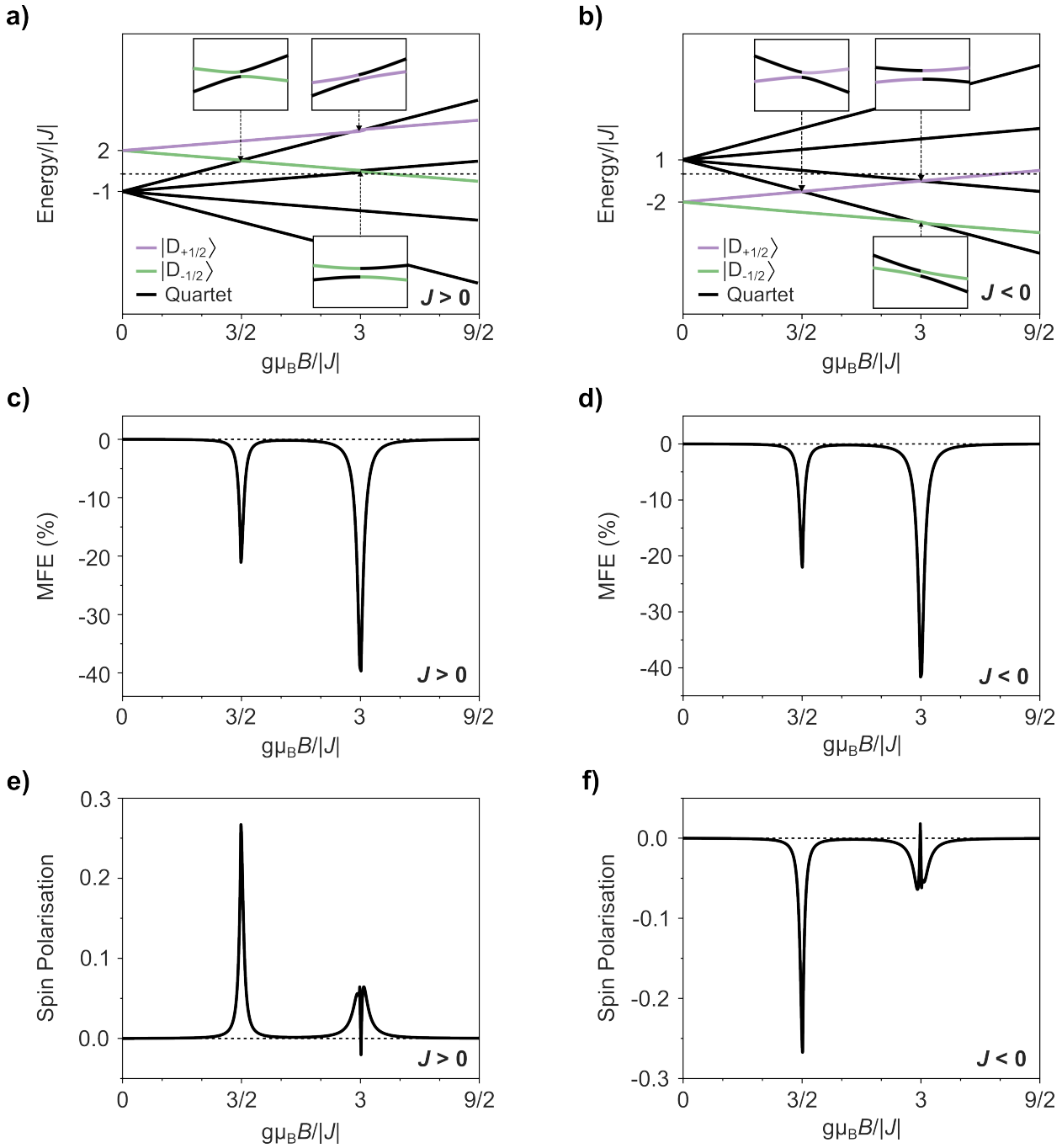

Figure 4.1: Magnetic response for strongly coupled radical-triplet pairs ($|J| = 20|D|$, i.e. $|J| \gg |D|$) that are randomly oriented to applied magnetic field. Zeeman splitting of radical-triplet pair states with applied magnetic field B, for a) ferromagnetic ($J > 0$) and b) antiferromagnetic ($J < 0$) exchange coupling. Insets: doublet-quartet anticrossings at triplet ZFS oriented to applied magnetic field direction, $\theta = \pi/4$. MFEs for doublet photoluminescence are shown for c) $J > 0$ and d) $J < 0$ radical-triplet exchange coupling. Magnetosensitivity for spin polarisation from radical-triplet systems with e) $J > 0$ and f) $J < 0$ exchange coupling.

At zero field, the eigenstates for the strongly coupled radical-triplet pair reflect those of the radical-triplet exchange interaction, i.e. pure trip-doublet or trip-quartet spin states with energy $+2J$ and $-J$ respectively. At magnetic fields ($g\mu_B B$) of $3|J|/2$ and $3|J|$, the Zeeman interaction leads to states with energy separations on the order of the ZFS parameter, $|D|$. At such fields, the ZFS interaction mixes pure spin eigenstates such that they form doublet-quartet mixtures. The hybridisation of these states results in anticrossings, with the spread of trip-doublet character resulting in a decrease in doublet photoluminescence for negative MFE, irrespective of $J > 0$ or $J < 0$.

Away from such anticrossings, application of a magnetic field alters the energy of the radical-triplet pair eigenstates but not the distribution of their spin character. Consequently, no magnetic field effect (MFE) for doublet emission or spin polarisation is observed outside the doublet-quartet anticrossings for strongly coupled radical-triplet pairs.

The lower field anticrossing ($g\mu_B B = 3|J|/2$) only takes place for one of the trip-doublet states, with the asymmetrical distribution of trip-doublet character resulting in excited-state doublet spin polarisation. The sign of this polarisation is characteristic of the sign of the exchange interaction, with $J < 0$ and $J > 0$ showing negative and positive spin polarisation respectively as defined by Equation 4.3.

A second field region around $g\mu_B B = 3|J|$ shows spin polarisation where both trip-doublet states undergo anticrossings with trip-quartet states. In addition to a broader feature of the same spin polarisation sign as at $g\mu_B B = 3|J|/2$, there is a narrow feature of inverted spin polarisation. The broader feature arises for systems with ferromagnetic exchange coupling ($J > 0$) from the greater strength that the ZFS interaction mixes the $|\mathrm{D}_{-1/2}\rangle$ and $|\mathrm{Q}_{+1/2}\rangle$ states compared to the $|\mathrm{D}_{+1/2}\rangle$ and $|\mathrm{Q}_{+3/2}\rangle$ states. For a ZFS tensor orientated at angle θ to an applied magnetic field $|\langle \mathrm{Q}_{+1/2}|\hat{H}_{\mathrm{ZFS}}|\mathrm{D}_{-1/2}\rangle| = \frac{\sqrt{2}}{4}D\sin 2\theta$, whilst $|\langle \mathrm{Q}_{+3/2}|\hat{H}_{\mathrm{ZFS}}|\mathrm{D}_{+1/2}\rangle| = \frac{\sqrt{6}}{12}D\sin 2\theta$ (Section 4.3.2). Inversion of spin polarisation arises from the doublet-quartet anticrossings at $g\mu_B B = 3|J|$ being offset by the previous anticrossing at $g\mu_B B = 3|J|/2$. Radical-triplet systems with antiferromagnetic exchange coupling ($J < 0$) follow a similar trend arising from the greater strength that the ZFS interaction mixes the $|\mathrm{D}_{+1/2}\rangle$ and $|\mathrm{Q}_{-1/2}\rangle$ states compared to the $|\mathrm{D}_{-1/2}\rangle$ and $|\mathrm{Q}_{-3/2}\rangle$.

4.3.2 Crystalline Systems

Strongly-coupled radical-triplet systems that are crystalline (such that all triplets have a uniform orientation to the applied magnetic field) show similar MFEs at fields equivalent to $3|J|/2$ and $3|J|$. However, Figure 4.2 shows that the width of magnetic response varies with triplet orientation due to different interaction strengths for spin mixing of trip-doublet and trip-quartet states by $\hat{H}_{\mathrm{ZFS}}$.

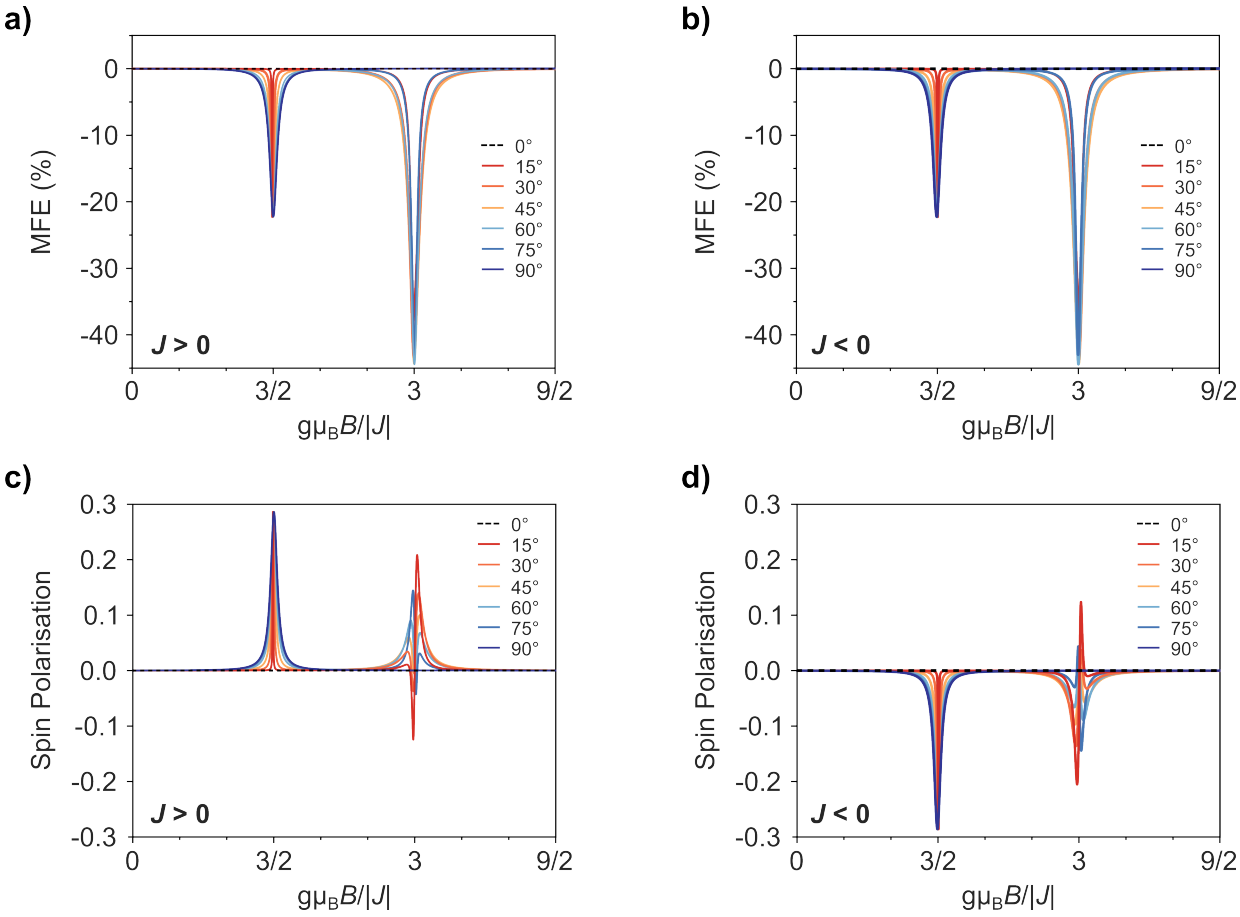

Figure 4.2: Magnetic response for a system of strongly coupled radical-triplet pairs ($|J| = 20|D|$, i.e. $|J| \gg |D|$) with all triplet states at a specified orientation to an applied magnetic field. MFEs for doublet photoluminescence are shown for a) ferromagnetic ($J > 0$) and b) antiferromagnetic ($J < 0$) radical-triplet exchange coupling with varying triplet ZFS tensor orientation to an applied magnetic field. MFEs for the excited doublet state spin polarisation of the radical are similarly shown for c) $J > 0$ and d) $J < 0$ radical-triplet exchange coupling with varying triplet ZFS orientation to an applied magnetic field.

The width of MFEs resulting from doublet-quartet anticrossings at both $g\mu_{\mathrm{B}}B = 3|J|/2$ and $g\mu_{\mathrm{B}}B = 3|J|$ are seen to vary with triplet orientation. For $|J| \gg |D|$ the ZFS interaction ($\hat{H}_{\mathrm{ZFS}}$) can be treated as a small perturbation to $\hat{H}^{(0)} = \hat{H}_{\mathrm{ex}} + \hat{H}_{\mathrm{Z}}$. In strongly-coupled radical-triplet systems away from anticrossings, the radical-triplet eigen-

states $|P_j\rangle$ states can be approximated with only the radical-triplet exchange and Zeeman interactions as $|P_j^{(0)}\rangle$:

$$\hat{H}^{(0)}\,|P_j^{(0)}\rangle = E_j^0\,|P_j^{(0)}\rangle \tag{4.4}$$

This results in $|P_j^{(0)}\rangle$ as the overall spin states for the radical-triplet system, i.e. $|\mathrm{D}_{\pm1/2}\rangle$, $|\mathrm{Q}_{\pm3/2}\rangle$, $|\mathrm{Q}_{\pm1/2}\rangle$.

Time-independent perturbation theory can be used to estimate the radical-triplet eigenstates near to anticrossings with the addition of the ZFS interaction $|P_j^{(1)}\rangle$. To first order with non-degenerate $|P_j^{(0)}\rangle$:

$$|P_j^{(1)}\rangle = |P_j^{(0)}\rangle + \sum_{j\neq k} |P_k^{(0)}\rangle \frac{\langle P_k^{(0)}|\hat{H}_{\mathrm{ZFS}}|P_j^{(0)}\rangle}{E_j^{(0)} - E_k^{(0)}} \tag{4.5}$$

The width of MFE features for luminescence/spin polarisation depends on the rate that doublet character is hybridised as an anticrossing is approached. The MFE width is affected both by the convergence rate of radical-triplet eigenstates P_j at the anticrossing (i.e. relative magnetic field quantum numbers of states k and j) and the magnitude of $\langle P_k^{(0)}|\hat{H}_{\mathrm{ZFS}}|P_j^{(0)}\rangle$.

For a ZFS tensor with principal axis at an angle θ to the applied magnetic field, $\langle P_k^{(0)}|\hat{H}_{\mathrm{ZFS}}|P_j^{(0)}\rangle$ can be calculated for all possible state intersections:

$$\langle \mathrm{Q}_{+3/2}|\hat{H}_{\mathrm{ZFS}}|\mathrm{D}_{+1/2}\rangle = -\frac{\sqrt{6}}{12} D \sin 2\theta \tag{4.6}$$

$$\langle \mathrm{Q}_{+1/2}|\hat{H}_{\mathrm{ZFS}}|\mathrm{D}_{+1/2}\rangle = \frac{\sqrt{2}}{12} D\,(3\cos 2\theta + 1) \tag{4.7}$$

$$\langle \mathrm{Q}_{-1/2}|\hat{H}_{\mathrm{ZFS}}|\mathrm{D}_{+1/2}\rangle = \frac{\sqrt{2}}{4} D \sin 2\theta \tag{4.8}$$

$$\langle \mathrm{Q}_{-3/2}|\hat{H}_{\mathrm{ZFS}}|\mathrm{D}_{+1/2}\rangle = \frac{\sqrt{6}}{6} D \sin^2\theta \tag{4.9}$$

$$\langle \mathrm{Q}_{+3/2}|\hat{H}_{\mathrm{ZFS}}|\mathrm{D}_{-1/2}\rangle = -\frac{\sqrt{6}}{6} D \sin^2\theta \tag{4.10}$$

$$\langle \mathrm{Q}_{+1/2}|\hat{H}_{\mathrm{ZFS}}|\mathrm{D}_{-1/2}\rangle = \frac{\sqrt{2}}{4} D \sin 2\theta \tag{4.11}$$

$$\langle \mathrm{Q}_{-1/2}|\hat{H}_{\mathrm{ZFS}}|\mathrm{D}_{-1/2}\rangle = -\frac{\sqrt{2}}{12} D\,(3\cos 2\theta + 1) \tag{4.12}$$

$$\langle \mathrm{Q}_{-3/2}|\hat{H}_{\mathrm{ZFS}}|\mathrm{D}_{-1/2}\rangle = -\frac{\sqrt{6}}{12} D \sin 2\theta \tag{4.13}$$

For both $g\mu_B B = 3|J|/2$ and $g\mu_B B = 3|J|$, the width of MFE features is seen to increase with $|D|$. At $g\mu_B B = 3|J|/2$, the width of the MFE feature varies with $\sin^2\theta$, whilst at $g\mu_B B = 3|J|$ the width of both intersections varies with $\sin 2\theta$.

4.4 Weakly-Coupled ($|J| \ll |D|$) Radical-Triplet

4.4.1 Disordered Systems

Figure 4.3 shows the magnetic response for weakly coupled radical-triplet pairs ($|J| = 0.02|D|$, i.e.$|J| \ll |D|$) that are also oriented randomly to an applied magnetic field. In contrast to the strongly coupled regime, an immediate onset of MFEs for doublet emission and spin polarisation are observed on going from zero to applied external magnetic field.

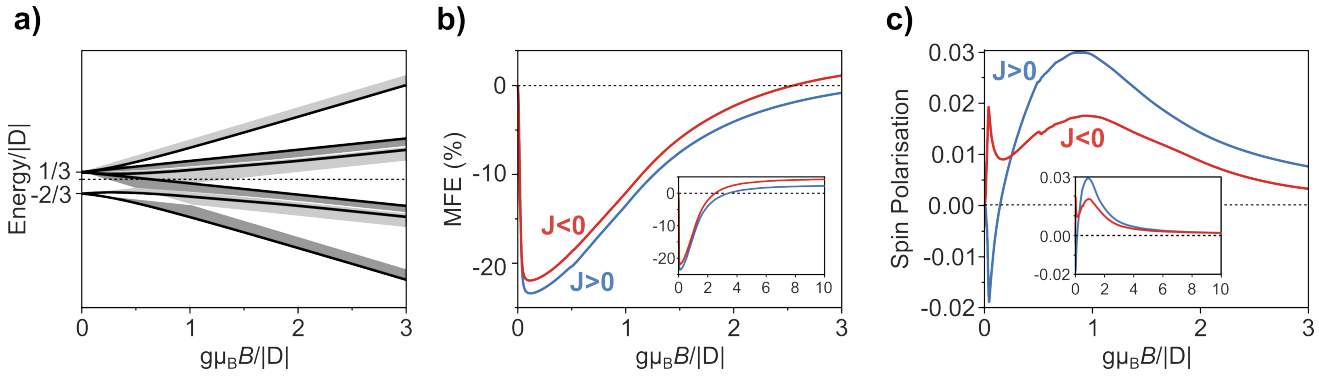

Figure 4.3: Magnetic response for weakly coupled radical-triplet pairs ($|J| = 0.02|D|$, i.e.$|J| \ll |D|$) that are randomly oriented to applied magnetic field. a) Zeeman splitting of radical-triplet pair states with applied magnetic field B. Dark line shows radical-triplet pair for triplet ZFS tensor $\theta = \pi/2$. Grey shaded regions show states from varying triplet orientations. b) MFE for doublet photoluminescence from radical-triplet systems with ferromagnetic ($J > 0$, blue) and antiferromagnetic ($J < 0$, red) exchange coupling. c) Magnetosensitivity for spin polarisation from radical-triplet systems with ferromagnetic ($J > 0$, blue) and antiferromagnetic ($J < 0$, red) exchange coupling. Insets in b) and c) show effects extending to $g\mu_B B = 10|D|$.

For weakly-coupled systems, the eigenstates of the radical-triplet pair at zero magnetic field result from the triplet zero-field splitting interaction. The zero-field eigenstates are composed of linear combinations of trip-doublet and trip-quartet character. The result is a ZFS quartet and doublet with energy $+D/3$ and $-2D/3$ respectively, where 2/3 of the initial trip-doublet spin character is found within the ZFS quartet and 1/3 in the ZFS doublet at zero field.

The introduction of a magnetic field causes hybridisation between states that are energetically separated on the order of $|J|$. At lower fields, this results in rapid redistribution

of trip-doublet character primarily within the ZFS quartet, leading to magnetic effects for the excited doublet populations that peak for fields on the order of $2|J|$. Further changes to the distribution of trip-doublet character are seen as the magnetic field is increased above $2|J|$, although this tends to a limiting case for fields on the order of $2|D|$.

For weakly coupled systems, the exact shape of the magnetic response between $0 < g\mu_B B < 2|D|$ strongly depends on the relative orientation of the triplet ZFS tensor to the applied magnetic field. This can result in magnetic responses for both the total doublet photoluminescence and spin polarisation which are dependent on triplet orientation (Section 4.4.2).

The MFEs in weakly-coupled systems for both photoluminescence and spin polarisation do not cancel out for disordered systems with random triplet orientation. A characteristic decrease in photoluminescence is seen on the order of $2|J|$, followed by a brightening in emission that returns towards the luminescence at zero field on the order of $2|D|$. Photoluminescence at $|B| > 2|D|$ is observed to saturate with emission greater than at zero field.

A sharp initial feature in spin polarisation is observed in weakly coupled systems: both peaking and falling on the order of $2|J|$. This is followed by a second broader feature, peaking on the order of $|D|$ before then slowly decreasing to zero for systems where the ZFS has zero transversal component ($E = 0$). The sign of the initial sharp peak in spin polarisation is determined by the sign of the exchange parameter, with $J < 0$ and $J > 0$ leading to positive and negative spin polarisations, respectively. Similarly, the second broader feature is determined by the sign of the ZFS interaction, with $D > 0$ and $D < 0$ leading to positive and negative spin polarisation, respectively.

4.4.2 Crystalline Systems

Figure 4.4 shows how the exact shape of the magnetic response between $0 < g\mu_B B < 2|D|$ strongly depends on the relative orientation of the triplet ZFS tensor to the applied magnetic field for weakly-coupled radical-triplet systems.

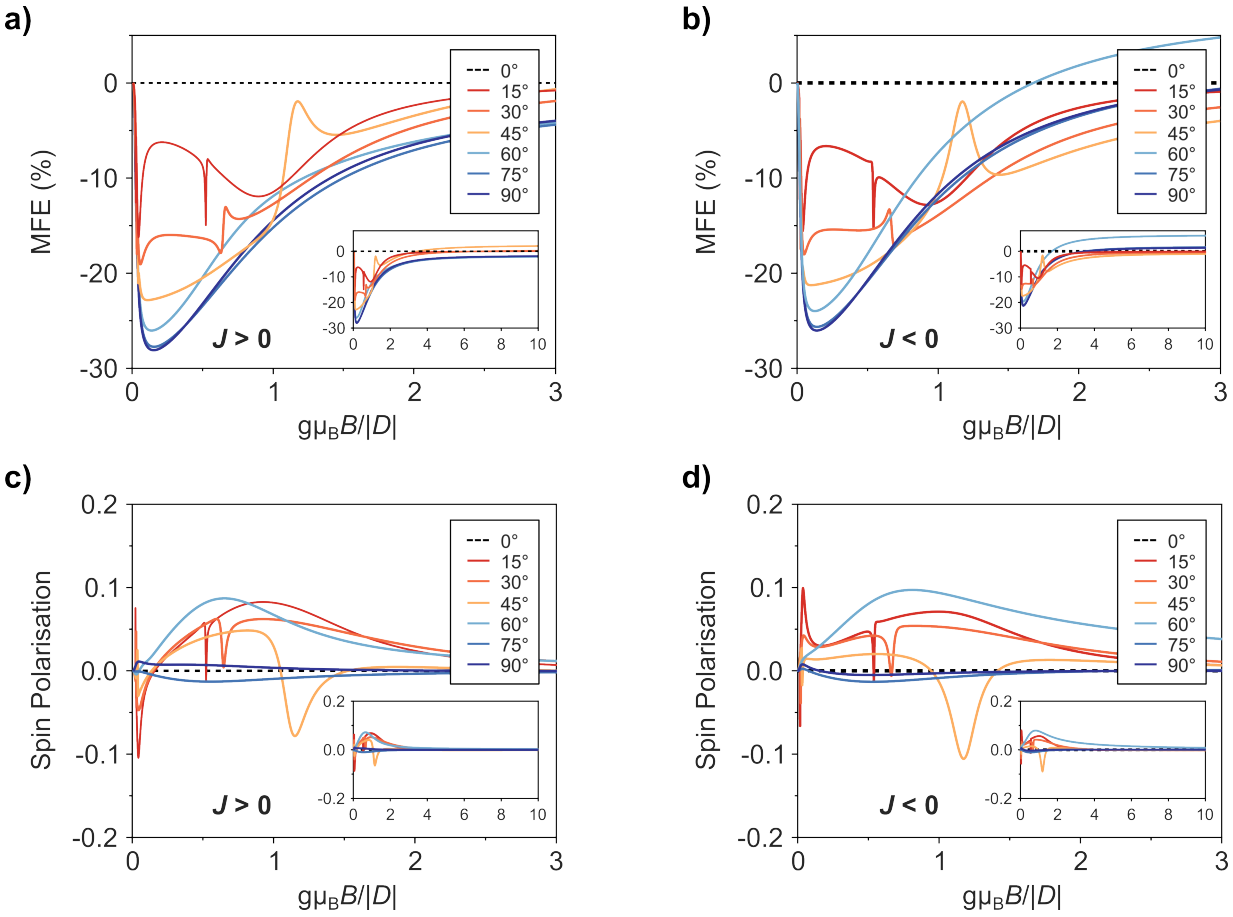

Figure 4.4: Magnetic response for a system of weakly coupled radical-triplet pairs ($|J| = 0.02|D|$, i.e. $|J| \ll |D|$) with all triplet states at a specified orientation to an applied magnetic field. MFEs for doublet photoluminescence are shown for a) ferromagnetic ($J > 0$) and b) antiferromagnetic ($J < 0$) radical-triplet exchange coupling with varying triplet ZFS tensor orientation to an applied magnetic field. Inset: MFEs extending up to $g\mu_B B = 10|D|$. MFEs for the excited doublet state spin polarisation of the radical are similarly shown for c) $J > 0$ and d) $J < 0$ radical-triplet exchange coupling with varying triplet ZFS orientation to an applied magnetic field. Inset: MFEs extending up to $g\mu_B B = 10|D|$.

Whilst MFEs are not observed for both doublet photoluminescence or spin polarisation for a ZFS tensor oriented parallel to the applied magnetic field, introduction of a small angular offset leads to rapid formation of a broad dip in photoluminescence around $g\mu_B B = |D|$ (discussed further in Section 4.5.2) enabling systems to act as sensitive magnetic field inclination sensors.

4.5 Radical-Triplet Design Towards Magnetosensitivity

4.5.1 Tailoring of Radical-Triplet Kinetics

In order to observe magnetosensitivity for photoluminescence and spin polarisation in our kinetic scheme $\epsilon = \gamma_-/\gamma_D$ must be non-zero. For large effects, systems should be engineered such that the rate of reverse triplet-doublet energy transfer is large compared to the rate of triplet dissociation. Furthermore, spin-polarisation will be increased for systems where the rate of forward energy transfer (γ_+) is maximised with respect to the radiative rate γ_r as seen in Equation 4.3. Balancing the luminescent yield and dynamics that maximise the spin effects is required to optimise the optical read-out for magnetosensitivity and will be investigated in future experiments beyond this thesis.

4.5.2 Design of Molecular Spin-Interactions

Magnetosensitivity in radical-triplet systems arises from the interplay of the exchange interaction and triplet ZFS interaction with the Zeeman interaction from an applied magnetic field. Changes in both photoluminescence and spin polarisation are observed upon redistribution of the trip-doublet character across the radical-triplet eigenstates.

For both weakly- and strongly coupled chromophore-radical systems, the amorphously averaged magnetic response shows a magnetic field effect for photoluminescence that peaks on the order of $|J|$ with a width of $|D|$. In addition, across both systems we observe the generation of spin-polarisation whose sign can give insights into the exchange and ZFS interaction for the triplet-doublet components.

Towards designing radical-triplet systems for a specific magnetic response, it can be seen that systems which are strongly-coupled will have lower sensitivity to the orientation of triplet states that those that are weakly-coupled. For strongly-coupled systems, we note that our ability to observe such phenomena is dependent on reaching $g\mu_B B = 3|J|/2$ and so it is not necessary to maximise the exchange interaction but instead keep $|J|/\mu_B B < 2T$.

In the weakly-coupled limit where spin mixing is driven by ZFS, the directionality of the magnetic dipolar interaction can be used as the basis of a magnetic field inclination sensor. In Figure 4.5 the doublet photoluminescence yield shows enhanced sensitivity where $g\mu_B B = |D|$. The widths of the angular response are related to $|J/D|$. Intuitively, the magnetic field inclination sensitivity can be tailored, in principle, by engineering of the spin interactions. This provides design guidelines and the basis of structure-function relationships for tuning the doublet-triplet pair through molecular 'structure' modifications

to target ‘function’ in compass response.

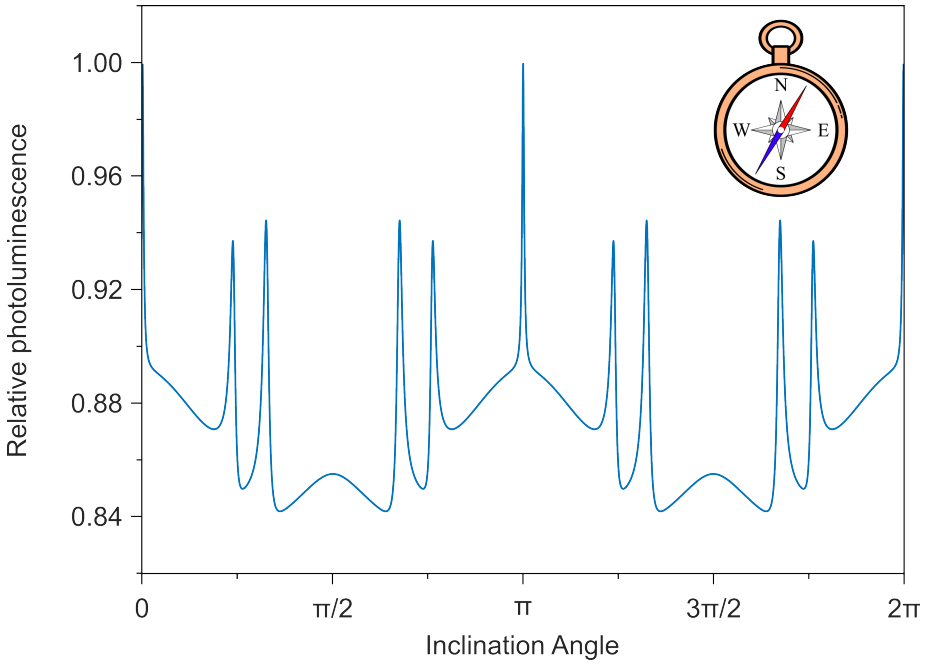

Figure 4.5: Variation in doublet photoluminescence for a weakly-coupled radical-triplet pair ($|J| = 0.02|D|$, i.e. $|J| \ll |D|$. $J > 0$) with varying inclination angle between the triplet ZFS tensor and the applied magnetic field ($g\mu_B B = |D|$). Photoluminescence values are normalised to the photoluminescence intensity for an inclination angle of 0°.

We do consider that alternative interactions which result in doublet-quartet spin mixing exist apart from the ZFS interaction, including the hyperfine and a Δg-like mechanism. The hyperfine interaction is typically of particular importance to magnetosensitivity in radical-pair systems, with singlet-triplet spin mixing resulting in MFEs through the Radical Pair Mechanism (RPM).[14] Whilst the hyperfine interaction is also present in radical-triplet systems, the mixing of spin states from the ZFS interaction for molecular triplets is typically orders of magnitude greater than that from the hyperfine interaction. The effect of the hyperfine interaction on magnetosensitivity of the radical-triplet pair for this reason was not considered in this work. For radical-triplet systems, a Δg-mechanism can induce spin-mixing resulting in magnetic field effects. However, for purely organic materials ($\Delta g \approx 0.001$) these effects happen at fields far greater than those equivalent to $|J|$ or $|D|$ for strongly or weakly coupled systems respectively (Appendix A.3).

4.6 Conclusions and Outlook

Here we examined the magnetosensitivity of energy transfer for luminescent doublet-triplet pairs from the interplay of magnetic spin interactions between molecular spins and magnetic fields. For strongly coupled doublet-triplet pairs, light read-out and spin polarisation initialisation following reversible energy transfer reflects the size and sign of spin exchange interactions. A light-based compass sensor from tailoring of spin interactions demonstrates one potential application of weakly coupled doublet-triplet pairs. Our work reveals the optical and spin properties of luminescent radical-triplet systems with potential applications in spintronic and quantum technology platforms using molecular spin materials.

Chapter 5

Dipole Mediated Triplet-to-Doublet Energy Transfer in Phosphor-Radical Systems

Spin-orbit coupling in organometallic complexes can recover luminescence from triplet states in optoelectronic devices and generate triplet spin polarisation towards opto-spintronic applications. Energy transfer from organometallic triplet species to fluorescent radicals could enable OLEDs with increased lifetime and simplified design, as well as allowing triplets to act as 'spin sensitisers' for radical-based opto-spintronics. In this chapter, we combine the organometallic deep-blue phosphor FIr6 with the 'fruit-fly' TTM-1Cz radical, demonstrating triplet-doublet energy transfer with nanosecond lifetime ($k = 3.1 \times 10^7$ s^{-1}), high efficiency ($85 \pm 25\%$), and without the need for triplet diffusion in the film blends. We limit the activation energy for energy transfer to $<$ 5 meV through temperature-dependent studies, indicating that energy transfer occurs through a dipole-dipole Förster resonance energy transfer (FRET) based mechanism. Highlighting the insensitivity of FRET to the spin of the triplet states, we set out design rules for maximising and minimising the FRET rate towards optoelectronic and spintronic applications respectively.

The findings presented in this chapter are in preparation as paper [3] in the List of Publications.

5.1 Introduction

The spin of ground and excited molecular states dictates both the optical transitions and available transfer mechanisms of energy and charge for molecular systems. In closed-shell molecules, the arrangement of lowest energy excited triplet excitons with spin singlet ground states can reduce electroluminescence efficiency in OLEDs due to the spin flip required for triplet emission. Luminescence is established by molecular engineering of the singlet-triplet energy gap to promote transfer to fluorescent singlet excitons[21,142] or designs that enhance phosphorescence.[19] These strategies act to recover luminescence from non-luminescent lowest lying excited states by working against the typical exciton energy level arrangements for closed-shell materials.

Open-shell organic radical semiconductors have doublet spin ground states with excited doublet and quartet levels. Efficient luminescence was observed in radicals such as TTM-1Cz from arrangement of lowest lying excited states having doublet (not quartet) character, enabling efficient fluorescence to the doublet ground state.[1,48] The photophysical properties of organic radicals make them attractive as terminal, metal-free light-emitting components in 'colour by blue' displays as fluorescent filters for red light from blue back-panel OLEDs.[90]

Energy transfer from singlet and triplet excitons of thermally activated delayed fluorescence (TADF) host components to TTM-radical derivatives was previously investigated.[143–145] For the triplet-doublet energy transfer channel the 'extra spin' of the radical can enable efficient energy transfer with spin conservation via a Dexter mechanism. This process is electron-exchange mediated and requires close proximity of the host exciton to the radical for sufficient orbital overlap. This leads to reduced transfer efficiency and the rate of emission from the radical component becoming limited by triplet exciton diffusion to be in range for transfer.

In this chapter we investigate the photophysics and mechanism of triplet-doublet energy transfer from a blue phosphorescent iridium organometallic complex (FIr6) to an organic radical (TTM-1Cz). The ability to initiate triplet excitons from rapid intersystem crossing (sub-100 fs) following photoexcitation provides a platform to focus on triplet-doublet energy transfer and the interplay of Dexter energy transfer with the Förster resonance energy transfer (FRET) mechanism that becomes activated by increased oscillator strength for radiative transitions from triplet exciton states.

We consider, as well as energy harvesting in optoelectronic applications, spin transfer that accompanies energy transfer and radical-triplet spin polarisation mechanisms[112,120]

could enable optical interfaces of spin control in opto-spintronics. In these applications a high triplet yield on photoexcitation is necessary to initiate any subsequent spin polarisation on the radical.

We postulate that spin polarisation of triplet state sub-levels formed by intersystem crossing can enable 'spin sensitisation' of luminescent organic radicals in addition to energy transfer in aligned systems. In Figure 5.1 we set out a spin-conserving Dexter-based mechanism for energy transfer from triplet to doublet states where spin polarisation is translated from the triplet to the doublet excited state.

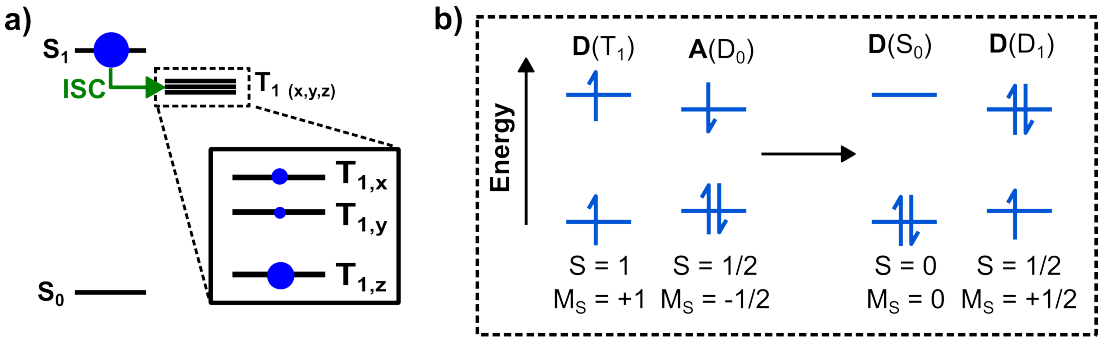

Figure 5.1: a) Diagram of spin polarisation of triplet sub-levels following differential population via intersystem crossing from the S_1 excited state. b) Schematic showing triplet-doublet Dexter energy transfer with spin-conservation.

We note that towards spin sensitisation, FRET from organometallic triplet states will excite doublet states of both polarisations equally, and so acts as a detrimental pathway that minimises the generation of doublet spin polarisation.

Our study of FIr6:TTM-1Cz in this chapter aims to broaden our understanding of energy transfer mechanisms with radicals towards enabling future designs that may target specific applications and functionality (e.g. maximised efficiency, rate of transfer, specific mechanism, spin sensitisation).

5.2 Triplet-Doublet Model System for Energy Transfer

Organometallic phosphors are established materials in optoelectronics as spin-orbit coupling enhanced phosphorescence acts to 'recover' luminescence from triplets formed in OLED operation. However the phosphorescence rates are typically slow (> 200 ns[146] to µs[19]) and can lead to exciton quenching processes that limit device performance.[29] Figure 5.2 highlights phosphorescent OLED architectures that overcome this long emission lifetime by harvesting triplets via triplet-singlet Förster resonance energy transfer

(FRET) onto a fluorescent closed-shell emitter, reducing emission lifetimes to 100 ns timescales.[147] Further benefits are higher colour purity of light emission from narrower emission linewidth of the terminal emitter that can be decoupled from the design considerations of the phosphor.[148]

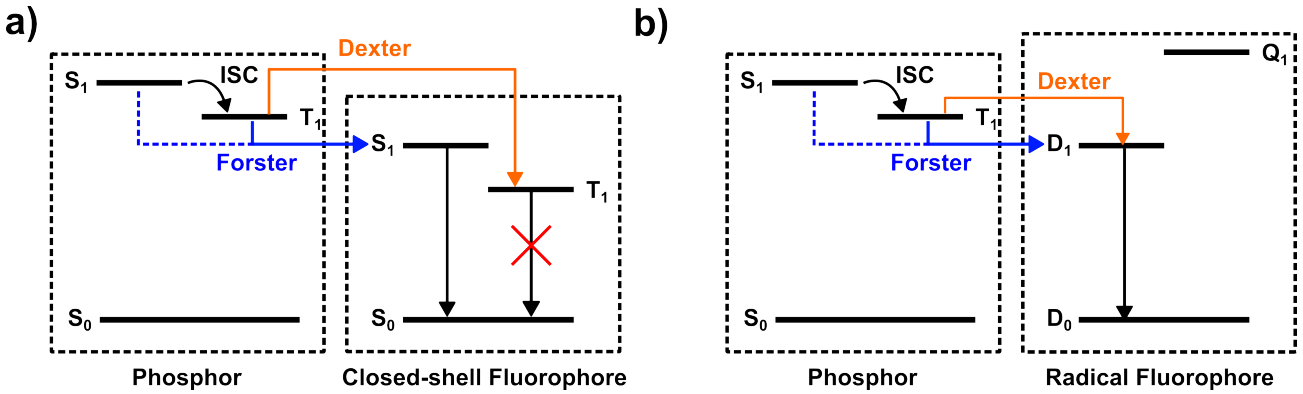

Figure 5.2: Schematic of excited state energy transfer for a phosphor emitter in combination with a) a closed-shell fluorescent dopant and b) a radical fluorescent dopant. Energy transfer via Förster (blue) and Dexter (orange) processes are highlighted. Förster energy transfer from phosphor singlet to fluorophore singlet or radical doublet excited states (dashed blue line) is assumed to be negligible for platinum-iridium based phosphors which show intersystems crossing (ISC) on sub-100 fs timescales.

Whilst phosphor:emitters blends in closed-shell systems have been successfully demonstrated in photophysical studies and in OLEDs, they work against the normal energy ordering of levels in these systems and can present luminescence losses via triplets.[149] Triplet energy transfer from host T_1 to dopant T_1 generates a non-emissive state that competes with formation of fluorescent dopant S_1 states.[150] Phosphor:emitter:host blends are used to engineer the average phosphor-emitter distance, with host components acting as spacers in the film such that the phosphor-emitter distance is in range for triplet-singlet FRET but out of range for the detrimental triplet-triplet Dexter channel.[147] Using two-component instead of three-component light-emitting layers is attractive for any translation from the laboratory to commercial applications.

Figure 5.2 shows the ordering of excited states on replacing closed-shell terminal emitters with organic radicals. The doublet exciton D_1 states of radicals can harvest singlet and triplet excitons from the phosphor via FRET and Dexter mechanisms. In contrast with energy transfer to closed-shell emitters, here the Dexter mechanism becomes a potential pathway to luminescence with radicals.

Here we use TTM-1Cz as a luminescent radical that represents a 'fruit fly' example for the class of materials based on the TTM motif.[151] To study energy transfer from the phosphor triplet state to TTM-1Cz, a type-I heterojunction of the frontier levels is required as depicted in Figure 5.3. The second requirement is the TTM-1Cz D_1 (1.8 eV)[152] state lying at lower energy than the FIr6 T_1 (2.7 eV) state.[153] Figure 5.3a shows the chemical structure for the deep-blue phosphor FIr6, which was selected as an energy donor with E(HOMO) = –6.1 eV and E(LUMO) = –3.1eV,[153] in comparison to TTM-1Cz with E(HOMO)= –5.4 eV and E(SOMO, reduction) = –3.8 eV.

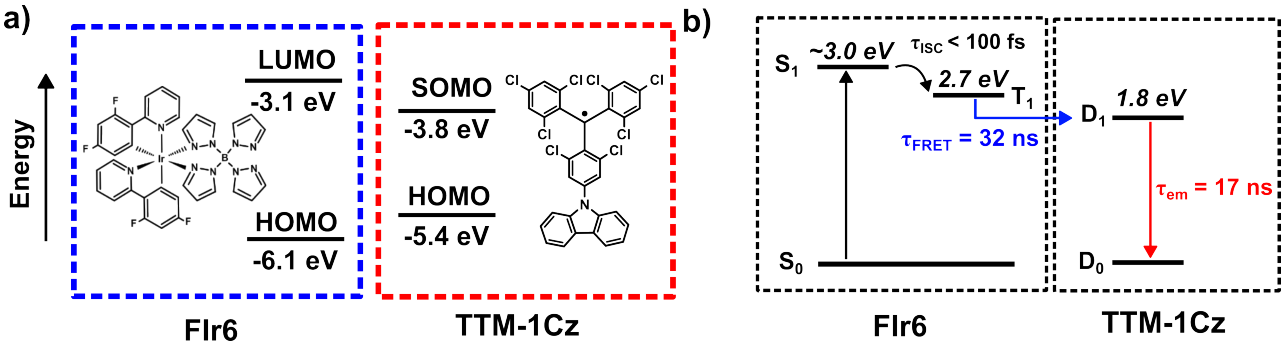

Figure 5.3: a) Molecular structures and frontier molecular orbital energies for FIr6 and TTM-1Cz. b) Schematic for emission from FIr6:TTM-1Cz systems following FIr6 photoexcitation, rapid singlet-to-triplet intersystem crossing (ISC) in FIr6, followed by FRET-mediated triplet-doublet energy transfer from phosphor to radical. The FIr6 S_1 energy was estimated from the edge of absorption.[154]

5.3 Sample Preparation

CzSi and FIr6 were obtained from Ossila. TTM-1Cz was synthesised as previously reported by Prof. Feng Li's group.[36] FIr6, TTM-1Cz and CzSi were dissolved in chloroform at 5 mg/mL concentration and combined to form pure FIr6 (100 wt%), mixed FIr6:TTM-1Cz (96:4 wt%) and CzSi:TTM-1Cz (96:4 wt%) solutions. Films were fabricated through dynamic spin coating of solutions at 4000 rpm for 20 s onto UV-grade quartz substrates, followed by thermal annealing at 90°C for 10 minutes. Samples for transient absorption measurements were encapsulated using a separate UV-quartz substrate and sealed using UV-set epoxy. All samples were prepared under a nitrogen atmosphere (<1 ppm O_2, < 0.5 ppm H_2O).

5.4 Results and Discussion

5.4.1 Steady State Absorption and Photoluminescence

Figure 5.4a shows the steady state absorption spectrum for FIr6 and TTM-1Cz in solution (100 μM in chlorobenzene). The lowest energy absorption bands for FIr6 and TTM-1Cz start at 460 nm and 680 nm, respectively. Excitation between 460-680 nm is expected to result in radical excitation, whilst excitation below 460 nm is expected to result in excitation of both the radical and phosphor.

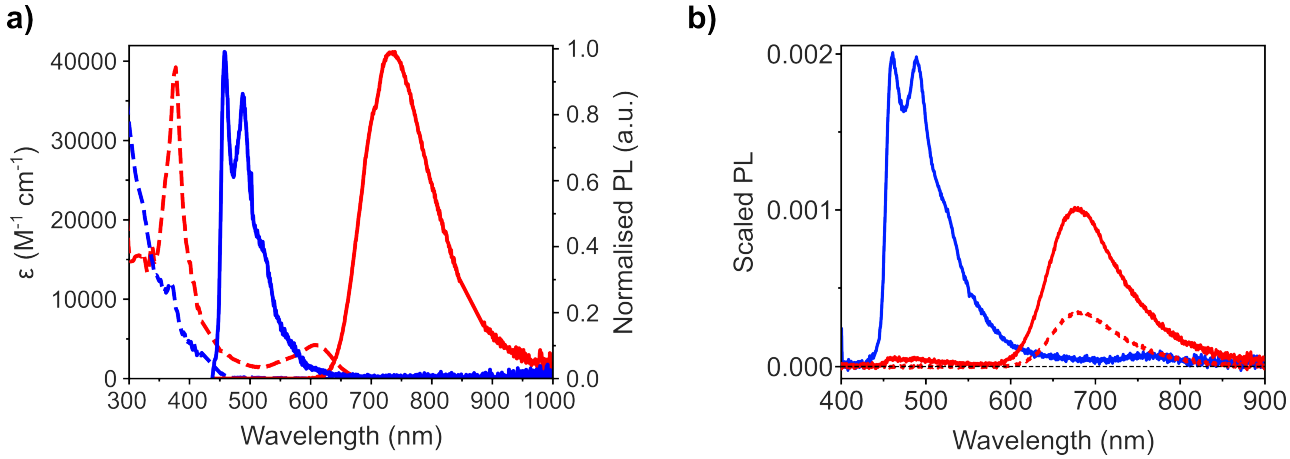

Figure 5.4: a) Extinction coefficient (dashed lines) and normalised photoluminescence (solid lines) profiles for FIr6 (blue) and TTM-1Cz (red) in chlorobenzene solution. b) Steady-state photoluminescence (PL) spectra for thin films of neat FIr6 (blue) and mixed FIr6:TTM-1Cz (96:4 wt%, solid red) with λ_{ex} = 385 nm, and CzSi:TTM-1Cz (96:4 wt%, dashed red) with λ_{ex} = 375 nm. PL spectra are measured inside an integrating sphere, and are scaled such that the excitation peak has a height of 1 for the measurement of a blank sample under identical conditions.

Figure 5.4b shows steady-state photoluminescence measurements for FIr6, FIr6:TTM-1Cz (96:4 wt%) and CzSi:TTM-1Cz (96:4 wt%) thin-films excited at 385 nm. FIr6 films have deep-blue emission with strong vibronic features at 458 nm and 488 nm as expected.[155] Irradiation below 460 nm for FIr6:TTM-1Cz (96:4 wt%) results primarily in excitation of the FIr6 phosphor due to its high concentration within the film. FIr6 phosphorescence is substantially quenched in the FIr6:TTM-1Cz film, with new broad emission at 680 nm attributed to TTM-1Cz. CzSi acts as a high-energy bandgap molecular host such that CzSi:TTM-1Cz films were used as reference for the emissive properties of TTM-1Cz in a thin film,[30,78] with emission from CzSi:TTM-1Cz films matching that seen in FIr6:TTM-1Cz.

5.4.2 Photoluminescence Quantum Yield (PLQY)

Table 5.1 shows the photoluminescence quantum yield (PLQY, Φ) obtained for neat FIr6, mixed CzSi:FIr6:TTM-1Cz and CzSi:TTM-1Cz films measured under a constant flow of nitrogen. Emission between 440-620 nm (Φ_{FIr6}) and 620-900 nm ($\Phi_{\text{TTM-1Cz}}$) was attributed to FIr6 phosphorescence ($T_1 \rightarrow S_0 + h\upsilon$) and TTM-1Cz luminescence ($D_1 \rightarrow D_0 + h\upsilon$) respectively. Neat FIr6 and mixed CzSi:FIr6:TTM-1Cz films were excited at 385 nm. We note that CzSi:TTM-1Cz films were measured at 375 nm for maximum TTM-1Cz absorption, but that the PLQY of TTM-1Cz within the film is assumed to be the same for excitation at 375 nm and 385 nm due to Kasha's rule. Stated absorption and Φ values are the mean value obtained from measurement of two separate films. The error in absorption and Φ values was estimated from the effect of the noise level on the maximum/minimum possible integrated areas for excitation and photoluminescence peaks.

Sample	λ_{ex} (nm)	A	Φ_{FIr6} (%)	$\Phi_{\text{TTM-1Cz}}$ (%)
CzSi:FIr6 (90:10 wt%)	385	0.014 ± 0.002	25 ± 1	–
FIr6 (100 wt%)	385	0.088 ± 0.002	15 ± 1	–
CzSi:FIr6:TTM-1Cz (86:10:4 wt%)	385	0.037 ± 0.002	0.4 ± 0.2	12 ± 1
FIr6:TTM-1Cz (96:4 wt%)	385	0.107 ± 0.002	0.4 ± 0.2	11 ± 1
CzSi:TTM-1Cz (96:4 wt%)	375	0.029 ± 0.002	–	12 ± 1

Table 5.1: Photoluminescence quantum yield measurements for phosphor-radical films.

Table 5.1 shows that FIr6 emission underwent concentration quenching between dilute (10 wt%) and neat (100 wt%) films, with Φ_{FIr6} dropping from 25% to 15%. However, PLQY measurements of TTM-1Cz emission were insensitive to FIr6 concentration with $\Phi_{\text{TTM-1Cz}}$ equal to 11-12% for CzSi:FIr6:TTM-1Cz in [0: 96%: 4%], [96%: 0%: 4%] and [86%: 10%: 4%] blends. This suggests that energy transfer from photoexcited FIr6 species to TTM-1Cz is efficient with $\Phi_{\text{TTM-1Cz}}$ in the blend limited by the efficiency of TTM-1Cz as a terminal emitter, and that FIr6 to TTM-1Cz energy transfer can outcompete mechanisms for FIr6 concentration quenching.

Estimation of Efficiency of FIr6 to TTM-1Cz Energy Transfer

We note that irradiation of mixed FIr6:TTM-1Cz films at 385 nm is expected to result in photoexcitation of both FIr6 and TTM-1Cz. In this section, we deconvolve direct photoexcitation and indirect radical excitation via FIr6 to find a transfer efficiency for

triplet-doublet energy transfer.

Comparison of the absorption of FIr6 and FIr6:TTM-1Cz films is used to estimate the absorption of TTM-1Cz, with the PLQY of CzSi:TTM-1Cz films used to estimate the intensity of TTM-1Cz emission from direct photoexcitation. This is subtracted from the total TTM-1Cz emission to give the intensity of emission resulting from indirect energy transfer. Translating this into a population of doublet excited states, we compare this to the absorption of FIr6 to find the transfer efficiency for triplet-doublet energy transfer. We note that this methodology assumes that samples have uniform film thickness, no aggregation and similar morphology. Whilst not available at the time, future experiments should look to verify film uniformity both across a sample and between samples through use of a stylus profilometer or ellipsometer. In addition, measurement over a larger number of samples (>7 films) should be performed to get statistically significant standard deviations for the absorption and photoluminescence intensities of films.

Table 5.2 shows the integrated intensity for both the excitation peak (L) and emission peaks for FIr6 phosphorescence (440-620 nm, P_{FIr6}) and TTM-1Cz emission (620-900 nm, $P_{TTM\text{-}1Cz}$) from PLQY measurements of neat FIr6 and mixed FIr6:TTM-1Cz (96:4 wt%) films previously shown in Table 5.1. All areas are normalised to the measured intensity of the laser for a blank substrate.

Sample	L	P_{FIr6}	$P_{TTM\text{-}1Cz}$
Blank	1	–	–
FIr6 (100 wt%)	0.816 ± 0.002	$(4.3 \pm 0.2) \times 10^{-2}$	–
FIr6:TTM-1Cz (96:4 wt%)	0.782 ± 0.002	$(9 \pm 5) \times 10^{-4}$	$(2.3 \pm 0.2) \times 10^{-2}$

Table 5.2: Normalised areas for the 385 nm excitation peak (L) and emission peaks (FIr6 phosphorescence and TTM-1Cz luminescence areas, P_{FIr6} and $P_{TTM\text{-}1Cz}$ respectively) for neat FIr6 and mixed FIr6:TTM-1Cz (96:4 wt%) films. All areas are normalised to the measured intensity of the laser for a blank substrate.

Addition of TTM-1Cz to FIr6 increases absorption at 385 nm from 0.088 ± 0.001 (neat FIr6 films) to 0.107 ± 0.001 (FIr6:TTM-1Cz films). With assumption of similar densities and molecular weight of FIr6 and TTM-1Cz, the absorption component of FIr6 in FIr6:TTM-1Cz is approximated to be $0.96 \times 0.088 = 0.084$. TTM-1Cz accounts for the remaining 0.023 of light absorption. From this we approximate that 385 nm excitation will photoexcite 79% FIr6 and 21% TTM-1Cz in FIr6:TTM-1Cz (96:4 wt%) films.

Table 5.2 shows radical emission in FIr6:TTM-1Cz films is $(2.3 \pm 0.2) \times 10^{-2}$ of

the initial laser excitation peak. Assuming that 21% of photoexcitation occurs directly to TTM-1Cz at 385 nm and that once TTM-1Cz is photoexcited it has a PLQY of 12% (from Φ in CzSi:TTM-1Cz films), we can calculate that direct excitation constitutes 24 $\pm$ 7% of total radical emission. From assuming that 76 $\pm$ 7% of radical emission results from indirect excitation via FIr6 and that 12% of excitations given to TTM-1Cz result in emission, we can estimate the population of excited doublet states formed from triplet-doublet energy transfer are equivalent to if a 0.15 $\pm$ 0.04 fraction of the initial excitation intensity was absorbed.

In total a 0.218 $\pm$ 0.002 fraction is absorbed by the FIr6:TTM-1Cz sample. Assuming that 79% of this absorption results in FIr6 photoexcitation, the absorption of FIr6 excited states is equivalent to an 0.172 $\pm$ 0.005 area of the initial excitation peak. Through assuming that intersystem crossing in FIr6 is fast and forms triplet states with 100% efficiency,[155] we can compare the area for FIr6 excitation and for indirect transfer to the doublet to get a triplet-doublet energy transfer efficiency of 85 $\pm$ 25%.

FIr6 phosphorescence in FIr6:TTM-1Cz (96:4 wt%) is 3% of that in FIr6 films, such that we assume that 97% of photoexcited triplet states are quenched by TTM-1Cz. We assume that any difference between the efficiency of triplet-doublet energy transfer and the proportion of triplet states quenched by TTM-1Cz results from the TTM-1Cz introducing new non-radiative relaxation pathways to FIr6.

5.4.3 Transient Photophysical Characterisation

Transient photophysical measurements were carried out using photoexcitation from the 2nd (515 nm) or 3rd (343 nm) harmonic of an 1030 nm ultrafast pulsed laser source as outlined in Experimental Methods Section 3.4.2. Cumulative photoluminescence, femtosecond transient absorption and spectrally-resolved transient photoluminescence were measured as outlined in Experimental Methods Sections 3.4.3-3.4.4. Samples for transient photoluminescence were held within a Linkam LTS420E-P cryostat under a constant purge of nitrogen gas to prevent photo-oxidation.

Cumulative photoluminescence spectra for neat FIr6 (100 wt%) and mixed FIr6:TTM-1Cz (96:4 wt%) films were recorded with varying fluence for 343 nm and 515 nm excitation. Power series measurements shown on Figure 5.5 suggest minimal influence on kinetics from bimolecular exciton annihilation processes, with samples demonstrating a linear relationship between excitation power and emission from TTM-1Cz and FIr6. Subsequent transient photophysical measurements were taken within this linear excitation regime.

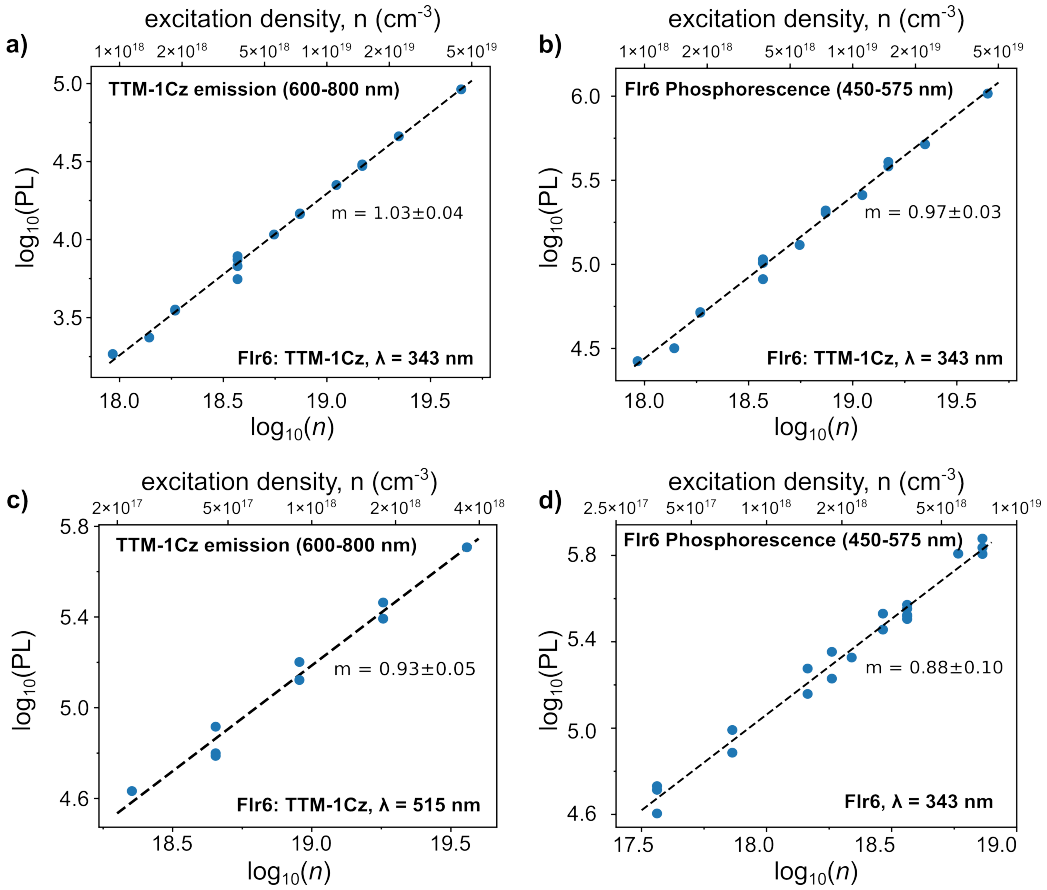

Figure 5.5: Pulsed excitation density versus photoluminescence for thin films. a) TTM-1Cz emission in FIr6:TTM-1Cz (96:4 wt%), λ_{ex} = 343 nm. b) FIr6 phosphorescence in FIr6:TTM-1Cz (96:4 wt%), λ_{ex} = 343 nm. c) TTM-1Cz emission in FIr6:TTM-1Cz (96:4 wt%), λ_{ex} = 515 nm. d) FIr6 phosphorescence in FIr6 (100%), λ_{ex} = 343 nm.

5.4.4 Femtosecond Transient Absorption (fsTA)

Figure 5.6 shows fsTA results for FIr6 in chlorobenzene solution (100 µM) as well as FIr6 and FIr6:TTM-1Cz (96:4 wt%) films. Samples were excited at 343 nm with a fluence of 28 mJ/cm^2.

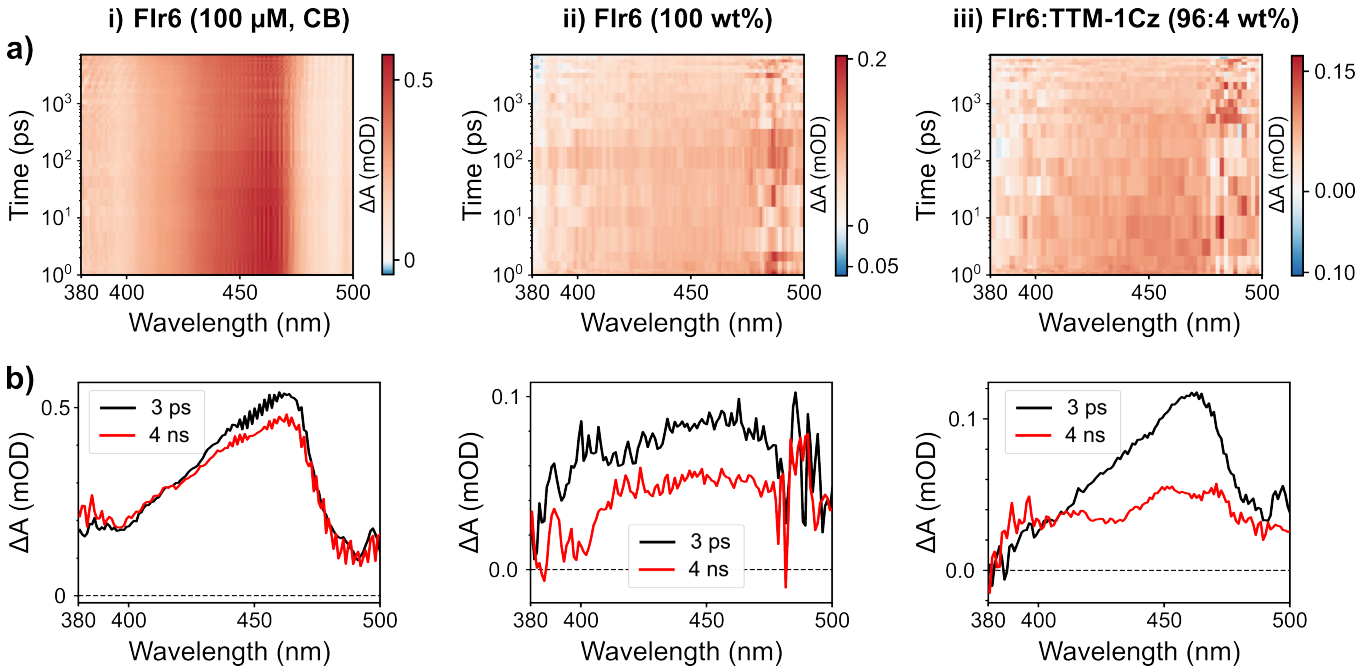

Figure 5.6: a) False-colour maps and b) transient absorption spectra for solution-based fsTA measurement of i) FIr6 (100 µM in chlorobenzene (CB)) and film-based measurements of ii) FIr6 (100 wt%) and iii) FIr6:TTM-1Cz (96:4 wt%) films with λ_{ex} = 385 nm (fluence = 28 mJ/cm^2).

The excited state absorption (ESA) for the FIr6 triplet state in solution is identified as a broad absorption peaking at 460 nm. Similar to previous literature we are not able to observe the transition from the singlet to the triplet state of FIr6 following excitation,[155] and so assume that intersystem crossing is faster that the time resolution of our experiment (< 100 fs). With ISC occuring on sub 100 femtosecond timescales, we assume that any energy transfer from singlet to doublet states is minimal, such that this chapter studies the transfer of energy solely from triplet to doublet excited states.

In FIr6 solution, we observe the FIr6 triplet ESA to undergo minimal spectral evolution over 20 ps before remaining constant over the 7.5 ns measurement window. Spectral evolution is attributed to reorganisation of the organometallic excited state.

Thin films of FIr6 and FIr6:TTM-1Cz show weak signal in transient absorption, preventing definitive assignment or deconvolution of excited state features. However, in the neat FIr6 (100 wt%) film, we observe an ESA peaked at 460 nm which we assume to result from the FIr6 triplet. This ESA decays with a lifetime of 1-2 ns which with later evidence of spectral evolution for phosphorescence (see Section 5.4.5) is attributed to a combination of relaxation of the triplet within the FIr6 density of states and FIr6 concentration-based quenching in the solid-state.

In the mixed FIr6:TTM-1Cz films, we observe an additional ESA between 430-460 nm which we attribute to the ESA of TTM-1Cz following direct excitation. Figure 5.7 shows the kinetics for the transient absorption of neat FIr6 (100 wt%) and mixed FIr6:TTM-1Cz (96:4 wt%) films integrated between 430-460 nm and 460-490 nm.

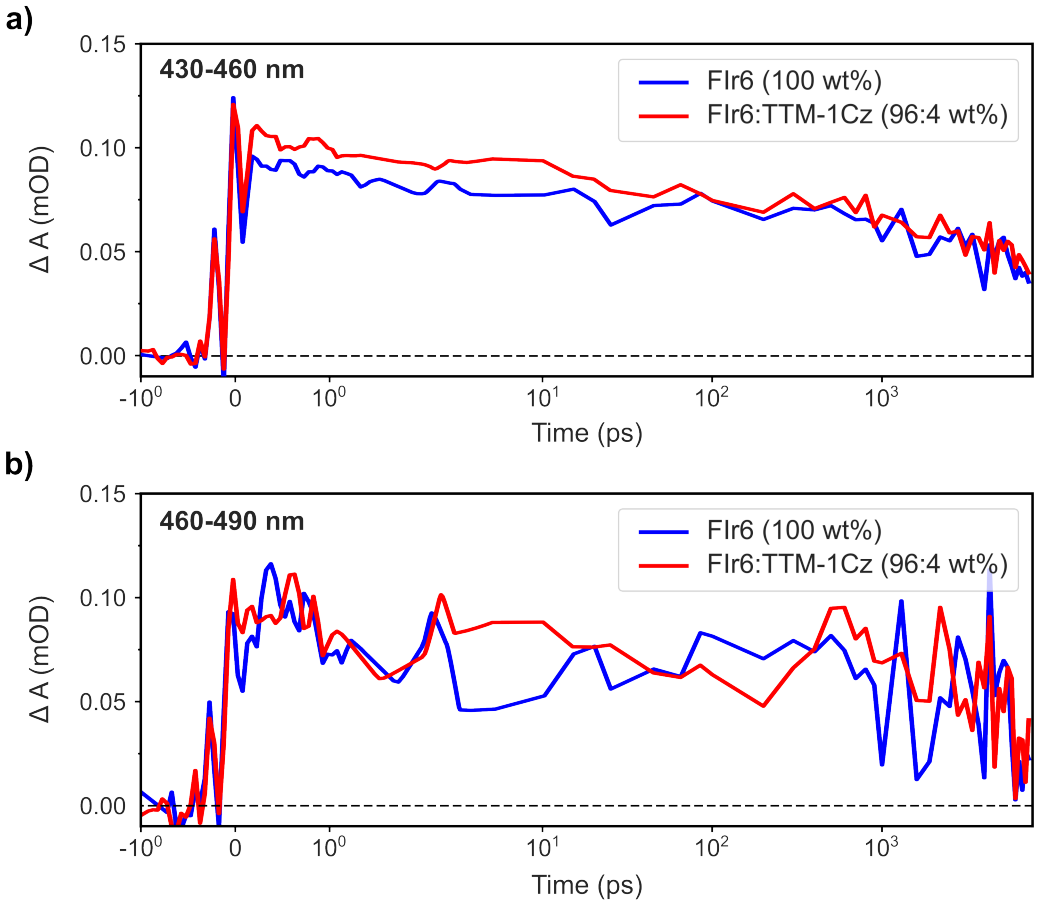

Figure 5.7: ΔA measured between a) 430-460 nm and b) 460-490 nm for FIr6 (100 wt%, blue) and FIr6:TTM-1Cz (96:4 wt%, red) films with $\lambda_{ex} = 385$ nm (fluence = 28 mJ/cm^2).

Whilst increased signal is observed in mixed FIr6:TTM-1Cz (96:4 wt%) films between 430-460 nm, we do not observe further growth of the TTM-1Cz doublet ESA. We further are unable to resolve differences in lifetimes for FIr6 and FIr6:TTM-1Cz ESAs either between 430-460 nm or 460-490 nm with both decaying on the order of 10 ns. Together these suggest that triplet-doublet energy transfer does not take place on sub-nanosecond timescales. With FIr6 intersystem crossing occurring on sub-picosecond timescales, energy transfer from the FIr6 singlet state to TTM-1Cz is assumed to be minimal.

Future studies should look to fabricate thicker films for neat FIr6 (100 wt%), FIr6:TTM-1Cz (96:4 wt%) and CzSi:TTM-1Cz (96:4 wt%) towards collection of tran-

sient absorption spectra with higher signal-to-noise. This would allow for deconvolution of FIr6 and TTM-1Cz ESAs through global or target analysis fitting.

5.4.5 Transient Photoluminescence (trPL)

Figure 5.8a shows the cumulative phosphorescence from FIr6 and mixed FIr6:TTM-1Cz films. For neat FIr6 films, 90% of total emission occurs by 2.5 µs after photoexcitation. In FIr6:TTM-1Cz, 90% of FIr6 emission occurs by 70 ns with substantial quenching due to triplet-doublet energy transfer. Microsecond phosphorescence lifetime for FIr6 only films is in agreement with previous reports for the molecule.[155–157] However, it was found that fitting of the FIr6 phosphorescence kinetics to a mono- or bi-exponential decay did not accurately describe kinetics in neat FIr6 films over the entire lifetime of emission. We assume that this is due to previously documented concentration-induced self-quenching mechanisms between FIr6 molecules,[158] which can be observed in Table 5.1 from the photoluminescence quenching between CzSi:FIr6 (90:10 wt%) and neat FIr6 (100 wt%) films from 25 ± 1% to 15 ± 1% respectively.

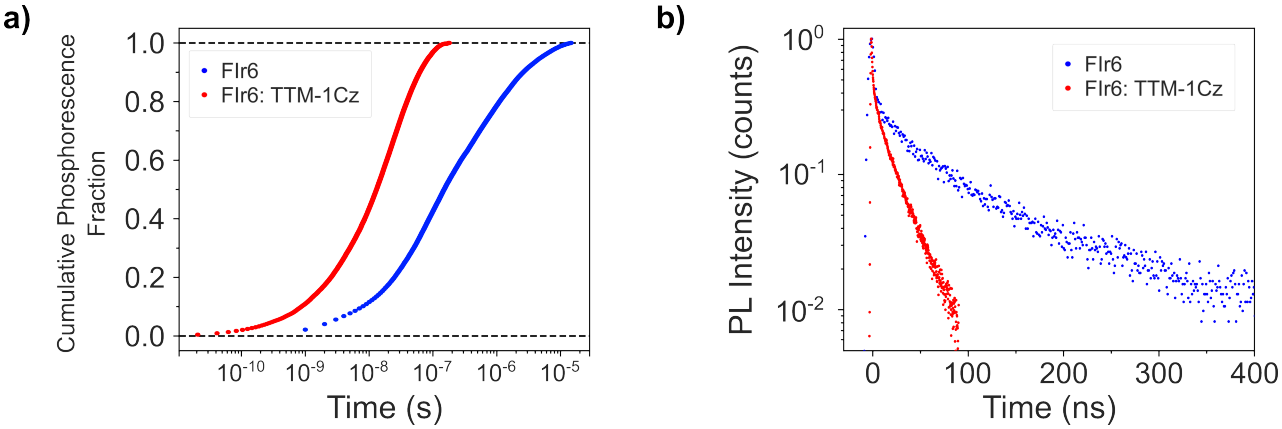

Figure 5.8: Transient kinetics for FIr6 phosphorescence. a) Cumulative FIr6 phosphorescence as a function of time for thin-films of FIr6 (blue) and FIr6:TTM-1Cz (red), λ_{ex} = 343 nm. b) Normalised transient phosphorescence on 100s ns timescales for FIr6 (blue) and FIr6:TTM-1Cz (red), λ_{ex} = 343 nm.

Figure 5.8b displays the transient PL profiles for FIr6 and FIr6:TTM-1Cz films up to 400 ns following photoexcitation. Here the transient emission profiles are fitted to a biexponential decay, with a sharp initial decay in phosphorescence for both FIr6 and FIr6:TTM-1Cz films with lifetime $\tau \approx 2$ ns. Nanosecond relaxation is accompanied by a red shifting of phosphorescence for both films as shown in Figure 5.9 such that we attribute this kinetic to relaxation within the FIr6 density of states to lower energy T_1 states with lower oscillator strength for emission. Red-shifting is still observed in films measured at –175°C, and so we assume that relaxation is mediated by FRET to lower energy states.

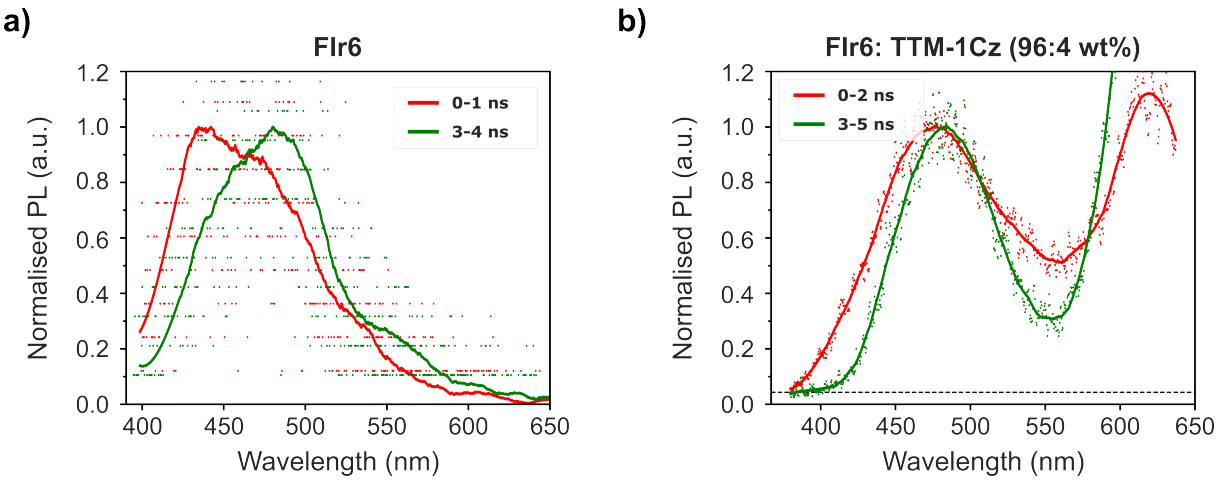

Figure 5.9: Evolution of transient photoluminescence (PL) spectra collected for FIr6 phosphorescence directly after photoexcitation (λ_{ex} = 343 nm) and after 3 ns in a) neat FIr6 (100 wt%) and b) mixed FIr6:TTM-1Cz (96:4 wt%) films.

Following relaxation within the FIr6 density of states, phosphorescence decays with a lifetime of 110 ns in FIr6 and 23 ns in FIr6:TTM-1Cz films. We can estimate that TTM-1Cz quenches FIr6 triplet states at rate $k_Q = 3.5 \times 10^7$ s^{-1} in FIr6:TTM-1Cz (96:4 wt%) films. Using Section 5.4.2, we can then estimate energy transfer to occur at $k_{ET} = 3.1 \times 10^7$ s^{-1}.

Figure 5.10 highlights the transient decays of TTM-1Cz photoluminescence where the radical was directly photoexcited (λ_{ex} = 515 nm, black) versus indirectly excitated via FIr6 triplet states (λ_{ex} = 343 nm, red).

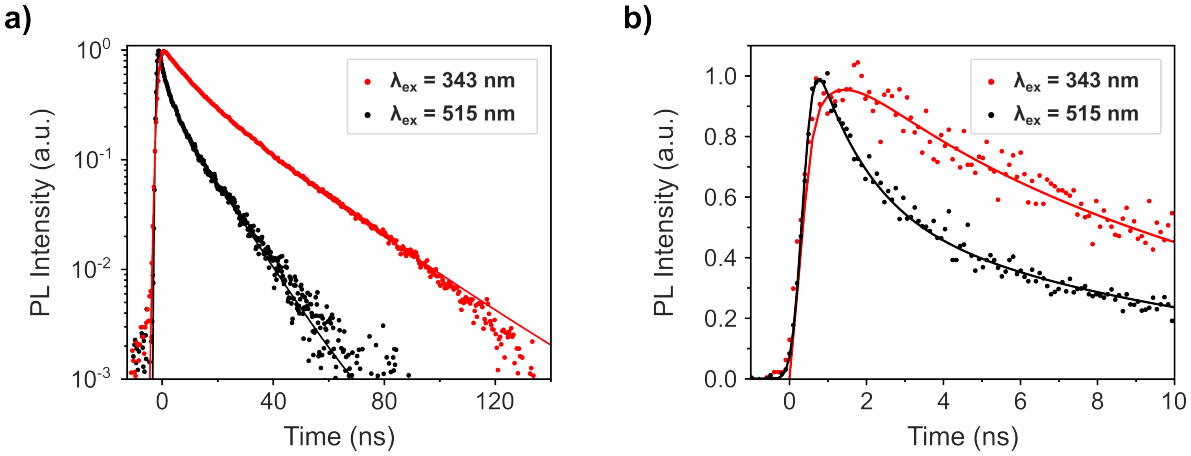

Figure 5.10: Transient photoluminescence decay for TTM-1Cz emission (600-750 nm) in mixed FIr6:TTM-1Cz films measured separately over a) 10's of nanosecond and b) nanosecond timescales for λ_{ex} = 343 nm (red dots) and λ_{ex} = 515 nm (black dots). Lines are provided to guide the viewer as to the rise and decay of signal.

Following direct TTM-1Cz excitation (515 nm) in mixed FIr6:TTM-1Cz films, radical emission is observed to follow a biexponential decay with time constants of 1.4 ns (12%) and 10.8 ns (88%). The initial 1.4 ns decay for radical luminescence is accompanied by red shifting of emission from 650 nm to 680 nm as shown in Figure 5.11. Similar to FIr6, we believe this kinetic is related to relaxation within the radical density-of-states to lower energy D_1 with lower oscillator strength.

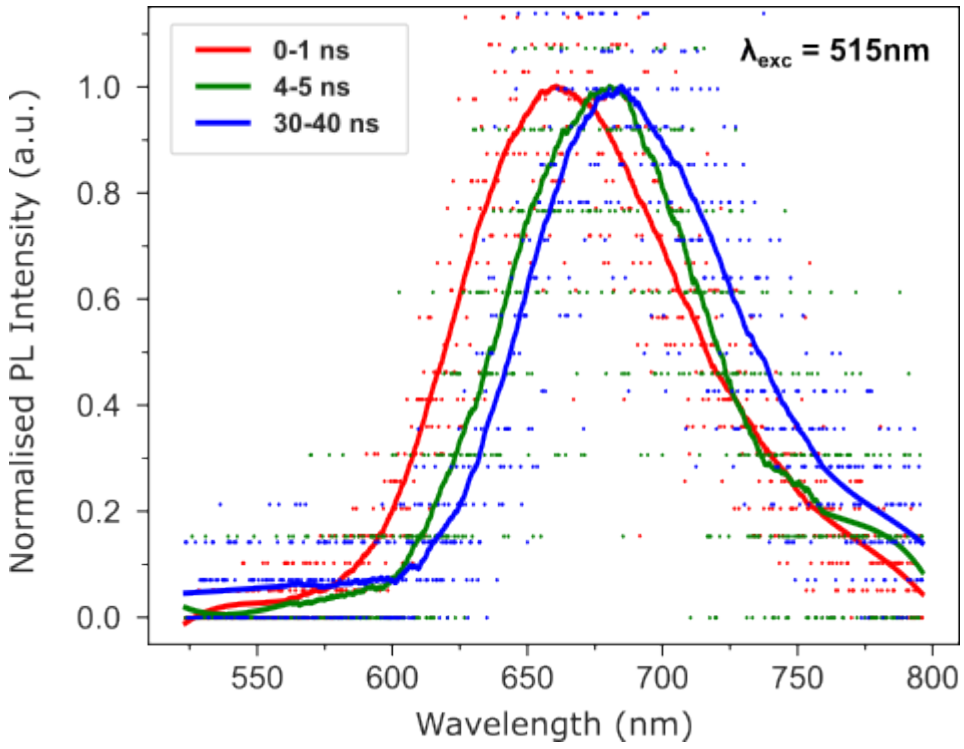

Figure 5.11: Evolution of transient PL spectra for FIr6:TTM-1Cz films following photoexcitation, λ_{ex} = 515 nm. Lines are provided to guide the viewer as to the shape of photoluminescence.

As previously noted, irradiation of mixed FIr6:TTM-1Cz films at 343 nm results in preferential population of FIr6 excited states, with 93% FIr6 excitation and 7% TTM-1Cz radical excitation. This 'indirect' excitation of TTM-1Cz following energy transfer from FIr6 results in radical emission with a lifetime of 22 ns. FIr6 phosphorescence in films is similarly seen to decay in films with a matching lifetime on the order of 25 ns. Measurement of FIr6:TTM-1Cz films over nanosecond timescales shows a distinct rise in of radical emission intensity over the first 2 ns of emission (Figure 5.10b). The emission kinetics for excitation at 343nm result from the convolution of emission coming from the 7% of radical states that are directly excited, and the remaining indirectly excited doublet states. The increase in lifetime for TTM-1Cz emission under indirect excitation is attributed to energy transfer from FIr6 to TTM-1Cz acting as the rate-limiting step in radical emission, which we estimate to occur at 4.4×10^7 s^{-1} in FIr6:TTM-1Cz (96:4 wt%) films.

5.4.6 Temperature-Dependent trPL

Temperature-dependent measurements were taken through cooling the Linkam LTS420E-P cryostat used for trPL measurements with liquid nitrogen in combination with a Linkam T96-S temperature controller.

FIr6 Phosphorescence

Towards understanding the mechanisms for phosphor-radical energy transfer, temperature-dependent trPL measurements were taken for TTM-1Cz emission from mixed FIr6:TTM-1Cz films, as well as phosphorescence from neat FIr6 films. Figure 5.12 shows temperature-dependent transient kinetics for FIr6 phosphorescence in neat FIr6 films for 298-98 K.

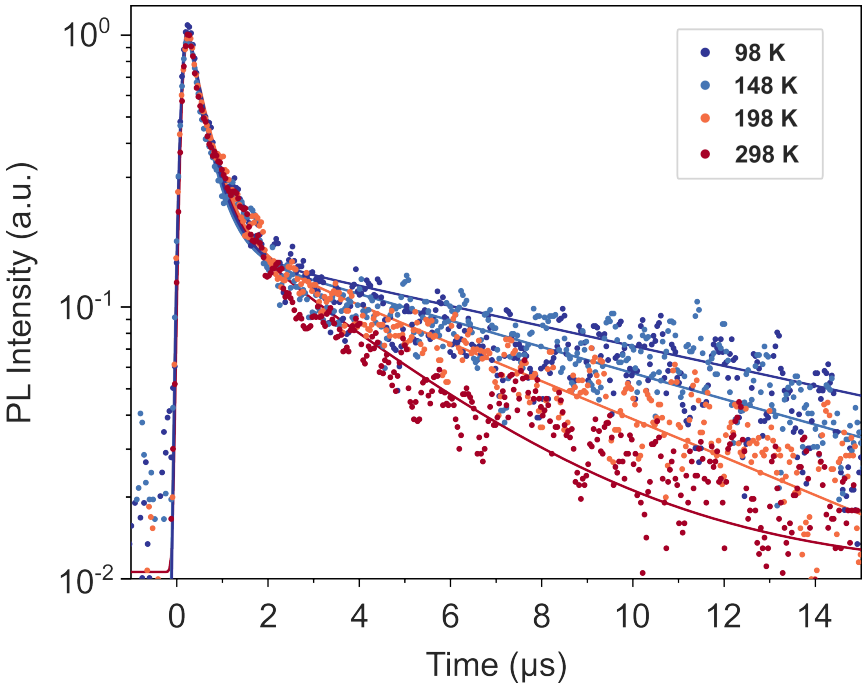

Figure 5.12: Transient FIr6 phosphorescence for neat FIr6 (100 wt%) films following photoexcitation (λ_{ex} = 343 nm) measured between 98-298 K.

FIr6 phosphorescence lifetimes in neat FIr6 films showed little variation with temperature on sub-microsecond timescales. Transient decays were fit to a biexponential decay convolved with a gaussian as described in Section 3.4.3 of the Experimental Methods. Fitting of FIr6 phosphorescence after 2 μs shows the emission lifetime to increase from 6 μs to 12 μs when cooled from 298 K to 98 K, with the increased lifetime attributed to the suppression of non-radiative relaxation pathways in FIr6. Quenching of FIr6 emission in FIr6:TTM-1Cz films resulted in substantially longer streak camera measurements being required to quantify FIr6 phosphorescence lifetime. As a result, temperature-dependent measurements of FIr6 phosphorescence lifetime could not be collected for mixed FIr6:TTM-

1Cz films, with measurement windows exceeding the time that cryogenic temperatures could be maintained.

TTM-1Cz Fluorescence

FIr6:TTM-1Cz films show minimal variation in TTM-1Cz emission timescales following direct excitation at 515 nm for 298-98 K. TTM-1Cz emission following indirect excitation (343 nm) is similarly unaffected above 148K. Through fitting TTM-1Cz fluorescence to a gaussian convolved with an exponential decay as described in Section 3.4.3, the lifetime of TTM-1Cz emission following indirect excitation is seen to increase from 22 ns between 148-298 K to 25 ns and 27 ns at 123 K and 98 K respectively (Figure 5.13a). From this, the rate of energy transfer from FIr6 to TTM-1Cz can be estimated to drop from 4.5×10^7 s^{-1} at 148 K to 4.0×10^7 s^{-1} at 123 K and 3.7×10^7 s^{-1} at 98 K.

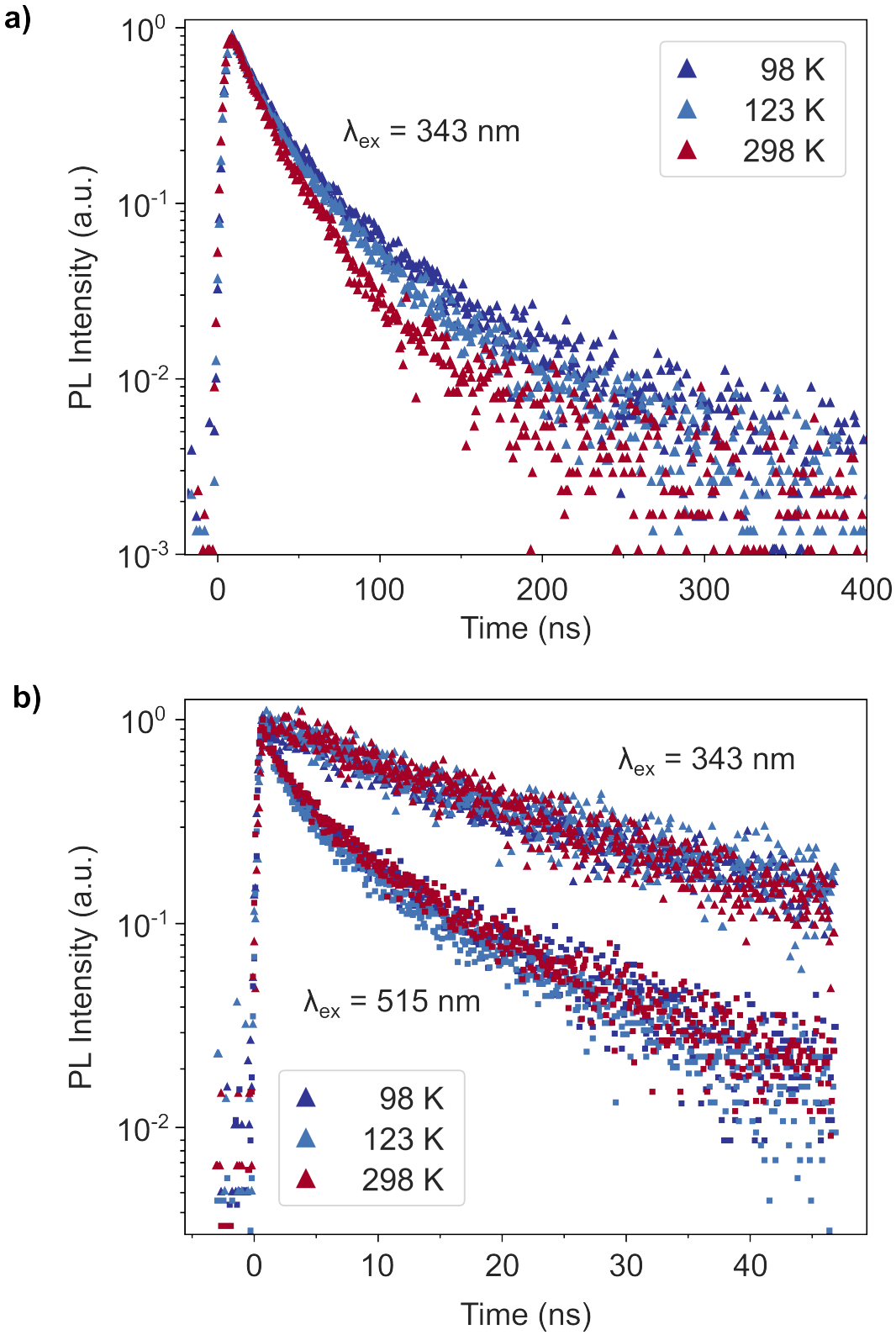

Figure 5.13: Temperature dependence of TTM-1Cz emission (600-750 nm). a) trPL for TTM-1Cz in mixed FIr6:TTM-1Cz films measured between 98-298 K for λ_{ex} = 343 nm. b) nanosecond-timescale kinetics for TTM-1Cz emission in mixed FIr6:TTM-1Cz films measured between 98-298 K for λ_{ex} = 343 nm (triangles) and λ_{ex} = 515 nm (squares).

Figure 5.13b highlights the temperature dependence for nanosecond emission timescales, where we can see no significant change for the growth in of TTM-1Cz emission signal after indirect excitation via FIr6 at 343 nm. Approximating the temperature-dependence of energy transfer with an Arrhenius relationship $\left(k \propto \exp\left(-\frac{E_a}{k_B T}\right)\right)$, we can place an upper limit on the activation energy for triplet-doublet energy transfer at 4.7 ± 1.1 meV.

5.5 Discussion

5.5.1 Interrogating Mechanisms for Energy Transfer

An activation energy of 4.7 ± 1.1 meV is significantly below what would be expected for energy transfer resulting from either a Dexter[159,160] or 2-step Marcus-like mechanism.[161,162] In previous studies, energy transfer from singlet and triplet excitons of TADF-host components to radical derivatives was shown to have $E_a > 20$ meV, with activation energies for energy transfer attributed to Dexter-mediated triplet-diffusion.[144,145]

Instead, the low activation energy for transfer strongly suggests that energy transfer results from Förster dipole-dipole mechanism from the FIr6 triplet to an excited TTM-1Cz doublet state. Whilst Förster-coupling from triplet states is typically very weak due to virtual-photon emission being spin-forbidden, it has been demonstrated that significant spin-orbit coupling in organometallic complexes can result in singlet-triplet mixing such that the 'triplet' state can undergo energy transfer via a Förster-like mechanism.[158,163]

5.5.2 FRET Rate Estimation for FIr6:TTM-1Cz Films

FRET occurs through space with the rate of energy transfer being dependent on the spectral overlap between the donor emission and acceptor absorption. As set out in Section 2.2.1, we can use the spectral overlap integral J for a donor: acceptor systems to define a FRET radius, R_0, at which energy transfer to an acceptor and spontaneous decay of the excited donor are equally probable. From the steady-state absorption of TTM-1Cz, and PL spectrum of FIr6, we can estimate the spectral overlap integral for FIr6-TTM-1Cz energy transfer, J_{TD} to be 1.3×10^{14} M^{-1} cm^{-1} nm^4, resulting in $R_0 = 3.8$ nm.

With assumption of similar mass densities (~ 1.1 g cm^{-3})[164–167] and molecular weight for FIr6 and TTM-1Cz, the molecular density of films are estimated as 7.8×10^{20} cm^{-3}. For a FIr6:TTM-1Cz (90:4 wt%) film, we can therefore estimate that uniformly dispersed TTM-1Cz molecules are separated by 3.0 nm.

For a TTM-1Cz molecule in a cube with side length $a = 3.0$ nm, we can both computationally and analytically[168] find the average separation between a randomly excited FIr6 molecule and the nearest TTM-1Cz to be 1.42 nm. We can similarly compute the expectation value for R^6 with random FIr6 excitation to be $\left\langle R^6 \right\rangle = 0.0288\ a^6$. Using Equation 2.7 and a radiative lifetime for FIr6 of 6 μs, we estimate the average rate of FRET is $3.1 \times 10^7\ s^{-1}$. This result comes in good agreement with the experimentally determined rate of energy transfer estimated from FIr6 quenching to be $3.2 \times 10^7\ s^{-1}$.

5.5.3 Radicals as Efficient Energy Harvesters

For FIr6:TTM-1Cz (96:4 wt%) films, the average separation between a photoexcited FIr6 molecule to a TTM-1Cz radical is expected to be lower than the FIr6:TTM-1Cz FRET radius. In combination with a lack of temperature dependence for energy transfer, this strongly suggests that FIr6 triplets can transfer energy to TTM-1Cz without the need for triplet diffusion.

CzSi:FIr6:TTM-1Cz films possess similar PLQY values independent of FIr6 concentration, suggesting that FRET can outcompete mechanisms for FIr6 concentration quenching. Overall system efficiency for emission is currently limited by that of TTM-1Cz ($\Phi = 12\%$), such that future systems should look to use phosphor:radical combinations where radical emission is as efficient as possible.

Whilst phosphor-radical energy transfer is efficient, the excited-state lifetime of the system is limited by the triplet-doublet FRET rate rather than the D_1 excited-state lifetime. In FIr6:TTM-1Cz, the FRET rate is limited by the weak oscillator strength of the FIr6 triplet, however, other iridium-based phosphors have demonstrated sub-microsecond lifetimes for phosphorescence. We envisage that systems using organometallic complexes with phosphorescence lifetimes on the order of 440 ns[146,169] could demonstrated triplet-doublet FRET rates $= 4.2 \times 10^8\ s^{-1}$. This holds promise towards using radicals as efficient energy harvesters in optoelectronic systems, with system design not being limited by timescales for triplet-diffusion.

5.6 Conclusions for Energy Transfer

In this chapter we have demonstrated triplet-doublet energy transfer from the organometallic phosphor FIr6 to the 'fruit fly' radical TTM-1Cz. Nanosecond-lifetimes for energy transfer from FIr6 to TTM-1Cz ($k = 3.1 \times 10^7$ s^{-1}) are such that triplet states efficiently transfer (85 ± 25)% their energy to doublet states. Through temperature-dependent transient photoluminescence measurements, we have limited the activation energy for energy transfer $E_a < 5$ meV, highlighting that energy transfer is dipole-dipole mediated via FRET. Energy transfer to TTM-1Cz occurs through space without the need for triplet diffusion and is able to outcompete FIr6 self-quenching mechanisms that limit overall system efficiency. Luminescent radicals allow for the simplified design of emitting layers towards 'colour by blue' applications, with lowest lying doublet states allowing for efficient emission from systems without the need to engineer average molecular distances through the use of molecular hosts. Future work should look to expand the range of phosphor:radical systems towards increased FRET rates, and look towards translating phosphor:radical systems into working OLED devices.

5.6.1 Outlook Towards Spin Transfer

Whilst useful towards energy harvesting applications, efficient FRET can excite radical doublet states irrespective of their ground-state spin. Therefore, whilst high levels of SOC are able to generate spin polarised triplet states, efficient triplet-doublet FRET will act as a detrimental mechanism for passing any spin polarisation to a radical species. If SOC is to be used to generate spin polarised states, the efficiency of triplet generation will need to be balanced with keeping the FRET rate sufficiently low compared to rates for Dexter transfer. Towards spin-sensitisation, efforts must be made to find intermolecular systems with maximised wavefunction overlap or intramolecular systems such that Dexter energy transfer is maximised.

Chapter 6

Radicals as Energy Harvesters in Magnetosensitive Acene Systems

Acene-based molecules demonstrate efficient upconversion and downconversion, with triplet-triplet annihilation and singlet fission holding promise for fields from solar energy harvesting to optoelectronics and medical imaging. Key insights into the magnetic interactions between molecular spins are gained through measuring the magnetosensitivity of emission from systems. In this chapter, radical doublet species are introduced into acene films demonstrating cyclic singlet fission and triplet-triplet annihilation to explore action as singlet exciton energy harvesters. The introduction of triphenylamine- and carbazole-based luminescent radicals into rubrene thin films is seen to result in quenching of both the intensity and magnetosensitivity of rubrene emission. Radical photoluminescence is additionally quenched in rubrene:radical films. We explore possible mechanisms for radical quenching in rubrene films, in particular highlighting how Dexter energy transfer from doublet to triplet excited states can act as a parasitic loss mechanism to the use of radicals as energy harvesters.

The work presented in Chapters 6 and 7 was carried out in tandem with the building of a magnetic-field dependent photoluminescence setup for probing the magnetic properties of systems including luminescent radicals. Chapter 6 focusses on the addition of radicals to rubrene, a molecular system known to show magnetic field dependent photoluminescence. Through measuring the magnetic response of rubrene-based systems, methodologies for synchronous control of the magnetic field with a spectrometer were developed. In Chapter 7, these updated protocols were applied to a doublet-triplet energy transfer system for which the magnetosensitivity of emission was unknown.

6.1 Energy Harvesting In Upconversion Systems

Molecular upconversion converts multiple lower energy excitations into a single higher energy excitation,[170] holding promise in fields from solar energy harvesting[171,172] to optoelectronics[173] and medical imaging.[174,175] Triplet-triplet annihilation (TTA) is a form of upconversion in molecular systems in which two separate T_1 triplet excited states are converted into an excited state (S_1) and ground state (S_0) singlet:

$$T_1 + T_1 \rightleftharpoons {}^1(TT) \rightarrow S_1 + S_0 \tag{6.1}$$

For TTA to conserve energy, the two annihilating triplet states must together have energy greater than the S_1 state ($2 \times E(T_1) \geq E(S_1)$). TTA will additionally only occur if triplet states meet with overall singlet spin character, such that the overall spin of the system is conserved.

For systems where $E(S_1) \geq 2 \times E(T_1)$, singlet fission (SF) can take place as the reverse process of TTA, in which two lower energy T_1 triplet excited states are formed from the encounter of S_1 and S_0 states:

$$S_1 + S_0 \rightarrow {}^1(TT) \rightarrow T_1 + T_1 \tag{6.2}$$

Molecular acenes have demonstrated an ability to perform both efficient TTA and SF, with TTA typically favoured in anthracene-based systems, and SF favoured in pentacene-based systems. Tetracene-based derivatives have demonstrated the ability for both TTA and SF. The photophysical behaviour of these systems follow the trend of decreasing exciton energy with relatively fixed S_1-T_1 energy difference ($\sim$ 1 eV) on going from anthracene to tetracene to pentacene.

Rubrene (5,6,11,12-tetraphenylnaphthacene) has well placed S_1 and T_1 energy levels (2.32 eV and 1.14 eV, respectively)[176] towards exhibiting both SF and TTA, with previous reports demonstrating the rapid formation of an equilibrium between triplet and singlet species in the solid-state on picosecond-timescales.[176] Figure 6.1a highlights architectures utilising rubrene towards optoelectronics, in which closed-shell fluorophores have been used as emissive dopants that are able to depopulate the excited singlet states formed by TTA in rubrene. Closed shell energy harvesters such as tetraphenyldibenzoperiflanthene (DBP) are utilised to drive cyclic SF and TTA towards the singlet state, increasing the photoluminescence upconversion efficiency for systems[177,178] as well as enabling increased colour purity for emission.[179]

Terminal emitters for an upconversion system should be designed to have a maximised rate of singlet-singlet FRET to the terminal emitter, a minimal loss in energy after transfer, a maximised internal efficiency for emission of the terminal emitter, and reduced spin-orbit coupling to minimise decay to dark triplet states. However, as depicted in Figure 6.1a, the triplet excited states of terminal emitters must additionally be engineered to lie energetically above the triplet states of both the upconversion and triplet sensitisation systems to avoid introducing a parasitic triplet loss pathway.

Figure 6.1b shows the ordering of excited states for such upconversion systems on replacing the closed-shell terminal emitter again with a luminescent organic radical. Radicals have doublet lowest energy excited states, such that we do not need to consider parasitic loss of triplet states to dark radical states.

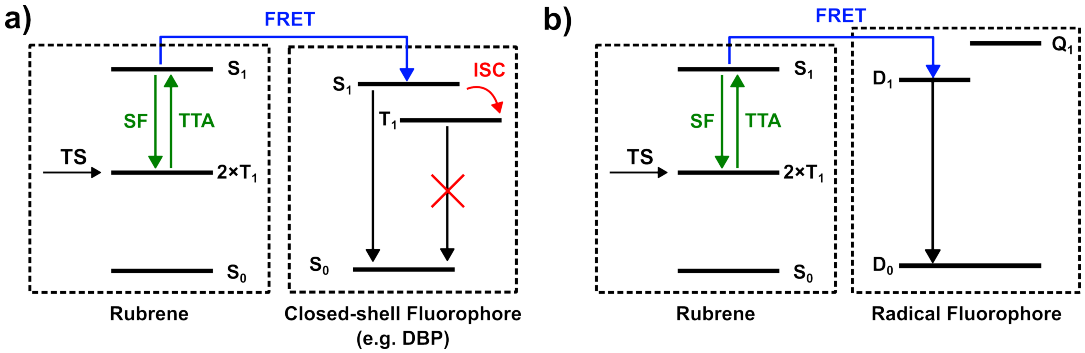

Figure 6.1: Schematic highlighting cyclic singlet fission (SF) and triplet-triplet annihilation (TTA) of rubrene excited states following triplet sensitisation (TS), and the use of a) a closed-shell fluorescent dopant and b) a radical fluorescent dopant as energy harvesters for singlet states.

On design of the system in this chapter, following studies of the previous chapter, it is expected that singlet-doublet FRET could be realised on picosecond timescales for upconversion systems that then exploit the radicals' nanosecond timescales for terminal emission. We explore systems utilising radicals as terminal emitters following upconversion and the resulting energy transfer mechanisms that set performance in radical versus non-radical terminal emitters.

6.2 Radical Systems Towards Singlet-Doublet Energy Transfer

Here we combine rubrene with luminescent radicals that contain the triphenylamine (TPA) electron donating group. As shown in Figure 6.2a, TTM-TPA and PyBTM'-TPA have HOMO levels of –5.4 eV[180] and –5.0 eV[181] respectively, which lie equal to or above the energy of the rubrene HOMO at –5.4 eV.[182] The comparatively high HOMO energy for these radicals (compared to other carbazole-based radical systems) enables them to form a type-I heterojunction with rubrene towards driving energy transfer to the radical. Energy transfer via singlet-doublet FRET is considered to be the most likely pathway for energy transfer in dilute radical films (<5 wt% doping) due to the average intermolecular distance from photoexcited rubrene states to a radical being over 1 nm.

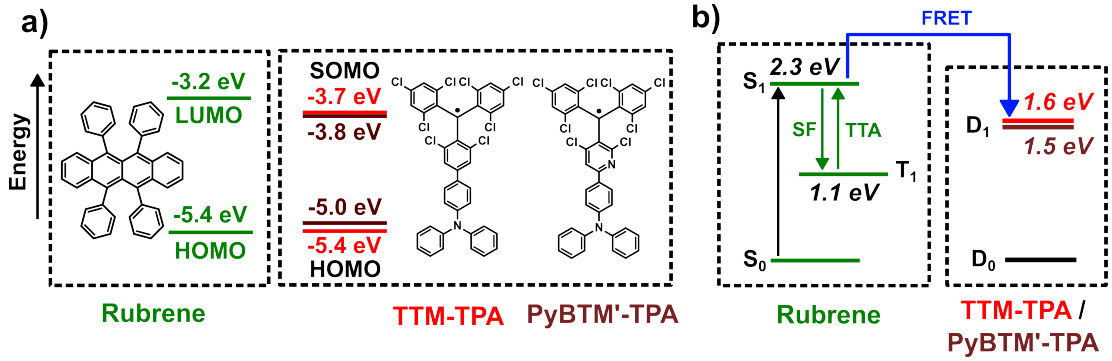

Figure 6.2: a) Molecular structures and frontier molecular orbital energies for rubrene and TTM-TPA / PyBTM'-TPA. b) Jablonski diagram highlighting excitonic energies for rubrene: TTM-TPA / PyBTM'-TPA systems. Excitonic and orbital energies for rubrene were estimated from literature.[176,180,181]

As set out in Figure 6.2b, TTM-TPA and PyBTM'-TPA are expected to have D_1 energies of 1.6 eV and 1.5 eV respectively, placing them above the rubrene triplet energy and so avoiding parasitic loss pathways for rubrene triplets.

6.3 Sample Preparation

Rubrene was obtained from Ossila. TTM-TPA was synthesised as previously reported by Prof. Feng Li's group,[183] whilst PyBTM'-TPA was synthesised as previously reported by Prof. Tetsuro Kusamoto's group.[181] Rubrene, TTM-TPA and PyBTM'-TPA were dissolved in anhydrous toluene at concentrations of 11.0 mg/mL, 7.8 mg/ml and 7.8 mg/mL respectively, before being passed through a 0.2 μm PTFE filter. Rubrene and radical solutions were combined in a 10:1 ratio to produce a 10 mg/mL rubrene solution with 5 mol% radical doping. Solutions with 0.5 and 2 mol% radical doping were produced through dilution

of TTM-TPA and PyBTM'-TPA solutions prior to combination with rubrene. Solutions were spun coat onto quartz-coated glass substrates at 1000 rpm for 60 s before being encapsulated with a glass cover slip and UV-set epoxy. All samples were prepared under a nitrogen atmosphere (< 10 ppm O_2, < 0.5 ppm H_2O).

6.4 Steady State Photophysics

Figure 6.3 shows the steady state absorption spectra for rubrene, TTM-TPA and PyBTM'-TPA in toluene solution, in addition to their normalised steady-state photoluminescence profiles.

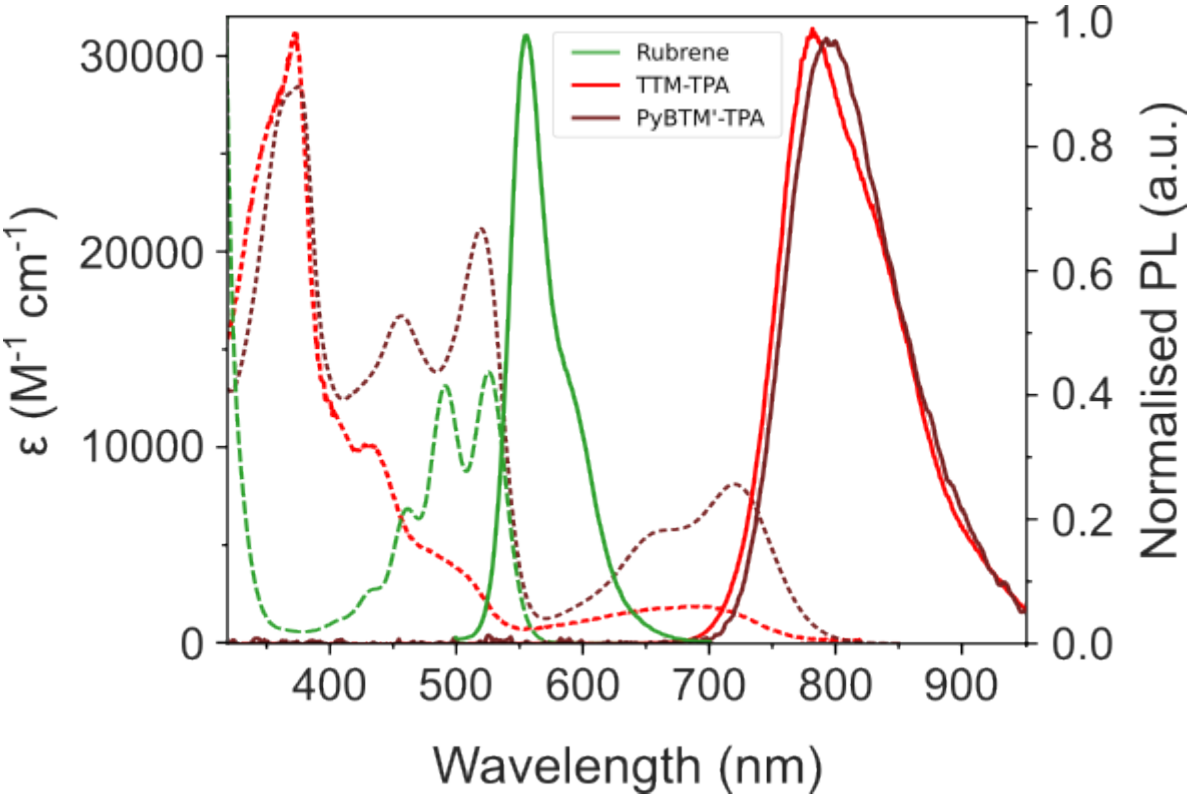

Figure 6.3: Extinction coefficient (dashed lines) and normalised photoluminescence (solid lines) profiles for rubrene (green), TTM-TPA (red) and PyBTM'-TPA (brown) in toluene solution.

The lowest energy absorption band for rubrene is seen to start at 570 nm, whilst for TTM-TPA and PyBTM'-TPA starts at 800 nm. Rubrene shows green fluorescence peaking at 555 nm with an observable vibronic feature at 580 nm as expected.[184] Meanwhile, TTM-TPA and PyBTM'-TPA both show broad radical emission peaking at 780 and 795 nm respectively as expected.[181,185]

Figure 6.4 shows steady-state photoluminescence measurements for rubrene and rubrene:TTM-TPA films (0.5, 2 or 5 wt% radical concentration) excited at 520 nm. At 520 nm, irradiation is expected to primarily result in photoexcitation of rubrene (98.5% for films doped with 5% TTM-TPA). A 550 nm long-pass filter was placed in the collection path for photoluminescence, such that we observe broad emission extending from 550 nm up to 850 nm for rubrene thin films.[186]

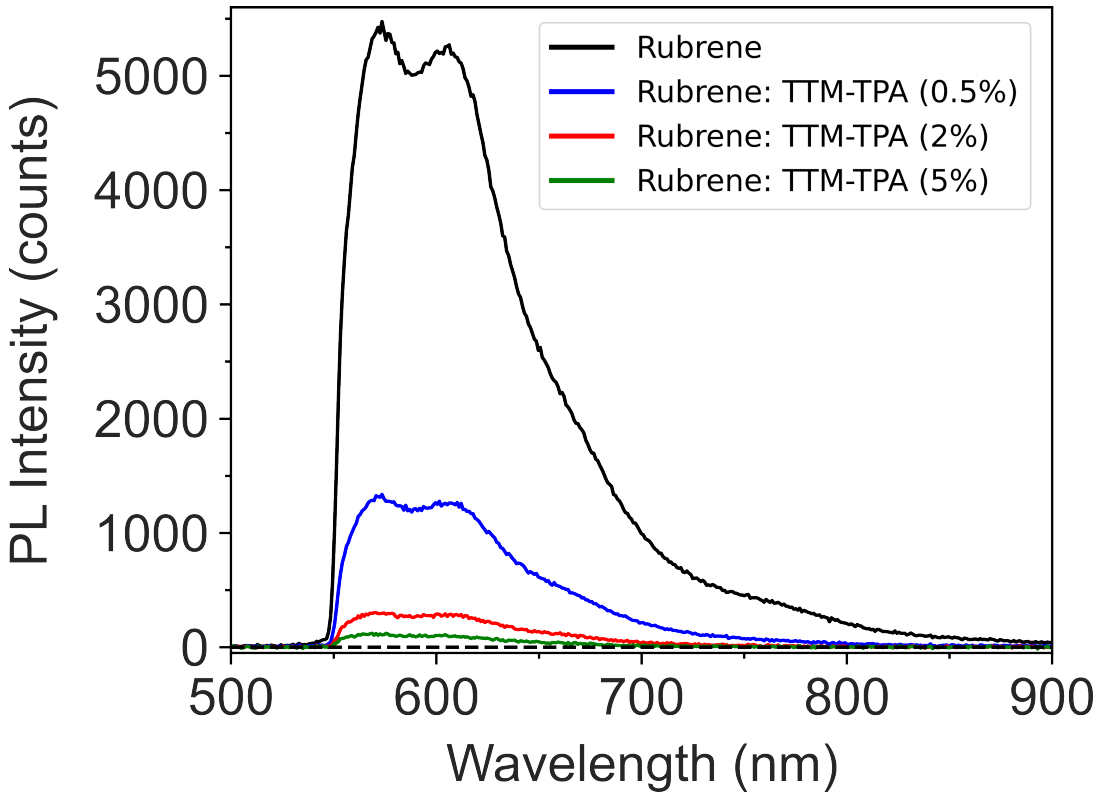

Figure 6.4: Steady-state photoluminescence for thin films of rubrene doped with TTM-TPA (0%, 0.5%, 2%, 5%) for $\lambda_{ex} = 520$ nm (fluence = 40 mW cm^{-2}).

Rubrene:TTM-TPA films showed progressive quenching of rubrene emission with increased radical concentration. No emission was observed from TTM-TPA in these films. Rubrene emission from rubrene:TTM-TPA films was quenched to 25%, 5% and 2% of that from neat rubrene films with 0.5, 2 and 5 mol% radical doping respectively.

6.4.1 Magnetically Sensitive Photoluminescence

Towards understanding the quenching of rubrene by TTM-TPA, films were continuously photoexcited at 520 nm and placed within a magnetic field that varied sinusoidally between 0 and 200 mT at a 0.05 Hz frequency. Figure 6.5 shows the total integrated emission of rubrene (550-850 nm) in rubrene:TTM-TPA films over 1200 s, demonstrating both

gradual changes in photoluminescence over time and a periodic variation over 20 s that corresponds to the 0.05 Hz applied magnetic field frequency.

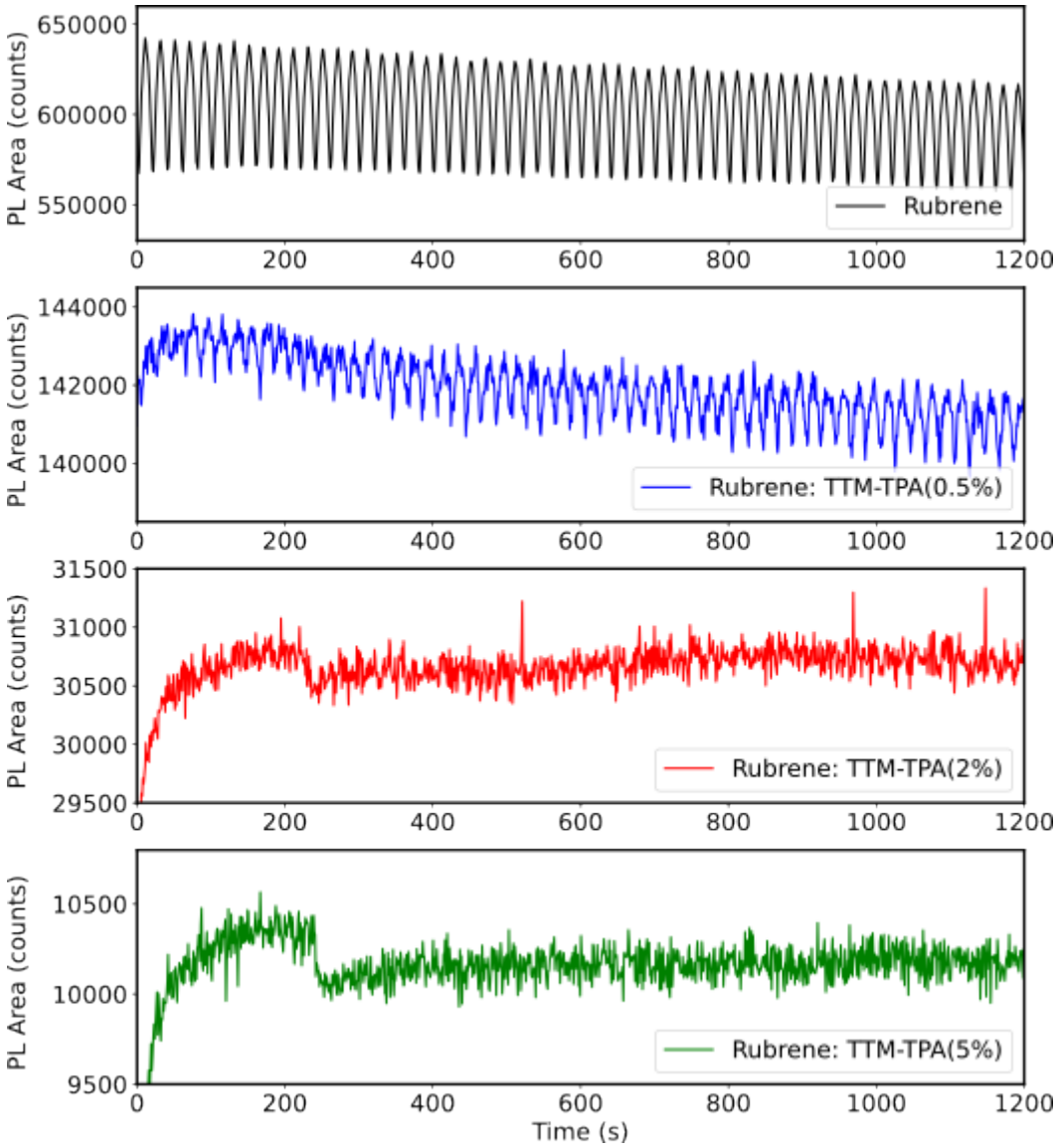

Figure 6.5: Temporal variation in integrated rubrene emission (550-850 nm) for rubrene:TTM-TPA films under a sinusoidally varying magnetic field (0 mT<$|B|$<200 mT, f = 0.05 Hz) with continuous photoexcitation (λ_{ex} = 520 nm, fluence = 40 mW cm^{-2})

A Savitzky-Golay filter was applied to the data, acting over 60 s windows to find the general trend in photoluminescence separate from its periodic variation. The original photoluminescence data was compared to this trend in PL, allowing an estimate for the change in photoluminescence from the magnetic field to be estimated at any one moment.

To evaluate the size of the magnetic field effects, measurements separated by 20 s were collected to find an average magnetic field effect for a particular point through the

cycle of the magnetic field. Figure 6.6 shows the collected values for the MFE = 100 × PL(B)/PL(B=0 mT) from binning the entire spectra over a 20 s cycle, assuming minimum photoluminescence occurs at zero field.[187]

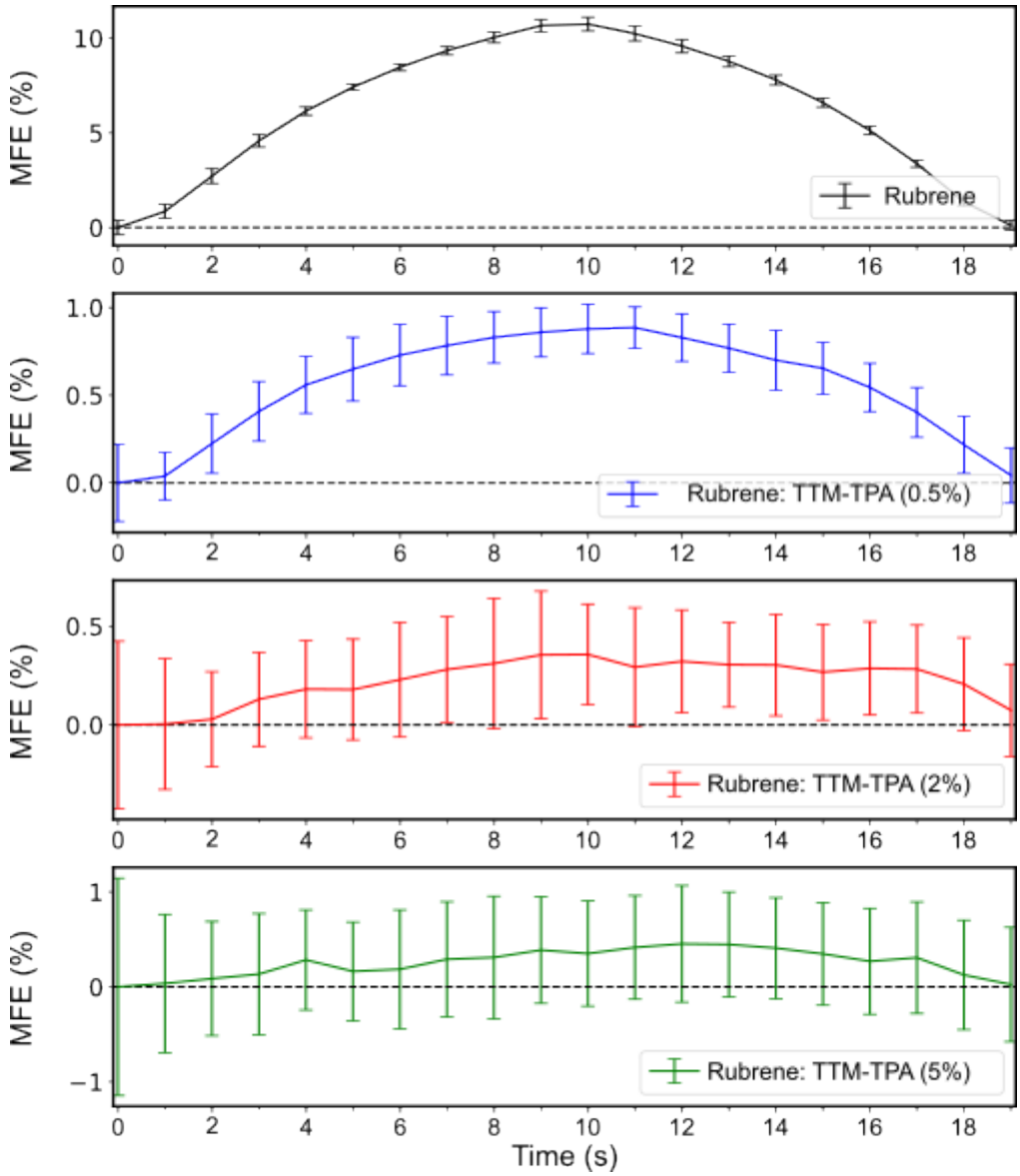

Figure 6.6: Photoluminescence intensity of rubrene:TTM-TPA films under CW excitation (λ_{ex} = 520 nm, fluence = 40 mW cm^{-2}) binned over the 20 s period of a varying magnetic field (0 mT<|B|<200 mT, f = 0.05 Hz)

Figure 6.7 shows this magnetic response for each film when the time through the 20 s period is converted to an estimated field strength.

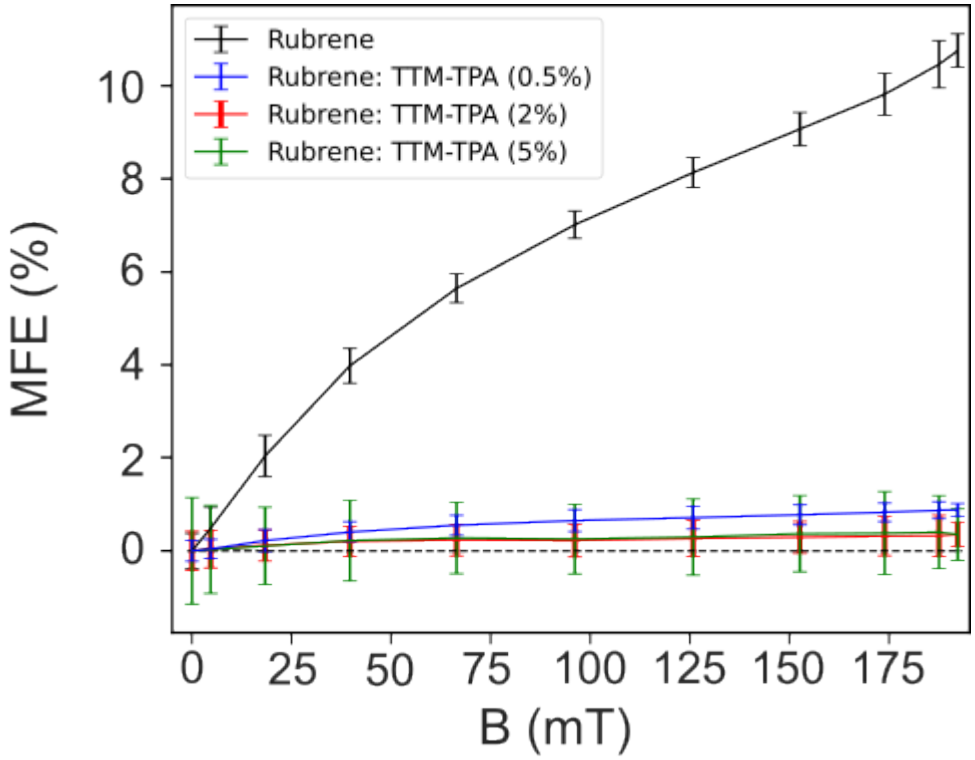

Figure 6.7: Photoluminescence MFE versus magnetic field for rubrene:TTM-TPA films under CW excitation (λ_{ex} = 520 nm, fluence = 40 mW cm^{-2}).

Addition of TTM-TPA results in significant quenching of the magnetosensitivity of rubrene emission. Positive MFEs for B = 150 mT are seen to drop from 9.1 ± 0.3% for pure rubrene films to 0.7 ± 0.2% for rubrene:TTM-TPA (0.5 mol%) films, with higher radical concentrations resulting in even further magnetosensitivity quenching.

Figure 6.8a shows the photoluminescence of rubrene:PyBTM'-TPA films, with radical inclusion similarly resulting in quenching of the intensity and magnetosensitivity of rubrene emission and no growth in PyBTM'-TPA emission. For irradiation at 520 nm, 7% of total photoexcitation is expected to occur directly to PyBTM'-TPA, suggesting that emission from excited doublet states is quenched in rubrene films.

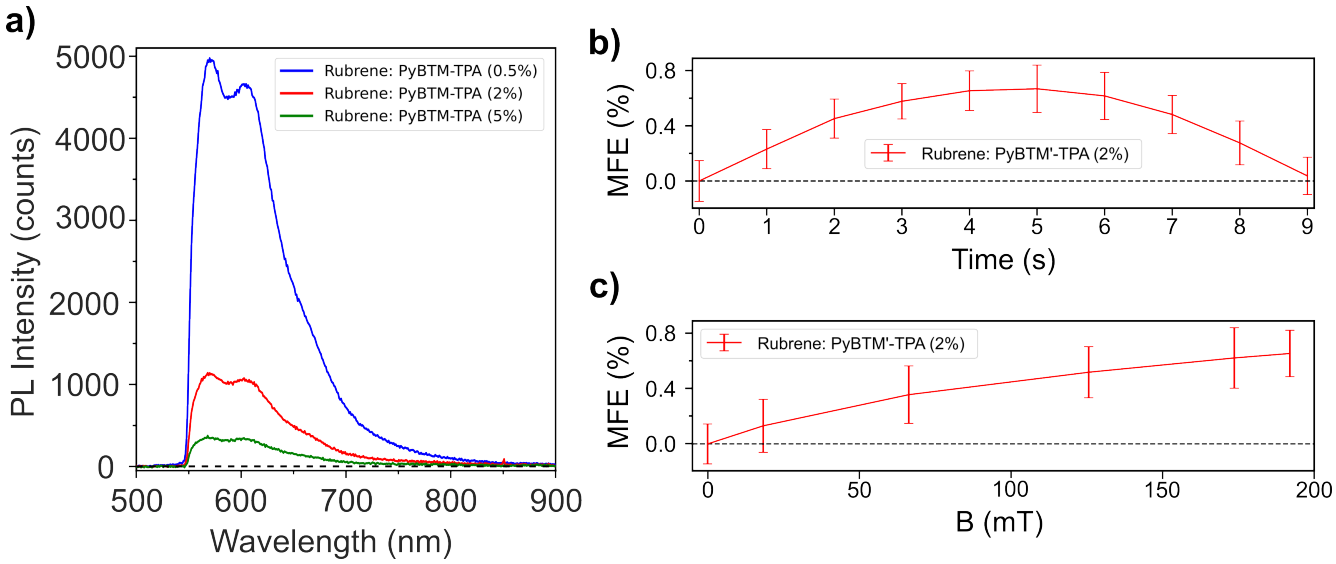

Figure 6.8: a) Steady-state photoluminescence spectra for rubrene:PyBTM'-TPA films (0.5%, 2%, 5%) with $\lambda_{ex} = 520$ nm. b) Photoluminescence intensity of a rubrene:PyBTM'-TPA (2 wt%) film under CW excitation ($\lambda_{ex} = 520$ nm, fluence = 40 mW cm^{-2}) versus the time through a cycle of a sinusoidally varying magnetic field (0 mT<|B|<200 mT, f = 0.1 Hz). c) MFE for photoluminescence versus magnetic field for rubrene:PyBTM'-TPA films under CW excitation ($\lambda_{ex} = 520$ nm, fluence = 40 mW cm^{-2}).

The magnetosensitivity of photoluminescence was additionally measured for rubrene films doped with 2 mol% of PyBTM'-TPA. Figures 6.8b and c highlight PL measurements taken under a sinusoidally varying magnetic field (0 mT<|B|<200 mT, $f = 0.1$ Hz), showing a similarly quenching of the magnetosensitivity of rubrene photoluminescence.

6.5 Steady State PL of Alternative Acene:Radical Systems

Towards understanding the mechanisms underlying a lack of radical emission, films of the radical PyBTM'-TPA were combined with the anthracene-based molecules 9,10-bis(phenylethynyl)anthracene (BPEA) and 1-chloro-9,10-bis(phenylethynyl)anthracene (CBPEA).

As shown in Figure 6.9b, BPEA and CBPEA possess HOMO energies of –5.5 eV[188,189] and –5.6 eV[190] respectively towards the creation of a larger driving force for energy transfer to PyBTM'-TPA.

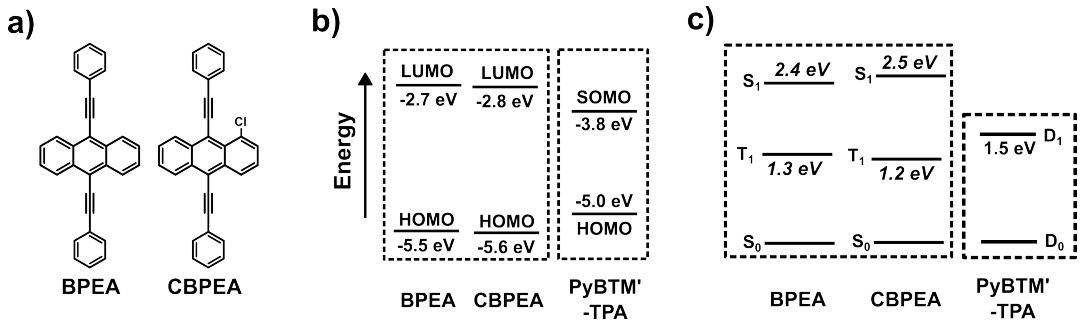

Figure 6.9: a) Molecular structures for BPEA and CBPEA. b) Frontier molecular orbital energies and c) excitonic energies for BPEA, CBPEA and PyBTM'-TPA. Orbital and excitonic energies for BPEA and CBPEA were estimated from literature.[188–195]

BPEA and CBPEA were obtained from Merck. BPEA and CBPEA films were fabricated similarly to rubrene films, however, lower solubility of BPEA and CBPEA in toluene resulted in radical-doped solutions of BPEA and CBPEA being at a 3 mg/mL and 5 mg/mL concentrations respectively. PyBTM'-TPA solutions were diluted to produce the required 0.5, 2 and 5 mol% doping in the final solution, with spin-coating and encapsulation performed identically to rubrene films under a nitrogen atmosphere.

Figure 6.10 shows steady-state photoluminescence measurements for thin-films of BPEA and CBPEA doped with PyBTM'-TPA at 0, 0.5, 2 and 5 mol% concentrations. In both cases we observe emission stretching from 550 nm up to 800 nm that we attribute to BPEA and CBPEA respectively.[195,196]

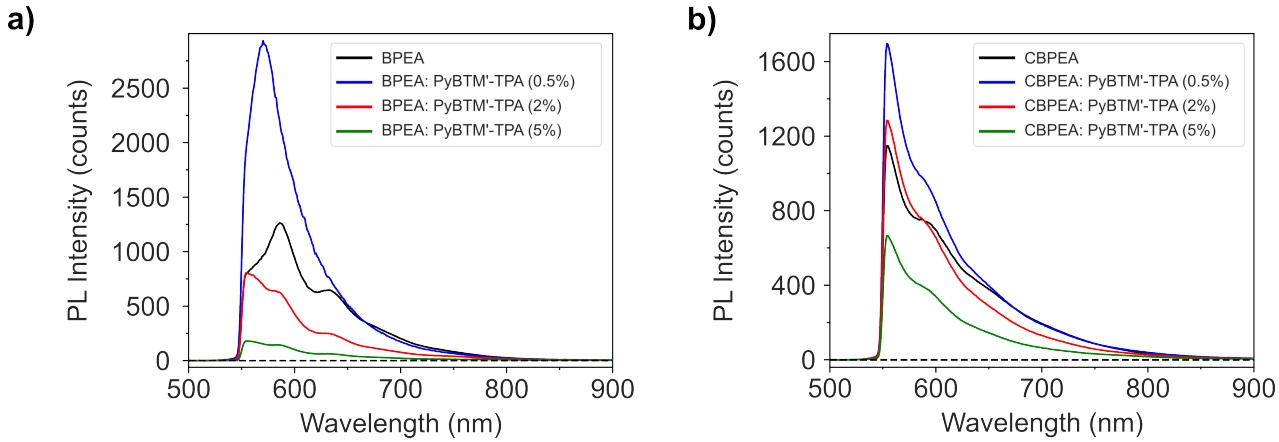

Figure 6.10: a) Steady-state photoluminescence for thin films of a) BPEA and b) CBPEA doped with PyBTM'-TPA (0, 0.5, 2 and 5 mol%) under CW excitation (λ_{ex} = 520 nm, fluence = 40 mW cm^{-2}).

We are unable to observe any radical emission in either BPEA or CBPEA films. An

increase in emission is initially seen upon addition of 0.5 mol% PyBTM'-TPA to both BPEA and CBPEA films, which we attribute to morphological changes in films that additionally affect the vibronic features of annihilator emission. With further addition of radical, we return to observing quenching of BPEA and CBPEA emission like rubrene films.

Towards interrogating the differences in mechanisms occurring for pure samples of BPEA and CBPEA versus those doped with radical, future experiments should look to manufacture films through thermal deposition to minimise the morphological difference between films with varying compositions.

6.6 Investigating Quenching Mechanisms for Singlet and Doublet States

From these studies, we observe that introduction of radicals results in partial quenching of rubrene/anthracene systems and total quenching of any photoexcited radical states. Towards elucidating the mechanisms from which doublet and singlet states are quenched, we looked towards systems that change the driving force towards formation of charge transfer states.

6.6.1 Steady State Photophysics for B=0

TTM-3NCz is a luminescent radical based on the carbazole moiety that has shown photoluminescence quantum yields of 86% in the solid state.[31] The greater electron donating character of the carbazole-based moiety leads to a luminescent radical with a HOMO level at –5.7 eV[31] as shown in Figure 6.11a. As such rubrene and TTM-3NCz are expected to form a type-II heterojunction that has a tendency towards driving charge transfer.

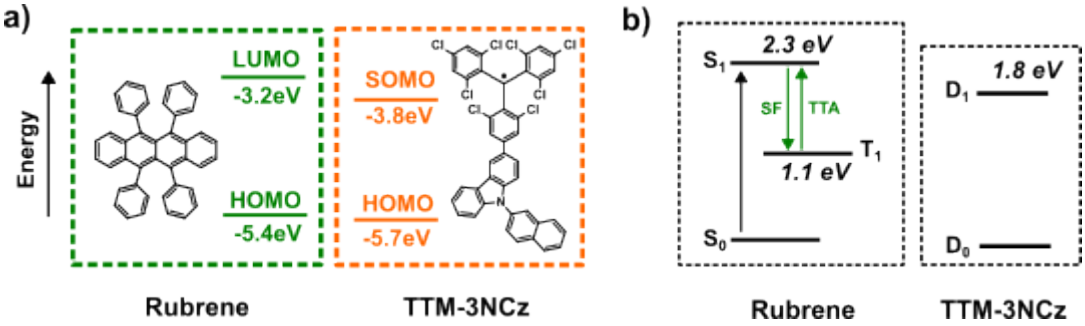

Figure 6.11: a) Molecular structures and frontier molecular orbital energies for rubrene and TTM-3NCz. b) Jablonski diagram highlighting excitonic energies for rubrene:TTM-3NCz systems. Orbital and excitonic energy levels for rubrene were estimated from literature.[176,182]

The 1.8 eV energy of D_1 for TTM-3NCz places it significantly above the energy of the rubrene triplet state at 1.1 eV. Ignoring the effects of any coulombic stabilisation, the rubrene:TTM-3NCz charge-transfer state is estimated to lie at 1.6 eV - placing it 0.7 eV below the singlet excited state and 0.2 eV below the doublet excited state.

TTM-3NCz was synthesised as previously reported by Prof. Feng Li's group, with rubrene:TTM-3NCz sample fabrication performed identical to rubrene:TTM-TPA films.

Figure 6.12a shows the steady state absorption spectrum for rubrene and TTM-3NCz in toluene solution. The lowest energy absorption bands for rubrene and TTM-3NCz start at 570 nm and 700 nm respectively, such that irradiation at 520 nm results in majority excitation of rubrene (99% of total photoexcitation). TTM-3NCz shows higher energy emission than TTM-TPA or PyBTM'-TPA, with emission centred at 710 nm.

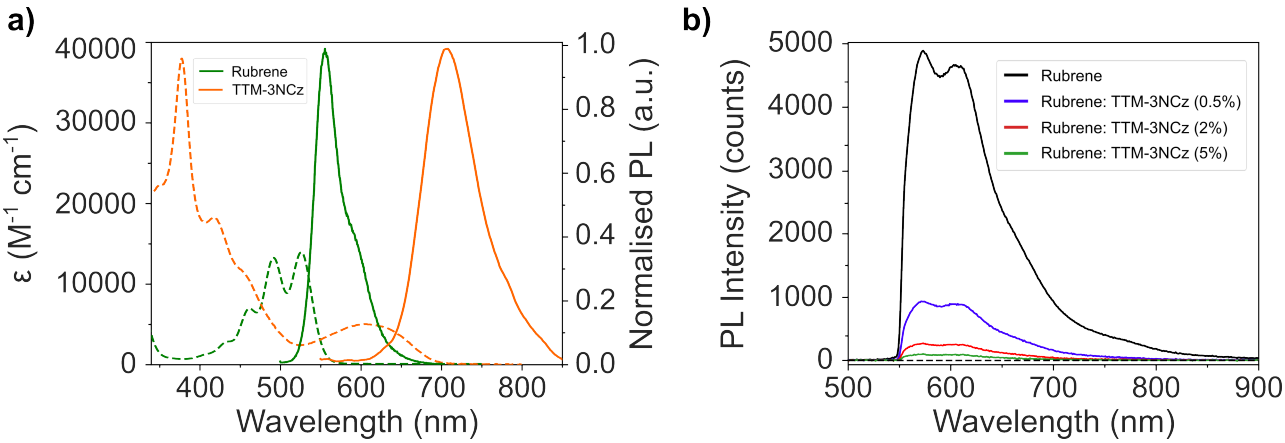

Figure 6.12: a) Extinction coefficient (dashed lines) and normalised photoluminescence (solid lines) profiles for rubrene (green) and TTM-3NCz (red) in toluene solution b) Steady-state photoluminescence for thin films of rubrene doped with various amounts of TTM-3NCz (0, 0.5, 2 and 5 mol%) for $\lambda_{ex} = 520$ nm.

Figure 6.12b shows steady-state photoluminescence measurements for rubrene:TTM-3NCz (0%, 0.5%, 2%, 5%) thin-films. As with the trend of previous measurements, we are unable to see any doublet emission and see quenching of rubrene emission upon addition of the TTM-3NCz radical. Rubrene emission in rubrene:TTM-3NCz films was quenched to 18%, 5% and 2% of that from neat rubrene films with 0.5, 2 and 5 mol% radical doping.

6.6.2 Magnetically Sensitive Photoluminescence

Figure 6.13 shows the magnetosensitivity of rubrene photoluminescence intensity, which was measured using the same measurement conditions as used in TTM-TPA doped films (sinusoidal field, (0 mT<|B|<200 mT, f = 0.05 Hz).

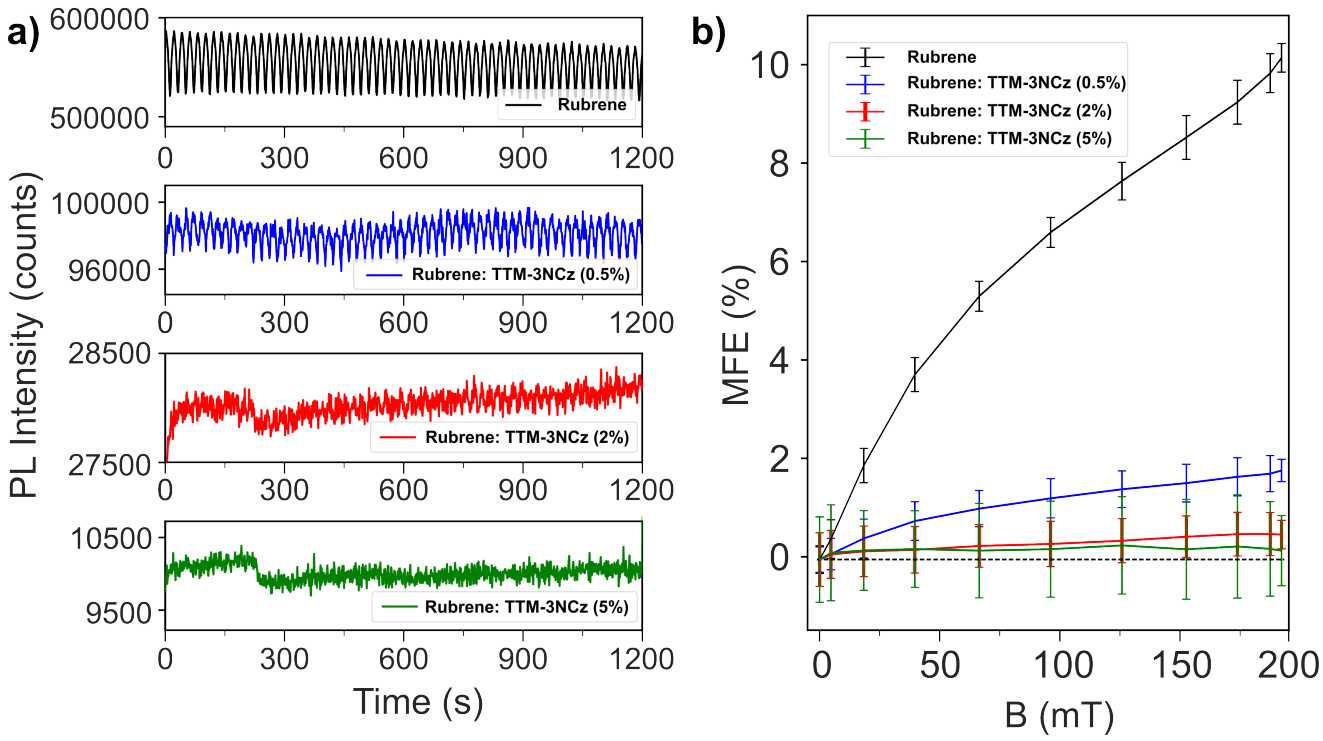

Figure 6.13: a) Photoluminescence intensity of rubrene emission (550-850 nm) over time from rubrene:TTM-3NCz films with CW excitation (λ_{ex} = 520 nm, Fluence = 40 mW cm^{-2}) under a sinusoidally varying magnetic field (0 mT<|B|<200 mT, f = 0.05 Hz). b) Photoluminescence MFE versus magnetic field for rubrene:TTM-3PCz films under CW excitation (λ_{ex} = 520 nm, Fluence = 40 mW cm^{-2}).

The magnetosensitivity of photoluminescence is maintained for rubrene films doped with TTM-3NCz rather than with TTM-TPA, with 0.5 mol% TTM-3NCz doped films showing a MFE of 1.8±0.3% MFE at 150 mT.

Figure 6.14 shows transient photoluminescence spectra of rubrene:TTM-3NCz films taken on a streak camera. We observe no radical emission following 515 nm excitation (fluence = 40 μJ cm^{-2}) for any of the rubrene:TTM-3NCz films.

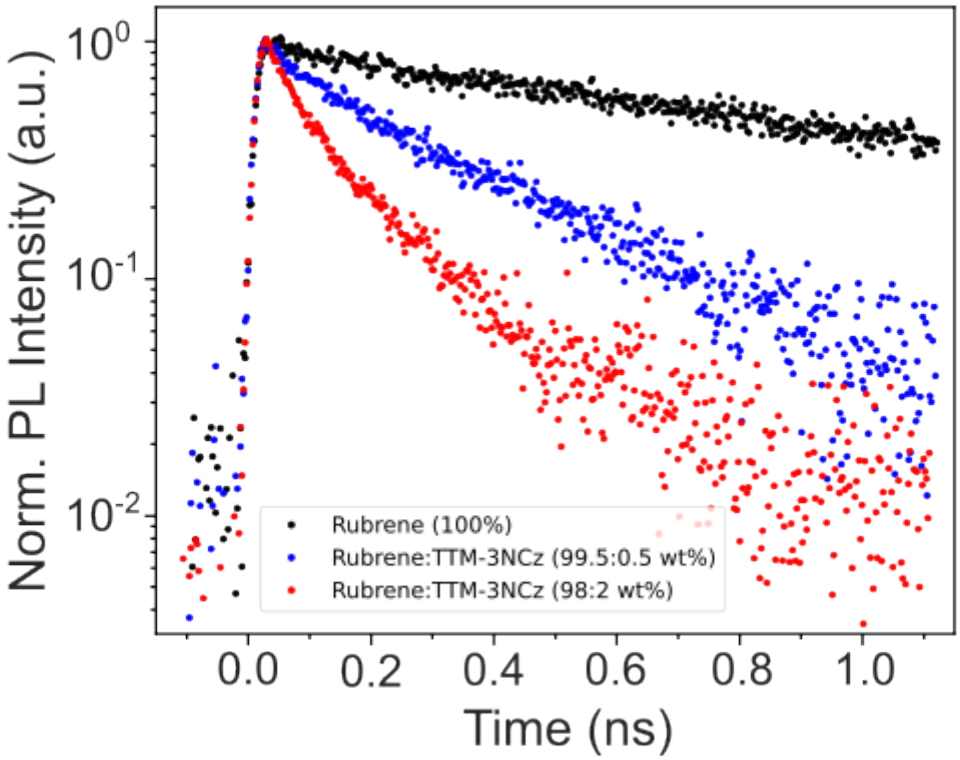

Figure 6.14: Transient photoluminescence decays for rubrene emission (550-700 nm) in rubrene:TTM-3NCz films (0, 0.5 and 2 mol%) films under pulsed excitation (λ_{ex} = 515 nm, fluence = 40 μJ cm^{-2}).

6.6.3 Transient Photoluminescence

The transient PL profiles for rubrene and rubrene:TTM-3NCz films are fitted to monoexponential decays, with fitted lifetimes for rubrene emission presented in Table 6.1.

Sample	PL Lifetime (ns)
Rubrene	2.8 ± 0.2
Rubrene:TTM-3NCz (99.5:0.5 wt%)	0.29 ± 0.02
Rubrene:TTM-3NCz (98:2 wt%)	0.12 ± 0.02

Table 6.1: PL Lifetimes for rubrene emission in rubrene:TTM-3PCz films (0, 0.5 and 2 mol%) excited at 515 nm (Fluence = 40 μJcm^{-2}). Lifetimes were obtained through fitting of PL transients to a monoexponential decay.

From the change in lifetime, we estimate TTM-3NCz to quench rubrene emission at a rate of 3.1 × 10^9 s^{-1} and 8.0 × 10^9 s^{-1} for 0.5 and 2 mol% doped films, respectively.

6.7 Discussion

Quenching of rubrene emission occurs in films doped with both TTM-TPA and TTM-3NCz. We suggest that possible mechanisms for rubrene quenching include Förster or Dexter energy transfer to the radical or the formation of a rubrene:radical CT state. Radical-enhanced intersystem crossing is ruled out in here as large radical-chromophore coupling is required and reports are typically limited to intramolecular (and not intermolecular) radical-triplet systems.[112]

The intermolecular spacing between radical molecules in rubrene: radical films is expected to be 3.3 nm for 0.5 mol% doping. As such, we assume that photoexcited rubrene molecules on average are separated by 1.6 nm from a radical molecule. Quenching mechanisms mediated by Dexter energy transfer are typically expected to have a maximum range of $\sim$1 nm, such that it is more likely in dilute films for rubrene to be quenched via FRET than other exchange-mediated quenching mechanisms.

Table 6.2 shows Förster radii and FRET rates that are estimated from the spectral overlap of rubrene with TTM-TPA, PyBTM'-TPA and TTM-3NCz. Rates are estimated using the average rubrene-radical separation for rubrene excitations that are randomly distributed in space, and are calculated from assuming that rubrene films have a PLQY of 4% and a radiative lifetime of 16 ns.[176]

System	$J(\mathrm{M^{-1}cm^{-1}nm^4})$	R_0 (nm)	$k_{\mathrm{ET(0.5\%)}}$ ($\mathrm{s^{-1}}$)	$k_{\mathrm{ET(2\%)}}$ ($\mathrm{s^{-1}}$)	$k_{\mathrm{ET(5\%)}}$ ($\mathrm{s^{-1}}$)
Rubrene:TTM-TPA	2.6×10^{14}	3.4	9.6×10^{7}	1.6×10^{9}	9.9×10^{9}
Rubrene:PyBTM-TPA	3.6×10^{14}	3.6	1.3×10^{8}	2.1×10^{9}	1.3×10^{10}
Rubrene:TTM-3NCz	4.2×10^{14}	4.2	1.4×10^{8}	2.2×10^{9}	1.4×10^{10}

Table 6.2: Förster radii and FRET rates for rubrene doped with 0.5, 2 and 5 mol% of TTM-TPA, PyBTM'-TPA or TTM-3NCz. Rates are estimated for a randomly photoexcited rubrene molecule in the film.

Figure 6.15 highlights previous work[176] in which FRET to energy harvesters, such as DBP, was considered in the picture of cyclic SF and TTA processes for rubrene nanoparticles. Rapid SF and TTA was observed on picosecond timescales, with magnetosensitivity arising from the spin evolution of weakly bound triplet-pairs with overall singlet character.

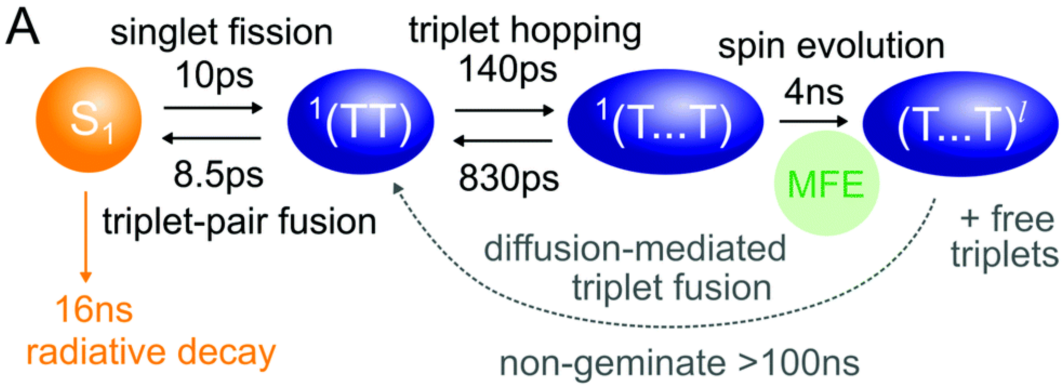

Figure 6.15: Schematic diagram summarising the photophysics of rubrene nanoparticles. Taken from J. Mater. Chem. C, 2022, 10, 4684-4696.[176]

Rates of FRET from rubrene to radical are expected to be at least an order of magnitude slower than rates for singlet fission or rubrene self-FRET (previously estimated[176] at 10^{11} s^{-1}), making it highly unlikely for energy transfer to occur prior to rubrene self-FRET or singlet fission. Instead, we suggest that cyclic processes of SF and TTA take place but that rubrene self-FRET results in diffusion of the S_1 excited state from the original location of photoexcitation. We suggest that timescales for radical-based rubrene quenching arise from the period it takes for singlet-diffusion to reduce rubrene-radical intermolecular distances, such that FRET can occur on sub 100 ps timescales ($<$ 1.2 nm for TTM-TPA and 1.1 nm for TTM-3NCz) and compete with singlet fission and diffusion.

In pure rubrene films we observe an initial decay with lifetime of 2.8 ns that we attribute to spin evolution of bound triplet states. In 0.5 and 2 mol% doped TTM-3NCz films, excitations must diffuse on the order of 1.6 nm and 1 nm respectively before the rate of FRET is comparable to that of SF (lifetime $<$ 100 ps). Assuming diffusion as a random walk, we can use $\langle r^2 \rangle = ka^2t$ to estimate the time it takes for singlet states to diffuse in rubrene films, where k is the hopping rate, a is the hopping distance and t is the time for a singlet to diffuse on average a distance r. Assuming a rate of self FRET of 20 ns^{-1} and a hopping distance of 0.7 A (intermolecular distance),[176] it would take 0.25 ns and 0.10 ns for the rubrene to diffuse into distance for FRET to a radical. This is seen to agree roughly with the quenched emission lifetimes that we see for rubrene:TTM-3NCz films. We envisage that design of radical materials towards greater spectral overlap with rubrene could enable Förster radii exceeding 4.5 nm, such that energy transfer could occur with reduced triplet diffusion.

Whilst rubrene quenching via FRET is most likely in dilute films, a lack of observable radical emission does motivate a discussion of whether singlet states could be quenched through formation of rubrene-radical charge transfer states. Ignoring the effects of coulombic stabilisation, CT state energies can be estimated to be 1.7 eV and 1.6 eV respectively for the rubrene:TTM-TPA and rubrene:TTM-3NCz systems as shown in Figure 6.16. We note that in both cases the CT state lies above the rubrene triplet state, and so this is not considered a new potential loss mechanism for triplet states.

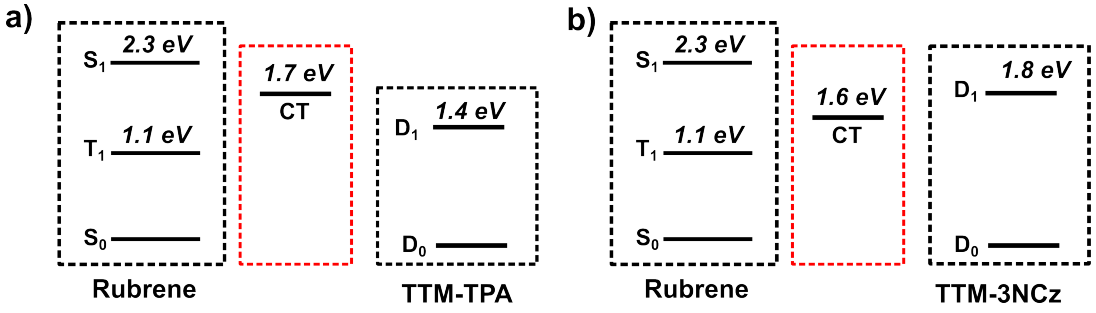

Figure 6.16: Schematic for rubrene:TTM-TPA and rubrene:TTM-3NCz films highlighting the energy of excitonic and charge-transfer (CT) states. Orbital and excitonic energy levels for rubrene were taken from literature.[176,180,182]

The rate of charge transfer between two states, k_{if} , where i and f are initial and final states respectively can be estimated using Marcus theory:

$$k_{if} = \frac{2\pi}{\hbar} J_{if}^2 \sqrt{\frac{1}{4\pi k_B T \lambda}} \exp\left(-\frac{E_a}{k_B T}\right) \tag{6.3}$$

with $E_a = \frac{\lambda}{4}\left[1 + \frac{\Delta G^0}{\lambda}\right]^2$, J_{if} as the electronic coupling between initial and final states, λ as the reorganisation energy for transfer, and ΔG^0 is the Gibbs free energy for electron transfer.[159,197] For similar electronic coupling between rubrene and radical states and $\lambda = 200$ meV, the rate of CT state formation would be expected to be 50 $\times$ greater for TTM-TPA than TTM-3NCz from the rubrene S_1 excited state. However, similar levels of photoluminescence quenching are observed on rubrene for both TTM-TPA and TTM-3NCz again pointing towards FRET being the dominant mechanism for quenching of rubrene singlet emission.

The lack of observed radical emission is therefore surprising considering we expect radicals to be excited by FRET and to have some direct photoexcitation when irradiated at 520 nm. Radicals have demonstrated bright emission previously in small molecular films, and so possible reasons for a lack of radical emission could result from the formation of charge-transfer states between the radical and rubrene, as well as Dexter doublet-triplet

energy transfer back to the rubrene triplet state.

Assuming that coulombic stabilisation of the CT state is below 100 meV, the rubrene:radical CT state is expected to lie above the D_1 excited state for TTM-TPA/PyBTM'-TPA but below the D_1 state in TTM-3NCz. A lack of radical emission from rubrene:TTM-TPA/PyBTM'-TPA films where the transition to a CT state is energetically unfavourable suggests doublet quenching taking place via energy transfer to the rubrene triplet state.

Rubrene and other acene systems possess low spin-orbit coupling, such that FRET from the radical D_1 to the rubrene T_1 state is expected to be negligible. Doublet-triplet energy transfer is therefore expected to be Dexter-mediated, with the paramagnetic spin of the radical enabling energy transfer with overall spin conservation. In rubrene films with low radical doping, it is expected that radical molecules will have rubrene as their nearest neighbouring molecules towards enabling Dexter energy transfer.

We note that radical quenching could additionally occur due to rubrene crystallisation forcing luminescent radicals into close proximity such that they undergo aggregation-induced quenching. Future studies should look to disperse rubrene:radical systems in polymers such as PMMA, allowing for control of average distances between rubrene and radical molecules towards understanding the role of phase segregation on emission.

Magnetosensitivity in systems is attributed to the spin evolution of weakly-coupled triplet pair states. Application of magnetic fields can change the rate that these weakly-coupled triplet pairs undergo spin evolution to be lost out of rapid cycle of singlet fission and triplet fusion. As FRET to radical species outcompetes spin evolution the number of triplet-pairs that undergo spin-evolution is reduced, such that overall magnetosensitivity of the system is reduced. Further generation of rubrene triplet states by radicals are expected to further decrease magnetosensitivity for emission through increasing the rate of non-geminate reformation of triplet-pairs.

6.8 Outlook for Radicals as Energy Harvesters in Upconversion Systems

We have shown that introduction of both triphenylamine- and carbazole-based radicals to rubrene films results in quenching of both the intensity and magnetosensitivity of rubrene photoluminescence. Quenching of rubrene is expected through FRET to the radicals, with further increases to energy transfer rates envisaged with better spectral overlap between rubrene and radical dopants. Whilst radicals do not themselves possess lower lying dark states, their ability to perform spin-conserving Dexter-mediated energy transfer back to rubrene triplet states results in a lack of radical emission and a parasitic loss mechanism for upconversion. Future systems may look to modulate the average distance between radicals and rubrene species towards enabling FRET and suppressing Dexter energy transfer through the use of intramolecular[198] or intermolecular[199] spacers. Towards a greater understanding of the mechanistic details of doublet-triplet energy transfer in films, we study the dynamics of doublet-triplet energy transfer in solution in the next chapter.

Chapter 7

On the Magnetosensitivity of Radical-Acene Systems with Reversible Triplet-Doublet Energy Transfer

Fluorescent radicals have been demonstrated as heavy-metal free triplet sensitisers for acene systems towards upconversion, showing doublet to triplet energy transfer in solution. In addition, radical-acene systems with low energetic offset between doublet and triplet states have been shown to undergo reversible doublet-triplet energy transfer. In this chapter, we investigate the magnetosensitivity for solution-based radical:acene systems demonstrating upconversion. Mechanistic studies are used to explore a lack of observed magnetosensitivity in radical:acene systems and the role of the CT state in mediating energy transfer, with results contextualised within the theoretical framework set out in Chapter 4. This chapter highlights how spin-conserving energy transfer between doublet and triplet excited states must be considered in the design of optoelectronic and spintronic systems, with rates of energy and charge-transfer engineered to achieve desired functionality.

trESR measurements on frozen TTM-1Cz:DPA solutions were performed by Dr Emrys Evans at Oxford University, whilst those on room-temperature solutions were performed by John Hudson in collaboration with Dr Emma Richards at Cardiff University. All subsequent analysis was performed by John Hudson.

7.1 Radicals as Triplet Sensitisers with Reversible Doublet-Triplet Energy Transfer

Fluorescent radicals have demonstrated doublet-triplet energy transfer in solution with acenes, acting as heavy-metal free triplet sensitisers towards TTA upconversion.[127,128] Triplet sensitisation has been demonstrated for systems with varying doublet-triplet energetic offsets (0.05 eV- 0.5 eV), with TTM-TPA:perylene demonstrating upconversion efficiencies of 6.8%. As shown in Figure 7.1, reverse triplet-doublet energy transfer has additionally been observed for systems with low triplet-doublet energetic offsets (< 0.1 eV) via delayed fluorescence.[128] As set out in Chapter 4, we envisage that reversible doublet-triplet energy transfer in systems could result in magnetic sensitivity for photoluminescence and spin polarisation.

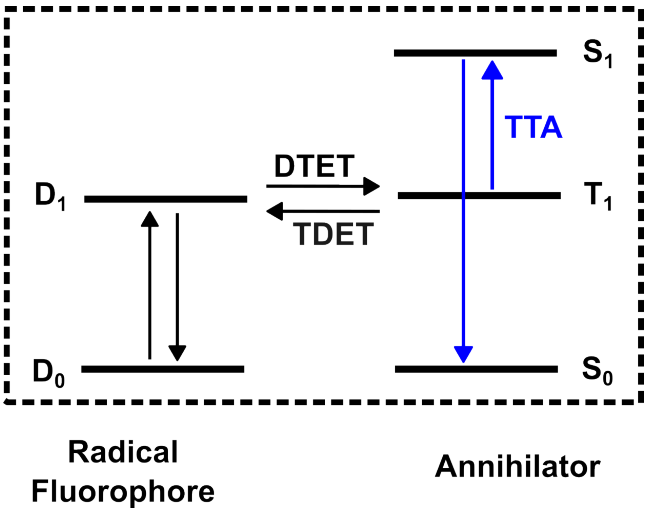

Figure 7.1: Schematic highlighting triplet sensitisation by photoexcited radical doublet states for annihilator molecules, indicating reversible doublet-triplet energy transfer (DTET) and triplet-doublet energy transfer (TDET). Sensitised annihilator triplet states are able to undergo triplet-triplet annihilation (TTA) to form the higher energy S_1 excited state.

Motivated by our observation of photoluminescence quenching for a variety of upconversion systems by fluorescent radicals in the solid-state, we explore the magnetosensitivity of doublet-triplet energy transfer systems in solution. FRET-mediated doublet-triplet energy transfer is assumed to be negligible due to the low optical transition dipole for triplet states in typical acene systems, such that photophysical and spin-resonance measurements allow us to probe the exchange mediated interactions of systems.

7.2 TTM-1Cz:DPA and TTM-1Cz:BPEA as Triplet Sensitisation Systems

Here we combine TTM-1Cz with 9,10-diphenylanthracene (DPA) or BPEA in toluene solution. The molecular structures and frontier molecular orbital energies for TTM-1Cz, DPA and BPEA are shown in Figure 7.2a, with DPA and BPEA forming a type-I heterojunction with TTM-1Cz.

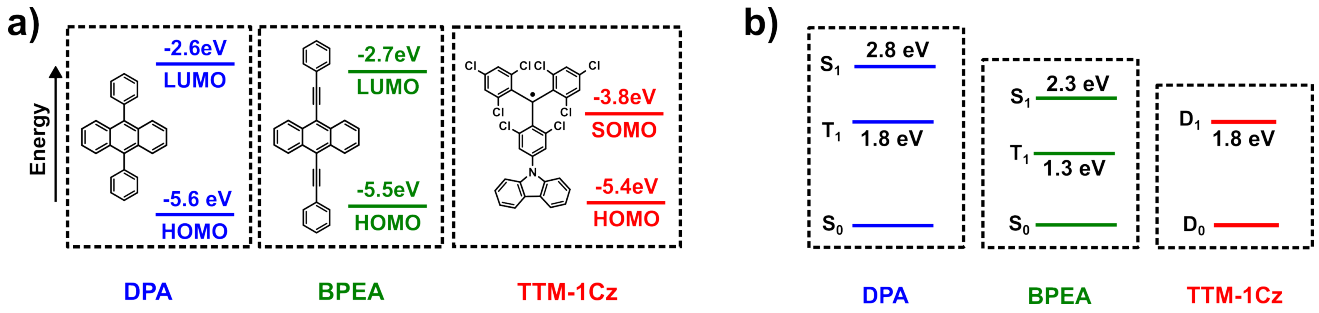

Figure 7.2: a) Molecular structures and frontier molecular orbital energies for DPA, BPEA, and TTM-1Cz. b) Jablonski diagram highlighting excitonic energies for DPA, BPEA and TTM-1Cz. Excitonic and orbital energies for DPA and BPEA were estimated from literature.[188,189,193,194,200,201]

Based off the anthracene moiety, both DPA and BPA have T_1 and S_1 energies suitable for TTA and have shown anti-Stokes shifts of 0.92 eV and 0.58 eV respectively using TTM-1Cz as a triplet sensitiser.[127,128] As shown in Figure 7.2b, the energy difference between doublet and triplet states in TTM-1Cz:DPA ($\sim$ 0.05 eV)[128] and TTM-1Cz:BPEA ($\sim$ 0.5 eV) allow us to probe the mechanistic differences for doublet-triplet energy transfer with varying energetic offset.

7.3 Sample Preparation

DPA was obtained from Merck. TTM-1Cz, DPA and BPEA were dissolved in anhydrous toluene to form stock solutions. Stock solutions were subsequently combined to form solutions with a 200 µM concentration of TTM-1Cz and 5-10 mM concentrations of BPEA or DPA. All sample preparation was carried out under nitrogen atmosphere ($<$ 10 ppm O_2, $<$ 0.5 ppm H_2O) before being transferred to UV-grade quartz cuvettes that were parafilmed to prevent ingression of oxygen.

7.4 Steady State Photophysics

Figure 7.3 shows the steady-state absorption and photoluminescence for TTM-1Cz, DPA and BPEA in toluene solution. The lowest energy absorption bands for TTM-1Cz, DPA and BPEA are observed to start at 700 nm, 420 nm and 490 nm respectively.

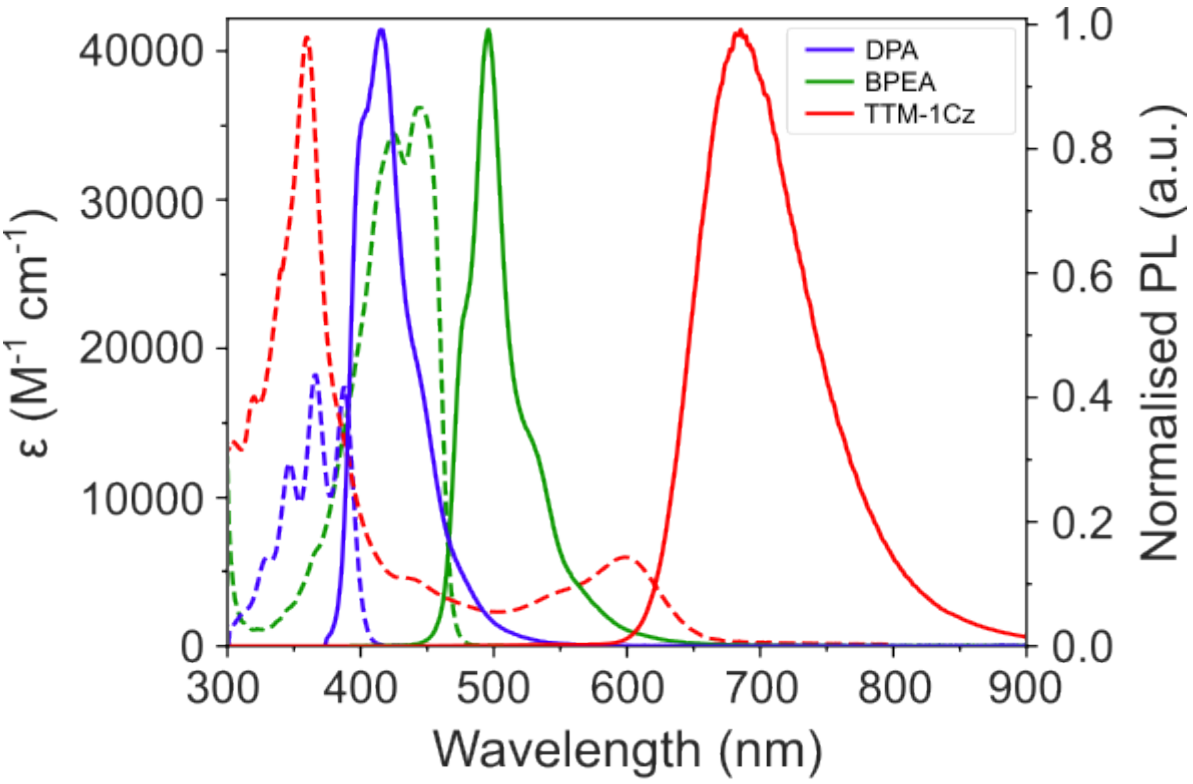

Figure 7.3: Extinction coefficient (dashed lines) and normalised photoluminescence (solid lines) profiles for TTM-1Cz (red), DPA (blue) and BPEA (green) in toluene solution.

DPA shows blue photoluminescence peaking at 430 nm with vibronic features at 415 nm and 440 nm, whilst BPEA shows green emission peaking at 510 nm with vibronic features at 495 nm and 545 nm, as expected.[202,203] TTM-1Cz in toluene shows broad red emission centred at 700 nm as expected.[48]

7.4.1 Demonstrating Upconversion

Figure 7.4a shows photoluminescence spectra for a TTM-1Cz (200 μM):DPA (10 mM) solution excited at 520 nm. At 520 nm, irradiation is expected to selectively photoexcite TTM-1Cz, however, both TTM-1Cz and higher-energy DPA emission are observed. Towards confirming that DPA emission results from TTA, the intensity of radical and annihilator emission under variable fluence (50-1000 mW cm^{-2}) are shown in Figure 7.4b.

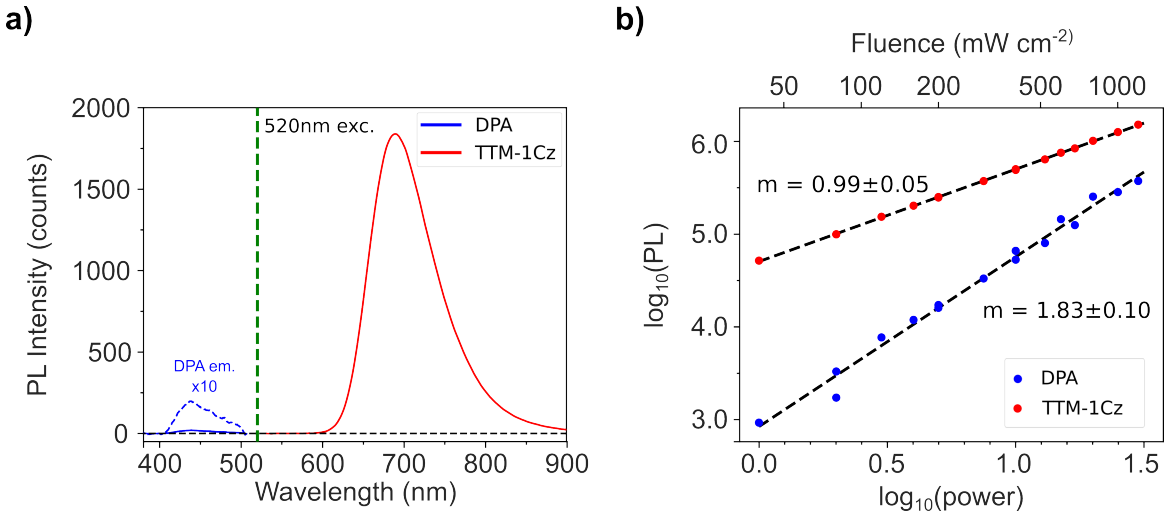

Figure 7.4: a) Steady-state photoluminescence spectra of the TTM-1Cz (200 μM):DPA(5 mM) system in toluene for $\lambda_{ex} = 520$ nm (fluence = 800 mW cm^{-2}). b) Photoluminescence intensity for TTM-1Cz emission (650-850 nm, red) and DPA upconversion (400-500 nm, blue) in the TTM-1Cz (200 μM):DPA(5 mM) toluene system versus the fluence of 520 nm excitation.

On a double-logarithmic plot of power versus photoluminescence, a gradient of 1 indicates that TTM-1Cz emission has a linear dependence on excitation fluence. A gradient of ~2 for DPA indicates that annihilator emission depends quadratically on fluence which is a charactersitic feature of TTA. In upconversion systems, a threshold intensity is typically defined at which the power dependence of upconverted emission transitions from a quadratic to a linear dependence. This results from higher triplet populations increasing the chance of triplet annihilation, such that a majority of triplets start decaying via upconverted singlet states.[204,205] Whilst previous reports highlight this threshold intensity for the TTM-1Cz:DPA systems in toluene to lie in the range of 180-200 mW cm^{-2}, we were unable to replicate this in our setup with a quadratic dependence on emission maintained up to fluences of 1000 mW cm^{-2} . We attribute this to solutions being prepared in a nitrogen glovebox with an O_2 concentration of < 10 ppm, compared to $< 10^{-2}$ ppm levels typically expected for solutions that have undergone three or more cycles of freeze-pump-thawing. For steady-state measurements, singlet-oxygen is expected to interact with sensitised triplet states resulting in quenching with μs timescales.

7.4.2 Magnetically-Sensitive PL

The magnetosensitivity of systems was measured using the updated protocol set out in Section 3.5. In brief, simultaneous control of magnetic field and spectrometer allowed for the measurement of photoluminescence at an explicit field value, followed by a reference spectrum at zero field to calculate an MFE value.

Towards confirmation of the updated protocol for measuring magnetosensitive PL, the updated protocol was applied to a rubrene film (fabricated as described in Section 6.3) excited at 520 nm. As shown in Figure 7.5a, the updated protocol enabled greater discrimination between applied field strengths, enabling observation of a drop in photoluminescence for fields below 30 mT before a subsequent increase in the brightness of emission. This magnetic behaviour has previously been documented and attributed to spin evolution resulting from triplet hopping in systems with varied rubrene orientation.[187]

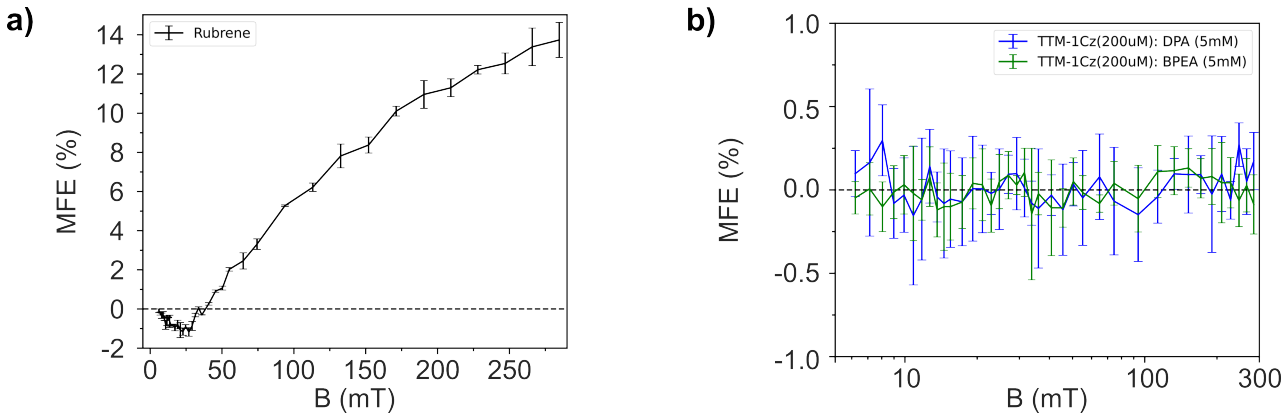

Figure 7.5: Photoluminescence MFE versus magnetic field using the updated magnetoPL setup for a) rubrene films and b) TTM-1Cz (200 μM):DPA (10 mM) and TTM-1Cz (200 μM):BPEA (5 mM) toluene solutions under CW excitation (λ_{ex} = 520 nm, fluence = 40 mW cm^{-2}).

Figure 7.5b shows magnetically-sensitive measurements of TTM-1Cz photoluminescence for the TTM-1Cz:DPA and TTM-1Cz:BPEA systems under 520 nm excitation (fluence = 40 mW cm^{-2}). Excitation was purposely kept below the threshold intensity for upconversion, towards interrogating the magnetic sensitivity of doublet-triplet energy transfer and not triplet-triplet annihilation.

We are unable to detect any magnetosensitivity of doublet photoluminescence in the TTM-1Cz:DPA and TTM-1Cz:BPEA systems within a 0.3% degree of error between 0-300 mT. Towards understanding the mechanisms of doublet-triplet energy transfer that could underpin this low magnetosensitivity, the rest of this chapter outlines transient photoluminescence, electron spin resonance and absorption characterisation of TTM-1Cz, TTM-1Cz:BPEA and TTM-1Cz:DPA systems.

7.5 Investigating the Mechanisms of Doublet-Triplet Energy Transfer through Transient Characterisation

7.5.1 Transient Photoluminescence

Figure 7.6 shows the transient decay of TTM-1Cz photoluminescence (670-690 nm) for solutions of TTM-1Cz (200 μM), TTM-1Cz (200 μM):DPA (10 mM) and TTM-1Cz (200 μM):BPEA (5 mM) in toluene.

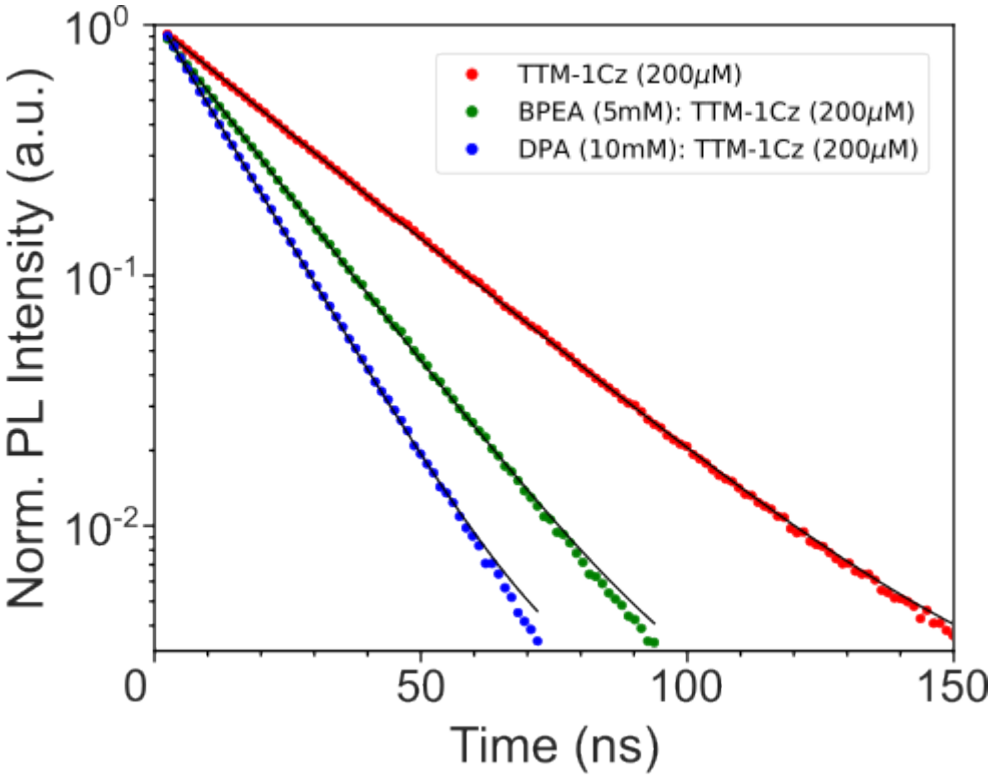

Figure 7.6: Transient photoluminescence of TTM-1Cz (λ_{em}=680 nm) emission under excitation at 635 nm. Decays are shown for solutions in toluene of TTM-1Cz (200 μM) in red, TTM-1Cz (200 μM):BPEA (5 mM) in green and TTM-1Cz (200 μM):DPA (5 mM) in blue.

TTM-1Cz emission is quenched by annihilators in solution. Table 7.1 shows initial lifetimes for emission, from which quenching rates can be estimated for BPEA (5 mM) and DPA (10 mM) of 4.3×10^7 s^{-1} and 2.3×10^7 s^{-1} respectively.

Sample	PL Lifetime (ns)
TTM-1Cz (200 μM)	25.3 ± 0.3
TTM-1Cz (200 μM):BPEA (5 mM)	16.1 ± 0.3
TTM-1Cz (200 μM):DPA (10 mM)	12.2 ± 0.3

Table 7.1: PL Lifetimes for TTM-1Cz emission (λ_{em}=670-690 nm) in TTM-1Cz:DPA/BPEA solutions. Lifetimes were obtained through fitting of PL transients to a monoexponential decay.

Assuming that the rate of quenching is proportional to the annihilator concentration, estimates of quenching constants in toluene of 4.3×10^9 $M^{-1}s^{-1}$ and 4.8×10^9 $M^{-1}s^{-1}$ for DPA and BPEA respectively agree with previous studies.[127,128]

7.5.2 Transient Electron Spin Resonance (trESR)

Figure 7.7 shows X-band transient ESR spectra for flash-frozen toluene solutions of TTM-1Cz (400 μM), DPA (20 mM) and TTM-1Cz (400 μM):DPA (20 mM) measured at 80 K. As set out in Section 3.6, samples were photoexcited using pulsed laser excitation at 20 Hz (5 ns pulse length) and changes in the absorption of microwave radiation were measured towards detecting changes in the distribution of spins in samples.

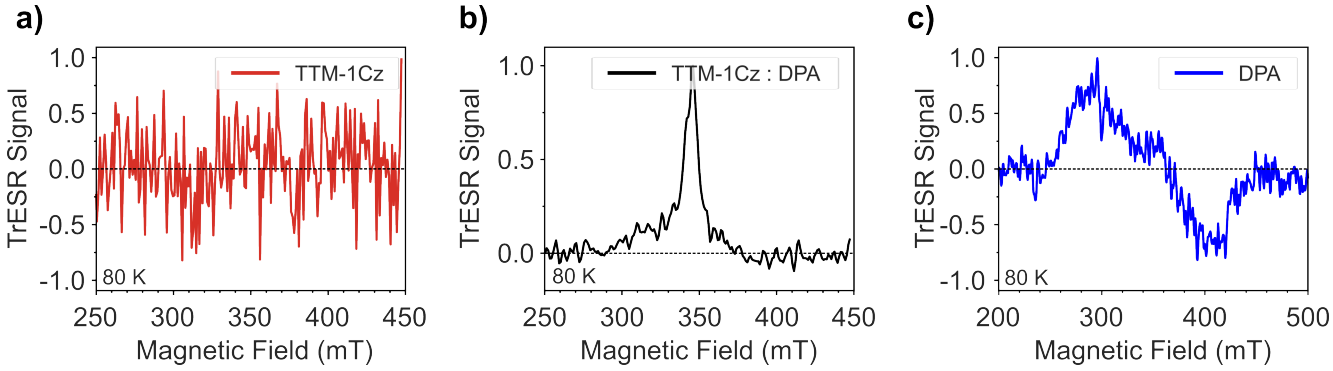

Figure 7.7: trESR signals measured at 80 K for flash-frozen toluene solutions of a) TTM-1Cz (400 μM) and b) TTM-1Cz (400 μM):DPA (20 mM) excited at 600 nm, as well as c) DPA (20 mM) excited at 355 nm. Displayed trESR signals are integrated from 1-2 μs following photoexcitation.

The trESR spectra for both TTM-1Cz and TTM-1Cz:DPA were measured following 600 nm excitation. Whilst isolated TTM-1Cz showed no detectable spin polarisation (Figure 7.7a), the trESR signal for TTM-1Cz:DPA displays both an absorptive central peak (full-width half maximum, FWHM = 10 mT) as well as a wider asymmetrical signal with absorptive (a) and emissive (e) phase. DPA solutions excited at 355 nm show a

trESR signal with aaa-eee phase that is indicative of ISC from singlet states resulting in preferential population of triplet sublevels.[206,207]

We observe that trESR signals are narrower in frozen solutions of TTM-1Cz:DPA (∼120 mT, Figure 7.7b) than in DPA (∼160 mT, Figure 7.7c). The width of the trESR signals arise from triplet zero-field splitting that manifests as 2/3 of the chromophore (DPA) triplet in chromophore-radical systems.[112] One fit model to the data follows net and multiplet polarisation similar to quartet signatures reported for chromophore-trityl radicals.[208] Further analysis of the mechanisms of interaction between doublet and triplet states is currently limited by low levels of signal enabling trESR data to be fit with a variety of spin-polarised species. Future work will look to obtain trESR signals for systems such that turning points can be identified towards assignment of underlying mechanisms for interaction.

Figure 7.8 shows trESR signals for toluene solutions of TTM-1Cz (200 μM) combined with DPA (5 mM) and BPEA (5 mM) that were collected at room temperature (298 K).

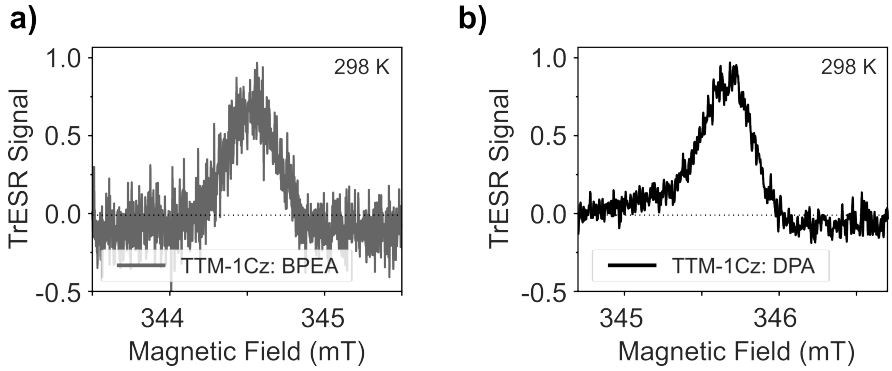

Figure 7.8: Narrow-field width trESR signals collected at 298K for toluene solutions of a) TTM-1Cz (200 μM):DPA (5 mM) and b) TTM-1Cz (200 μM):BPEA (5 mM) with λ_{ex} = 532 nm. Displayed trESR signals are integrated from 1-2 μs following photoexcitation.

At room temperature, the previously observed broad central peak is replaced by a narrow absorptive feature (FWHM = 0.3 mT). We assign this narrow feature to spin-polarisation of the doublet ground state, with the trESR signal observed on the microsecond timescales such that all excited doublet states have decayed. In TTM-1Cz:DPA we observe an additional asymmetrical trESR signal around the doublet spin polarisation, however, we are not able to observe enough structure of the signal to assign mechanisms for formation of spin polarisation.

7.5.3 Femtosecond Transient Absorption (fsTA)

Figure 7.9 shows fsTA data taken for TTM-1Cz (200 μM), TTM-1Cz (200 μM):DPA (5 mM) and TTM-1Cz (200 μM):BPEA (5 mM) solutions that were collected using the experimental setup outlined in Section 3.4.2. Solutions were excited at 2.5 kHz such that system were given 400 μs to relax to the ground state in between photoexcitation pulses.

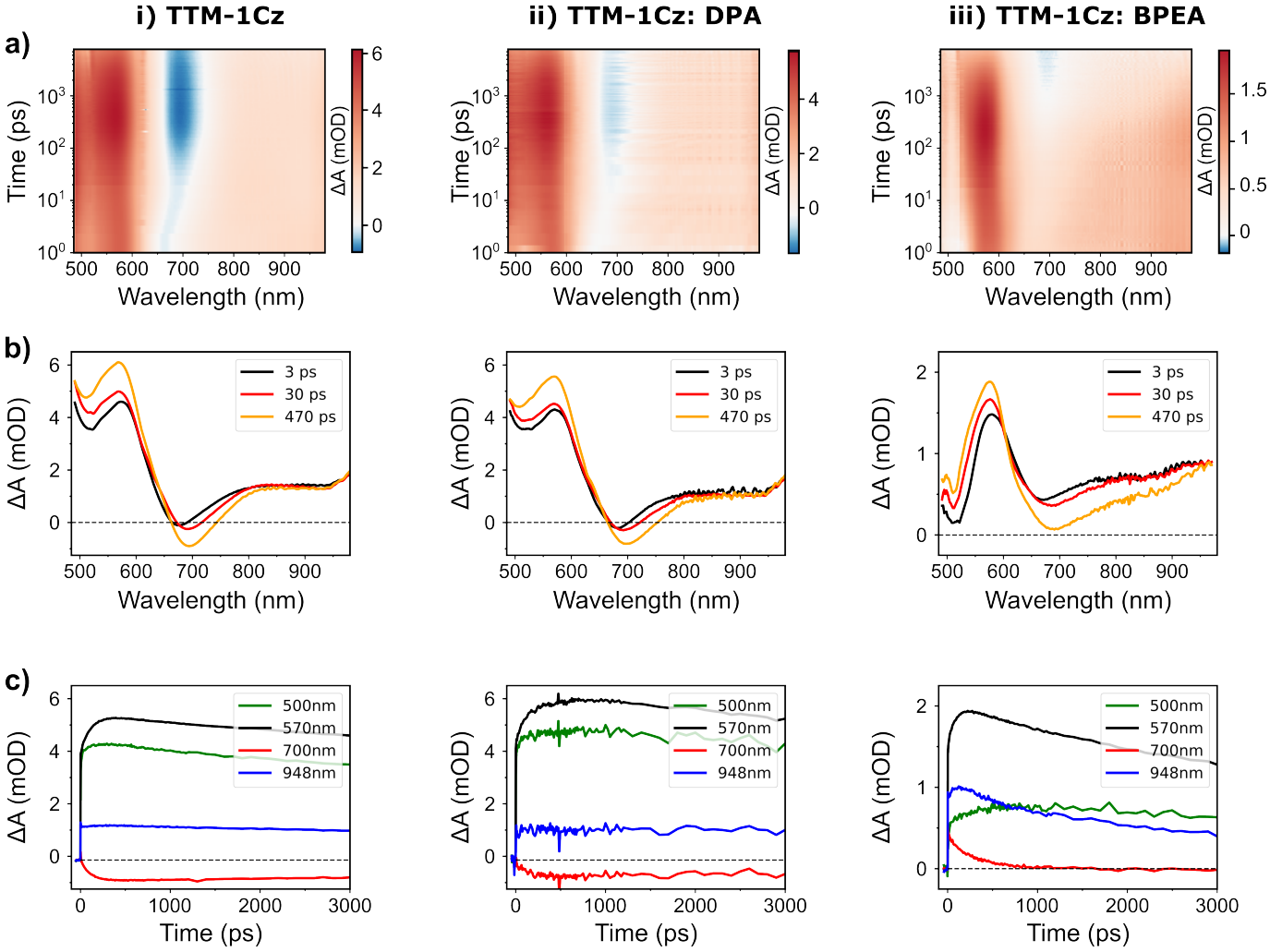

Figure 7.9: a) False-colour maps, b) transient absorption spectra and c) wavelength-resolved excited state kinetics for fsTA measurements on toluene solutions of i) TTM-1Cz (200 μM) and ii) TTM-1Cz (200 μM):DPA (5 mM) excited at 635 nm, and iii) TTM-1Cz (200 μM):BPEA (5 mM) excited at 530 nm.

fsTA measurements for TTM-1Cz in toluene show a strong photoinduced absorption that peaks around 570 nm and has a broad flat absorption between 800-950 nm. We additionally observe broad stimulated emission that is centered at 660 nm following photoexcitation that undergoes vibrational relaxation over a period of 30 ps to be centered at 700 nm. The amplitude of excited state absorption (ESA) at 570 nm and stimulated

emission (SE) at 700 nm are seen to grow in with a lifetime of 90 ± 6ps, before subsequently decaying with a lifetime of 20 ± 5 ns. The growth of absorption is attributed to molecular reorganisation that increases the electric dipole of the TTM-1Cz D_1 excited state, whilst lifetime for the decay of the D_1 excited state of 20 ± 5 ns is in agreement previous trPL measurements.

fsTA data for TTM-1Cz (200 μM):DPA (5 mM) solutions closely resembles that seen for TTM-1Cz, showing an ESA peaking at 570 nm with broad absorption between 800-950 nm, as well as red-shifting of SE over a period of 30 ps. Whilst it is difficult to accurately quantify the lifetime of the doublet excited state over a temporal window of 8 ns, the excited state absorption appears to be quenched by DPA with fitting of the 570 nm ESA giving with a new lifetime of 17 ± 5 ns. The excited state absorption at 570 nm increases up to 900 ps in TTM-1Cz:DPA solutions, in comparison to TTM-1Cz only solutions where absorption began to decay after 400 ps. This variation could indicate the formation of a new excited state with broad absorption below 600 nm on 100s of picosecond timescales, however further deconvolution of excited-state signatures is hampered through the lack of clear new ESA in the visible range. DPA has previously been reported to show strong T_1 ESA between 460-480 nm, such that future experiments should look to measure fsTA for films with probe light in the UV range (380-500nm) towards deconvoluting D_1 and T_1 ESAs.

fsTA of TTM-1Cz (200 μM):BPEA (5 mM) solutions shows the formation of a new excited-state species on sub-picosecond timescales with a ground-state bleach from 480-530 nm and a broad absorption from 650-950 nm, which is attributed to the TTM-1Cz:BPEA charge-transfer (CT) state. ESA due to the D_1 excited state is still observed suggesting that not all radicals perform charge-transfer on such timescales. On energetic grounds, the CT state is expected to result from hole transfer from the radical to the BPEA such that the CT state signatures arises from the combination of a BPEA cationic and radical anionic signatures. Previous literature has shown the BPEA cation to have a broad absorption signature stretching up to 850 nm[191] such that we attribute the increase in absorption from 850-950 nm to TTM-1Cz anion. Subsequent decay of this intermediate is accompanied with the growth of ESA at 500 nm that is characeristic of the BPEA T_1 excited state,[191] such that we suggest the CT state can mediate doublet-triplet energy transfer for TTM-1Cz:BPEA systems. Towards estimating the rate of triplet formation from the CT state, fsTA kinetics at 500 nm and 948 nm were fitted assuming an underlying D_1 population that grew and subsequently decayed with fixed lifetimes of 30 ps and 12 ns respectively. A third kinetic was fitted above the D_1 population to account for transition of the CT excited state to the BPEA T_1 excited state giving a transition lifetime of ∼1 ns.

7.6 Discussion

The observed dynamics for T_1 exciton formation in both TTM-1Cz:DPA and TTM-1Cz:BPEA solutions are an order of magnitude faster than expected for diffusion-limited bimolecular processes. Using quenching constants obtained from trPL of 4.3×10^9 $M^{-1}s^{-1}$ and 4.8×10^9 $M^{-1}s^{-1}$ for DPA and BPEA in toluene, 5 mM solutions are expected to quench doublet excited states with lifetimes of 47 and 42 ns respectively. However, sub-picosecond lifetimes for CT state formation in TTM-1Cz:BPEA and sub-nanosecond lifetimes for energy transfer for TTM-1Cz:DPA systems suggest that charge or energy transfer can occur without the need for diffusion. We attribute these lifetimes to complexation of radical and annihilator species in solutions such that they are in position following photoexcitation for charge or energy transfer. We note that fsTA dynamics were measured for annihilator solutions close to their solubility limit in toluene (5 mM), increasing the likelihood for complexation. Future studies should investigate fsTA dynamics of doublet-triplet energy transfer for both dilute and concentrated annihilator solutions, towards understanding the role of complexation on energy and charge-transfer dynamics.

Figure 7.10 shows the excitonic and CT state energies expected for the TTM-1Cz:DPA and TTM-1Cz:BPEA systems. The TTM-1Cz:BPEA CT state at 1.5 eV lies between the TTM-1Cz D_1 and BPEA T_1 excited states, with fsTA data highlighting that the CT state is an intermediate in complexed TTM-1Cz:BPEA systems for doublet-triplet energy transfer. In TTM-1Cz:DPA systems we do not observe significant formation of cationic anthracene signatures, suggesting that energy transfer occurs directly from the TTM-1Cz D_1 to the DPA T_1 excited state. The CT state for TTM-1Cz:DPA is predicted to lie below both the TTM-1Cz D_1 and DPA T_1 excited states, such that future studies should look into the possibility of CT state formation as both a loss mechanism for up-conversion and as a possible mediator of energy transfer between doublet and triplet states.

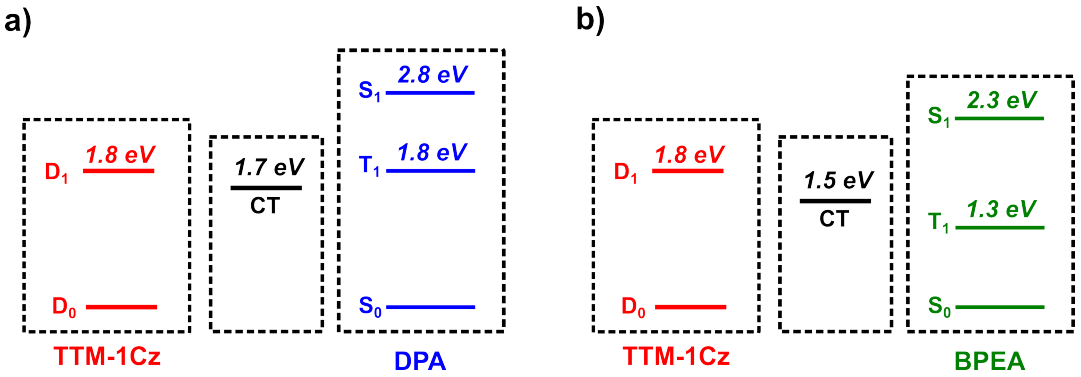

Figure 7.10: Schematic highlighting the energy of excitonic and charge-transfer (CT) states for TTM-1Cz:DPA and TTM-1Cz:BPEA. Excitonic energies for DPA and BPEA were estimated from literature.[193,194,201]

We were unable to detect magnetosensitivity for radical emission in either TTM-1Cz (200 μM):DPA (5 mM) or TTM-1Cz (200 μM):BPEA (5 mM) solutions. In Chapter 4 we discuss the need for doublet-triplet and triplet-doublet energy transfer rates to be competitive with radical emission towards achieving observable magnetosensitivity in radical-triplet systems. TTM-1Cz:BPEA systems have a large energetic offset between TTM-1Cz D_1 and BPEA T_1 states, such that a lack of magnetosensitivity can be attributed to negligible rates for reverse triplet-doublet energy transfer.

In TTM-1Cz:DPA systems, we were unable to identify reversible energy transfer between doublet and triplet species through fsTA or trPL measurements. However, previous reports have identified reverse energy transfer from DPA to TTM-1Cz with 50 μs lifetime.[128] Using the modelling set out in Chapter 4, we can estimate the magnetosensitivity of PL for TTM-1Cz:DPA systems interacting in solution using a doublet emitter with a 20 ns excited state lifetime, a 40 ns lifetime for doublet-triplet energy transfer (obtained from TCSPC) and a 50 μs lifetime for reverse TDET. For both weakly- or strongly-coupled systems, we obtain a maximum $|MFE| < 0.01\%$ which is below the 0.3% resolution for our current magnetic field dependent PL setup.

Future studies should look to decrease the doublet-triplet energy gap towards increasing the rate of reverse energy transfer to nanosecond timescales in solution,[209] with $|MFE| = 1\%$ predicted for the previous system if the rate of triplet-doublet energy transfer could match that of doublet-triplet energy transfer (40 ns lifetime). In the future, spatial control of doublet and triplet components in intramolecular or intermolecular systems may allow energy transfer rates to no longer be diffusion-limited.

Further work is required towards understanding the role of complexation in films, and reconciling sub-picosecond dynamics observed in fsTA with nanosecond timescales ob-

served for trPL. We envisage that faster rates for reversible energy transfer in complexes of TTM-1Cz and DPA may enable greater magnetosensitivity, however, further concentration studies are required towards understanding the fraction of TTM-1Cz molecules that undergo complexation in DPA solution and their effect on overall system dynamics. These studies should include both CW and trESR measurements towards understanding the interaction of doublet and triplet species in solution and whether they can be explained by doublet-triplet exchange that is variable or fixed. This should build on our current understanding for which we see quartet spin polarisation in TTM-1Cz:DPA frozen solutions but doublet ground spin polarisation at room temperature that is indicative of a radical-triplet pair mechanism resulting from diffusion of radical and triplet species.[14]

7.7 Outlook for Radicals as Triplet Sensitisers

In this chapter we probed the mechanisms for doublet-triplet energy transfer both in solutions of TTM-1Cz (200 μM):DPA (5 mM) and TTM-1Cz (200 μM):BPEA (5 mM). Our studies motivate future research towards understanding of the role that both the radical-acene CT state plays in mediating triplet-doublet energy transfer and that radical-acene complexation plays in solutions. Observation of excited state dynamics on picosecond to nanosecond timescales for radical:acene solutions is exciting towards future use of radicals as triplet-sensitisers in the solid state, and highlights the challenges faced towards using radicals as energy harvesters following upconversion as set out in the previous chapter.

Chapter 8

Conclusions and Outlook

In this thesis, research into luminescent radicals was motivated towards their application in optoelectronic and opto-spintronic devices. The emergent photo- and spin physics from the pairing of luminescent radicals with closed-shell organic molecules was investigated, in particular focussing on the role of spin in energy transfer between doublet and triplet states as well as doublet-triplet magnetic interactions.

A framework for the generation of spin polarisation and magnetosensitivity of radical photoluminescence following reversible doublet-triplet energy transfer was set out. The wider context of this work is establishing a platform for magneto-optical signatures that provide further evidence for the doublet exciton nature of luminescent radicals. Light read-out and spin polarisation following reversible energy transfer were shown to reflect the sign and size of spin-exchange interactions in strongly coupled doublet-triplet pairs. Immediate onset of magnetic field effects at low fields were demonstrated following reversible energy transfer in weakly-coupled doublet-triplet systems, with potential application as a light-based magnetic compass sensor.

The combination of triplets in organometallic complexes with luminescent radicals was explored, demonstrating Förster-mediated energy transfer from FIr6 to the TTM-1Cz radical without the need for triplet diffusion. Nanosecond-lifetimes for energy transfer ($k = 3.1 \times 10^7$ s^{-1}) from FIr6 to TTM-1Cz are such that triplet states efficiently transfer (85 $\pm$ 25 %) their energy to doublet states. The role of triplet spin-orbit coupling was discussed both towards the design of radicals as efficient energy harvesters in 'colour-by-blue' displays, and towards the optical generation of spin polarisation in radical opto-spintronics.

The interaction of radical doublet-states with acene-based chromophores was detailed in both solid-state and solution-based studies. Quenching of both the intensity and magnetosensitivity of rubrene emission in rubrene:radical films is attributed to FRET from the rubrene singlet to the radical doublet excited state, whilst Dexter-mediated

doublet-triplet energy transfer is observed to quench doublet emission. Solution-based studies of TTM-1Cz with the annihilators DPA and BPEA demonstrate a lack of magnetosensitivity for radical emission ($< 0.3\%$) for magnetic fields up to 300 mT. Increasing the rate of reverse triplet-doublet energy transfer is identified in the TTM-1Cz:DPA system towards increased magnetosensitivity of emission. Finally, the role of the CT state in mediating doublet-triplet energy transfer and complexation in radical-acene systems was explored towards using radicals as triplet sensitisers for upconversion.

Overall, this thesis tries to inform the design of radical-containing functional materials with a particular focus on how the paramagnetic nature of luminescent radicals results in different optical and magnetic behaviour to closed-shell systems. For example, whilst bright doublet states can interact through FRET similar to singlet states in closed-shell fluorophores, we show that the 'extra-spin' of the radical also allows spin-conserving Dexter-energy transfer between triplet and doublet states not available to singlet states.

With a growing number of researchers looking towards the synthesis of luminescent radical species, it is hoped that radical motifs beyond the TTM-moiety can be achieved towards both higher energy emission (green/blue), as well as raising of radical HOMO/SOMO levels towards forming type-I heterojunctions with a greater number of studied optoelectronic systems. In the context of radical-chromophore design towards opto-spintronic devices, systems will need sufficient exchange interaction towards driving Dexter-mediated processes between species, however care will need to be placed such that exchange interactions are not so strong that magnetic interactions cannot be probed with experimentally-accessible magnetic fields ($|\boldsymbol{B}| < 10$ T).

Through appreciation of mechanisms for energy transfer and their spin implications, it is hoped that the work in this thesis contributes towards the eventual goal of controlling the spin states of molecular systems with light.

Publication List

1. **J. M. Hudson**, T. J. H. Hele, E. W. Evans, "Efficient light-emitting diodes from organic radicals with doublet emission", *Journal of Applied Physics*, 129 (18), (2021), 180901

2. **J. M. Hudson**, Evans, E.W., "Radical Spin Polarization and Magnetosensitivity from Reversible Energy Transfer", *Journal of Physical Chemistry Letters*, 15, 15, (2024), 4130-4135

3. **J. M. Hudson**, E. W. Evans, (*In preparation*) "Dipole mediated triplet-to-doublet energy transfer in phosphor-radical systems"

Bibliography

[1] J. M. Hudson, T. J. H. Hele, and E. W. Evans. "Efficient light-emitting diodes from organic radicals with doublet emission". *Journal of Applied Physics,* 129.18 (2021), p. 180901.

[2] J. Clayden, N. Greeves, and S. Warren. *Organic Chemistry - Second Edition*. Oxford University Press, 2012.

[3] W. Barford. *Electronic and Optical Properties of Conjugated Polymers*. Oxford University Press, 2013.

[4] A. Kohler and H. Bassler. *Electronic Processes in Organic Semiconductors: An Introduction*. John Wiley & Sons, 2015.

[5] P. Atkins and R. Friedman. *Molecular Quantum Mechanics - Fifth Edition*. Oxford University Press, 2010.

[6] P. Atkins and R. Friedman. *Modern Molecular Photochemistry*. University Science Books, 1991.

[7] T. Forster. "Energiewanderung und Fluoreszenz". *Naturwissenschaften,* 33.6 (1946), pp. 166–175.

[8] B. R. Masters. "Paths to Förster's resonance energy transfer (FRET) theory". *The European Physical Journal H,* 39.1 (2014), pp. 87–139.

[9] D. Beljonne, C. Curutchet, G. D. Scholes, and R. J. Silbey. "Beyond Förster Resonance Energy Transfer in Biological and Nanoscale Systems". *The Journal of Physical Chemistry B,* 113.19 (2009), pp. 6583–6599.

[10] G. D. Scholes. "Long-Range Resonance Energy Transfer in Molecular Systems". *Annual Review of Physical Chemistry,* 54.1 (2003), pp. 57–87.

[11] D. L. Dexter. "A theory of sensitized luminescence in solids". *The Journal of Chemical Physics,* 21.5 (1953), pp. 836–850.

[12] F. Laquai, Y.-S. Park, J.-J. Kim, and T. Basche. "Excitation Energy Transfer in Organic Materials: From Fundamentals to Optoelectronic Devices". *Macromolecular Rapid Communications,* 30.14 (2009), pp. 1203–1231.

[13] J. Weil and J. Bolton. *Basic Principles of Paramagnetic Resonance*. John Wiley & Sons, Ltd, 2006.

[14] H. Hayashi. *Introduction to Dynamic Spin Chemistry*. WORLD SCIENTIFIC, 2004.

[15] N. M. Atherton. *Principles of electron spin resonance*. Ellis Horwood : PTR Prentice Hall, 1993.

[16] C. E. Tait, P. Neuhaus, H. L. Anderson, and C. R. Timmel. "Triplet State Delocalization in a Conjugated Porphyrin Dimer Probed by Transient Electron Paramagnetic Resonance Techniques". *Journal of the American Chemical Society,* 137.20 (2015), pp. 6670–6679.

[17] S. X. Jin, J. Li, J. Z. Li, J. Y. Lin, and H. X. Jiang. "GaN microdisk light emitting diodes". *Applied Physics Letters,* 76.5 (2000), pp. 631–633.

[18] H. X. Jiang and J. Y. Lin. "Nitride micro-LEDs and beyond - a decade progress review". *Optics Express,* 21.S3 (2013), A475–A484.

[19] M. A. Baldo, D. F. O'Brien, Y. You, A. Shoustikov, S. Sibley, M. E. Thompson, and S. R. Forrest. "Highly efficient phosphorescent emission from organic electroluminescent devices". *Nature,* 395.6698 (1998), pp. 151–154.

[20] C. Adachi, M. A. Baldo, M. E. Thompson, and S. R. Forrest. "Nearly 100% internal phosphorescence efficiency in an organic light-emitting device". *Journal of Applied Physics,* 90.10 (2001), pp. 5048–5051.

[21] H. Uoyama, K. Goushi, K. Shizu, H. Nomura, and C. Adachi. "Highly efficient organic light-emitting diodes from delayed fluorescence". *Nature,* 492.7428 (2012), pp. 234–238.

[22] M. Y. Wong and E. Zysman-Colman. "Purely organic thermally activated delayed fluorescence materials for organic light-emitting diodes". *Advanced Materials,* 29.22 (2017), p. 1605444.

[23] D. Di, A. S. Romanov, L. Yang, J. M. Richter, J. P. H. Rivett, S. Jones, T. H. Thomas, M. A. Jalebi, R. H. Friend, M. Linnolahti, M. Bochmann, and D. Credgington. "High-performance light-emitting diodes based on carbene-metal-amides". *Science,* 356.6334 (2017), pp. 159–163.

[24] A. Endo, K. Sato, K. Yoshimura, T. Kai, A. Kawada, H. Miyazaki, and C. Adachi. "Efficient up-conversion of triplet excitons into a singlet state and its application for organic light emitting diodes". *Applied Physics Letters,* 98.8 (2011), p. 083302.

[25] L.-S. Cui, A. J. Gillett, S.-F. Zhang, H. Ye, Y. Liu, X.-K. Chen, Z.-S. Lin, E. W. Evans, W. K. Myers, T. K. Ronson, H. Nakanotani, S. Reineke, J.-L. Bredas, C. Adachi, and R. H. Friend. "Fast spin-flip enables efficient and stable organic electroluminescence from charge-transfer states". *Nature Photonics,* 14.10 (2020), pp. 636–642.

[26] B. H. Wallikewitz, D. Kabra, S. Gelinas, and R. H. Friend. "Triplet dynamics in fluorescent polymer light-emitting diodes". *Physical Review B,* 85.4 (2012), p. 045209.

[27] D. Y. Kondakov. "Characterization of triplet-triplet annihilation in organic light-emitting diodes based on anthracene derivatives". *Journal of Applied Physics,* 102.11 (2007), p. 114504.

[28] C. Zhao and L. Duan. "Review on photo- and electrical aging mechanisms for neutral excitons and ions in organic light-emitting diodes". *Journal of Materials Chemistry C,* 8.3 (2020), pp. 803–820.

[29] C. Murawski, K. Leo, and M. C. Gather. "Efficiency roll-off in organic light-emitting diodes". *Advanced Materials,* 25.47 (2014), pp. 6801–6827.

[30] Q. Peng, A. Obolda, M. Zhang, and F. Li. "Organic light-emitting diodes using a neutral π radical as emitter: The emission from a doublet". *Angewandte Chemie - International Edition,* 54.24 (2015), pp. 7091–7095.

[31] X. Ai, E. W. Evans, S. Dong, A. J. Gillett, H. Guo, Y. Chen, T. J. Hele, R. H. Friend, and F. Li. "Efficient radical-based light-emitting diodes with doublet emission". *Nature,* 563.7732 (2018), pp. 536–540.

[32] Y. Hattori, T. Kusamoto, and H. Nishihara. "Luminescence, stability, and proton response of an open-Shell (3,5-dichloro-4-pyridyl)bis(2,4,6-trichlorophenyl)methyl radical". *Angewandte Chemie - International Edition,* 53.44 (2014), pp. 11845–11848.

[33] A. Abdurahman, Y. Chen, X. Ai, O. Ablikim, Y. Gao, S. Dong, B. Li, B. Yang, M. Zhang, and F. Li. "A pure red luminescent beta-carboline-substituted biphenylmethyl radical: photophysics, stability and OLEDs". *Journal of Materials Chemistry C,* 6.42 (2018), pp. 11248–11254.

[34] A. Abdurahman, Q. Peng, O. Ablikim, X. Ai, and F. Li. "A radical polymer with efficient deep-red luminescence in the condensed state". *Materials Horizons,* 6.6 (2019), pp. 1265–1270.

[35] M. Imran, C. M. Wehrmann, and M. S. Chen. "Open-shell effects on optoelectronic properties: antiambipolar charge transport and anti-Kasha doublet emission from a N-substituted bisphenalenyl". *Journal of the American Chemical Society,* 142.1 (2020), pp. 38–43.

[36] A. Obolda, X. Ai, M. Zhang, and F. Li. “Up to 100% formation ratio of doublet exciton in deep-red organic light-emitting diodes based on neutral pi-radical”. *ACS Applied Materials & Interfaces,* 8.51 (2016), pp. 35472–35478.

[37] Z. Cui, S. Ye, L. Wang, H. Guo, A. Obolda, S. Dong, Y. Chen, X. Ai, A. Abdurahman, M. Zhang, L. Wang, and F. Li. “Radical-based organic light-emitting diodes with maximum external quantum efficiency of 10.6%”. *The Journal of Physical Chemistry Letters,* 9.22 (2018), pp. 6644–6648.

[38] S. Dong, W. Xu, H. Guo, W. Yan, M. Zhang, and F. Li. “Effects of substituents on luminescent efficiency of stable triaryl methyl radicals”. *Physical Chemistry Chemical Physics,* 20.27 (2018), pp. 18657–18662.

[39] H. Guo, Q. Peng, X.-K. Chen, Q. Gu, S. Dong, E. W. Evans, A. J. Gillett, X. Ai, M. Zhang, D. Credgington, V. Coropceanu, R. H. Friend, J.-L. Bredas, and F. Li. “High stability and luminescence efficiency in donor-acceptor neutral radicals not following the Aufbau principle”. *Nature Materials,* 18.9 (2019), pp. 977–984.

[40] A. Abdurahman, T. J. H. Hele, Q. Gu, J. Zhang, Q. Peng, M. Zhang, R. H. Friend, F. Li, and E. W. Evans. “Understanding the luminescent nature of organic radicals for efficient doublet emitters and pure-red light-emitting diodes”. *Nature Materials,* 19.11 (2020), pp. 1224–1229.

[41] O. Armet, J. Veciana, C. Rovira, J. Riera, J. Castaner, E. Molins, J. Rius, C. Miravitlles, S. Olivella, and J. Brichfeus. “Inert carbon free radicals. 8. Polychlorotriphenylmethyl radicals: synthesis, structure, and spin-density distribution”. *The Journal of Physical Chemistry,* 91.22 (1987), pp. 5608–5616.

[42] J. Veciana and I. Ratera. “Polychlorotriphenylmethyl radicals: towards multifunctional molecular materials”. *Stable Radicals: Fundamentals and Applied Aspects of Odd-Electron Compounds* (2010), pp. 33–80.

[43] S. A. Green, D. J. Simpson, G. Zhou, P. S. Ho, and N. V. Blough. “Intramolecular quenching of excited singlet states by stable nitroxyl radicals”. *Journal of the American Chemical Society,* 112.20 (1990), pp. 7337–7346.

[44] G. I. Likhtenstein, K. Ishii, and S. Nakatsuji. “Dual chromophore-nitroxides: novel molecular probes, photochemical and photophysical models and magnetic materials”. *Photochemistry and Photobiology,* 83.4 (2007), pp. 871–881.

[45] Z. Wang, J. Zhao, A. Barbon, A. Toffoletti, Y. Liu, Y. An, L. Xu, A. Karatay, H. G. Yaglioglu, E. A. Yildiz, and M. Hayvali. “Radical-Enhanced Intersystem Crossing in New Bodipy Derivatives and Application for Efficient Triplet-Triplet Annihilation Upconversion”. *Journal of the American Chemical Society,* 139.23 (2017), pp. 7831–7842.

[46] M. T. Colvin, E. M. Giacobbe, B. Cohen, T. Miura, A. M. Scott, and M. R. Wasielewski. “Competitive Electron Transfer and Enhanced Intersystem Crossing in Photoexcited Covalent TEMPO-Perylene-3,4:9,10-bis(dicarboximide) Dyads: Unusual Spin Polarization Resulting from the Radical-Triplet Interaction”. *The Journal of Physical Chemistry A,* 114.4 (2010), pp. 1741–1748.

[47] C. E. Avalos, S. Richert, E. Socie, G. Karthikeyan, G. Casano, G. Stevanato, D. J. Kubicki, J. E. Moser, C. R. Timmel, M. Lelli, A. J. Rossini, O. Ouari, and L. Emsley. “Enhanced Intersystem Crossing and Transient Electron Spin Polarization in a Photoexcited Pentacene-Trityl Radical”. *The Journal of Physical Chemistry A,* 124.29 (2020), pp. 6068–6075.

[48] V. Gamero, D. Velasco, S. Latorre, F. López-Calahorra, E. Brillas, and L. Juliá. “[4-(N-Carbazolyl)-2,6-dichlorophenyl]bis(2,4,6-trichlorophenyl)methyl radical an efficient red light-emitting paramagnetic molecule”. *Tetrahedron Letters,* 47.14 (2006), pp. 2305–2309.

[49] Z. Cui, A. Abdurahman, X. Ai, and F. Li. “Stable Luminescent Radicals and Radical-Based LEDs with Doublet Emission”. *CCS Chemistry,* 2.4 (2020), pp. 1129–1145.

[50] H. Abroshan, V. Coropceanu, and J.-L. Bredas. “Radiative and Nonradiative Recombinations in Organic Radical Emitters: The Effect of Guest-Host Interactions”. *Advanced Functional Materials,* 30.35 (2020), p. 2002916.

[51] C. A. Coulson and G. S. Rushbrooke. “Note on the method of molecular orbitals”. *Mathematical Proceedings of the Cambridge Philosophical Society,* 36.2 (1940), pp. 193–200.

[52] R. B. Mallion and D. H. Rouvray. “The golden jubilee of the Coulson-Rushbrooke pairing theorem”. *Journal of Mathematical Chemistry,* 5.1 (1990), pp. 1–21.

[53] M. J. S. Dewar and H. C. Longuet-Higgins. “The Electronic Spectra of Aromatic Molecules I: Benzenoid Hydrocarbons”. *Proceedings of the Physical Society: Section A,* 67.9 (1954), p. 795.

[54] H. C. Longuet-Higgins and J. A. Pople. “The Electronic Spectra of Aromatic Molecules IV: Excited States of Odd Alternant Hydrocarbon Radicals and Ions”. *Proceedings of the Physical Society: Section A,* 68.7 (1955), p. 591.

[55] H. C. Longuet-Higgins. “Some Studies in Molecular Orbital Theory I. Resonance Structures and Molecular Orbitals in Unsaturated Hydrocarbons”. *The Journal of Chemical Physics,* 18.3 (1950), pp. 265–274.

[56] V. Diez-Cabanes, G. Seber, C. Franco, F. Bejarano, N. Crivillers, M. Mas-Torrent, J. Veciana, C. Rovira, and J. Cornil. “Design of Perchlorotriphenylmethyl (PTM) Radical-Based Compounds for Optoelectronic Applications: The Role of Orbital Delocalization”. *ChemPhysChem,* 19.19 (2018), pp. 2572–2578.

[57] C.-H. Liu, E. Hamzehpoor, Y. Sakai-Otsuka, T. Jadhav, and D. F. Perepichka. “A Pure-Red Doublet Emission with 90% Quantum Yield: Stable, Colorless, Iodinated Triphenylmethane Solid”. *Angewandte Chemie - International Edition,* 59.51 (2020), pp. 23030–23034.

[58] M. Ballester, J. Riera-Figueras, and A. Rodriguez-Siurana. “Synthesis and isolation of a perchlorotriphenylcarbonium salt”. *Tetrahedron Letters,* 11.42 (1970), pp. 3615–3618.

[59] X. Ai, Y. Chen, Y. Feng, and F. Li. “A Stable Room-Temperature Luminescent Biphenylmethyl Radical”. *Angewandte Chemie - International Edition,* 57.11 (2018), pp. 2869–2873.

[60] A. Tanushi, S. Kimura, T. Kusamoto, M. Tominaga, Y. Kitagawa, M. Nakano, and H. Nishihara. “NIR Emission and Acid-Induced Intramolecular Electron Transfer Derived from a SOMO-HOMO Converted Non-Aufbau Electronic Structure”. *The Journal of Physical Chemistry C,* 123.7 (2019), pp. 4417–4423.

[61] T. Nishiuchi, S. Aibara, and T. Kubo. “Synthesis and Properties of a Highly Congested Tri(9-anthryl)methyl Radical”. *Angewandte Chemie - International Edition,* 57.50 (2018), pp. 16516–16519.

[62] S. Dong, A. Obolda, Q. Peng, Y. Zhang, S. Marder, and F. Li. “Multicarbazolyl substituted TTM radicals: red-shift of fluorescence emission with enhanced luminescence efficiency”. *Materials Chemistry Frontiers,* 1.10 (2017), pp. 2132–2135.

[63] Y. Gao, W. Xu, H. Ma, A. Obolda, W. Yan, S. Dong, M. Zhang, and F. Li. “Novel Luminescent Benzimidazole-Substituent Tris(2,4,6-trichlorophenyl)methyl Radicals: Photophysics, Stability, and Highly Efficient Red-Orange Electroluminescence”. *Chemistry of Materials,* 29.16 (2017), pp. 6733–6739.

[64] Y. Hattori, E. Michail, A. Schmiedel, M. Moos, M. Holzapfel, I. Krummenacher, H. Braunschweig, U. Müller, J. Pflaum, and C. Lambert. “Luminescent Mono-, Di-, and Triradicals: Bridging Polychlorinated Triarylmethyl Radicals by Triarylamines and Triarylboranes”. *Chemistry - A European Journal,* 25.68 (2019), pp. 15463–15471.

[65] T. J. H. Hele, E. G. Fuemmeler, S. N. Sanders, E. Kumarasamy, M. Y. Sfeir, L. M. Campos, and N. Ananth. “Anticipating Acene-Based Chromophore Spectra with Molecular Orbital Arguments”. *The Journal of Physical Chemistry A,* 123.13 (2019), pp. 2527–2536.

[66] E. Cho, V. Coropceanu, and J.-L. Bredas. “Organic Neutral Radical Emitters: Impact of Chemical Substitution and Electronic-State Hybridization on the Luminescence Properties”. *Journal of the American Chemical Society,* 142.41 (2020), pp. 17782–17786.

[67] Y. Olivier, B. Yurash, L. Muccioli, G. D’Avino, O. Mikhnenko, J. C. Sancho-Garcia, C. Adachi, T.-Q. Nguyen, and D. Beljonne. “Nature of the singlet and triplet excitations mediating thermally activated delayed fluorescence”. *Physical Review Materials,* 1.7 (2017), p. 075602.

[68] P. K. Samanta, D. Kim, V. Coropceanu, and J.-L. Bredas. “Up-Conversion Intersystem Crossing Rates in Organic Emitters for Thermally Activated Delayed Fluorescence: Impact of the Nature of Singlet vs Triplet Excited States”. *Journal of the American Chemical Society,* 139.11 (2017), pp. 4042–4051.

[69] X.-K. Chen. “A Quantum-Chemical Insight into the Role of Charge-Transfer States in Organic Emitters for Electroluminescence”. *CCS Chemistry,* 2.4 (2020), pp. 1256–1267.

[70] G. W. Robinson. “Intensity Enhancement of Forbidden Electronic Transitions by Weak Intermolecular Interactions”. *The Journal of Chemical Physics,* 46.2 (1967), pp. 572–585.

[71] T. Kusamoto, S. Kume, and H. Nishihara. “Realization of SOMO-HOMO Level Conversion for a TEMPO-Dithiolate Ligand by Coordination to Platinum(II)”. *Journal of the American Chemical Society,* 130.42 (2008), pp. 13844–13845.

[72] Y. Beldjoudi, M. A. Nascimento, Y. J. Cho, H. Yu, H. Aziz, D. Tonouchi, K. Eguchi, M. M. Matsushita, K. Awaga, I. Osorio-Roman, C. P. Constantinides, and J. M. Rawson. “Multifunctional Dithiadiazolyl Radicals: Fluorescence, Electroluminescence, and Photoconducting Behavior in Pyren-1-yl-dithiadiazolyl”. *Journal of the American Chemical Society,* 140.20 (2018), pp. 6260–6270.

[73] Y. Hattori, T. Kusamoto, and H. Nishihara. “Highly photostable luminescent open-shell (3,5-dihalo-4-pyridyl)bis(2,4,6-trichlorophenyl)methyl radicals: significant effects of halogen atoms on their photophysical and photochemical properties”. *RSC Advances,* 5.79 (2015), pp. 64802–64805.

[74] C. He, Z. Li, Y. Lei, W. Zou, and B. Suo. “Unraveling the Emission Mechanism of Radical-Based Organic Light-Emitting Diodes”. *The Journal of Physical Chemistry Letters,* 10.3 (2019), pp. 574–580.

[75] S. Kimura, A. Tanushi, T. Kusamoto, S. Kochi, T. Sato, and H. Nishihara. “A luminescent organic radical with two pyridyl groups: high photostability and dual stimuli-responsive properties, with theoretical analyses of photophysical processes”. *Chemical Science,* 9.7 (2018), pp. 1996–2007.

[76] J. Kido and Y. Iizumi. “Fabrication of highly efficient organic electroluminescent devices”. *Applied Physics Letters,* 73.19 (1998), pp. 2721–2723.

[77] N. C. Giebink and S. R. Forrest. “Quantum efficiency roll-off at high brightness in fluorescent and phosphorescent organic light emitting diodes”. *Physical Review B,* 77.23 (2008), p. 235215.

[78] D. Velasco, S. Castellanos, M. Lopez, F. Lopez-Calahorra, E. Brillas, and L. Julia. “Red Organic Light-Emitting Radical Adducts of Carbazole and Tris(2,4,6-trichlorotriphenyl)methyl Radical That Exhibit High Thermal Stability and Electrochemical Amphotericity”. *The Journal of Organic Chemistry,* 72.20 (2007), pp. 7523–7532.

[79] Q. Gu, A. Abdurahman, R. H. Friend, and F. Li. “Polymer Light Emitting Diodes with Doublet Emission”. *The Journal of Physical Chemistry Letters,* 11.14 (2020), pp. 5638–5642.

[80] P. Mayorga-Burrezo, V. G. Jimenez, D. Blasi, T. Parella, I. Ratera, A. G. Campana, and J. Veciana. “An Enantiopure Propeller-Like Trityl-Brominated Radical: Bringing Together a High Racemization Barrier and an Efficient Circularly Polarized Luminescent Magnetic Emitter”. *Chemistry - A European Journal,* 26.17 (2020), pp. 3776–3781.

[81] P. Mayorga-Burrezo, V. G. Jimenez, D. Blasi, I. Ratera, A. G. Campana, and J. Veciana. “Organic Free Radicals as Circularly Polarized Luminescence Emitters”. *Angewandte Chemie - International Edition,* 58.45 (2019), pp. 16282–16288.

[82] H. Li, X. Wang, Y. Zhu, and Z. Li. “Innovative Organic Electroluminescent Materials with a Doublet Ground State: A Theoretical Investigation”. *The Journal of Physical Chemistry A,* 124.4 (2020), pp. 662–673.

[83] M. Pope and C. E. Swenberg. *Electronic processes in organic crystals and polymers*. Oxford University Press, 1999.

[84] L. Ji, J. Shi, J. Wei, T. Yu, and W. Huang. “Air-Stable Organic Radicals: New-Generation Materials for Flexible Electronics?” *Advanced Materials,* 32.32 (2020), p. 1908015.

[85] M. A. Fox, E. Gaillard, and C. C. Chen. “Photochemistry of stable free radicals: the photolysis of perchlorotriphenylmethyl radicals”. *Journal of the American Chemical Society,* 109.23 (1987), pp. 7088–7094.

[86] L. Yuan, C. Franco, N. Crivillers, M. Mas-Torrent, L. Cao, C. S. S. Sangeeth, C. Rovira, J. Veciana, and C. A. Nijhuis. “Chemical control over the energy-level alignment in a two-terminal junction”. *Nature Communications,* 7.1 (2016), p. 12066.

[87] M. Souto, L. Yuan, D. C. Morales, L. Jiang, I. Ratera, C. A. Nijhuis, and J. Veciana. "Tuning the Rectification Ratio by Changing the Electronic Nature (Open-Shell and Closed-Shell) in Donor-Acceptor Self-Assembled Monolayers". *Journal of the American Chemical Society,* 139.12 (2017), pp. 4262–4265.

[88] F. Bejarano, I. J. Olavarria-Contreras, A. Droghetti, I. Rungger, A. Rudnev, D. Gutierrez, M. Mas-Torrent, J. Veciana, H. S. J. van der Zant, C. Rovira, E. Burzuri, and N. Crivillers. "Robust Organic Radical Molecular Junctions Using Acetylene Terminated Groups for C-Au Bond Formation". *Journal of the American Chemical Society,* 140.5 (2018), pp. 1691–1696.

[89] J. A. de Sousa, F. Bejarano, D. Gutierrez, Y. R. Leroux, E. M. Nowik-Boltyk, T. Junghoefer, E. Giangrisostomi, R. Ovsyannikov, M. B. Casu, J. Veciana, M. Mas-Torrent, B. Fabre, C. Rovira, and N. Crivillers. "Exploiting the versatile alkyne-based chemistry for expanding the applications of a stable triphenylmethyl organic radical on surfaces". *Chemical Science,* 11.2 (2020), pp. 516–524.

[90] A. Monkman. "Why Do We Still Need a Stable Long Lifetime Deep Blue OLED Emitter?" *ACS Applied Materials & Interfaces,* 14.18 (2022), pp. 20463–20467.

[91] J. Lee, C. Jeong, T. Batagoda, C. Coburn, M. E. Thompson, and S. R. Forrest. "Hot excited state management for long-lived blue phosphorescent organic light-emitting diodes". *Nature Communications,* 8.1 (2017), p. 15566.

[92] K. An, G. Xie, S. Gong, Z. Chen, X. Zhou, F. Ni, and C. Yang. "Monoradically luminescent polymers by a super acid-catalyzed polymerization and deep-red electroluminescence". *Science China Chemistry,* 63.9 (2020), pp. 1214–1220.

[93] Y. Hattori, S. Kimura, T. Kusamoto, H. Maeda, and H. Nishihara. "Cation-responsive turn-on fluorescence and absence of heavy atom effects of pyridyl-substituted triarylmethyl radicals". *Chemical Communications,* 54.6 (2018), pp. 615–618.

[94] Y. Hattori, T. Kusamoto, T. Sato, and H. Nishihara. "Synergistic luminescence enhancement of a pyridyl-substituted triarylmethyl radical based on fluorine substitution and coordination to gold". *Chemical Communications,* 52.91 (2016), pp. 13393–13396.

[95] Y. Ogino, T. Kusamoto, Y. Hattori, M. Shimada, M. Tsuchiya, Y. Yamanoi, E. Nishibori, K. Sugimoto, and H. Nishihara. "Solvent-Controlled Doublet Emission of an Organometallic Gold(I) Complex with a Polychlorinated Diphenyl(4-pyridyl)methyl Radical Ligand: Dual Fluorescence and Enhanced Emission Efficiency". *Inorganic Chemistry,* 56.7 (2017), pp. 3909–3915.

[96] R. Gautam, S. J. Petritis, A. V. Astashkin, and E. Tomat. “Paramagnetism and Fluorescence of Zinc(II) Tripyrrindione: A Luminescent Radical Based on a Redox-Active Biopyrrin”. *Inorganic Chemistry,* 57.24 (2018), pp. 15240–15246.

[97] J. Wade, J. N. Hilfiker, J. R. Brandt, L. Liiro-Peluso, L. Wan, X. Shi, F. Salerno, S. T. J. Ryan, S. Schoche, O. Arteaga, T. Javorfi, G. Siligardi, C. Wang, D. B. Amabilino, P. H. Beton, A. J. Campbell, and M. J. Fuchter. “Natural optical activity as the origin of the large chiroptical properties in π-conjugated polymer thin films”. *Nature Communications,* 11.1 (2020), p. 6137.

[98] G. Albano, G. Pescitelli, and L. D. Bari. “Chiroptical Properties in Thin Films of π-Conjugated Systems”. *Chemical Reviews,* 120.18 (2020), pp. 10145–10243.

[99] D. D. Nuzzo, C. Kulkarni, B. Zhao, E. Smolinsky, F. Tassinari, S. C. J. Meskers, R. Naaman, E. W. Meijer, and R. H. Friend. “High Circular Polarization of Electroluminescence Achieved via Self-Assembly of a Light-Emitting Chiral Conjugated Polymer into Multidomain Cholesteric Films”. *ACS Nano,* 11.12 (2017), pp. 12713–12722.

[100] Q. Jin, S. Chen, Y. Sang, H. Guo, S. Dong, J. Han, W. Chen, X. Yang, F. Li, and P. Duan. “Circularly polarized luminescence of achiral open-shell π-radicals”. *Chemical Communications,* 55.46 (2019), pp. 6583–6586.

[101] P. M. Blok and H. P. Dekkers. “Discrimination between $3\pi\pi^*$ and $3n\pi^*$ states in organic molecules by circular polarization of phosphorescence”. *Chemical Physics Letters,* 161.2 (1989), pp. 188–194.

[102] D. Blasi, D. M. Nikolaidou, F. Terenziani, I. Ratera, and J. Veciana. “Excimers from stable and persistent supramolecular radical-pairs in red/NIR-emitting organic nanoparticles and polymeric films”. *Physical Chemistry Chemical Physics,* 19.13 (2017), pp. 9313–9319.

[103] K. Kato, S. Kimura, T. Kusamoto, H. Nishihara, and Y. Teki. “Luminescent Radical-Excimer: Excited-State Dynamics of Luminescent Radicals in Doped Host Crystals”. *Angewandte Chemie - International Edition,* 58.9 (2019), pp. 2606–2611.

[104] S. Kimura, S. Kimura, H. Nishihara, and T. Kusamoto. “Excimer emission and magnetoluminescence of radical-based zinc(ii) complexes doped in host crystals”. *Chemical Communications,* 56.76 (2020), pp. 11195–11198.

[105] S. Kimura, S. Kimura, K. Kato, Y. Teki, H. Nishihara, and T. Kusamoto. “A ground-state-dominated magnetic field effect on the luminescence of stable organic radicals”. *Chemical Science,* 12.6 (2021), pp. 2025–2029.

[106] K. M. Salikhov, Y. N. Molin, R. Z. Sagdeev, and A. L. Buchachenko. *Spin polarization and magnetic effects in radical reactions*. 1984.

[107] P. Ballesteros, A. Cuadrado, A. Gilabert, L. Fajari, I. Sires, E. Brillas, M. P. Almajano, D. Velasco, J. M. Anglada, and L. Julia. "Formation of a stable bi-radical triplet state cation versus a closed shell singlet state cation by oxidation of adducts of 3,6-dimethoxycarbazole and polychlorotriphenylmethyl radicals". *Physical Chemistry Chemical Physics,* 21.36 (2019), pp. 20225–20231.

[108] J. Griffin, E. Spooner, and H. Hadi. *Spin Coating: Complete Guide to Theory and Techniques*. June 2024. URL: https://www.ossila.com/pages/spin-coating.

[109] J. C. de Mello, H. F. Wittmann, and R. H. Friend. "An improved experimental determination of external photoluminescence quantum efficiency". *Advanced Materials,* 9.3 (1997), pp. 230–232.

[110] M. A. de Araujo, R. Silva, E. de Lima, D. P. Pereira, and P. C. de Oliveira. "Measurement of Gaussian laser beam radius using the knife-edge technique: improvement on data analysis". *Applied Optics,* 48.2 (2009), pp. 393–396.

[111] M. R. Wasielewski, M. D. Forbes, N. L. Frank, K. Kowalski, G. D. Scholes, J. Yuen-Zhou, M. A. Baldo, D. E. Freedman, R. H. Goldsmith, T. Goodson, M. L. Kirk, J. K. McCusker, J. P. Ogilvie, D. A. Shultz, S. Stoll, and K. B. Whaley. "Exploiting chemistry and molecular systems for quantum information science". *Nature Reviews Chemistry,* 4.9 (2020), pp. 490–504.

[112] T. Quintes, M. Mayländer, and S. Richert. "Properties and applications of photoexcited chromophore-radical systems". *Nature Reviews Chemistry,* 7.2 (2023), pp. 75–90.

[113] E. M. Giacobbe, Q. Mi, M. T. Colvin, B. Cohen, C. Ramanan, A. M. Scott, S. Yeganeh, T. J. Marks, M. A. Ratner, and M. R. Wasielewski. "Ultrafast Intersystem Crossing and Spin Dynamics of Photoexcited Perylene-3,4:9,10-bis(dicarboximide) Covalently Linked to a Nitroxide Radical at Fixed Distances". *Journal of the American Chemical Society,* 131.10 (2009), pp. 3700–3712.

[114] M. L. Kirk, D. A. Shultz, P. Hewitt, J. Chen, and A. van der Est. "Excited State Magneto-Structural Correlations Related to Photoinduced Electron Spin Polarization". *Journal of the American Chemical Society,* 144.28 (2022), pp. 12781–12788.

[115] Y. Kandrashkin and A. van der Est. "Electron spin polarization of the excited quartet state of strongly coupled triplet-doublet spin systems". *The Journal of Chemical Physics,* 120.10 (2004), pp. 4790–4799.

[116] A. Ito, A. Shimizu, N. Kishida, Y. Kawanaka, D. Kosumi, H. Hashimoto, and Y. Teki. “Excited-State Dynamics of Pentacene Derivatives with Stable Radical Substituents”. *Angewandte Chemie - International Edition,* 53.26 (2014), pp. 6715–6719.

[117] Y. E. Kandrashkin and A. van der Est. “The triplet mechanism of electron spin polarization in moderately coupled triplet-doublet rigid complexes as a source of the enhanced +1/2 ⇔ -1/2 transitions”. *The Journal of Chemical Physics,* 151.18 (2019), p. 184301.

[118] M. Mayländer, S. Chen, E. R. Lorenzo, M. R. Wasielewski, and S. Richert. “Exploring Photogenerated Molecular Quartet States as Spin Qubits and Qudits”. *Journal of the American Chemical Society,* 143.18 (2021), pp. 7050–7058.

[119] M. T. Colvin, A. L. Smeigh, E. M. Giacobbe, S. M. M. Conron, A. B. Ricks, and M. R. Wasielewski. “Ultrafast Intersystem Crossing and Spin Dynamics of Zinc meso-Tetraphenylporphyrin Covalently Bound to Stable Radicals”. *The Journal of Physical Chemistry A,* 115.26 (2011), pp. 7538–7549.

[120] Y. Teki. “Excited-State Dynamics of Non-Luminescent and Luminescent π-Radicals”. *Chemistry - A European Journal,* 26.5 (2020), pp. 980–996.

[121] O. L. J. Gijzeman, F. Kaufman, and G. Porter. “Quenching of aromatic triplet states in solution by nitric oxide and other free radicals”. *Journal of the Chemical Society: Faraday Transactions 2,* 69 (1973), p. 727.

[122] M. Mayländer, O. Nolden, M. Franz, S. Chen, L. Bancroft, Y. Qiu, M. R. Wasielewski, P. Gilch, and S. Richert. “Accessing the triplet state of perylenediimide by radical-enhanced intersystem crossing”. *Chemical Science,* 13.22 (2022), pp. 6732–6743.

[123] Y. Kobori, A. Kawai, and K. Obi. “Direct Observation of CIDEP Generated through Enhanced Intersystem Crossing”. *The Journal of Physical Chemistry,* 98.26 (1994), pp. 6425–6429.

[124] X. Zhang, A. A. Sukhanov, E. A. Yildiz, Y. E. Kandrashkin, J. Zhao, H. G. Yaglioglu, and V. K. Voronkova. “Radical-Enhanced Intersystem Crossing in a Bay-Substituted Perylene Bisimide-TEMPO Dyad and the Electron Spin Polarization Dynamics upon Photoexcitation**”. *ChemPhysChem,* 22.1 (2021), pp. 55–68.

[125] V. Ern and R. E. Merrifield. “Magnetic Field Effect on Triplet Exciton Quenching in Organic Crystals”. *Physical Review Letters,* 21.9 (1968), pp. 609–611.

[126] S. Gorgon, K. Lv, J. Grüne, B. H. Drummond, W. K. Myers, G. Londi, G. Ricci, D. Valverde, C. Tonnelé, P. Murto, A. S. Romanov, D. Casanova, V. Dyakonov, A. Sperlich, D. Beljonne, Y. Olivier, F. Li, R. H. Friend, and E. W. Evans. "Reversible spin-optical interface in luminescent organic radicals". *Nature,* 620.7974 (2023), pp. 538–544.

[127] J. Han, Y. Jiang, A. Obolda, P. Duan, F. Li, and M. Liu. "Doublet-Triplet Energy Transfer-Dominated Photon Upconversion". *Journal of Physical Chemistry Letters,* 8.23 (2017), pp. 5865–5870.

[128] Y. Wei, K. An, X. Xu, Z. Ye, X. Yin, X. Cao, and C. Yang. "π-Radical Photosensitizer for Highly Efficient and Stable Near-Infrared Photon Upconversion". *Advanced Optical Materials,* 6 (2023).

[129] A. Kawai and K. Obi. "First observation of a radical-triplet pair mechanism (RTPM) with doublet precursor". *The Journal of Physical Chemistry,* 96.1 (1992), pp. 52–56.

[130] C. Blättler, F. Jent, and H. Paul. "A novel radical-triplet pair mechanism for chemically induced electron polarization (CIDEP) of free radicals in solution". *Chemical Physics Letters,* 166.4 (1990), pp. 375–380.

[131] V. Rozenshtein, A. Berg, E. Stavitski, H. Levanon, L. Franco, and C. Corvaja. "Electron spin polarization of functionalized fullerenes. Reversed quartet mechanism". *Journal of Physical Chemistry A,* 109.49 (2005), pp. 11144–11154.

[132] Y. Qiu, A. Equbal, C. Lin, Y. Huang, P. J. Brown, R. M. Young, M. D. Krzyaniak, and M. R. Wasielewski. "Optical Spin Polarization of a Narrow-Linewidth Electron-Spin Qubit in a Chromophore/Stable-Radical System". *Angewandte Chemie - International Edition,* 62.6 (2023).

[133] R. E. Merrifield. "Magnetic effects on triplet exciton interactions". *Pure and Applied Chemistry,* 27.3 (1971), pp. 481–498.

[134] M. Imran, M. Taddei, A. A. Sukhanov, L. Bussotti, W. Ni, P. Foggi, G. G. Gurzadyan, J. Zhao, M. D. Donato, and V. K. Voronkova. "Radical-Enhanced Intersystem Crossing in Perylene-Oxoverdazyl Radical Dyads". *ChemPhysChem,* 23.8 (2022), e202100912.

[135] D. G. Bossanyi, Y. Sasaki, S. Wang, D. Chekulaev, N. Kimizuka, N. Yanai, and J. Clark. "Spin Statistics for Triplet-Triplet Annihilation Upconversion: Exchange Coupling, Intermolecular Orientation, and Reverse Intersystem Crossing". *JACS Au,* 1.12 (2021), pp. 2188–2201.

[136] R. C. Johnson, R. E. Merrifield, P. Avakian, and R. B. Flippen. "Effects of Magnetic Fields on the Mutual Annihilation of Triplet Excitons in Molecular Crystals". *Physical Review Letters,* 19.6 (1967), pp. 285–287.

[137] R. E. Merrifield. “Theory of magnetic field effects on the mutual annihilation of triplet excitons”. *The Journal of Chemical Physics,* 48.9 (1968), pp. 4319–4320.

[138] L. R. Faulkner and A. J. Bard. “Magnetic field effects on anthracene triplet-triplet annihilation in fluid solutions”. *Journal of the American Chemical Society,* 91.23 (1969), pp. 6495–6497.

[139] S. L. Bayliss, L. R. Weiss, A. Rao, R. H. Friend, A. D. Chepelianskii, and N. C. Greenham. “Spin signatures of exchange-coupled triplet pairs formed by singlet fission”. *Physical Review B,* 94.4 (2016).

[140] D. G. Bossanyi, M. Matthiesen, S. Wang, J. A. Smith, R. C. Kilbride, J. D. Shipp, D. Chekulaev, E. Holland, J. E. Anthony, J. Zaumseil, A. J. Musser, and J. Clark. “Emissive spin-0 triplet-pairs are a direct product of triplet-triplet annihilation in pentacene single crystals and anthradithiophene films”. *Nature Chemistry,* 13.2 (2021), pp. 163–171.

[141] M. G. Kucherenko and S. A. Penkov. “Triplet Excitons Quenching By Doublet Centers in a Nanoreactor with an External Magnetic Field”. *Journal of Applied Spectroscopy,* 88.2 (2021), pp. 265–273.

[142] N. Aizawa, Y.-J. Pu, Y. Harabuchi, A. Nihonyanagi, R. Ibuka, H. Inuzuka, B. Dhara, Y. Koyama, K.-i. Nakayama, S. Maeda, F. Araoka, and D. Miyajima. “Delayed fluorescence from inverted singlet and triplet excited states”. *Nature,* 609.7927 (2022), pp. 502–506.

[143] F. Li, A. J. Gillett, Q. Gu, J. Ding, Z. Chen, T. J. H. Hele, W. K. Myers, R. H. Friend, and E. W. Evans. “Singlet and triplet to doublet energy transfer: improving organic light-emitting diodes with radicals”. *Nature Communications,* 13.1 (2022), p. 2744.

[144] H.-H. Cho, S. Gorgon, H.-C. Hung, J.-Y. Huang, Y.-R. Wu, F. Li, N. C. Greenham, E. W. Evans, and R. H. Friend. “Efficient and Bright Organic Radical Light-Emitting Diodes with Low Efficiency Roll-Off”. *Advanced Materials,* 35.45 (2023), p. 2303666.

[145] Q. Gu, S. Gorgon, A. S. Romanov, F. Li, R. H. Friend, and E. W. Evans. “Fast Transfer of Triplet to Doublet Excitons from Organometallic Host to Organic Radical Semiconductors”. *Advanced Materials,* n/a.n/a (2024), p. 2402790.

[146] M. Z. Shafikov, A. V. Zaytsev, and V. N. Kozhevnikov. “Trinuclear Cyclometalated Iridium(III) Complex Exhibiting Intense Phosphorescence of an Unprecedented Rate”. *Inorganic Chemistry,* 63.2 (2024), pp. 1317–1327.

[147] H.-G. Kim, K.-H. Kim, and J.-J. Kim. “Highly Efficient, Conventional, Fluorescent Organic Light-Emitting Diodes with Extended Lifetime”. *Advanced Materials,* 29.39 (2017), p. 1702159.

[148] S. C. Kim, C. H. Ryu, K. M. Lee, and J. Y. Lee. “Tetradentate Pt(II) Complex as Phosphorescent Sensitizer for Highly Efficient Green Organic Light-Emitting Diodes with Low Efficiency Roll-Off”. *Advanced Optical Materials,* 11.13 (2023), p. 2202698.

[149] P. Heimel, A. Mondal, F. May, W. Kowalsky, C. Lennartz, D. Andrienko, and R. Lovrincic. “Unicolored phosphor-sensitized fluorescence for efficient and stable blue OLEDs”. *Nature Communications,* 9.1 (2018), p. 4990.

[150] L. Paterson, A. Mondal, P. Heimel, R. Lovrincic, F. May, C. Lennartz, and D. Andrienko. “Perspectives of Unicolored Phosphor-Sensitized Fluorescence”. *Advanced Electronic Materials,* 5.12 (2019), p. 1900646.

[151] A. Mizuno, R. Matsuoka, T. Mibu, and T. Kusamoto. “Luminescent Radicals”. *Chemical Reviews,* 124.3 (2024), pp. 1034–1121.

[152] A. Obolda, W. Li, M. Abdulahat, F. Ma, B. Li, X. Ai, M. Zhang, and F. Li. “High-efficiency deep-red organic radical crystals and OLEDs with solid-state fluorescence and excellent photostability”. *Organic Electronics,* 107 (2022), p. 106564.

[153] R. J. Holmes, B. W. D’Andrade, S. R. Forrest, X. Ren, J. Li, and M. E. Thompson. “Efficient, deep-blue organic electrophosphorescence by guest charge trapping”. *Applied Physics Letters,* 83.18 (2003), pp. 3818–3820.

[154] C. Li, X. Fan, C. Han, and H. Xu. “A ternary phosphine oxide host featuring thermally activated delayed fluorescence for blue PHOLEDs with >20% EQE and extremely low roll-offs”. *The Journal of Materials Chemistry C,* 6.25 (2018), pp. 6747–6754.

[155] A. Endo, K. Suzuki, T. Yoshihara, S. Tobita, M. Yahiro, and C. Adachi. “Measurement of photoluminescence efficiency of Ir(III) phenylpyridine derivatives in solution and solid-state films”. *Chemical Physics Letters,* 460.1 (2008), pp. 155–157.

[156] B. W. D’Andrade, R. J. Holmes, and S. R. Forrest. “Efficient Organic Electrophosphorescent White-Light-Emitting Device with a Triple Doped Emissive Layer”. *Advanced Materials,* 16.7 (2004), pp. 624–628.

[157] K.-R. Wee, W.-s. Han, H.-J. Son, S. Kwon, and S. O. Kang. “Efficiency and colour optimization of carbazole based deep blue phosphorescent organic light emitting devices”. *Journal of Physics D: Applied Physics,* 42.23 (2009), p. 235107.

[158] Y. Kawamura, J. Brooks, J. J. Brown, H. Sasabe, and C. Adachi. “Intermolecular Interaction and a Concentration-Quenching Mechanism of Phosphorescent Ir(III) Complexes in a Solid Film”. *Physical Review Letters,* 96.1 (2006), p. 017404.

[159] L. Sudha Devi, M. K. Al-Suti, C. Dosche, M. S. Khan, R. H. Friend, and A. Kohler. "Triplet energy transfer in conjugated polymers. I. Experimental investigation of a weakly disordered compound". *Physical Review B,* 78.4 (2008), p. 045210.

[160] A. Kohler and H. Bassler. "What controls triplet exciton transfer in organic semiconductors?" *Journal of Materials Chemistry,* 21.12 (2011), pp. 4003–4011.

[161] R. A. Marcus. "On the Theory of Oxidation-Reduction Reactions Involving Electron Transfer. I". *The Journal of Chemical Physics,* 24.5 (1956), pp. 966–978.

[162] R. A. Marcus. "Electron transfer reactions in chemistry. Theory and experiment". *Protein electron transfer*. Garland Science, 2020, pp. 249–272.

[163] V. Cleave, G. Yahioglu, P. L. Barny, R. H. Friend, and N. Tessler. "Harvesting Singlet and Triplet Energy in Polymer LEDs". *Advanced Materials,* 11.4 (1999), pp. 285–288.

[164] C. Tonnele, M. Stroet, B. Caron, A. J. Clulow, R. C. R. Nagiri, A. K. Malde, P. L. Burn, I. R. Gentle, A. E. Mark, and B. J. Powell. "Elucidating the Spatial Arrangement of Emitter Molecules in Organic Light-Emitting Diode Films". *Angewandte Chemie - International Edition,* 56.29 (2017), pp. 8402–8406.

[165] J. C. Ribierre, A. Ruseckas, I. D. W. Samuel, S. V. Staton, and P. L. Burn. "Temperature dependence of the triplet diffusion and quenching rates in films of an $Ir(ppy)_3$-cored dendrimer". *Physical Review B,* 77.8 (2008), p. 085211.

[166] W. Holzer, A. Penzkofer, and T. Tsuboi. "Absorption and emission spectroscopic characterization of Ir(ppy)3". *Chemical Physics,* 308.1 (2005), pp. 93–102.

[167] J. Kalinowski, W. Stampor, M. Cocchi, D. Virgili, V. Fattori, and P. Di Marco. "Triplet energy exchange between fluorescent and phosphorescent organic molecules in a solid state matrix". *Chemical Physics,* 297.1 (2004), pp. 39–48.

[168] D. Bailey, J. Borwein, and R. Crandall. "Box integrals". *Journal of Computational and Applied Mathematics,* 206.1 (2007), pp. 196–208.

[169] M. Z. Shafikov, R. Daniels, and V. N. Kozhevnikov. "Unusually Fast Phosphorescence from Ir(III) Complexes via Dinuclear Molecular Design". *The Journal of Physical Chemistry Letters,* 10.22 (2019), pp. 7015–7024.

[170] J. Feng, J. Alves, D. M. de Clercq, and T. W. Schmidt. "Photochemical Upconversion". *Annual Review of Physical Chemistry,* 74.Volume 74, 2023 (2023), pp. 145–168.

[171] T. F. Schulze and T. W. Schmidt. "Photochemical upconversion: present status and prospects for its application to solar energy conversion". *Energy and Environmental Science,* 8.1 (2015), pp. 103–125.

[172] A. J. Carrod, V. Gray, and K. Borjesson. “Recent advances in triplet-triplet annihilation upconversion and singlet fission, towards solar energy applications”. *Energy and Environmental Science,* 15.12 (2022), pp. 4982–5016.

[173] C. Gao, W. W. H. Wong, Z. Qin, S.-C. Lo, E. B. Namdas, H. Dong, and W. Hu. “Application of Triplet-Triplet Annihilation Upconversion in Organic Optoelectronic Devices: Advances and Perspectives”. *Advanced Materials,* 33.45 (2021), p. 2100704.

[174] L. Zeng, L. Huang, J. Han, and G. Han. “Enhancing Triplet-Triplet Annihilation Upconversion: From Molecular Design to Present Applications”. *Accounts of Chemical Research,* 55.18 (2022), pp. 2604–2615.

[175] B. Zhang, K. D. Richards, B. E. Jones, A. R. Collins, R. Sanders, S. R. Needham, P. Qian, A. Mahadevegowda, C. Ducati, S. W. Botchway, and R. C. Evans. “Ultra-Small Air-Stable Triplet-Triplet Annihilation Upconversion Nanoparticles for Anti-Stokes Time-Resolved Imaging”. *Angewandte Chemie - International Edition,* 62.47 (2023), e202308602.

[176] D. G. Bossanyi, Y. Sasaki, S. Wang, D. Chekulaev, N. Kimizuka, N. Yanai, and J. Clark. “In optimized rubrene-based nanoparticle blends for photon upconversion, singlet energy collection outcompetes triplet-pair separation, not singlet fission”. *Journal of Materials Chemistry C,* 10.12 (2022), pp. 4684–4696.

[177] M. Wu, D. N. Congreve, M. W. B. Wilson, J. Jean, N. Geva, M. Welborn, T. V. Voorhis, V. Bulovic, M. G. Bawendi, and M. A. Baldo. “Solid-state infrared-to-visible upconversion sensitized by colloidal nanocrystals”. *Nature Photonics,* 10.1 (2016), pp. 31–34.

[178] M. Kinoshita, Y. Sasaki, S. Amemori, N. Harada, Z. Hu, Z. Liu, L. K. Ono, Y. Qi, N. Yanai, and N. Kimizuka. “Photon Upconverting Solid Films with Improved Efficiency for Endowing Perovskite Solar Cells with Near-Infrared Sensitivity”. *ChemPhotoChem,* 4.11 (2020), pp. 5271–5278.

[179] K. Okumoto, H. Kanno, Y. Hamada, H. Takahashi, and K. Shibata. “High efficiency red organic light-emitting devices using tetraphenyldibenzoperiflanthene-doped rubrene as an emitting layer”. *Applied Physics Letters,* 89.1 (2006), p. 013502.

[180] H.-H. Cho, S. Gorgon, G. Londi, S. Giannini, C. Cho, P. Ghosh, C. Tonnele, D. Casanova, Y. Olivier, T. K. Baikie, F. Li, D. Beljonne, N. C. Greenham, R. H. Friend, and E. W. Evans. “Efficient near-infrared organic light-emitting diodes with emission from spin doublet excitons”. *Nature Photonics,* 18.9 (2024), pp. 905–912.

[181] H.-H. Cho, S. Kimura, N. C. Greenham, Y. Tani, R. Matsuoka, H. Nishihara, R. H. Friend, T. Kusamoto, and E. W. Evans. "Near-Infrared Light-Emitting Diodes from Organic Radicals with Charge Control". *Advanced Optical Materials,* 10.21 (2022), p. 2200628.

[182] J. Zheng, Y. Hua, S. Yin, X. Feng, X. Wu, Y. Sun, Y. Li, C. Yang, and Z. Shuai. "White organic light-emitting devices using $Zn(BTZ)_2$ doped with Rubrene as emitting layer". *Chinese Science Bulletin,* 50.6 (2005), pp. 509–513.

[183] P. Ghosh, A. M. Alvertis, R. Chowdhury, P. Murto, A. J. Gillett, S. Dong, A. J. Sneyd, H.-H. Cho, E. W. Evans, B. Monserrat, F. Li, C. Schnedermann, H. Bronstein, R. H. Friend, and A. Rao. "Decoupling excitons from high-frequency vibrations in organic molecules". *Nature,* 629.8011 (2024), pp. 355–362.

[184] T. N. Singh-Rachford and F. N. Castellano. "Pd(II) Phthalocyanine-Sensitized Triplet-Triplet Annihilation from Rubrene". *The Journal of Physical Chemistry A,* 112.16 (2008), pp. 3550–3556.

[185] X. Li, W. Tan, X. Bai, and F. Li. "Stable Near-infrared-emitting Radical Nanoparticles for Fluorescence Imaging". *Chemical Research in Chinese Universities,* 39.2 (2023), pp. 192–196.

[186] Y. Chen, B. Lee, D. Fu, and V. Podzorov. "The Origin of a 650 nm Photoluminescence Band in Rubrene". *Advanced Materials,* 23.45 (2011), pp. 5370–5375.

[187] V. V. Tarasov, G. E. Zoriniants, A. I. Shushin, and M. M. Triebel. "The role of spin-lattice relaxation in magnetic field effects on the luminescence of amorphous and polycrystalline rubrene films". *Chemical Physics Letters,* 267.1 (1997), pp. 58–64.

[188] B. vander Zee, S. Paulus, R.-Q. Png, P. K. H. Ho, L.-L. Chua, G.-J. A. H. Wetzelaer, and P. W. M. Blom. "Role of Singlet and Triplet Excitons on the Electrical Stability of Polymer Light-Emitting Diodes". *Advanced Electronic Materials,* 6.8 (2020), p. 2000367.

[189] C. Wang, Y. Liu, Z. Ji, E. Wang, R. Li, H. Jiang, Q. Tang, H. Li, and W. Hu. "Cruciforms: assembling single crystal micro-and nanostructures from one to three dimensions and their applications in organic field-effect transistors". *Chemistry of Materials,* 21.13 (2009), pp. 2840–2845.

[190] F. Zhong and J. Zhao. "Phenyleneanthracene derivatives as triplet energy acceptor/emitter in red light excitable triplet-triplet-annihilation upconversion". *Dyes and Pigments,* 136 (2017), pp. 909–918.

[191] Y. J. Bae, G. Kang, C. D. Malliakas, J. N. Nelson, J. Zhou, R. M. Young, Y.-L. Wu, R. P. Van Duyne, G. C. Schatz, and M. R. Wasielewski. "Singlet Fission in 9,10-Bis(phenylethynyl)anthracene Thin Films". *Journal of the American Chemical Society,* 140.45 (2018), pp. 15140–15144.

[192] C. M. Sullivan, A. M. Szucs, A. P. Cantrell, K. E. Shulenberger, T. Siegrist, and L. Nienhaus. “Which Flavor of 9,10-Bis(phenylethynyl)Anthracene is Best for Perovskite-Sensitized Triplet-Triplet Annihilation?” *Advanced Energy Materials,* (2024), p. 2404130.

[193] T.-S. Fang, J. Lin, R. Schneider, T. Yamada, and L. Singer. “Studies on triplet-singlet energy transfer with 1,3-dibromo-9,10-bis-[phenylethynyl]-anthracene”. *Chemical Physics Letters,* 92.3 (1982), pp. 283–287.

[194] V. Gray, A. Dreos, P. Erhart, B. Albinsson, K. Moth-Poulsen, and M. Abrahamsson. “Loss channels in triplet-triplet annihilation photon upconversion: importance of annihilator singlet and triplet surface shapes”. *Physical Chemistry Chemical Physics,* 19.17 (2017), pp. 10931–10939.

[195] C. M. Sullivan and L. Nienhaus. “Recharging upconversion: revealing rubrene’s replacement”. *Nanoscale,* 14.46 (2022), pp. 17254–17261.

[196] D. Fatemi, H. Murata, C. Merritt, and Z. Kafafi. “Highly fluorescent molecular organic composites for light-emitting diodes”. *Synthetic Metals,* 85.1 (1997), pp. 1225–1228.

[197] V. Coropceanu, J. Cornil, D. A. da Silva Filho, Y. Olivier, R. Silbey, and J.-L. Brédas. “Charge Transport in Organic Semiconductors”. *Chemical Reviews,* 107.4 (2007), pp. 926–952.

[198] H.-H. Cho, D. G. Congrave, A. J. Gillett, S. Montanaro, H. E. Francis, V. Riesgo-Gonzalez, J. Ye, R. Chowdury, W. Zeng, M. K. Etherington, J. Royakkers, O. Millington, A. D. Bond, F. Plasser, J. M. Frost, C. P. Grey, A. Rao, R. H. Friend, N. C. Greenham, and H. Bronstein. “Suppression of Dexter transfer by covalent encapsulation for efficient matrix-free narrowband deep blue hyperfluorescent OLEDs”. *Nature Materials,* 23.4 (2024), pp. 519–526.

[199] G. Schwartz, K. Fehse, M. Pfeiffer, K. Walzer, and K. Leo. “Highly efficient white organic light emitting diodes comprising an interlayer to separate fluorescent and phosphorescent regions”. *Applied Physics Letters,* 89.8 (2006), p. 083509.

[200] S. Ye, J. Chen, C.-a. Di, Y. Liu, K. Lu, W. Wu, C. Du, Y. Liu, Z. Shuai, and G. Yu. “Phenyl-substituted fluorene-dimer cored anthracene derivatives: highly fluorescent and stable materials for high performance organic blue- and white-light-emitting diodes”. *Journal of Materials Chemistry,* 20.16 (2010), pp. 3186–3194.

[201] J. Brinen and J. Koren. “The lowest triplet state of 9, 10 diphenylanthracene”. *Chemical Physics Letters,* 2.8 (1968), pp. 671–672.

[202] C. Gao, B. Zhang, C. R. Hall, L. Li, Y. Chen, Y. Zeng, T. A. Smith, and W. W. H. Wong. “Triplet fusion upconversion using sterically protected 9,10-diphenylanthracene as the emitter”. *Physical Chemistry Chemical Physics,* 22.11 (2020), pp. 6300–6307.

[203] M. Mitsui, Y. Kawano, R. Takahashi, and H. Fukui. “Photophysics and photostability of 9,10-bis(phenylethynyl)anthracene revealed by single-molecule spectroscopy”. *RSC Advances,* 2.26 (2012), pp. 9921–9931.

[204] F. Edhborg, A. Olesund, and B. Albinsson. “Best practice in determining key photophysical parameters in triplet-triplet annihilation photon upconversion”. *Photochemical & Photobiological Sciences,* 21.7 (2022), pp. 1143–1158.

[205] Y. Murakami and K. Kamada. “Kinetics of photon upconversion by triplet-triplet annihilation: a comprehensive tutorial”. *Physical Chemistry Chemical Physics,* 23.34 (2021), pp. 18268–18282.

[206] M. Imran, X. Zhang, Z. Wang, X. Chen, J. Zhao, A. Barbon, and V. K. Voronkova. “Electron spin dynamics in excited state photochemistry: recent development in the study of intersystem crossing and charge transfer in organic compounds”. *Physical Chemistry Chemical Physics,* 23.30 (2021), pp. 15835–15868.

[207] S. Richert, C. E. Tait, and C. R. Timmel. “Delocalisation of photoexcited triplet states probed by transient EPR and hyperfine spectroscopy”. *Journal of Magnetic Resonance,* 280 (2017), pp. 103–116.

[208] O. Nolden, N. Fleck, E. R. Lorenzo, M. R. Wasielewski, O. Schiemann, P. Gilch, and S. Richert. “Excitation Energy Transfer and Exchange-Mediated Quartet State Formation in Porphyrin-Trityl Systems”. *Chemistry - A European Journal,* 27.8 (2021), pp. 2683–2691.

[209] K. Sandros, F. Haglid, R. Ryhage, and R. Stevens. “Transfer of Triplet State Energy in Fluid Solutions. III. Reversible Energy Transfer.” *Acta Chemica Scandinavica,* 18 (1964), pp. 2355–2374.

Appendix A

Kinetic Modelling of Doublet-Triplet Reversible Energy Transfer

A.1 Analytical Derivations for Doublet Populations

Starting with Scheme A.1:

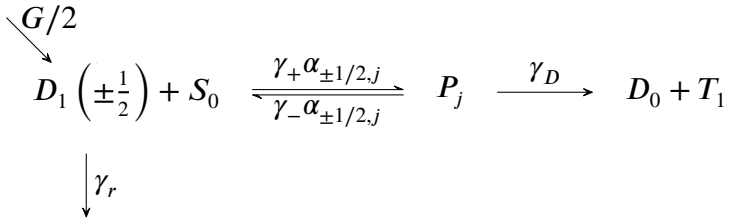

Scheme A.1: Kinetic mechanism for magnetosensitivity in luminescent radical-triplet systems

Expressions for the $\frac{\partial\left[D_{\pm\frac{1}{2}}\right]}{\partial t}$ and $\frac{\partial P_j}{\partial t}$ can be found, where $\left[D_{\pm\frac{1}{2}}\right]$ represent the population of the excited doublet. Assuming steady state conditions for $\left[D_{+\frac{1}{2}}\right]$,$\left[D_{-\frac{1}{2}}\right]$and P_j respectively:

$$\frac{G}{2} = \gamma_r\left[D_{+\frac{1}{2}}\right] + \sum_j\left(\gamma_+\alpha_{+\frac{1}{2},j}\left[D_{+\frac{1}{2}}\right] - \gamma_-\alpha_{+\frac{1}{2},j}P_j\right) \tag{A.1}$$

$$\frac{G}{2} = \gamma_r\left[D_{-\frac{1}{2}}\right] + \sum_j\left(\gamma_+\alpha_{-\frac{1}{2},j}\left[D_{-\frac{1}{2}}\right] - \gamma_-\alpha_{-\frac{1}{2},j}P_j\right) \tag{A.2}$$

$$P_j = \frac{\gamma_+\left(\alpha_{+\frac{1}{2},j}\left[D_{+\frac{1}{2}}\right] + \alpha_{-\frac{1}{2},j}\left[D_{-\frac{1}{2}}\right]\right)}{\gamma_D + \gamma_-\left(\alpha_{+\frac{1}{2},j} + \alpha_{-\frac{1}{2},j}\right)} \tag{A.3}$$

Substituting P_j from 4 into 2 and 3:

$$\frac{G}{2} = \gamma_r \left[D_{+\frac{1}{2}}\right] + \sum_j \left(\gamma_+ \alpha_{+\frac{1}{2},j} \left[D_{+\frac{1}{2}}\right] - \epsilon \gamma_+ \alpha_{+\frac{1}{2},j} \left(\frac{\alpha_{+\frac{1}{2},j} \left[D_{+\frac{1}{2}}\right] + \alpha_{-\frac{1}{2},j} \left[D_{-\frac{1}{2}}\right]}{1 + \epsilon \left(\alpha_{+\frac{1}{2},j} + \alpha_{-\frac{1}{2},j} \right)} \right) \right) \quad \text{(A.4)}$$

$$\frac{G}{2} = \gamma_r \left[D_{-\frac{1}{2}}\right] + \sum_j \left(\gamma_+ \alpha_{-\frac{1}{2},j} \left[D_{-\frac{1}{2}}\right] - \epsilon \gamma_+ \alpha_{-\frac{1}{2},j} \left(\frac{\alpha_{+\frac{1}{2},j} \left[D_{+\frac{1}{2}}\right] + \alpha_{-\frac{1}{2},j} \left[D_{-\frac{1}{2}}\right]}{1 + \epsilon \left(\alpha_{+\frac{1}{2},j} + \alpha_{-\frac{1}{2},j} \right)} \right) \right) \quad \text{(A.5)}$$

where $\epsilon = \frac{\gamma_-}{\gamma_D}$. Noting the separability of the terms in the summation over radical-triplet index j and that $\sum_j \alpha_{\pm\frac{1}{2},j} = 1$, relations for $\left[D_{+\frac{1}{2}}\right]$ and $\left[D_{-\frac{1}{2}}\right]$ can be collected:

$$\frac{G}{2} = \gamma_+ \left(\frac{\gamma_r}{\gamma_+} + 1 - \sum_j \left(\frac{\epsilon \left(\alpha_{+\frac{1}{2},j} \right)^2}{1 + \epsilon \left(\alpha_{+\frac{1}{2},j} + \alpha_{-\frac{1}{2},j} \right)} \right) \right) \left[D_{+\frac{1}{2}}\right] - \epsilon \gamma_+ \sum_j \left(\frac{\alpha_{+\frac{1}{2},j} \alpha_{-\frac{1}{2},j}}{1 + \epsilon \left(\alpha_{+\frac{1}{2},j} + \alpha_{-\frac{1}{2},j} \right)} \right) \left[D_{-\frac{1}{2}}\right] \quad \text{(A.6)}$$

$$\frac{G}{2} = \gamma_+ \left(\frac{\gamma_r}{\gamma_+} + 1 - \sum_j \left(\frac{\epsilon \left(\alpha_{-\frac{1}{2},j} \right)^2}{1 + \epsilon \left(\alpha_{+\frac{1}{2},j} + \alpha_{-\frac{1}{2},j} \right)} \right) \right) \left[D_{-\frac{1}{2}}\right] - \epsilon \gamma_+ \sum_j \left(\frac{\alpha_{-\frac{1}{2},j} \alpha_{+\frac{1}{2},j}}{1 + \epsilon \left(\alpha_{+\frac{1}{2},j} + \alpha_{-\frac{1}{2},j} \right)} \right) \left[D_{+\frac{1}{2}}\right] \quad \text{(A.7)}$$

Using the substitution $\kappa_j = \left(1 + \epsilon \left(\alpha_{+\frac{1}{2},j} + \alpha_{-\frac{1}{2},j} \right)\right)^{-1}$ and solving simultaneously:

$$\left[D_{\pm\frac{1}{2}}\right] = \frac{G}{2\gamma_+} \left\{ \frac{\frac{\gamma_r}{\gamma_+} + 1 + \epsilon \sum_j \kappa_j \left(\alpha_{\pm\frac{1}{2},j} \alpha_{\mp\frac{1}{2},j} - \left(\alpha_{\mp\frac{1}{2},j} \right)^2 \right)}{\prod_{i=\pm\frac{1}{2}} \left(\frac{\gamma_r}{\gamma_+} + 1 - \epsilon \sum_j \kappa_j \alpha_{i,j}^2 \right) - \epsilon^2 \left(\sum_j \kappa_j \alpha_{+\frac{1}{2},j} \alpha_{-\frac{1}{2},j} \right)^2} \right\} \quad \text{(A.8)}$$

Using these expressions, the total doublet photoluminescence, $\text{PL} = \gamma_r \left(\left[D_{+\frac{1}{2}}\right] + \left[D_{-\frac{1}{2}}\right] \right)$, can be found:

$$\mathrm{PL} = \frac{G\gamma_r}{\gamma_+}\left\{\frac{\frac{\gamma_r}{\gamma_+} + 1 - \frac{\epsilon}{2}\sum_j \kappa_j \left(\alpha_{+\frac{1}{2},j} - \alpha_{-\frac{1}{2},j}\right)^2}{\prod_{i=\pm\frac{1}{2}}\left\{\frac{\gamma_r}{\gamma_+} + 1 - \epsilon\sum_j \kappa_j \alpha_{i,j}^2\right\} - \epsilon^2\left(\sum_j \kappa_j \alpha_{+\frac{1}{2},j}\alpha_{-\frac{1}{2},j}\right)^2}\right\} \tag{A.9}$$

Similarly, the doublet spin polarisation in the excited state can be defined:

$$\frac{\left[D_{+\frac{1}{2}}\right] - \left[D_{-\frac{1}{2}}\right]}{\left[D_{+\frac{1}{2}}\right] + \left[D_{-\frac{1}{2}}\right]} = \frac{\epsilon}{2}\frac{\sum_j \kappa_j \left(\left(\alpha_{+\frac{1}{2},j}\right)^2 - \left(\alpha_{-\frac{1}{2},j}\right)^2\right)}{\frac{\gamma_r}{\gamma_+} + 1 - \frac{\epsilon}{2}\sum_j \kappa_j \left(\alpha_{+\frac{1}{2},j} - \alpha_{-\frac{1}{2},j}\right)^2} \tag{A.10}$$

A.2 Rate Constants used for Kinetic Scheme

Rate	Value (ns^{-1})	Source
γ_r	0.04	$\tau = 25$ ns assumed as typical radical excited state lifetime.[1,31]
γ_+	10	$\tau = 100$ ps. Utilising the rate of radical-enhanced ISC shown in previous radical-chromophore systems.[47,134]
γ_-	1	Chosen as $\gamma_+/10$
γ_D	0.1	Dissociation rate estimated for rubrene triplets from power dependence for the onset of bimolecular TTA.[135]

Table A.1: Rate constants used for modelling of reversible doublet-triplet energy transfer in Chapter 4.

A.3 Introduction of a Δg-Mechanism

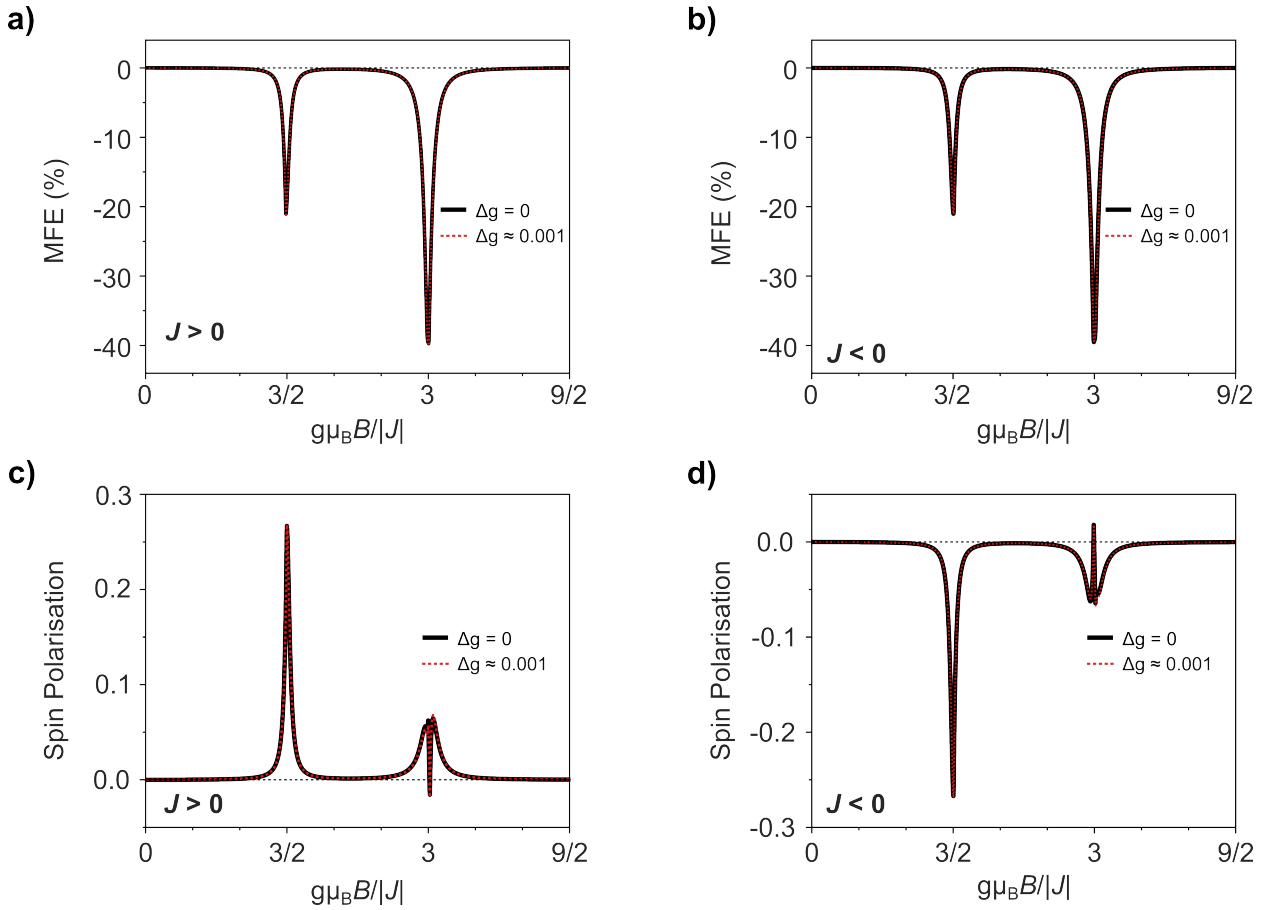

Figure A.1: Magnetic response for a system of strongly coupled radical-triplet pairs ($|J| = 20|D|$, i.e.$|J| \gg |D|$) that are randomly oriented with respect to an applied magnetic field. Results are shown either with $g_e = 2.0023$ for both radical and triplet ($\Delta g = 0$), or with $g_e = 2.0023$ for radical and 2.001 for triplet ($\Delta g \approx 0.001$). MFEs for doublet photoluminescence from radical-triplet systems with a) ferromagnetic ($J > 0$) and b) antiferromagnetic ($J < 0$) exchange coupling. Magnetosensitivity for spin polarisation from radical-triplet systems with c) $J > 0$ and d) $J < 0$ exchange coupling.

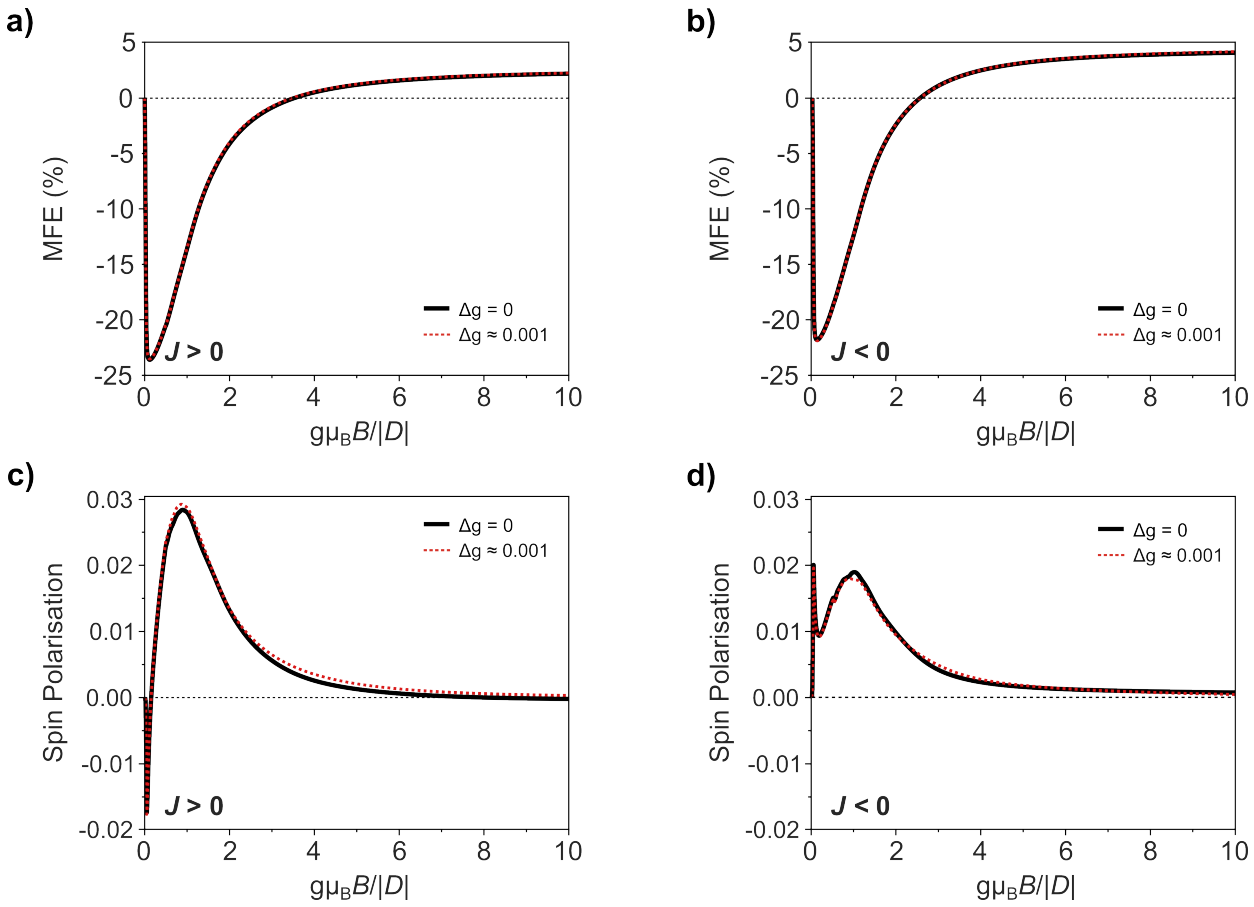

Figure A.2: Magnetic response for a system of weakly coupled radical-triplet pairs ($|J| = 0.02|D|$, i.e.$|J| \ll |D|$) that are randomly oriented with respect to an applied magnetic field. Results are shown either with $g_e = 2.0023$ for both radical and triplet ($\Delta g = 0$), or with $g_e = 2.0023$ for radical and 2.001 for triplet ($\Delta g \approx 0.001$). MFEs for doublet photoluminescence from radical-triplet systems with a) ferromagnetic ($J > 0$) and b) antiferromagnetic ($J < 0$) exchange coupling. Magnetosensitivity for spin polarisation from radical-triplet systems with c) $J > 0$ and d) $J < 0$ exchange coupling.